Computational modelling and parameter estimation in fixed beds of non-spherical pellets

Important note
To cite this publication, please use the final published version (if applicable).
Please check the document version above.

Computational Modelling and Parameter Estimation in Fixed Beds of Non-Spherical Pellets

Proefschrift

ter verkrijging van de graad van doctor

aan de Technische Universiteit Delft,

op gezag van de Rector Magnificus prof. dr. ir. T.H.J.J. van der Hagen,

voorzitter van het College voor Promoties,

in het openbaar te verdedigen op vrijdag 22 februari 2019 om 10:00 uur

door

Elyas MOHAMMADZADEH MOGHADDAM

Master of Science in Chemical Engineering,

Iran University of Science and Technology, Iran,

geboren te Gonabad, Iran

Computational Modelling and Parameter Estimation in Fixed Beds of Non-Spherical Pellets

Dissertation

For the purpose of obtaining the degree of doctor

at Delft University of Technology

by the authority of Rector Magnificus, Prof.dr.ir. T.H.J.J. van der Hagen,

chair of the Board for Doctorates

to be defended publicly on

Friday 22 February 2019 at 10:00 o'clock

by

Elyas MOHAMMADZADEH MOGHADDAM

Master of Science in Chemical Engineering,

Iran University of Science and Technology, IRAN

Born in Gonabad, IRAN

TUDelft Delft University of Technology

Dedicated to my beloved parents Zohreh and Hassan, my sister Soheila and my brothers Abolfazl and Amin,

and

to whom not only judged the world, but also changed it for the benefit of humanity...

Synopsis

Fixed bed arrangements find wide applications, particularly in reaction engineering, where they are employed as multi-tubular catalytic reactors for the transformation of reactants into desired products. The importance of such complicated reactors can be realized by their extensive applications as the process workhorse in various industries, e.g. chemical, pharmaceutical and petrochemical. The design of such systems is predominantly rooted in macroscopic models, e.g. pseudo-continuum approaches, with effective parameters extracted from averaged semi-empirical correlations. However, such simplistic design procedures are inadequate for design of tubular fixed beds with low tube-to-particle diameter ratios, say $d_t/d_p<10$, where lateral heterogeneities of the tortuous structure lead to dominance of localised phenomena. These local or "pellet-scale" effects cannot be captured nor explained by pseudo-continuum models, and call for 3D spatially-resolved simulations of flow and transport scalars. However, majority of the prevailing efforts within the context of "particle-revolved CFD simulation", have dealt with fixed beds of spheres, because generating random packing of non-spherical pellets necessitates a cumbersome and complicated strategy to account for the orientation freedom of such pellets, specifically when collisions occur.

The main aim of this research is therefore to develop and validate/benchmark an efficient and integrated workflow to predict the in-situ behaviour of hydrodynamics and thermal field in fixed beds containing non-spherical and even non-convex pellets with high accuracy. The workflow consists of a sequential Rigid Body Dynamics and Computational Fluid Dynamics (RBD-CFD) approach, applied to perform particle-resolved CFD simulations in fixed beds of (non-)spherical and non-convex pellets. RBD is an analytical scheme capable of simulating the dynamic behaviour of assemblies of pellets based on Newton's laws of motion and Lagrangian mechanics. The concept of RBD is used to develop a hard-body random packing algorithm to synthesize realistic packing structures of non-spherical pellets. The proposed algorithm uses impulse theory together with a quadratic optimization routine to model collision phenomena. The RBD-algorithm is used to generate random packing of spheres, cylinders and Raschig rings and then benchmarked against published analytical and empirical data. Using the RBD-algorithm, the influence of physio-mechanical properties of pellets such as friction and restitution coefficient on packing densification are investigated. A series of steps is then pursued to construct a computational CFD grid over the RBD-generated packing of spheres, cylinders and Raschig rings. These steps involve an inflationary meshing scheme for such complicated tortuous topologies using a combination of patch conforming and patch independent meshing approaches. This meshing approach provides a high-quality mesh to

appropriately capture phenomena at the contact regions, and immensely facilitates solution convergence in the turbulent region, without the need to manipulate the under-relaxation factors. The workflow, i.e. RBD-CFD methodology, is then benchmarked for a wall-heated fixed bed problem, where particle-resolved CFD simulations of hydrodynamics and heat transfer are performed in laminar, transient and turbulent regimes, for $5 \leq Re_p \leq 3,000$, in random packing of spheres, cylinders and Raschig rings with tube-to-pellet diameter ratios ranging from 2.29 to 6.1. The results are compared with literature data concerning azimuthally-averaged axial velocity profile, pressure drop and particle-to-fluid heat transfer Nusselt number, Nu_{fs}. The post-processing of RBD-CFD simulation results reveal a large influence of local structure on the velocity and temperature distributions at the pellet scale, particularly in narrow packings, where the spatial heterogeneity of the structure is very strong along the bed axis. Compared to random packing of spheres, in random packing of cylinders and Raschig rings more intense inhomogeneities in local velocity and temperature fields are observed. This feature is completely neglected when using pseudo-continuum models with averaged parameters. Furthermore, the results demonstrate that the azimuthal averaging of velocity and temperature fields lead to underestimating local velocity and temperature values by more than 400% and 50 K, respectively. The last part of this thesis is centered around the classical pseudo-continuum models, where we employed the results of RBD-CFD simulations, i.e. so-called numerical experiments, to elucidate the effective heat transfer parameters introduced in the 2D axial dispersive plug flow pseudo-homogenous model, i.e. 2D-ADPF heat transfer model. The results demonstrate that the reactor length-dependency of the values of k_{er} and h_w are conceptually inherent in such effective thermal parameters and stems from the evolutionary trend of the thermal (dis-)equilibrium between fluid and catalyst phases along the bed length. A detailed sensitivity analysis is conducted to find the influence of pellet shape and thermal conductivity, as well as tube-to-pellet diameter ratio, on the effective heat transfer parameters. The results provide an intuitive picture of the contributions of the different transport mechanisms to the effective thermal properties, concluding that the models of Specchia/Baldi/Gianetto/Sicardi for all flow regimes and of Martin/Nilles for the turbulent regime can be recommended for practical use for spherical pellets. Overall, the results of this thesis show that the RBD-CFD methodology is a robust and reliable tool, providing detailed information on the "pellet-scale" behavior of transport processes in fixed bed reactors of non-spherical pellets. Furthermore, the methodology can be used as a tool to tune simplistic pseudo-continuum models to improve their reliability.

Samenvatting

Gepakte bedden hebben veel toepassingen, met name in reactor engineering, waar ze worden ingezet als multitubulaire katalytische reactoren voor de omzetting van reactanten in gewenste producten. Het belang van dergelijke gecompliceerde reactoren wordt duidelijk door hun uitgebreide toepassing als proces werkpaard in allerlei industrieën, zoals de chemische, farmaceutische en petrochemische. Het ontwerp van deze systemen is voornamelijk op basis van macroscopische modellen, met bijvoorbeeld een pseudo-continue aanpak, met effectieve parameters uit gemiddelde semi-empirische correlaties. Dergelijke simplistische ontwerpprocedures zijn echter ontoereikend voor het ontwerp van tubulaire gepakte bedden met een lage tube-tot-deeltje diameter ratio, zeg $d_t/d_p < 10$, waar laterale inhomogeniteiten van de bochtige structuren leiden tot overwegend gelokaliseerde fenomenen. Deze lokale of "deeltjes-schaal" effecten kunnen niet gevangen worden, noch verklaard worden, door pseudo-continue modellen, en vragen om 3D ruimtelijke simulaties van stroming en scalaire transportgrootheden. Echter, de meeste "deeltjes-opgeloste CFD simulaties" hebben zich bezig gehouden met gepakte bedden van bollen, omdat het genereren van een willekeurige pakking van niet-ronde deeltjes noodzakelijkerwijs een lastige en gecompliceerde strategie vereist om rekening te houden met de rotatie vrijheid van zulke deeltjes, met name wanneer er botsingen optreden.

Het voornaamste doel van dit onderzoek is daarom het ontwikkelen en valideren van een efficiënte en geïntegreerde werkstroom die de in-situ hydrodynamica en thermische velden in gepakte bedden met niet-ronde en zelfs niet-convexe deeltjes met hoge nauwkeurigheid kan voorspellen. De werkstroom bestaat uit een opeenvolgende Rigid Body Dynamics en Computational Fluid Dynamics (RBD-CFD) aanpak, welke wordt toegepast om deeltjes-opgeloste CFD simulaties van gepakte bedden met niet-ronde en niet-convexe deeltjes uit te voeren. RBD is een analytische aanpak waarmee het dynamische gedrag van een verzameling deeltjes kan worden gesimuleerd, gebaseerd op Newton's bewegingswetten en Lagrangiaanse mechanica. Het concept van RBD is gebruikt om een algoritme te ontwikkelen voor harde lichamen, waarmee realistische willekeurige pakkingen van niet-ronde deeltjes gegenereerd kunnen worden. Het voorgestelde algoritme maakt gebuik van impulstheorie, tezamen met een kwadratische optimalisatie routine, om de botsingsfenomenen te modeleren. Het RBD algoritme is gebruikt om willekeurige pakkingen te genereren voor bollen, cilinders en Raschig ringen, en is vervolgens vergeleken met gepubliceerde analytische en empirische data. Met behulp van het RBD algoritme is de invloed van fysisch-mechanische eigenschappen van de deeltjes, zoals wrijving en restitutiecoëfficiënt, op de pakkingsdichtheid onderzocht. Vervolgens

is een serie stappen ondernomen om een CFD rooster te construeren, over de RBD-gegenereerde pakkingen van bollen, cilinders en Raschig ringen. Deze stappen omvatten een inflatoir roosterschema voor dergelijke gecompliceerde bochtige topologieën, met behulp van een combinatie van een patch conforming en patch onafhankelijke roosteraanpak. Deze roosteraanpak leidt tot een hoge kwaliteit rooster welke de fenomenen in de contactregio's goed kan vangen, en de convergentie van de oplossing in de turbulente regio's vergemakkelijkt, zonder de noodzaak om onderrelaxatiefactoren aan de passen. De werkstroom, d.w.z. de RBD-CFD methodologie, is vervolgens gebenchmarked voor een wandverwarmd gepakt bed probleem, waarin de deeltjes-opgeloste CFD simulaties van hydrodynamica en warmteoverdracht zijn uitgevoerd in het laminaire, transitie en turbulente regime, voor $5 \leq \mathrm{Re_p} \leq 3{,}000$, in willekeurige pakkingen van bollen, cilinders en Raschig ringen met tube-tot-deeltje diameter ratio's variërend van 2.29 tot 6.1. De resultaten zijn vergeleken met literatuurdata over azimutaal-gemiddelde axiale snelheidsprofielen, drukval en deeltje-naar-vloeistof warmteoverdracht Nusselt nummer, $\mathrm{Nu_{fs}}$. Post-processing van de RBD-CFD simulatieresultaten laten een grote invloed van de lokale deeltjes structuur op de snelheids- en temperatuurdistributie op de deeltjesschaal zien, met name in smalle pakkingen, waar de ruimtelijke heterogeniteit van de structuur langs de as van het bed heel sterk is. Vergeleken met willekeurige pakkingen van bollen, worden in willekeurige pakkingen van cilinders en Raschig ringen meer intensieve inhomogeniteiten in lokale snelheids- en temperatuurvelden waargenomen. Dit kenmerk wordt compleet genegeerd wanneer men pseudo-continue modellen met gemiddelde parameters gebruikt. De resultaten laten zien dat azimutaal middelen van snelheids- en temperatuurvelden leidt tot een onderschatting van de lokale snelheid en temperatuur van meer dan, respectievelijk, 400% en 50K. Het laatste onderdeel van dit proefschrift concentreert zich op klassieke pseudo-continue modellen, waar we de resultaten van RBD-CFD simulaties hebben gebruikt in zogenaamde numerieke experimenten, om de effectieve warmteoverdrachtsparameters te vinden welke gebruikt kunnen worden in een 2D axiaal dispersieve propstroom pseudo-homogeen (2D-ADPF) warmteoverdrachtsmodel. De resultaten laten zien dat de reactor-lengte afhankelijkheid voor de waarden van k_{er} en h_w conceptueel onafscheidelijk verbonden zijn aan dergelijke effectieve thermische eigenschappen, en veroorzaakt zijn door de evolutionaire trend van het thermische (niet-)evenwicht tussen vloeistof en vaste fases langs de hoogte van het bed. Een gedetailleerde gevoeligheidsanalyse laat de invloed zien van deeltjesvorm en thermische geleiding, alsmede de tube-tot-deeltjes diameter ratio, op de effectieve warmteoverdrachtsparameters.

De resultaten bieden een intuïtief beeld van de bijdragen van verschillende transportmechanismen aan de effectieve thermische eigenschappen, met de conclusie dat de

iv

modellen van Specchia/Baldi/Gianetto/Sicardi voor alle stromingsregimes en van Martin/Nilles voor het turbulente regime aangeraden kunnen worden voor praktisch gebruik voor ronde deeltjes. De resultaten van dit proefschift laten zien dat de RBD-CFD methodologie een robuust en betrouwbaar gereedschap is, welke gedetailleerde informatie kan verschaffen over het gedrag op deeltjes-schaal van transport processen in gepakte bed reactoren met niet-ronde deeltjes. De methodologie kan verder gebruikt worden om parameters in simplistische pseudo-continue modellen af te schatten, en zo de betrouwbaarheid van deze modellen te verhogen.

Table of Contents

List of Figures

List of Tables

Chapter 1

Introduction

1.1.   Background

Fixed bed arrangements are widely used in processing industries, for example as catalytic reactors, separators, absorbers, dryers, and heat exchangers, where aspects of heat transfer play a crucial role in determining the overall performance of such units. The most extensive application of fixed bed systems can be found in the field of reaction engineering, where they play a dominant role (due to enhanced wall-to-bed transport rate) in highly endothermic catalytic reactions such as methane steam reforming [1,2] and in highly exothermic catalytic reactions such as oxidation of n-butane to maleic anhydride [3]. An optimal and safe design of such systems, with predominantly low bed-to-particle diameter ratios, N, stacked in multi-tubular fixed bed arrangements, requires dependable information on lateral heat transfer through the tortuous structure. Poor radial heat transfer is considered as a major problem, with the possibility of a thermal runaway, i.e. uncontrolled temperatures in specific locations within the reactor.

The best course of action for the design of such complicated systems is to adopt refined models, capable of reflecting the underpinning physiochemical concepts and therefore predictively mimicking system behavior. Because of the crucial role of heat transfer in the design of fixed beds, numerous researchers have paid particular attention to this subject over the past few decades, covering various modeling approaches and "effective" design parameters [4]. However, the main trend of most of these research efforts has been towards developing or improving simple (macroscopic) models, e.g. pseudo-homogenous models, which reflect a few selected features of such systems, suitable for fast and repetitive engineering calculations for the study of design, control, parametric sensitivity, etc. There are a number of prevailing doubts and shortcomings connected with such pseudo-continuum approaches, including the lack of universality as well as a remarkable disagreement between existing correlations for effective parameters. The shortcomings can be ascribed to the concepts and approximations behind such models, e.g. pseudo-homogeneity, unidirectional plug flow assumption, and (lumped) effective parameters [5]. This has made it extremely difficult for designers of fixed bed reactors in selecting appropriate/dependable design approaches, particularly in case of narrow tubular fixed beds where the radial heat transfer (especially at vicinity of tube wall) is one of the most important design aspects [6,7]. Moreover, the problematic roles of wall-effects in radial thermal behaviour of such low-N beds, say $N \leq 10$, have exacerbated the intricacies associated with the design of such complicated arrangements. In narrow tubular fixed beds, the modeling of the near-wall heat transfer with a single apparent wall heat transfer coefficient, h_w, is very questionable: this effective parameter is used to describe the temperature jump at

the wall that is not physically present but which, based on experimental results, cannot be described more accurately [4]. Despite extensive research efforts on modelling of transport processes in fixed bed systems, even sophisticated macroscopic models still rely on simplifying assumptions and, consequently, disparity and disagreement between various existing design correlations are evident [5,8–10]. This situation effectively forces the designers to seek validation of their design calculations through supplementary experimental studies, thereby imposing large additional expenses to a project.

Over the last few decades, advances in computer performance and computational techniques have allowed researchers to conduct comprehensive 3D simulations of flow fields and transport scalars within tubular fixed beds containing several hundred particles using Computational Fluid Dynamics (CFD) and Lattice Boltzmann methods (LBM), see e.g. [11–16]. However, majority of these particle-resolved efforts have concentrated on spherical packing structures, whilst applications of catalyst pellets of non-spherical shape such as cylinders, Raschig rings, trilobe, quadrulobe, hollow extrudates, etc. are common in industry because of their potential to enhance transport processes (e.g. Raschig rings are used in ethylene epoxidation, and multi-hole shaped catalyst pellets are used in methane steam reforming units). The dominance of spherical packing studies can be attributed to the cumbersome and complicated strategies needed to generate 3D models for packing structures of non-spherical pellets, which is an essential prerequisite for CFD simulations. The orientational freedom of non-spherical particles makes the procedure of packing simulations very problematic, both in terms of modeling the collision phenomena and computational expense. Nonetheless, the amount of literature addressing the structural properties of non-spherical packings is very scarce, see e.g. [14,17–19].

With all these outstanding issues on simulation and design of tubular fixed beds, the research described in this thesis is aimed at tackling and addressing certain aspects of the overall problem, in particular aspects of the prevailing heat transfer. The methodology not only needs to improve on the main limitations of earlier models, but it should also be found on realistic hypotheses about the underpinning physicochemical concepts, and lead to an improvement of our understanding of localised phenomena, e.g. the role of spatial heterogeneity of the tortuous structure and shape of the pellets on system performance. We will employ a novel and integrated computational approach based on sequential Rigid Body Dynamics (RBD) and Computational Fluid Dynamics to characterise flow hydrodynamics and heat transfer features in tubular fixed beds containing (non)-spherical pellets. This RBD approach enables us to synthesize random packing structures of non-spherical and even non-convex particles, which are then compared, in terms of both global and local topological properties,

with realistic random packing arrangements. The generated structures are then fed to a CFD simulation tool for further analysis of the in-situ behaviour of hydrodynamics as well as the prevailing temperature fields inside tortuous structures.

In the post-processing of the RBD-CFD simulation results, we will strive to elucidate the role of tortuous structure and flow mal-distribution and, accordingly, the interaction between radial temperature field and velocity distribution. The RBD-CFD simulation results will also be used to explain the prevailing ambiguities connected with pseudo-homogeneous models, and, moreover, to investigate the influence of particles of different shape on the thermal behaviour of random packing structures.

1.2. Scope of thesis

The main aim of this study is to characterise the hydrodynamics and heat transfer in fixed beds through a novel integrated workflow based on the sequential RBD-CFD methodology. We will focus on wall-heated fixed beds for a wide range of particle Reynolds numbers, covering all relevant flow regimes. In particular, this study is aimed at:

1. Development of a hard-body random packing algorithm to synthesize realistic packing topologies of non-spherical and non-convex pellets.

2. Investigation of the influence of the physio-mechanical properties of pellets, e.g. surface friction factor and coefficient of restitution, on packing densification.

3. Development, verification and validation of an integrated workflow to perform particle-resolved CFD simulation of flow hydrodynamics and heat transfer in randomly packed fixed beds of non-spherical pellets.

4. Post-processing analysis of RBD-CFD simulation results. The in-situ behavior of velocity and thermal fields as well as the role of structural heterogeneity are meticulously addressed.

5. Investigating the influence of dimensionality (tube over pellet diameter) and pellet design changes on the thermal behaviour of random packing structures.

6. Elucidating and explaining the shortcomings linked with macroscopic models, i.e. tailor-made pseudo-homogeneous models.

Identifying and quantifying bed length effects on the effective heat transfer parameters (design parameters).

The findings of this research should contribute significantly to the subject matter of transport processes in fixed bed systems, and show that the methodology of "Numerical

Experiments" can achieve and access data comparable to those obtained from expensive advanced experimental techniques such as MRI and 3D-CT.

1.3. Outline of thesis

This thesis is arranged in seven chapters as outlined below:

Chapter 2, "Literature Review on Modelling of Tubular Fixed Bed Reactors: Aspects of Hydrodynamics and Heat Transfer", presents a comprehensive review concerning design aspects of tubular fixed bed reactors. The main concerns, as well as the often-cited hindrances towards modeling of hydrodynamics and wall-to-bed heat transfer in narrow fixed beds, are highlighted. This review highlights the still unresolved problems that call for further research.

In **Chapter 3, "A Rigid Body Dynamics Algorithm for Modelling Random Packing Structures of Non-Spherical and Non-Convex Pellets"**, we propose and validate a novel physics-based hard-body packing algorithm, based on Rigid Body Dynamics (RBD), to simulate fixed bed arrangements of non-spherical and non-convex pellets.

Chapter 4, "RBD-CFD Simulation of Fluid Flow and Heat Transfer: Preprocessing, Setup and Validation Study", presents an integrated workflow consisting of a sequential RBD and CFD approach to simulate the hydrodynamics and heat transfer in fixed beds containing non-spherical pellets. The stepwise flowchart of the workflow will be elaborated. The problem of a wall-heated fixed bed system will be explicitly described. The chapter is completed by a thorough benchmark analysis for simulations of hydrodynamics and heat transfer, covering wide range of particle Reynolds number, in random packings of spheres, cylinders and Raschig rings.

Chapter 5, "RBD-CFD Simulation of Fluid Flow and Heat Transfer: Importance of Heterogeneities and Inadequacy of Pseudo-Continuum Approaches", deals with the post-processing of RBD-CFD simulation results for the problem of a wall-heated fixed bed described in Chapter 4. The in-situ behavior of velocity and thermal fields in random packings of spheres, cylinders and Raschig rings are meticulously analyzed. The chapter is completed by addressing and explaining the inadequacies of modified versions of pseudo-continuum approaches in predicting radial heat transfer.

In **Chapter 6, "Evaluation of Effective Heat Transfer Parameters in Tubular Fixed Beds of Non-Spherical Pellets"**, we perform numerical experiments to elucidate the effective heat transfer parameters introduced in the classical k_{er}-h_w pseudo-homogenous model. A part of this chapter deals with the problem of reactor length-dependency of the values of k_{er}

and h_w, as well as the roles of shape and thermal conductivity of pellets and tube-to-pellet diameter ratio on k_{er} and h_w. The chapter is completed with a benchmark analysis, where the most promising literature correlations for Pe_{er} and Nu_w are examined to compare the predicted radial temperature profiles using k_{er}-h_w pseudo-homogenous model with those obtained from RBD-CFD simulation results.

Finally, in **Chapter 7, "Conclusions and Recommendations"**, we summarize the main conclusions and provide suggestions for future work.

Bibliography

[1]   E.H. Stitt, Reactor technology for syngas and hydrogen, in: Sustainable Strategies for the Upgrading of Natural Gas: Fundamentals, Challenges, and Opportunities, Springer, 2005: pp. 185–216.

[2]   M.T. Zambon, D.A. Asensio, G.F. Barreto, G.D. Mazza, Application of computational fluid dynamics (CFD) for the evaluation of fluid convective radial heat transfer parameters in packed beds, Industrial & Engineering Chemistry Research. 53 (2014) 19052–19061.

[3]   F. Trifirò, R.K. Grasselli, How the yield of maleic anhydride in n-butane oxidation, using VPO catalysts, was improved over the years, Topics in Catalysis. 57 (2014) 1188–1195.

[4]   A.G. Dixon, Fixed bed catalytic reactor modelling—the radial heat transfer problem, The Canadian Journal of Chemical Engineering. 90 (2012) 507–527.

[5]   A.G. Dixon, M. Nijemeisland, E.H. Stitt, Packed tubular reactor modeling and catalyst design using computational fluid dynamics, Advance in Chemical Engineering. 31 (2006) 307–389. doi:10.1016/S0065-2377(06)31005-8.

[6]   M.G. Freiwald, W.R. Paterson, Accuracy of model predictions and reliability of experimental data for heat transfer in packed beds, Chemical Engineering Science. 47 (1992) 1545–1560. doi:10.1016/0009-2509(92)85003-T.

[7]   P. Magnico, Pore-scale simulations of unsteady flow and heat transfer in tubular fixed beds, AIChE Journal. 55 (2009) 849–866. doi:10.1002/aic.11806.

[8]   M. Winterberg, E. Tsotsas, Correlations for effective heat transport coefficients in beds packed with cylindrical particles, Chemical Engineering Science. 55 (2000) 5937–5943. doi:10.1016/S0009-2509(00)00198-6.

[9]   O. Bey, G. Eigenberger, Gas flow and heat transfer through catalyst filled tubes, International Journal of Thermal Sciences. 40 (2001) 152–164. doi:10.1016/S1290-0729(00)01204-7.

[10]   D. Wen, Y. Ding, Heat transfer of gas flow through a packed bed, Chemical Engineering Science. 61 (2006) 3532–3542. doi:10.1016/j.ces.2005.12.027.

[11]   A.G. Dixon, G. Walls, H. Stanness, M. Nijemeisland, E.H. Stitt, Experimental validation of high Reynolds number CFD simulations of heat transfer in a pilot-scale fixed bed tube, Chemical Engineering Journal. 200–202 (2012) 344–356. doi:10.1016/j.cej.2012.06.065.

[12]   M. Behnam, A.G. Dixon, M. Nijemeisland, E.H. Stitt, A New Approach to Fixed Bed Radial Heat Transfer Modeling Using Velocity Fields from Computational Fluid Dynamics Simulations BT - Industrial & Engineering Chemistry Research, Industrial

and Engineering Chemistry Research. 52 (2013) 15244–15261. doi:10.1021/ie4000568.

[13]   T. Eppinger, K. Seidler, M. Kraume, DEM-CFD simulations of fixed bed reactors with small tube to particle diameter ratios, Chemical Engineering Journal. 166 (2011) 324–331. doi:10.1016/j.cej.2010.10.053.

[14]   G.D. Wehinger, T. Eppinger, M. Kraume, Evaluating catalytic fixed-bed reactors for dry reforming of methane with detailed CFD, Chemie-Ingenieur-Technik. 87 (2015). doi:10.1002/cite.201400153.

[15]   M. V Tabib, S.T. Johansen, S. Amini, A 3D CFD-DEM methodology for simulating industrial scale packed bed chemical looping combustion reactors, Industrial and Engineering Chemistry Research. 52 (2013) 12041–12058. doi:10.1021/ie302028s.

[16]   A. Singhal, S. Cloete, S. Radl, R. Quinta-Ferreira, S. Amini, Heat transfer to a gas from densely packed beds of monodisperse spherical particles, Chemical Engineering Journal. 314 (2017) 27–37. doi:10.1016/j.cej.2016.12.124.

[17]   G. Boccardo, F. Augier, Y. Haroun, D. Ferre, D.L. Marchisio, Validation of a novel open-source work-flow for the simulation of packed-bed reactors, Chemical Engineering Journal. 279 (2015) 809–820. doi:10.1016/j.cej.2015.05.032.

[18]   B. Partopour, A.G. Dixon, An integrated workflow for resolved-particle packed bed models with complex particle shapes, Powder Technology. 322 (2017) 258–272. doi:10.1016/j.powtec.2017.09.009.

[19]   A. Singhal, S. Cloete, S. Radl, R. Quinta-Ferreira, S. Amini, Heat transfer to a gas from densely packed beds of cylindrical particles, Chemical Engineering Science. 172 (2017) 1–12. doi:10.1016/j.ces.2017.06.003.

Chapter 2

Literature Review on Modelling of Tubular Fixed Bed Reactors: Aspects of Hydrodynamics and Heat Transfer

Abstract

A comprehensive review concerning design aspects of tubular fixed bed catalytic reactors is presented. The main concerns, as well as the often-cited hindrances towards modeling of hydrodynamics and wall-to-bed heat transfer in narrow fixed beds, are highlighted. The review shows that the prevailing radial porosity data are restricted to random packings of spheres, and few experimental works have dealt with non-spherical pellets. Recent advances in pseudo-continuum models are addressed and the position of Computational Fluid Dynamics (CFD) as a design tool for predicting the in-situ behavior of flow field and heat transfer is addressed. An overview of the most widely-used correlations for pressure drop and effective heat transfer parameters is presented. A comparison between published correlations demonstrates a large scatter of the predicted values for both effective Peclet number, Pe_{er}, and apparent wall Nusselt number, Nu_w, evidencing lack of a consensus between researchers concerning the description of the radial heat dispersion using pseudo-continuum models. This review discusses the current progress of the field and highlights the still unresolved problems that call for further research.

2.1.   Introduction

Fixed bed arrangements have found wide applications, particularly in reaction engineering where they are used as catalytic reactors for the transformation of reactants into desired products. A fixed bed reactor (FBR) is an assembly of usually uniformly sized catalytic particles, which are randomly arranged and firmly held in position within a vessel or tube. In such reactors, the reactants are supplied to the reactor with the bulk of fluid, flowing through the voids of the bed and in this way, the reactants are transported firstly from the bulk of the fluid to the catalyst external surface, then through catalyst pores, where the reactants adsorb on catalytic sites on the surface of the pores and then undergo chemical transformation. The products are then desorbed and are eventually transported back into the fluid bulk. FBRs are usually equipped with external heating or cooling systems, whereby the rates of reactions, bulk temperature and accordingly the product yield and selectivity are controlled. In some cases, hindrances associated with the process controllability (e.g. thermal run-away) may lead to a particular design of fixed beds, so-called shell side fixed beds, in which thermal tubes, including cooling or heating media, pass longitudinally through a shell filled by catalyst pellets.

The design of fixed bed catalytic reactors is very challenging because of the complexities inherent in the behaviour of transport scalars in a tortuous flow pattern, which make optimizing towards the product selectivity and yield, energy consumption as well as the total capital cost of a unit very problematic. The best course of action for a safe and reliable design is to develop appropriate models, describing the underpinning physio-chemical concepts, to mimic the behaviour of the system at the pellet scale. Most of the prevailing models, e.g.

pseudo-continuum models, have been developed for fixed beds of high tube-to-pellet diameter ratios (N), where the gradients in thermal and flow fields are reasonably mild, and hence can be averaged over the bed radius. However, handling highly exothermic or endothermic catalytic reactions (e.g. methane steam reforming and ethylene epoxidation) requires specific thermal management to avoid thermal runaway condition. This has led to employment of state-of-the-art fixed bed configurations with $N < 10$, i.e. multi-tubular fixed beds. The modelling of such a narrow tubular fixed bed is very complicated because of the presence of wall effects across the entire of tube radius, resulting in very sharp gradients in both flow and temperature fields. Such flow and thermal fields cannot be thoroughly addressed by simplistic pseudo-homogenous plug flow models with averaged transport properties [1–5]. In fact, the premise behind these models does not allow us to take the roles of topological non-uniformities as well as local flow maldistribution into account, whereas these can strongly influence the distribution of transport scalars within the narrow-tube fixed bed reactors [5–8]. In the 1990s, a series of investigations have been conducted to improve the classical models in terms of dispersion and fluid flow. For example, Stewart et al. [9] proposed the data-based Green's function methodology, and Kronberg and Westerterp [10] suggested a new "wave" model of dispersion and fluid flow. A group of researchers were inspired by the void fraction distribution, and thus strived to explain the radial inhomogeneities in the overall velocity field by flow channeling in the wall region, where the local porosity approaches one. This group suggested coupling a simplified version of a radially varying axial velocity profile, $v_z(r)$, with homogenous heat transfer models to account for the roles of velocity field, e.g. [11–13]. However, these modifications could not compensate for the oversimplifications inherent in homogenous models, e.g. using so-called "effective" heat and mass transfer parameters to describe the local transport processes and mechanisms, specifically in low-N fixed bed reactors.

Major developments in computer performance and numerical computations in the 2000s have allowed researchers to use Computational Fluid Dynamics (CFD) simulations to obtain a better understanding of transport processes within fixed beds. In fact, a more rigorous "discrete particle" or "particle resolved" CFD simulation of fixed bed reactors can provide further details of a reacting flow and transport processes at the pellet scale, aiding a more safe and reliable design of the system compared with the macroscopic pseudo-continuum approaches. A large quantity of publications has appeared, indicating the importance of CFD in providing valuable information on the nature of transport processes occurring within fixed beds [8,14–19]. However, the majority of these efforts have concentrated on spherical pellet packing structures, whilst application of catalyst pellets of non-spherical shapes such as cylinders, Raschig rings, trilobe, quadrulobe, hollow extrudates, etc. is becoming more popular

in industry because of their potential to enhance transport processes (e.g. Raschig rings are used in ethylene epoxidation process and multi-hole shaped catalyst pellets are used for methane steam reforming). The relative absence in CFD literature may be attributed to the difficulties inherent in discrete pellet modeling of random packing structures of such non-spherical pellets [20].

The aim of this chapter is to address the progress in modeling and design aspects of fixed bed reactors, with an emphasis on hydrodynamics and heat transfer. We will shed light on current progress, bottlenecks of the design, and areas that call for further research.

2.2. Fixed bed structures

The design of randomly-packed fixed bed reactors is strongly influenced by the structure of the packing matrix, which in turn is governed by the shape, dimensions and the loading of the constituent particles. Fundamentally, the structure of a packing affects the hydrodynamics, heat and mass transport at the pellet scale, which, in turn, influences macroscopic parameters, e.g. yield and selectivity, in reaction processes. This has inspired researchers to delve profoundly into the topological features of random packing structures, e.g. [22–35]. These studies can be classified into three main categories, based on their main point of interest: (i) bulk porosity, (ii) radial porosity distribution, and (iii) algorithms for generating random packing structures. Here a brief review of the bulk and local porosity is given, whilst a deep coverage of the third category will be presented in chapter three.

2.2.1. Bulk porosity

The packing structure of spherical particles is the most well-studied topology in fixed bed systems. The minimum bulk porosity, corresponding to the highest packing density, of such a packing is reported as 0.36 for uniform-sized spheres, while values for real random packings typically fall in the range of 0.36 to 0.42, [33]. Similar to spheres, cylindrical pellets are prevalent in chemical engineering applications, where they have remarkable advantages for enhancing transport processes in fixed bed unit operations. However, the packing structure is fundamentally different from sphere packings, because cylinders have orientational degrees of freedom, and their geometry embraces a diversity of surface elements, i.e. sharp corners as well as flat and curved surfaces. These essential differences have resulted in more diverse packing geometries of cylinders, which is evidenced by the wide range of bulk porosity values reported in the literature, e.g. the bulk porosity for random packings of equilateral cylinders varies from 0.25 (Roblee et al. [36]) to 0.445 (Coelho et al. [37]), which is evidently much broader than for spheres. From a practical point of view, this observation may suggest that correlating the bulk

heat and mass transport properties for packings of cylinders is significantly more difficult than for packings of spheres. Similar interpretations can be found for other non-spherical pellets, e.g. Raschig rings, hollow cylinders, trilobes, etc., although the amount of literature on packings of non-convex pellet shapes is very scarce. The most-used correlations for bulk porosity relate to the experimental works by Dixon [23] and Foumeny and coworkers [29,38,39]. Dixon [23] measured the bulk porosity of a number of packings, including spheres, equilateral cylinders and Raschig rings, and developed correlations as a function of column-to-pellet diameter ratio, N. However, in this work, the columns were packed by slow pouring of the packing material manually without tamping, resulting in certain random loose packings. Foumeny and coworkers have measured the bulk void fraction of packings of different pellets shapes, including spheres, cylinders with different aspect ratios and Raschig rings, and proposed empirical correlations for dense packing porosities. In these works, pellets were simply poured into a column and gently vibrated in order to generate a much denser structure. Table 2.1 gives a summary of the correlations proposed by these research groups.

Table 2.1 Summary of the most-used predictive correlations for bulk porosity

Pellet shape	Authors	Correlations	N
Sphere	Dixon [23]	$\varepsilon = 0.4 + 0.05/N + 0.412/N^2$	≥ 2
	Foumeny et al. [39]	$\varepsilon = 0.383 + 0.254N^{-0.923}\dfrac{1}{\sqrt{0.723N - 1}}$	≥ 1.86
Cylinder	Dixon [23]	$\varepsilon = 0.36 + 0.1/N_{pv} + 0.7/N_{pv}^2$	≥ 1.67
	Foumeny & Roshani [29]	$\varepsilon = 0.293 + 0.684N_{pv}^{-0.85}\dfrac{1}{\sqrt{1.837N_{pv} - 1}}$	≥ 1.86
Raschig rings	Dixon [23]	$\left(1 - \varepsilon_{hc}\right) = \left(1 + 2(d_i/d_o - 0.5)^2(1.145 - 1/N_{pv})\right)$ $\times \left(1 - (d_i/d_o)^2\right)\left(1 - \varepsilon_{sc}\right)$	≥ 1.67
	Foumeny & Benyahia [38]	$\varepsilon_{hc} = \varepsilon_{sc} + 0.97\left(1 - \varepsilon_{sc}\right)(d_i/d_o)^2$	≥ 1.86

2.2.2. Radial porosity distribution

The porosity variation of randomly-packed fixed beds in the near wall region has been investigated intensely during the last four decades as it influences the pressure drop, bed permeability, transport properties and residence time distribution. The role of the near wall region becomes more significant in tubular fixed beds with small bed-to-particle diameter ratios, typically less than 10 [5]. Roblee et al. [36] were one of the first research groups to measure the radial void fraction distribution in the near wall region experimentally. The authors used packing cardboard cylinders with cork spheres and filled the void space with molten wax. After the wax solidified in the void volumes, sections were cut out and the wax

fraction in each section was analyzed. The authors reported a damped oscillatory trend for the radial void fraction distribution, which approaches a constant value after 4 to 5 particle diameters from the wall. After this finding, several investigations were devoted to the determination of the radial porosity distribution in fixed bed arrangements [7,8,22,24,30,33,40–43]. Virtually all these studies showed that the local porosity varies in an oscillatory pattern with an amplitude declining with increasing distance from the wall, and this oscillation is damped after a distinct number of particles (from 4 to 6) from the wall (see Fig.1). However, a major part of these studies focused on random packings of spheres, whilst only a few works have dealt with the local porosity variation in non-spherical packings [12,44]. Table 2.2 presents the correlations proposed by de Klerk [30] for sphere packings, which have been widely-used in several studies, and by Roshani [44] for cylindrical pellets.
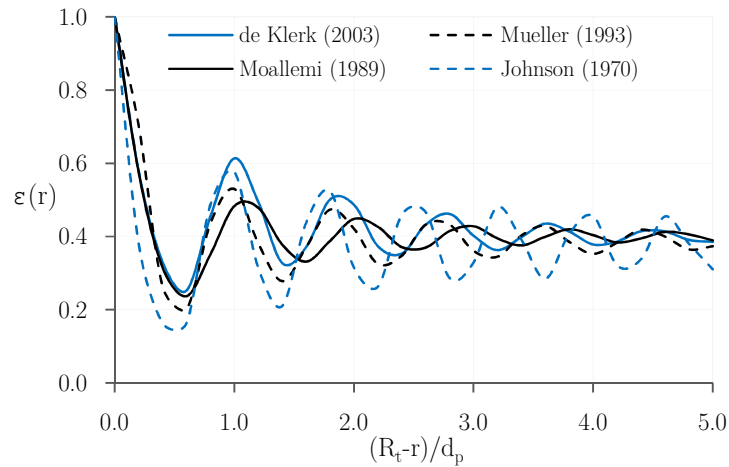
Fig. 2.1 Radial porosity distribution for random sphere packings for $N = 10$.

Table 2.2 Predictive correlations for radial porosity distribution where X is the dimensionless distance from tube wall based on the diameter of an equivalent sphere volume, i.e. $X = (R_t\text{-}r)/d_{pv}$.

Pellet shape	Authors	Correlations
Sphere	de Klerk [30]	$\varepsilon(X) = 2.14X^2 - 2.5X + 1$ for $X \leq 0.637$ $\varepsilon(X) = \varepsilon_b + 0.29Exp(-0.6X)\big(\cos(2.3\pi - 0.16)\big)$ $+ 0.15Exp(-0.9X)$ for $X > 0.637$ where $\varepsilon_b = 0.365 + 0.22/N$ Mueller (1993)
Cylinder	Roshani [44]	$\varepsilon(X) = 1 - \alpha_1\left(1 - Exp(-\alpha_2 X^{\alpha_4})\cos(\alpha_3 X^{\alpha_5})\right)$ where $\alpha_1 = N_{pv}\big/\big(1.375N_{pv} + 0.526\big)$, $\alpha_2 = N_{pv}\big/\big(0.542N_{pv} + 0.032\big)$ $\alpha_3 = N_{pv}\big/\big(0.145N_{pv} + 0.048\big)$, $\alpha_4 = 4.7 \times 10^{-4}N_{pv}^2 - 0.012N_{pv} + 0.392$ $\alpha_5 = 1.236N_{pv}^{-0.61}$

2.3. Hydrodynamics in fixed beds

In fixed bed reactors, radial heterogeneities in the packing structure, as evidenced by the radial porosity distribution, are present due to topological constraints imposed by the confining wall. This lateral heterogeneity becomes very pronounced in moderate to low N beds, say N<10, significantly influencing the pressure drop, local flow distribution and consequently the propagation of heat and species across the bed [4,17,19,45–47]. Numerous experimental and analytical studies have thus been devoted to the flow structure and pressure drop in fixed beds. A brief review of these studies is given in the following subsections.

2.3.1. Pressure drop

A precise prediction of pressure drop in fixed beds is of great importance as it determines the energy requirements of the supplying pumps and compressors. Numerous studies have dealt with the pressure drop, both experimentally and theoretically, and a general consensus has been reached as to the way of describing the roles of Re_p and mean porosity, ε, in infinite beds. The pressure drop for a large range of Reynolds numbers of fluid flow through a packed column with spherical particles is commonly described by the semi-empirical Ergun equation:

$$\frac{\Delta P}{L} = \frac{A_E \mu (1-\varepsilon)^2 u_s}{\varepsilon^3 d_p^2} + \frac{B_E (1-\varepsilon) \rho u_s^2}{\varepsilon^3 d_p} \tag{2.1}$$

where ΔP is the pressure drop, L is the bed length, u_s is the superficial flow velocity (i.e. volumetric flow rate divided by the cross-sectional area of the tube), ρ is the fluid density, μ is the molecular viscosity of fluid, d_p is the pellet diameter, ε is the mean porosity of the bed, and the constants A_E and B_E equal to 150 and 1.75, respectively. However, the Ergun and similar equations, e.g. [48], do not reflect the role of confining walls, specifically in tubular fixed beds, nor of pellets of different shape [49–52]. Several researchers have addressed the wall-effect on the pressure drop in low N beds, resulting in elaborate correlations, such as those proposed by [49,51,53–55]. One of the most promising correlations was proposed by Eisfield and Schnitzlein [49], who presented a thorough review on the wall-effect in fixed beds and took a database of several thousands of experiments from 24 published studies, thereby improving the parameters of the friction coefficient proposed by Reichelt [53]. Relatively recent studies on pressure drop have also scrutinized the influence of confining walls [51,52]. Cheng [52] proposed a capillary-type model to improve the Ergun equation constants in terms of bed-to-pellet diameter ratios, say 1.1 < N < 50.5. The author also discussed the suitability of his proposed formula by comparing it to other well-known correlations. Nonetheless, the opinions concerning the influence of different pellet shape, specifically in tubular fixed beds, on the

predicted pressure drop are very contradictory. Most investigators have tried to cater for the role of shape by using an effective particle diameter as well as a shape factor in the Ergun equation [56–58].

Here we present some of the most-used correlations for pressure drop in a dimensionless form, called the pore-based friction factor F which is expressed as:

$$F = \frac{\varepsilon^3}{1-\varepsilon} \frac{\Delta P}{\rho u_s^2} \frac{d_p}{L} = \frac{\varepsilon d_p}{(1-\varepsilon)} \frac{\Delta P}{\rho(u_s / \varepsilon)^2 L} \tag{2.2}$$

Rearranging the Ergun equation in the form of Eq. (2.2), we obtain:

$$F_E = \frac{A_E}{Re_E} + B_E \tag{2.3}$$

where Re$_E$ is the modified particle Reynolds number computed from:

$$Re_E = \frac{\rho u_s d_p}{\mu(1-\varepsilon)} = \frac{Re_p}{(1-\varepsilon)} \tag{2.4}$$

One of the earlier attempts to deal with the influence of confining walls in the pressure drop was that of Mehta and Hawley [48]. The investigators proposed the hydraulic radius, R$_H$, to account for the influence of the walls on the pressure drop in narrow fixed beds, i.e. low N beds. Based on their proposition, R$_H$ is modified as follows:

$$R_H = \frac{\varepsilon d_p}{6(1-\varepsilon)M} \tag{2.5}$$

$$\text{and } M = 1 + \frac{2}{3N(1-\varepsilon)} \tag{2.6}$$

This modification has been frequently pursued by other researchers working on the pressure drop in tubular fixed beds, e.g. [49,52,59, etc.]. Using the modification factor M, Eqs. (2.3-4) are revised to:

$$\Psi_W = \frac{F_E}{M} = \frac{\varepsilon^3}{1-\varepsilon} \frac{\Delta P}{\rho u_s^2} \frac{d_p}{L} \frac{1}{M} = \frac{\varepsilon d_p}{(1-\varepsilon)} \frac{\Delta P}{\rho(u_s / \varepsilon)^2 L} \frac{1}{M} = \frac{A_W}{Re_W} + B_W \tag{2.7}$$

$$\text{or } F_E = \frac{A_W M^2}{Re_E} + B_W M \tag{2.8}$$

where Re$_W$ = Re$_E$ / M and A$_W$ and B$_W$ are constants.

Table 3 summarizes the constants A$_W$ and B$_W$ for some of the most famous correlations used for predicting pressure drop in tubular fixed beds.

Table 2.3 Empirical correlations proposed for evaluating A_W and B_W

Authors	A_W	B_W	N
Mehta &Hawley [48]	150	1.75	7—91
Reichelt [53]	150 for sphere 200 for cylinder	$\left[1.5N^{-2} + 0.88\right]^{-2}$ for sphere $\left[2N^{-2} + 0.80\right]^{-2}$ for cylinder	1.7—91
Fumeny et al. [60]	$\dfrac{130}{M^2}$	$\dfrac{N}{M(2.28 + 0.335N)}$	3.23—23.8
Eisfield & Schnitzlein [49]	154 for sphere 190 for cylinder	$\left[1.15N^{-2} + 0.87\right]^{-2}$ for sphere $\left[2N_{ps}^{-2} + 0.77\right]^{-2}$ for cylinder	1.624—250
Montillet et al. [59]	$\dfrac{1000\alpha}{M^2(1-\varepsilon)}N^{0.2}$ where α=0.061 & 0.05 for dense and loose packings, respectively	$\dfrac{12\alpha}{M}N^{0.2}$	3.8—14.5
Cheng [52]	$\left[185 + 17\dfrac{\varepsilon}{(1-\varepsilon)}(\dfrac{N}{N-1})^2\right]\dfrac{1}{M^2}$	$\left[1.3(\dfrac{\varepsilon}{1-\varepsilon})^{1/3} + 0.03(\dfrac{N}{N-1})^2\right]\dfrac{1}{M}$	1.1—50.5

Allen et al. [58] have recently revisited the Ergun equation concerning the prediction of pressure drop in a rectangular duct packed with rough spheres, smooth cylinders, cubes and crushed rock. The authors reported a poor estimation of Ergun equation in beds of non-spherical pellets, e.g. under-estimating the pressure drop through beds of rocks by a factor as high as 5. The investigators measured the pressure drop in a wide range of N from 11 to 100 and proposed some modifications and corrections on the Ergun equation to account for the role of pellet shape.

A group of researchers have used CFD tools to investigate hydrodynamics and pressure drop in tubular fixed beds, e.g. [4,7,19,45,46,61–63]. Because of the high computational costs, these studies have been limited to low-N packing structures of spheres with several hundred particles. This coverage was adequate to address the role of walls on pressure drop, but the essential difficulties with generating random packings of non-spherical pellets remained. CFD studies of the flow field in fixed beds of non-spherical pellets are very scarce [19,25,64]. It is worth mentioning that the treatment of the pellet contact points to generate the packing can strongly affect the bulk porosity of the model, and thus the predicted pressure drop [46].

2.3.2. Flow structure

A detailed knowledge of the flow field is essential for a proper design of fixed bed reactors as it directly affects the temperature and mass distribution inside the tortuous structure. This has inspired several researchers to use noninvasive experimental methods to measure the local flow structures in fixed beds. McGreavy et al. [65] used Laser Doppler velocimetry (LDV) in low-N fixed beds, for both liquid and gas experiments. Rashidi et al. [66] and Stephenson and Stewart [67] used particle tracking methods. The latter authors employed marker bubbles as a noninvasive approach to measure the in-situ radial distribution of velocity of a matched-refractive index fluid in a packing of transparent cylinders with $N = 10.7$. They found that the global maxima and minima of local superficial velocities occur at $0.2d_p$ and $0.5d_p$ from the wall, respectively. Moreover, both studies reported an oscillatory trend for a radial velocity profile. The same pattern for radial velocity profile was also found using LDV by Giese et al. [12] for packed columns of spheres and cylinders with $N = 10$. Some researchers have used Magnetic Resonance Imaging (MRI) to characterize the flow field. For example, a quantitative MRI analysis by Sederman et al. [68,69] demonstrated generally accepted flow concepts such as velocity increase in void spaces, as well as inhomogeneous velocity distribution in different pores, in columns packed with ballotini spheres with $N = 9$, 14 and 19. The same results have been reported based on LDV measurements of radially-varying axial velocity by Krischke [70]. Ren et al. [71] have also used MRI to investigate the in-situ behavior of interstitial velocity distribution in packed columns of spheres for a wide range of N from 1.4 to 32. The authors demonstrated that the radial velocity distribution displays an oscillatory pattern, which reflects the ordering of the void spaces in the bed cross section. They also found a velocity rise near the tube wall of up to a factor of 4 of the average velocity. Baker et al. [25] used an image-based meshing technique to create a packing geometry from MRI scans of fixed beds of cylindrical particles, which is a prerequisite to start CFD simulations of the flow field. The authors discussed the potential of this approach for re-structuring such complex geometries based on MRI and CT techniques to access the in-situ flow field information using supplementary CFD analysis. Despite the invaluable information of the interstitial flow behavior achieved by such non-invasive experimental techniques, each of these approaches is subject to severe limitations [5].

Several researchers have been inspired by the similarities between the radial distribution of the axial velocities and the radial distribution of void fraction, and thus try to relate the former to the latter; this similarity is particularly clear for flow channeling at the wall region, where the local porosity approaches one. Giese et al. [12] and Bey and Eigenberger [11,72] have proposed a form of the Brinkman-Forcheimer-extended Darcy (BFD) equations and a modified

momentum balance, respectively, to describe the superficial velocity profile inside a packing structure. Their approaches assume a certain averaged velocity distribution, usually in the form of a radially-varying axial velocity field. Such models use an "effective turbulent viscosity" to account for turbulent flow fluctuations inside the packing. The main disadvantage of such approaches is the necessary use of effective parameters which lump the transport mechanisms occurring in a real fluid-porous system, possibly in a turbulent regime. These models can be regarded as an extension of the classical pseudo-continuum approach, in which a real solid-fluid flow system is modelled as two inter-penetrating continua. The extended Brinkman equation proposed by Bey and Eigenberger [11] is expressed as:

$$\frac{dp}{dz} = -150\eta_f \frac{\left(1-\varepsilon(r)\right)^2}{\varepsilon(r)^2 d_{pv}^2} v(r) - 1.75\rho_f \frac{\left(1-\varepsilon(r)\right)}{\varepsilon(r)d_{pv}} v(r)^2 + \frac{\eta_{eff}}{\varepsilon(r)} \frac{1}{r} \frac{d}{dr}\left[\varepsilon(r)r\frac{dv(r)}{dr}\right] \tag{2.9}$$

where the inlet velocity is computed by $v_{0,z} = \frac{2}{R_t^2} \int_0^{R_t} v(r)\varepsilon(r)rdr$, and the correlations for the effective viscosity are as follows:

$$\eta_{eff}/\eta_f = 1 + \left(7 \times 10^{-6} N + 2 \times 10^{-5}\right)\left(Re_p\right) \qquad \text{for spheres}$$

$$\eta_{eff}/\eta_f = 1 + \left(1.7 \times 10^{-5} N - 1.7 \times 10^{-5}\right)\left(Re_p\right) \qquad \text{for cylinders} \tag{2.10}$$

$$\eta_{eff}/\eta_f = 1 + \left(0.0815\, d_t/d_H - 1.088\right)\left(Re_{p,H}\right) \qquad \text{for Raschig rings}$$

where d_H is the hydraulic diameter of a hollow cylinder after Brauer [73], which is expressed as:

$$d_H = \frac{6}{a} \times 1.9 \times \left(\frac{1-\varepsilon_i}{1+(2/3)\sqrt{\varepsilon_i} - \varepsilon_i/3}\right) \tag{2.11}$$

$$\text{where} \quad \varepsilon_i = \left(d_i/d_o\right)^2$$

and a is the specific surface area of a Raschig ring.

Developments in computer performance and computational techniques during the two last decades have allowed researchers to increasingly make use CFD to model flow systems occurring in reaction engineering [74]. Several CFD studies have been devoted to the hydrodynamics in fixed beds, e.g. [7,45,62,75–77]. Virtually all of these efforts have considered tubular fixed beds containing several hundred spheres. Just a few works have recently been published, which cover shaped particles [8,19,78,79]. This is primarily due to the difficulties connected to generating a realistic packing of non-spherical particles, and also due to difficulties in meshing the resulting complex geometries. This is unfortunate because many common industrial processes use non-spherical particle shapes, such as Raschig rings for ethylene

epoxidation and multi-hole cylindrical particles for methane steam reforming. A detailed review of the application of CFD in this field will be given in Chapter 4.

2.4.   The problem of wall-to-bed heat transfer

A precise and safe design of fixed-bed chemical reactors requires an appropriate description of reaction kinetics, and radial heat and mass transfer processes. Among these, the role of wall-to-bed heat transfer is of great importance, particularly in multi-tubular catalytic reactors which are often employed to handle highly exothermic and endothermic reactions. However, both measurements and simulations of radial temperature profiles in fixed beds have posed problems for many years, especially for narrow (tubular) fixed beds, because of the dominance of wall-effects across the entire tube cross-section [15,77]. The importance of this problem is evidenced by the amount of reviews over the last five decades that are either focused on fixed bed radial heat transfer, or have it as a major component [2,5,13,15,80–87]. Recent studies have mostly focused on the in-situ behavior of fluid flow by means of CFD tools, and reviews of the literature have concentrated on how the flow will affect heat transfer, e.g. [8,17,77]. Nonetheless, the amount of CFD literature directly studying the heat transfer in fixed beds is very scarce, as such studies require making a mesh inside the pellets as well, imposing a great deal of computational expenses [8,16,78,81]. A detailed review of the relevant published material will be given in chapter 4.

As mentioned above, a full 3D CFD study of the flow field and heat and mass transport in a bed of several thousand particles comes at a large computational expense. Besides, the inherent topological complexities associated with non-spherical pellets are restricting the application of this methodology. Therefore, there is a continued interest in usage of classical pseudo-homogenous models, with a focus on selected features of flow and transport. Numerous researchers have dealt with the pseudo-continuum or macroscopic models of fixed bed reactors, which are based on fairly radical simplifications, such as unidirectional axial plug flow, pseudo-homogeneity, effective transport parameters and uniform catalyst pellet surroundings. The simplest pseudo-homogenous model is one-dimensional (along the axial direction), and contains an overall heat transfer coefficient (U) based on the difference between the radially averaged temperature of the bed and the corresponding wall temperature [88]. A detailed review on this form of macroscopic models was given by Dixon [89]. The author used a model matching approach based on a one-point collocation method to correlate U as a function of the two-dimensional pseudo-homogenous model parameters. A more complicated version of pseudo-homogenous heat transfer models is two-dimensional (along the axial and radial direction), with either a plug flow or an axially-dispersed plug flow assumption. The former is often

referred to as the 2D-PF model and uses an effective radial thermal conductivity, k_{er}, and an apparent wall heat transfer coefficient, h_w, while the latter is called the 2DADPF model and utilizes an effective axial thermal conductivity, k_{ea}, to account for axial dispersion as well [90]. Here, k_{er} lumps all mechanisms engaged in the radial heat transfer from the bed center up to the reactor wall. However, the observed increase in thermal resistance near the reactor wall has been a great challenge. One of the most-used concepts to describe this phenomenon is to idealize thermal resistance at the wall and lump all the mechanisms into an apparent wall heat transfer coefficient, h_w. The following dimensionless equations represent the pseudo-homogeneous two-dimensional axially-dispersed plug flow (2D-ADPF) heat transfer model:

$$\frac{\partial \theta}{\partial \zeta} = \frac{1}{Pe_{er}}\left(\frac{2}{N}\right)\left(\frac{\partial^2 \theta}{\partial \omega^2} + \frac{1}{\omega}\frac{\partial \theta}{\partial \omega}\right) + \frac{1}{Pe_{ea}}\left(\frac{2}{N}\right)\left(\frac{\partial^2 \theta}{\partial \zeta^2}\right) \tag{2.12}$$

$$\text{for } \zeta = 0 \;\; \rightarrow \theta = 1 \tag{2.13}$$

$$\text{for } \omega = 0 \;\; \rightarrow \frac{\partial \theta}{\partial \omega} = 0 \tag{2.14}$$

$$\text{for } \omega = 1 \;\; \rightarrow \frac{\partial \theta}{\partial \omega} + Bi\theta = \begin{cases} Bi & (\zeta > 0) \\ 0 & (\zeta < 0) \end{cases} \tag{2.15}$$

where θ is dimensionless temperature defined as $\theta = (T_w - T)/(T_w - T_0)$, ζ and ω are dimensionless axial and radial coordinates defined as $\zeta = z/R_t$ and $\omega = r/R_t$, respectively, Pe_{er} and Pe_{ea} are dimensionless effective radial and axial Peclet numbers defined as $Pe_{er} = (\rho v_0 cp_f d_p)/k_{er}$ and $Pe_{ea} = (\rho v_0 cp_f d_p)/k_{ea}$, respectively, and Bi is the apparent wall Biot number defined as $Bi = (h_w R_t)/k_{er}$. The effective parameters can be obtained by comparing accurate experimental results to the solutions of the pseudo-homogenous heat transfer model, i.e. by effectively solving the inverse problem. A detailed review has recently appeared which describes the current state of research and the perception of lateral heat transfer in fixed bed reactors [81]. The author describes the classical pseudo-homogenous k_{er}-h_w model, and explains the problems concerned with obtaining and analyzing experimental heat transfer data to compute k_{er} and h_w. Furthermore, the author has evaluated the prevailing correlations for k_{er}, and highlighted the existing debates over the meaning and fitness of h_w to predict heat transfer at the wall region. This effective parameter has been correlated to both Biot and Nusselt numbers in literature, which can be interrelated by means of the so-called Stanton number for heat transfer, St_h. The Stanton number is a dimensionless parameter, relating heat transfer coefficient to heat capacity of the fluid stream per unit cross-sectional area per unit time, and can be composed from either Nusselt or Biot number as:

$$St_{h,w} = \frac{ah_w R_t}{\rho_f v_0 cp_f} = \frac{Nu_w}{Re_p Pr} = \frac{Bi}{Pe_{er}}\left(\frac{2}{N}\right) \tag{2.16}$$

Tables 2.4 and 2.5 summarize the frequently-used correlations for Pe_{er} and Bi or Nu_w.

Table 2.4 Empirical correlations of Pe_{er}

Authors	Correlations
Yagi and Wakao [91]	$Pe_{er} = \dfrac{Re_P Pr}{\alpha + \beta Re_P Pr}$ For glass spheres and broken solids : $\alpha = 6$ and $\beta = \begin{cases} 0.11 & 0.021 < 1/N < 0.072 \\ 0.09 & 0.12 < 1/N < 0.17 \end{cases}$ For metal spheres : $\alpha = 13$ and $\beta = 0.11, \quad 0.021 < 1/N < 0.086$
Bauer and Schlünder [92,93]	$Pe_{er} = \dfrac{Re_P Pr}{\left(k_{er}/k_f\right)_{convection} + \left(k_{er}/k_f\right)_{conduction}}$ $\left(\dfrac{k_{er}}{k_f}\right)_{conv.} = \dfrac{Re_P Pr}{Pe_{rf}}$ and $Pe_{rf} = \dfrac{8}{F}\left[2 - (1 - \dfrac{2}{N_{pv}})^2\right]$ where $F = \begin{cases} 1.15 & \text{For spheres} \\ 1.75 & \text{For cylinders} \end{cases}$ $\left(\dfrac{k_{er}}{k_f}\right)_{cond.} = 1 - \sqrt{1-\varepsilon} + \sqrt{1-\varepsilon}\,\dfrac{k_{es,r}}{k_f}$ $\dfrac{k_{es,r}}{k_f} = \dfrac{2}{1-B\kappa^{-1}}\left[\dfrac{B(1-\kappa^{-1})}{(1-B\kappa^{-1})^2}\ln(\dfrac{\kappa}{B}) - \dfrac{B-1}{1-B\kappa^{-1}} - \dfrac{B+1}{2}\right]$ & $\kappa = \dfrac{k_p}{k_f}$ $B = C(\dfrac{1-\varepsilon}{\varepsilon})^{10/9}, \quad C_f = \begin{cases} 1.25 & \text{(Spheres)} \\ 2.5 & \text{(Cylinders)} \\ 2.5\left[1 + (\dfrac{d_i}{d_p})\right] & \text{(Raschig Rings)} \end{cases}$
Specchia et al. [94]	$Pe_{er} = \dfrac{Re_P Pr}{\left(k_{er}/k_f\right)_{convection} + \left(k_{er}/k_f\right)_{conduction}}$ $\left(\dfrac{k_{er}}{k_f}\right)_{conv.} = \dfrac{Re_P Pr}{Pe_{rf}}$ and $Pe_{rf} = 8.65\left[1 + 19.4(\dfrac{1}{N_{pv}})^2\right]$ $\left(\dfrac{k_{er}}{k_f}\right)_{cond.} = \varepsilon + \dfrac{\beta(1-\varepsilon)}{\varphi + \gamma\dfrac{k_f}{k_p}}$ where $\beta=1, \gamma=2/3, \varphi=0.22\varepsilon^2$

Authors	Correlations
Dixon and Cresswell [95] and Dixon [23]	$\dfrac{1}{Pe_{er}} = \dfrac{1}{Pe_{rf}} + \dfrac{k_{rs}/k_f}{Re_P\,Pr}\left[\dfrac{Bi_f+4}{Bi_f}\right]\left[\dfrac{8}{N_s}+\dfrac{Bi_s+4}{Bi_s}\right]^{-1}$ $\quad(Re_P>50)$ $\dfrac{1}{Pe_{er}} = \dfrac{1}{Pe_{rf}} + \left[\dfrac{Bi_s+4}{Bi_s}\right]\left[\dfrac{8}{N_f}+\dfrac{Bi_f+4}{Bi_f}\right]^{-1}+\dfrac{k_{rs}/k_f}{Re_P\,Pr}$ $\quad(Re_P<50)$ where $\dfrac{k_{rs}}{k_f}$ is evaluated based on Bauer and Schlünder (1978a, 1978b) $Bi_f = Nu_{wf}\left(d_t/2d_{pv}\right)\left(Pe_{rf}/(Re_p\,Pr)\right),$ $Nu_{wf} = 0.523\left(1-1/N_{pv}\right)Re_P^{0.738}\,Pr^{1/3}$ (Colldge and Parerson, 1984) $Nu_{fs} = 2.0 + 1.1Re_P^{0.6}\,Pr^{1/3}$ (Wakao et al., 1979) $Bi_s = \begin{cases}2.41+0.156(d_t/d_{pv}-1)^2 & \text{Spheres}\\0.48+0.192(d_t/d_{pv}-1)^2 & \text{Cylinders}\end{cases}$ $N_s = \dfrac{0.25(1-\varepsilon)\left(A_p/V_p\right)N_{pv}^2}{\dfrac{k_{rs}}{k_f}\left[\dfrac{1}{Nu_{fs}}+\dfrac{1}{\beta}\dfrac{k_f}{k_p}\right]},\quad N_f = \dfrac{0.25(1-\varepsilon)\left(A_p/V_p\right)N_{pv}^2}{\dfrac{Re_P\,Pr}{Pe_{rf}}\left[\dfrac{1}{Nu_{fs}}+\dfrac{1}{\beta}\dfrac{k_f}{k_p}\right]}$ $\beta = \begin{cases}10 & \text{Spherical particle}\\8 & \text{Cylindrecal particle}\end{cases}$
Borkink and Westertrep [96]	$Pe_{er} = \dfrac{Re_P\,Pr}{k_{rs}/k_f+\dfrac{Re_P\,Pr}{Bo_{hr}^{\infty}}}$ For glass spheres: $k_{rs}/k_f = 6.2$ and $Bo_{hr}^{\infty} = 10.9$ (For $7<N<14$) For Alumina cylinders: $k_{rs}/k_f = 4$ and $Bo_{hr}^{\infty} = 7.6$ (For $8<N<17$) For Alumina Raschig rings: $k_{rs}/k_f = 4.5$ and $Bo_{hr}^{\infty} = 4.2$ (For $8<N<16$)
Bey and Eigenberger [72]	$Pe_{er} = \dfrac{Re_P\,Pr}{k_{rs}/k_f+0.1Re_P\,Pr}$ where, $\dfrac{k_{rs}}{k_f} = \left[\dfrac{k_p}{k_f}\right]^n,$ $n=0.28-0.757\log(\varepsilon)-0.057\log(\dfrac{k_p}{k_f})$ (Krupiczka, 1967)

Table 2.5 Empirical correlations of Bi and Nu_w

Authors	Correlations
Li and Finlayson [83]	$\mathrm{Nu_w} = 0.17\,\mathrm{Re_P^{0.79}}$ for spheres $\quad$ (5<N<20) $\mathrm{Nu_w} = 0.16\,\mathrm{Re_P^{0.93}}$ for cylinders $\quad$ (3<N<20)
Dixon et al. [97]	$\mathrm{Nu_w} = 11.46 N^{-0.5}\,\mathrm{Pr}\left[0.11\mathrm{Re_P} + 20.64\right]\mathrm{Re_P^{-0.262}}$ $\quad$ (5<N<12) $\mathrm{Bi} = 5.73\sqrt{N}\,\mathrm{Re_P^{-0.262}}$
Specchia et al. [94]	$\mathrm{Nu_w} = \left(\mathrm{Nu_w}\right)_{\text{conduction}} + \left(\mathrm{Nu_w}\right)_{\text{convection}}$ $\left(\mathrm{Nu_w}\right)_{\text{conv.}} = \begin{cases} 0.0835\,\mathrm{Re_P^{0.91}}\,\mathrm{Pr^{1/3}} & \text{for } 10<\mathrm{Re_P}<1200 \\ 1.23\,\mathrm{Re_P^{0.53}}\,\mathrm{Pr^{1/3}} & \text{for } 1200<\mathrm{Re_P}<10000 \end{cases}$ $\left(\mathrm{Nu_w}\right)_{\text{cond.}} = 2\varepsilon + \dfrac{(1-\varepsilon)}{\gamma_W\dfrac{k_f}{k_p} + \varphi_W}$ where $\gamma_W = 1/3$ and $\varphi_W = 0.0024 N_{pv}^{1.58}$
Dixon et al. [98]	$\mathrm{Bi} = \dfrac{N}{2}\left(1 - 1.5N^{1.5}\right)\mathrm{Re_P^{-0.41}}\,\mathrm{Pr^{-2/3}}\left(\mathrm{Pe_{rf(\infty)}}\right)$ where $8<\mathrm{Pe_{rf(\infty)}}<10$
Dixon [99]	$\mathrm{Nu_w} = \dfrac{8\beta_s}{N} + \mathrm{Nu_{wf}}\left[1 + \beta_s\dfrac{\mathrm{Pe_{rf}}}{\mathrm{Re_P}\,\mathrm{Pr}}\right]$ $\quad$ $(\mathrm{Re_P}>50)$ $\mathrm{Nu_w} = \dfrac{8\beta_f}{N} + 2\mathrm{Bi_s}\dfrac{k_{rs}}{k_f}N\left[1 + \dfrac{\beta_f}{k_{rs}/k_f}\right]$ $\quad$ $(\mathrm{Re_P}<50)$ $\beta_s = \dfrac{k_{rs}/k_f}{\dfrac{8}{N_s} + \dfrac{\mathrm{Bi_s}+4}{\mathrm{Bi_s}}}$ and $\beta_f = \dfrac{\mathrm{Re_P}\,\mathrm{Pr}/\mathrm{Pe_{rf}}}{\dfrac{8}{N_s} + \dfrac{\mathrm{Bi_f}+4}{\mathrm{Bi_f}}}$ The definitions of k_{rs}, $\mathrm{Bi_s}$, $\mathrm{Bi_f}$, $\mathrm{Nu_{wf}}$ and $\mathrm{Pe_{rf}}$ are given in their correlation for effective radial Peclet number (see Table 2.4).
Martin and Nilles [100]	$\mathrm{Nu_w} = \left(1.3 + \dfrac{5}{N}\right)\dfrac{k_{rs}}{k_f} + 0.19\,\mathrm{Re_P^{0.75}}\,\mathrm{Pr^{-0.42}}$ $\dfrac{k_{rs}}{k_f}$ is evaluated based on Bauer and Schlünder (1978)
Bey and Eigenberger [72]	$\mathrm{Nu_w} = 2.4\dfrac{k_{rs}}{k_f} + 0.054\left(1 - \dfrac{1}{N}\right)\mathrm{Re_P}\,\mathrm{Pr^{1/3}}$ where, $\dfrac{k_{rs}}{k_f} = \left[\dfrac{k_p}{k_f}\right]^n$, $n = 0.28 - 0.757\log(\varepsilon) - 0.057\log\left(\dfrac{k_p}{k_f}\right)$ (Krupiczka, 1967)

Even though these effective parameters (design data) have been investigated through extensive research attempts over the last five decades, wide disagreements on the experimental values and predictive correlations, particularly in apparent wall heat transfer coefficient can be observed [15,101]. Fig. 2.2 illustrates a large deviation between the values of Nu_w and Pe_{er} predicted by frequently-used correlations over Re_p.
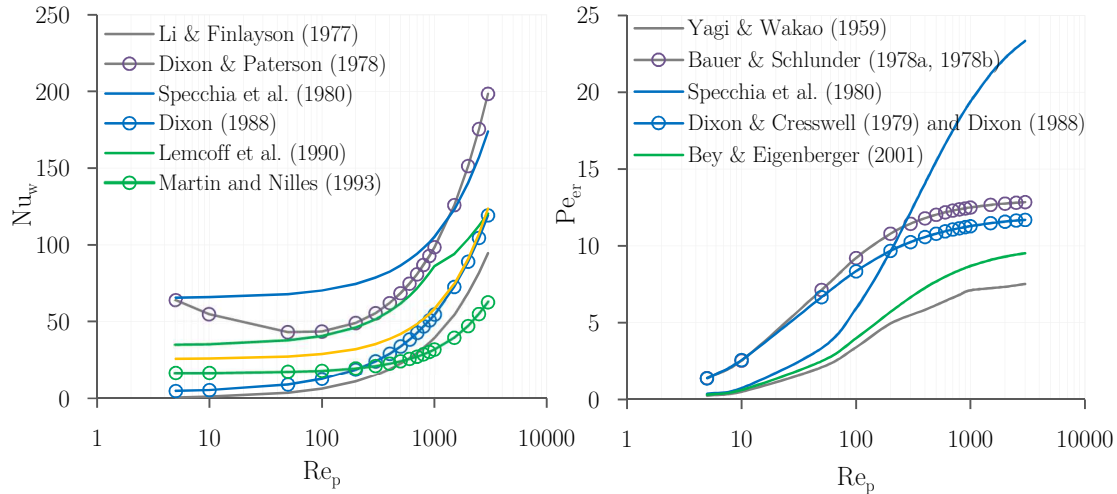
Fig. 2.2 Empirical correlations of Nu_w and Pe_{er} for tubular fixed beds of alumina sphere with $N = 3.1$.

Several researchers have assessed the difficulties concerned with the prediction of wall-to-bed heat transfer in low-N reactors and also discussed the inadequacy of pseudo-homogenous models in prediction of the behavior of transport scalers in such cases due to wall-effect phenomenon [1,77,78,102,103].

The major efforts towards improvements the classical pseudo-homogenous k_{er}-h_w models have been commenced in 1990s, where several researchers have tried to account for the role of velocity field in the models to address both the lateral heterogeneity in topology, and accordingly flow maldistribution. One of the interesting modifications relates to the work of Winterberg and Tsotsas [3,104], who proposed a quasi-homogeneous model for heat transport, so-called $\Lambda_r(r)$-model, accounting for laterally uneven distributions of porosity, radially-varying axial velocity profile and effective thermal conductivity. Even though a remarkable improvement on predicting radial temperature profile compared to the classical k_{er}-h_w models has been presented, the $\Lambda_r(r)$-model still requires the effective heat transfer parameters to describe heat transfer mechanisms, and even introduces another effective parameter, i.e. the effective bed viscosity. This implies the re-correlating of these parameters using models that include the velocity profile, where the parameters still represent several lumped transport processes. It is of noteworthy that the $\Lambda_r(r)$-model uses the real boundary condition, i.e. $T = T_w$

at the wall zone instead of the artificial one, i.e. Eq. (2.15). Bey and Eigengerger [72] have coupled BFD approach, i.e. Eq. (2.9-11), with axial dispersive k_{er}-h_w model to account for the role of wall-effect in the modeling of wall-to-bed heat transfer. The authors have claimed improved predictions of reactor behavior at low-N beds, confirming that the next generation of models needs to embrace more information concerning the flow field in the reactor. However, the same drawbacks to the $\Lambda_r(r)$-model can be counted for this simplistic version of CFD model. Magnico [15] has compared the predicted temperature profile by 2DPF heat transfer model, i.e. k_{er}-h_w model without axial dispersion, based on different effective heat transfer parameter correlations with the CFD results of heat transfer for random packing models of sphere with N = 5.6 and 7.8 at Re_p laying between 80-160. The author demonstrated that the radial and axial profiles of temperature show a good agreement with the model of Zehner and Schlünder [105] research group and the model of Martin and Nilles [100]. A number of investigators have exercised the Zehner-Schlünder equations to obtain pointwise values of effective stagnant thermal radial conductivity, to cater for the change of this parameter across the radial position in the bed cross section, e.g. [106,107]. The former research group have suggested that a sophisticated representation of the bed structure is needed, and they substituted the radial porosity distribution, $\varepsilon(r)$, into the Zehner–Schlünder equations to obtain $k_{er,s}(r)$. However, they have not presented any justification as to the procedure of this modification. Dixon et al. [107] conducted CFD simulations of a 3D annular fixed bed (ordered-packing of sphere with N = 4) without flow to determine radial porosity and temperature profiles, and then used the computed $\varepsilon(r)$ in the Zehner–Schlünder formulas to assess the pointwise effective thermal conductivity, $k_{er,s}(r)$. The authors then applied the modified Zehner–Schlünder model in a 1D pseudo-homogenous model using the finite element package COMSOL Multiphysics v.3.5. They demonstrated a very good agreement between the temperature profiles from the modified pseudo-homogenous model and that found from 3D CFD model. Behnam et al. [77] presented an improved version of velocity-based pseudo-continuum model, which uses the pointwise-based Zehner–Schlünder model to reproduce the 2D contour plot of temperature field obtained by 3D CFD simulations. They used an averaged axial and radial velocity components extracted from detailed 3D CFD simulations in a 2D velocity-based homogenous model, which is then solved in COMSOL Multiphysics v. 3.5 software, and compared with the 3D CFD results of heat transfer. The advantage of this model is that the usual effective radial thermal conductivity and apparent wall heat transfer coefficient are not incorporated into the model, and there are no further adjustable parameters.

Despite the inherent inadequacies connected with the classical pseudo-continuum approaches, as evidenced and addressed by vast bulk of researches in this field, astonishingly,

there is still a continued interest in the use of such simplistic models, particularly in the works within the context of catalysis and synthesis, e.g. [108–111]. However, the prevailing doubts and ambiguities as to the reliability of pseudo-continuum approach have hardly assisted designers of fixed bed reactors in selecting appropriate/dependable predictive correlations. Such situations effectively force the designers to seek validation of their design calculations through supplementary experimental studies, thereby imposing large additional expenses to a project. It is for the noted reasons that the effective heat transfer parameters need to be given further attention, in particular in relation to: (i) effects of tube and catalyst pellet shapes and size, (ii) wall-effects and high amounts of azimuthal asymmetry emerging in moderate-to-low N structures, and (iii) the importance of tube length-dependence.

2.5.   Concluding remarks

In this chapter we presented a comprehensive literature review on the modeling of hydrodynamics and heat transfer in fixed bed reactors. The topological features of random packing structures were described and some of the most-used correlations for bulk and local porosity in packings of spheres, cylinders and Raschig rings were presented. The review showed that the prevailing radial porosity data are visually restricted to random packings of spheres, and only a few experimental works have dealt with non-spherical pellets.

We also surveyed the literature on fluid flow hydrodynamics in fixed beds. The role of the wall-effect on pressure drop and widely-used correlations have been presented. The review showed a scarcity of information concerning pressure drop in random packings of non-spherical pellets. We described the progress in both experimental and theoretical studies of the velocity field within fixed bed systems and highlighted the disadvantages of simplistic BFD models and limitations of experimental techniques. The advantages and limitations of CFD approaches in predicting the in-situ behavior of the flow field were also highlighted. The problem of lateral heat transfer, i.e. wall-to-bed heat transfer, in tortuous structures was explained. This was followed by a deep survey of the relevant literature on the radial heat transfer problem, covering a range of approaches from the most simplistic pseudo-homogenous to more recent advances such as the velocity-based pseudo-continuum approach, based on the pointwise version of the Zehner–Schlünder model. Finally, we addressed the often-cited disagreement between the literature data on effective heat transfer parameters and the limitations connected with the classical k_{er}-h_w models.

This review has highlighted the prevailing concerns as well as limitations in this field and directed us towards the crucial areas which call for further research.

Nomenclature

a	Specific surface area	[$m^2.m^{-3}$]
cp	Heat capacity	[$J.kg^{-1}.K^{-1}$]
d_p	Pellet diameter	[m]
d_{pv}	Diameter of a sphere of equal volume	[m]
d_{ps}	Diameter of a sphere of equal specific surface area	[m]
d_t	tube diameter	[m]
g	gravity acceleration	[ms^{-2}]
h_w	Apparent wall heat transfer coefficient	[$Wm^{-2}K$]
k	Molecular thermal conductivity	[$Wm^{-1}K$]
L	Bed length	[m]
N	Tube to pellet diameter ratio	[-]
N_{pv}	Tube to pellet diameter ratio based on d_{pv}	[-]
N_{ps}	Tube to pellet diameter ratio based on d_{ps}	[-]
r	Radial direction	[m]
R_t	Bed radius	[m]
Re_p	Reynolds number based on d_{pv}: $\rho u_s d_{pv}/\mu$	[-]
u_s	Superficial velocity	[$m.s^{-1}$]
$v_z(r)$	Artificial velocity after Bey and Eigenberger [11]	[$m.s^{-1}$]
X	dimensionless distance from tube wall ($(R_t-r)/d_{pv}$)	[-]
z	Axial coordinate	[m]

Greek Letters

ε	bulk porosity	[-]
ε_{hc}	bulk porosity of packings of hollow cylinders	[-]
ε_{sc}	bulk porosity of packings of solid cylinders	[-]
$\varepsilon(r)$	radial porosity	[-]
μ	Molecular viscosity	[$kg.m^{-1}s^{-1}$]
ΔP	pressure drop	[$kg.m^{-1}s^{-2}$]
ρ_f	Fluid phase density	[$kg.m^{-3}$]
η_{eff}	Effective viscosity	[$kg.m^{-1}s^{-1}$]
ω	Dimensionless radial coordinate (r/R_t)	[-]
ζ	Dimensionless axial coordinate (z/R_t)	[-]

Bibliography

[1] D. Vortmeyer, E. Haidegger, Discrimination of three approaches to evaluate heat fluxes for wall-cooled fixed bed chemical reactors, Chemical Engineering Science. 46 (1991) 2651–2660. doi:10.1016/0009-2509(91)80058-7.

[2] M.G. Freiwald, W.R. Paterson, Accuracy of model predictions and reliability of experimental data for heat transfer in packed beds, Chemical Engineering Science. 47 (1992) 1545–1560. doi:10.1016/0009-2509(92)85003-T.

[3] M. Winterberg, E. Tsotsas, A. Krischke, D. Vortmeyer, A simple and coherent set of coefficients for modelling of heat and mass transport with and without chemical reaction in tubes filled with spheres, Chemical Engineering Science. 55 (2000) 967–979. doi:10.1016/S0009-2509(99)00379-6.

[4] H. Freund, T. Zeiser, F. Huber, E. Klemm, G. Brenner, F. Durst, G. Emig, Numerical simulations of single phase reacting flows in randomly packed fixed-bed reactors and experimental validation, Chemical Engineering Science. 58 (2003) 903–910. doi:10.1016/S0009-2509(02)00622-X.

[5] A.G. Dixon, M. Nijemeisland, E.H. Stitt, Packed tubular reactor modeling and catalyst design using computational fluid dynamics, Advance in Chemical Engineering. 31 (2006) 307–389. doi:10.1016/S0065-2377(06)31005-8.

[6] M. Nijemeisland, A.G. Dixon, Comparison of CFD simulations to experiment for convective heat transfer in a gas-solid fixed bed, Chemical Engineering Journal. 82 (2001) 231–246. doi:10.1016/S1385-8947(00)00360-0.

[7] T. Eppinger, K. Seidler, M. Kraume, DEM-CFD simulations of fixed bed reactors with small tube to particle diameter ratios, Chemical Engineering Journal. 166 (2011) 324–331. doi:10.1016/j.cej.2010.10.053.

[8] Y. Dong, B. Sosna, O. Korup, F. Rosowski, R. Horn, Investigation of radial heat transfer in a fixed-bed reactor: CFD simulations and profile measurements, Chemical Engineering Journal. 317 (2017) 204–214. doi:10.1016/j.cej.2017.02.063.

[9] W.E. Stewart, D.F. Marr, T.T. Nam, A.M. Gola-Galimidi, Transport modelling of packed-tube reactors—I. Framework for a data-based approach, Chemical Engineering Science. 46 (1991) 2905–2911.

[10] A.E. Kronberg, K.R. Westerterp, Nonequilibrium effects in fixed-bed interstitial fluid dispersion, Chemical Engineering Science. 54 (1999) 3977–3993.

[11] O. Bey, G. Eigenberger, Fluid flow through catalyst filled tubes, Chemical Engineering Science. 52 (1997) 1365–1376.

[12] M. Giese, K. Rottschafer, D. Vortmeyer, Measured and modeled superficial flow profiles in packed beds with liquid flow, AIChE J. 44 (1998) 484–490. doi:10.1002/aic.690440225.

[13]   M. Winterberg, E. Tsotsas, Correlations for effective heat transport coefficients in beds packed with cylindrical particles, Chemical Engineering Science. 55 (2000) 5937–5943. doi:10.1016/S0009-2509(00)00198-6.

[14]   M. Coussirat, A. Guardo, B. Mateos, E. Egusquiza, Performance of stress-transport models in the prediction of particle-to-fluid heat transfer in packed beds, Chemical Engineering Science. 62 (2007) 6897–6907. doi:10.1016/j.ces.2007.08.071.

[15]   A. Torkkeli, Droplet microfluidics on a planar surface, VTT Publications. 55 (2003) 3–194. doi:10.1002/aic.

[16]   F. Augier, F. Idoux, J.Y. Delenne, Numerical simulations of transfer and transport properties inside packed beds of spherical particles, Chemical Engineering Science. 65 (2010) 1055–1064. doi:10.1016/j.ces.2009.09.059.

[17]   A.G. Dixon, G. Walls, H. Stanness, M. Nijemeisland, E.H. Stitt, Experimental validation of high Reynolds number CFD simulations of heat transfer in a pilot-scale fixed bed tube, Chemical Engineering Journal. 200–202 (2012) 344–356. doi:10.1016/j.cej.2012.06.065.

[18]   G.D. Wehinger, T. Eppinger, M. Kraume, No Title, 87 (2015) 734–745. doi:10.1002/cite.201400153.

[19]   G. Boccardo, F. Augier, Y. Haroun, D. Ferre, D.L. Marchisio, Validation of a novel open-source work-flow for the simulation of packed-bed reactors, Chemical Engineering Journal. 279 (2015) 809–820. doi:10.1016/j.cej.2015.05.032.

[20]   G. Lu, J.R. Third, C.R. Müller, Discrete element models for non-spherical particle systems: From theoretical developments to applications, Chemical Engineering Science. 127 (2015) 425–465. doi:10.1016/j.ces.2014.11.050.

[21]   Y. Wu, X. An, A.B. Yu, DEM simulation of cubical particle packing under mechanical vibration, Powder Technology. 314 (2017) 89–101. doi:10.1016/j.powtec.2016.09.029.

[22]   R.F. Benenati, C.B. Brosilow, Void fraction distribution in beds of spheres, AIChE Journal. 8 (1962) 359–361. doi:10.1002/aic.690080319.

[23]   A.G. Dixon, Correlations for wall and particle shape effects on fixed bed bulk voidage, The Canadian Journal of Chemical Engineering. 66 (1988) 705–708. doi:10.1002/cjce.5450660501.

[24]   G.E. Mueller, Radial porosity in packed beds of spheres, Powder Technology. 203 (2010) 626–633. doi:10.1016/j.powtec.2010.07.007.

[25]   M.J. Baker, P.G. Young, G.R. Tabor, Image based meshing of packed beds of cylinders at low aspect ratios using 3D MRI coupled with computational fluid dynamics, Computers and Chemical Engineering. 35 (2011) 1969–1977. doi:10.1016/j.compchemeng.2011.03.017.

[26]   N. Zobel, F. Behrendt, Transient heat transfer in packed beds : The significance of the history term, 51 (2008) 3816–3824. doi:10.1016/j.ijheatmasstransfer.2007.10.040.

[27]   N. Zobel, T. Eppinger, F. Behrendt, M. Kraume, Influence of the wall structure on the void fraction distribution in packed beds, Chemical Engineering Science. 71 (2012) 212–219. doi:10.1016/j.ces.2011.12.029.

[28]   W. Soppe, Computer simulation of random packings of hard spheres, Powder Technology. 62 (1990) 189–197.

[29]   E.A. Foumeny, S. Roshani, Mean voidage of packed beds of cylindrical particles, Chemical Engrnerrmg Science. 46 (1991) 2363–2364. doi:10.1080/19447012408661000.

[30]   A. De Klerk, Voidage variation in packed beds at small column to particle diameter ratio, AIChE Journal. 49 (2003) 2022–2029. doi:10.1002/aic.690490812.

[31]   F. Benyahia, K.E. O'Neill, Enhanced Voidage Correlations for Packed Beds of Various Particle Shapes and Sizes, Particulate Science and Technology. 23 (2005) 169–177. doi:10.1080/02726350590922242.

[32]   W.I. Salvat, N.J. Mariani, G.F. Barreto, O.M. Martínez, An algorithm to simulate packing structure in cylindrical containers, in: Catalysis Today, 2005: pp. 513–519. doi:10.1016/j.cattod.2005.07.108.

[33]   W. Zhang, K.E. Thompson, A.H. Reed, L. Beenken, equilateral cylindrical particles, Chemical Engineering Science. 61 (2006) 8060–8074. doi:10.1016/j.

[34]   C.G. du Toit, Radial variation in porosity in annular packed beds, Nuclear Engineering and Design. 238 (2008) 3073–3079. doi:10.1016/j.nucengdes.2007.12.018.

[35]   R. Caulkin, A. Ahmad, M. Fairweather, X. Jia, R.A. Williams, Digital predictions of complex cylinder packed columns, Computers and Chemical Engineering. 33 (2009) 10–21. doi:10.1016/j.compchemeng.2008.06.001.

[36]   L.H.S. Roblee, R.M. Baird, J.W. Tierney, Radial porosity variations in packed beds, AIChE Journal. 4 (1958) 460–464.

[37]   D. Coelho, J.-F. Thovert, P.M. Adler, Geometrical and transport properties of random packings of spheres and aspherical particles, Physical Review E. 55 (1997) 1959–1978. doi:10.1103/PhysRevE.55.1959.

[38]   E. A. Foumeny, F. Benyahia, Predictive characterization of mean voidage in packed beds, Heat Recovery Systems and CHP. 11 (1991) 127–130. doi:10.1016/0890-4332(91)90126-O.

[39]   E.A. Foumeny, H.A. Moallemi, C. Mcgreavy, J.A.A. Castro, Elucidation of mean voidage in packed beds, The Canadian Journal of Chemical Engineering. 69 (1991) 1010–1015. doi:10.1002/cjce.5450690425.

[40]   H. Martin, Low Peclet number particle-to-fluid heat and mass transfer in packed beds,

Chemical Engineering Science. 33 (1978) 913–919.

[41]   Y. Cohen, A.B. Metzner, Wall effects in laminar flow of fluids through packed beds, AIChE Journal. 27 (1981) 705–715.

[42]   G.E. Mueller, Angular void fraction distributions in randomly packed fixed beds of uniformly sized spheres in cylindrical containers, Powder Technology. 77 (1993) 313–319. doi:10.1016/0032-5910(93)85023-3.

[43]   H.A. Moallemi, Predictive characterisation of packed bed structure, Leeds, UK: University of Leeds (Doctoral Dissertation). (1989).

[44]   S. Roshani, Elucidation of Local and Global Structural Prperties of Packed Bed configurations, The University of Leeds, 1990.

[45]   P. Magnico, Hydrodynamic and transport properties of packed beds in small tube-to-sphere diameter ratio: pore scale simulation using an Eulerian and a Lagrangian approach, Chemical Engineering Science. 58 (2003) 5005–5024. doi:10.1016/S0009-2509(03)00282-3.

[46]   G.W. Koning, Heat and Mass Transport in Tubular Packed Bed Reactors at Reacting and Non-Reacting Conditions, Measurement. 48 (2002) 272.

[47]   G.D. Wehinger, T. Eppinger, M. Kraume, Detailed numerical simulations of catalytic fixed-bed reactors: Heterogeneous dry reforming of methane, Chemical Engineering Science. 122 (2015) 197–209. doi:10.1016/j.ces.2014.09.007.

[48]   D. Mehta, M.C. Hawley, Wall effect in packed columns, Industrial & Engineering Chemistry Process Design and Development. 8 (1969) 280–282.

[49]   B. Eisfeld, K. Schnitzlein, The influence of confining walls on the pressure drop in packed beds, Chemical Engineering Science. 56 (2001) 4321–4329.

[50]   R. Di Felice, L.G. Gibilaro, Wall effects for the pressure drop in fxed beds, Chemical Engineering Science. 59 (2004) 3037–3040. doi:10.1016/j.ces.2004.03.030.

[51]   Y.S. Choi, S.J. Kim, D. Kim, A semi-empirical correlation for pressure drop in packed beds of spherical particles, Transport in Porous Media. 75 (2008) 133–149.

[52]   N. Cheng, Wall effect on pressure drop in packed beds, Powder Technology. 210 (2011) 261–266. doi:10.1016/j.powtec.2011.03.026.

[53]   W. Reichelt, Zur Berechnung des Druckverlustes einphasig durchströmter Kugel-und Zylinderschüttungen, Chemie Ingenieur Technik. 0 (1972) 1068–1071. doi:10.1002/cite.330441806.

[54]   R. Di Felice, L.G. Gibilaro, Wall effects for the pressure drop in fixed beds, Chemical Engineering Science. 59 (2004) 3037–3040.

[55]   G.J. Cheng, A.B. Yu, P. Zulli, Evaluation of effective thermal conductivity from the

structure of a packed bed, Chemical Engineering Science. 54 (1999) 4199–4209.

[56]   E. Ozahi, M.Y. Gundogdu, M.Ö. Carpinlioglu, A modification on Ergun's correlation for use in cylindrical packed beds with non-spherical particles, Advanced Powder Technology. 19 (2008) 369–381. doi:10.1163/156855208X314985.

[57]   L. Li, W. Ma, Experimental Study on the Effective Particle Diameter of a Packed Bed with Non-Spherical Particles, Transport in Porous Media. 89 (2011) 35–48. doi:10.1007/s11242-011-9757-2.

[58]   K.G. Allen, T.W. von Backstrom, D.G. Kroger, Packed bed pressure drop dependence on particle shape, size distribution, packing arrangement and roughness, Powder Technology. 246 (2013) 590–600. doi:10.1016/j.powtec.2013.06.022.

[59]   A. Montillet, E. Akkari, J. Comiti, About a correlating equation for predicting pressure drops through packed beds of spheres in a large range of Reynolds numbers, 46 (2007) 329–333. doi:10.1016/j.cep.2006.07.002.

[60]   E.A. Foumeny, F. Benyahia, J.A.A. Castro, H.A. Moallemi, S. Roshani, Correlations of pressure drop in packed beds taking into account the effect of confining wall, International Journal of Heat and Mass Transfer. 36 (1993) 536–540.

[61]   H.P.A. Calis, J. Nijenhuis, B.C. Paikert, F.M. Dautzenberg, C.M. Van Den Bleek, CFD modeling and experimental validation of pressure drop and flow profile in a novel structured catalytic reactor packing, Chemical Engineering Science. 56 (2001) 1713–1720. doi:10.1016/S0009-2509(00)00400-0.

[62]   T. Atmakidis, E.Y. Kenig, CFD-based analysis of the wall effect on the pressure drop in packed beds with moderate tube/particle diameter ratios in the laminar flow regime, Chemical Engineering Journal. 155 (2009) 404–410. doi:10.1016/j.cej.2009.07.057.

[63]   M. Icardi, G. Boccardo, D.L. Marchisio, T. Tosco, R. Sethi, Pore-scale simulation of fluid flow and solute dispersion in three-dimensional porous media, Physical Review E. 90 (2014) 013032. doi:10.1103/PhysRevE.90.013032.

[64]   G.D. Wehinger, C. Fu, M. Kraume, Contact Modi fi cations for CFD Simulations of Fixed-Bed Reactors : Cylindrical Particles, (2017). doi:10.1021/acs.iecr.6b03596.

[65]   C. McGreavy, E.A. Foumeny, K.H. Javed, Characterization of transport properties for fixed bed in terms of local bed structure and flow distribution, Chemical Engineering Science. 41 (1986) 787–797.

[66]   M. Rashidi, A. Tompson, T. Kulp, L. Peurrung, 3-D microscopic measurement and analysis of chemical flow and transport in porous media, Journal of Fluids Engineering. 118 (1996) 470–480.

[67]   J.L. Stephenson, W.E. Stewart, Optical measurements of porosity and fluid motion in packed beds, Chemical Engineering Science. 41 (1986) 2161–2170. doi:10.1016/0009-

2509(86)87132-9.

[68]   A.J. Sederman, M.L. Johns, P. Alexander, L.F. Gladden, Structure-flow correlations in packed beds, Chemical Engineering Science. 53 (1998) 2117–2128.

[69]   M.D. Mantle, A.J. Sederman, L.F. Gladden, Single-and two-phase flow in fixed-bed reactors: MRI flow visualisation and lattice-Boltzmann simulations, Chemical Engineering Science. 56 (2001) 523–529.

[70]   A.M. Krischke, Modellierung und experimentelle Untersuchung von Transportprozessen in durchstromten Schuttungen, VDI VERLAG, 2001.

[71]   X. Ren, S. Stapf, B. Blümich, Magnetic resonance visualisation of flow and pore structure in packed beds with low aspect ratio, Chemical Engineering and Technology. 28 (2005) 219–225. doi:10.1002/ceat.200407092.

[72]   O. Bey, G. Eigenberger, Gas flow and heat transfer through catalyst filled tubes, International Journal of Thermal Sciences. 40 (2001) 152–164. doi:10.1016/S1290-0729(00)01204-7.

[73]   H. Brauer, Druckverlust in Füllkörpersäulen bei Einphasenströmung, Chemie Ingenieur Technik. 29 (1957) 785–790.

[74]   A.G. Dixon, M. Nijemeisland, CFD as a design tool for fixed-bed reactors, in: Industrial and Engineering Chemistry Research, 2001: pp. 5246–5254. doi:10.1021/ie001035a.

[75]   H. Freund, J. Bauer, T. Zeiser, G. Emig, Detailed simulation of transport processes in fixed-beds, Industrial and Engineering Chemistry Research. 44 (2005) 6423–6434. doi:10.1021/ie0489453.

[76]   a. Jafari, P. Zamankhan, S.M. Mousavi, K. Pietarinen, Modeling and CFD simulation of flow behavior and dispersivity through randomly packed bed reactors, Chemical Engineering Journal. 144 (2008) 476–482. doi:10.1016/j.cej.2008.07.033.

[77]   M. Behnam, A.G. Dixon, M. Nijemeisland, E.H. Stitt, A New Approach to Fixed Bed Radial Heat Transfer Modeling Using Velocity Fields from Computational Fluid Dynamics Simulations BT - Industrial & Engineering Chemistry Research, Industrial and Engineering Chemistry Research. 52 (2013) 15244–15261. doi:10.1021/ie4000568.

[78]   G.D. Wehinger, C. Füterer, M. Kraume, Contact modifications for CFD simulations of fixed-bed reactors: Cylindrical particles, Industrial and Engineering Chemistry Research. 56 (2017) 87–99. doi:10.1021/acs.iecr.6b03596.

[79]   B. Partopour, A.G. Dixon, An integrated workflow for resolved-particle packed bed models with complex particle shapes, Powder Technology. 322 (2017) 258–272. doi:10.1016/j.powtec.2017.09.009.

[80]   M. Nijemeisland, A.G. Dixon, CFD Study of Fluid Flow and Wall Heat Transfer in a Fixed Bed of Spheres, AIChE Journal. 50 (2004) 906–921. doi:10.1002/aic.10089.

[81]   A.G. Dixon, Fixed bed catalytic reactor modelling—the radial heat transfer problem, The Canadian Journal of Chemical Engineering. 90 (2012) 507–527.

[82]   A.P. de Wasch, G.F. Froment, Heat transfer in packed beds, Chemical Engineering Science. 27 (1972) 567–576. doi:10.1016/0009-2509(72)87012-X.

[83]   B.A. Li, Chi-Hsiung; and Finlyson, HEAT TRANSFER IN PACKED BEDS-A REEVALUATION, Chemical Engineering Transaction. 32 (1976) 1055–1066.

[84]   E.U. Schlünder, Heat transfer from heated walls to packed beds of metal particles at various pressures, International Journal of Heat and Mass Transfer. 17 (1974) 1087–1091. doi:10.1016/0017-9310(74)90189-6.

[85]   P.W. Dietz, Effective thermal conductivity of packed beds, Industrial & Engineering Chemistry Fundamentals. 18 (1979) 283–286.

[86]   A. Cybulski, G. Eigenberger, A. Stankiewicz, Operational and Structural Nonidealities in Modeling and Design of Multitubular Catalytic Reactors, Industrial and Engineering Chemistry Research. 36 (1997) 3140–3148. doi:10.1021/ie960596s.

[87]   S.J. Romkes, F.. Dautzenberg, C.. van den Bleek, H.P.. Calis, CFD modelling and experimental validation of particle-to-fluid mass and heat transfer in a packed bed at very low channel to particle diameter ratio, Chemical Engineering Journal. 96 (2003) 3–13. doi:10.1016/j.cej.2003.08.026.

[88]   N. Wakao, S. Kaguei, H. Nagai, Effective diffusion coefficients for fluid species reacting with first order kinetics in packed bed reactors and discussion on evaluation of catalyst effectiveness factors, Chemical Engineering Science. 33 (1978) 183–187.

[89]   A.G. Dixon, An improved equation for the overall heat transfer coefficient in packed beds, Chemical Engineering and Processing: Process Intensification. 35 (1996) 323–331.

[90]   N. Wakao, S. Kagei, Heat and mass transfer in packed beds, Taylor & Francis, 1982.

[91]   S. Yagi, N. Wakao, Heat and mass transfer from wall to fluid in packed beds, AIChE Journal. 5 (1959) 79–85.

[92]   R. Bauer, E.U. Schlunder, Effective radial thermal-conductivity of packings in gas-flow. 1. Convective transport coefficient, International Chemical Engineering. 18 (1978) 181–188.

[93]   R. Bauer, E.U. Schlunder, Effective Radial Thermal-Conductivity of Packings in Gas-Flow. 2. Thermal-Conductivity of Packing Fraction without Gas-Flow, International Chemical Engineering. 18 (1978) 189–204.

[94]   V. Specchia, G. Baldi, S. Sicardi, Heat Transfer in Packed Bed Reactors With One Phase Flow, Chemical Engineering Communications. 4 (1980) 361–380. doi:10.1080/00986448008935916.

[95]   A. Dixon, D. Cresswell, Theoretical prediction of effective heat transfer parameters in

packed beds, AIChE Journal. 25 (1979) 663–676. doi:10.1002/aic.690250413.

[96]   J.G.H. Borkink, K.R. Westerterp, Determination of Effective Heta Transport Coefficients for Wall-Cooled Packed Beds, Chemical Engineering Science. 47 (1992) 2337–2342.

[97]   A. Dixon, D.L. Cresswell, W.R. Paterson, Heat Transfer in Packed Beds of Low TubejParticle Diameter Ratio, Edinburgh, 1978. http://www.worldcat.org/title/heat-transfer-in-packed-beds-of-low-tubeparticle-diameter-ratio/oclc/638440257   (accessed December 15, 2017).

[98]   A.G. Dixon, M.A. DiCostanzo, B.A. Soucy, Fluid-phase radial transport in packed beds of low tube-to-particle diameter ratio, International Journal of Heat and Mass Transfer. 27 (1984) 1701–1713. doi:10.1016/0017-9310(84)90153-4.

[99]   A.G. DIXON, Wall and particle-shape effects on heat transfer in packed beds, Chemical Engineering Communications. 71 (1988) 217–237. doi:10.1080/00986448808940426.

[100] H. Martin, M. Nilles, Radiale Warmeleitung in durchstromten Schuttungsrohren, Chemie Ingenieur Technik. 65 (1993) 1468–1477.

[101] D. Wen, Y. Ding, Heat transfer of gas flow through a packed bed, Chemical Engineering Science. 61 (2006) 3532–3542. doi:10.1016/j.ces.2005.12.027.

[102] E. Tsotsas, E.-U. Schlünder, Heat transfer in packed beds with fluid flow: remarks on the meaning and the calculation of a heat transfer coefficient at the wall, Chemical Engineering Science. 45 (1990) 819–837. doi:10.1016/0009-2509(90)85005-X.

[103] G.B. Liu, K.T. Yu, X.G. Yuan, C.J. Liu, A computational transport model for wall-cooled catalytic reactor, Industrial and Engineering Chemistry Research. 47 (2008) 2656–2665. doi:10.1021/ie070737y.

[104] M. Winterberg, E. Tsotsas, Modelling of heat transport in beds packed with spherical particles for various bed geometries and/or thermal boundary conditions, International Journal of Thermal Sciences. 39 (2000) 556–570. doi:10.1016/S1290-0729(00)00251-9.

[105] P. Zehner, E.U. Schlünder, Wärmeleitfähigkeit von Schüttungen bei mäßigen Temperaturen, Chemie Ingenieur Technik. 42 (1970) 933–941.

[106] W. Van Antwerpen, C.G. Du Toit, P.G. Rousseau, A review of correlations to model the packing structure and effective thermal conductivity in packed beds of mono-sized spherical particles, Nuclear Engineering and Design. 240 (2010) 1803–1818. doi:10.1016/j.nucengdes.2010.03.009.

[107] A.G. Dixon, A.K. Gurnon, M. Nijemeisland, E.H. Stitt, CFD testing of the pointwise use of the Zehner – Schlünder formulas for fixed-bed stagnant thermal conductivity, International Communications in Heat and Mass Transfer. 42 (2013) 1–4. doi:10.1016/j.icheatmasstransfer.2012.12.013.

[108] M.H. Rafiq, H.A. Jakobsen, R. Schmid, J.E. Hustad, Experimental studies and modeling of a fixed bed reactor for Fischer–Tropsch synthesis using biosyngas, Fuel Processing Technology. 92 (2011) 893–907.

[109] Y.-P. Zhu, S. Tu, Z.-H. Luo, Modeling for the catalytic coupling reaction of carbon monoxide to diethyl oxalate in fixed-bed reactors: Reactor model and its applications, Chemical Engineering Research and Design. 90 (2012) 1361–1371. doi:10.1016/j.cherd.2011.12.004.

[110] N.R. Parlikkad, S. Chambrey, P. Fongarland, N. Fatah, A. Khodakov, S. Capela, O. Guerrini, Modeling of fixed bed methanation reactor for syngas production: Operating window and performance characteristics, Fuel. 107 (2013) 254–260.

[111] X.P. Dai, P.Z. Liu, Y. Shi, J. Xu, W.S. Wei, Fischer–Tropsch synthesis in a bench-scale two-stage multitubular fixed-bed reactor: Simulation and enhancement in conversion and diesel selectivity, Chemical Engineering Science. 105 (2014) 1–11.

Chapter 3

A Rigid Body Dynamics (RBD) Algorithm for Modelling Random Packing Structures of Non-Spherical and Non-Convex Pellets

Abstract

Structural features of random packings play an essential role in the design of fixed bed reactors. Despite common use of non-spherical catalyst pellets in chemical engineering applications, packing structures of such pellets have not been as systematically studied and characterized as spherical packings. Here, we propose and scrutinize a novel physics-based random packing algorithm, based on Rigid Body Dynamics (RBD), to simulate fixed bed arrangements of non-spherical and possibly non-convex pellets. The proposed algorithm uses a hard-body approach to detect the collision/contact incidence and employs impulse theory to model the collision phenomena. The novelty is that the transition between moving and resting particles is controlled by a cut-off on the relative contact velocities, instead of artificially damping linear and angular velocities to stabilize the algorithm. The packing algorithm is used to synthesize random packing of spheres, equilateral solid cylinders and Raschig rings with tube-to-pellet diameter ratios ranging from 3 to 9.16. The packings are examined and validated in terms of bulk porosity and radial void fraction distribution, finding satisfactory agreement with the literature data for both global and local bed properties. Furthermore, a thorough analysis concerning the influence of physio-mechanical properties of catalyst pellets on packing densification is performed. Denser packing structures can be generated with restitution coefficients closer to one, and friction factors closer to zero. In all cases, the confining tube walls play an important role, especially for narrow packing geometries, with highly fluctuating bulk porosities. The novel physics-based packing algorithm can aid in furthering the knowledge of design of fixed bed unit operations.

3.1. Introduction

Fixed bed arrangements find extensive applications, particularly in reaction engineering, where they are employed as catalytic reactors for the transformation of reactants into desired products. The design of such systems is highly influenced by the structure of the packing matrix, which, in turn, is governed by the pellet and container size and shape, the loading method, and the subsequent treatment of the bed. Classical approaches in modeling fixed bed reactors, from the most simplistic model such as the pseudo-homogenous plug flow model to the more improved $\Lambda(r)$ model proposed by Winterberg and Tsotsas [1], which imposes a Brinkman-Forcheimer-extended Darcy (BFD) model to account for the axial velocity field, incorporate global and local bed properties, including bulk porosity and radial void fraction distribution. However, these pseudo-continuum models cannot provide an accurate prediction of the temperature field in tubular fixed beds, particularly for those with narrow to moderate tube-to-pellet diameter ratios (N), say N≤10, where the role of wall effects as well as pellet shape is completely neglected in such simplistic models [2–4].

During the last decades, advanced numerical techniques such as Computational Fluid Dynamics (CFD) and Lattice Boltzmann (LB) methodologies are increasingly used to fully resolve the three-dimensional mass-, momentum-, and heat transport around (and inside) individual catalyst pellets inside a bed [5–10]. Before such detailed simulations can be executed, we need to know the positions and orientations of the individual catalyst pellets inside the bed. This has persuaded researchers to delve profoundly into topological details of random packing structures through either experimental techniques such as Magnetic Resonance Imaging (MRI) and X-ray Computer Tomography (CT), e.g. [11–14], through numerical procedures in the form of inhouse and ad hoc algorithms, e.g. [15–18], or even through commercial codes such as PFC3D, which is a commercial Discrete Element Method (DEM) package, e.g. [19].

The majority of the prevailing efforts have concentrated on random packings of spheres, whilst application of catalyst pellets of non-spherical and often non-convex shapes, such as cylinders, Raschig rings, pall rings, trilobes, etc., are becoming increasingly popular, particularly in chemical reaction applications because of their specific potential to enhance transport processes [4]. The amount of literature addressing structural properties of such non-spherical packings is scarce [8,10,14,20,21]. This can be ascribed to the cumbersome and complicated strategies necessary to predict the trajectories of non-spherical objects during the loading process, where the orientational freedom of such pellets may not only be very problematic in terms of collision modelling, but also leads to exceptionally high computational expenses [22,23].

The main aim of this contribution is to propose and examine a novel physics-based hard-body packing algorithm, capable of simulating the dynamics of the random packing process of non-spherical and even non-convex pellets. The novelty of our method lies in the combination of an explicit treatment of instantaneous binary collisions with a global treatment of network of contacts between multiple particles when they are reaching their resting state. The transition between moving and resting particles is controlled by a cut-off on the mutual contact velocity. The fidelity and robustness of the proposed packing procedure in reproducing the statistical mean properties of realistic fixed bed arrangements is then thoroughly investigated and validated using published experimental and analytical data. Before introducing the proposed algorithm, a detailed survey on previous research efforts in this field is given, highlighting their advantages and restrictions.

3.1.1. Literature review

Topological features of random packing structures have been the subject of numerous analytical and experimental studies during the last five decades [11,14,29–33,15,17,22,24–28]. Nonetheless, only a minor selection of these studies has concentrated on evaluation and assessment of the spatial distribution of catalyst particles inside a bed, e.g. [11,15,31,33–35], whereas the amount of literature dealing with non-spherical pellets is scarce, e.g. [14,20,33]. Their generally opaque nature prohibits the exertion of conventional optical imaging techniques to address the spatial distribution of pellets of different shapes in random packing arrangements [22]. To circumvent this, several research groups have utilized advanced experimental techniques such as non-invasive imaging methods, e.g. MRI and 3D-CT [12–14,29,36]. For example, Sederman et al. [12] have used MRI in combination with image analysis techniques to characterize random packing structures of spheres with N = 9, 14 and 19. Ren et al. [13] have employed MRI, coupled with velocity encoding and pulsed-field-gradient nuclear magnetic resonance (PFG-NMR), to analyze the flow structure in random packings of cylinders and spheres with N in the range of 1.4 to 32. Zhang et al. [29] have coupled X-ray micro-tomography with a digital packing algorithm, which combines Monte Carlo and Distinct Element Methods, to reconstruct packing structures of equilateral cylinders with N = 12.8 from the micro-tomography images on a pellet-by-pellet basis. Baker et al. [14] have investigated the fidelity of an image-based meshing approach as a tool for reconstructing random packing structures through pellet-scale data extracted from non-invasive methods such as MRI and CT. Fundamentally, using such non-invasive methods, an automated image-based algorithm must be used to extract the pellet-scale information, which is challenging even for realistic packings of spheres (see refs [37,38]). However, for the case of non-spherical pellets, where their geometry embraces a variety of surface elements, i.e. flat and curved surfaces as well as corners, more complicated and rigorous reconstruction techniques are needed to accurately compute the positions and orientations of each pellet in a bed [36].

On the whole, the complexities and costs associated with non-invasive experimental measurement of full 3D granular systems, together with the large computational costs for post-processing, have persuaded researchers to seek alternative numerical methods. This has resulted in a multiplicity of packing algorithms, models and codes for generating random packing structures numerically [11,15,17,31,34,35,39]. Even though the specific details make each model unique, the majority of the prevailing algorithms can be classified into one of the following categories: i) Sequential-Deposition or deterministic algorithms, ii) Collective Rearrangement algorithms, and iii) Physics-based methods.

Sequential Deposition (SD) algorithms are principally initialized by either a sphere or sphere cluster. The packing structure is then generated based on a procedure known as random settlement [40,41], whereby the filling process is usually modeled by instantaneous placement of a new sphere in contact with either three spheres or with two spheres and the container wall, all of which are already fixed in their positions. A subcategory of deterministic approaches is the drop-and-roll type algorithm [42], in which a packing is initially assembled in vertical direction and then is compacted through lateral displacements of pellets by imposing a gravitational force field. Coelho et al. [43] proposed a sequential packing model based on the successive deposition of grains in a gravitational field. Their model initiates with random placement of grains above the bed, and then the filling process is continued layer after a layer, until the grain particles reach a local minimum of their potential energy. The algorithm allows any displacement and rotation of particles that contributes to a lowering of their barycenters. Atmakidis and Kenig [44] have employed an improved version of this approach proposed by Kainourgiakis et al. [45] to generate random packing model of spheres with $N = 5$. Mueller [39] has investigated four different deterministic algorithms including modified Bennett [46], layer, alternate and percentage methods, to synthesize packing geometries of mono-sized spheres. What distinguishes these proposed approaches are the methods adopted to model the loading process, viz. the procedures devised for placement of new spheres in the alternative positions. Mueller demonstrated that the percentage model gives the best results for radial void fraction distribution out of the other approaches considered. The basis of this method is to locate a sphere at the lowest alternative vertical positions based on a prescribed percentage. It means that the resting site for a new sphere is determined by comparison between the percentages of accessible alternative sites and the prescribed one. Mueller suggested that the optimum value of this percentage corresponds to the lowest bed porosity, however his further analyses demonstrated the severe dependence of this value on N, where for N ranging from 3.96 to 20.3, the optimum value of the percentage decreases from 70% to 10%. Furthermore, it was noticed that the accuracy of these deterministic approaches becomes lower as the bed-to-pellet diameter ratio increases. Mueller has improved his algorithm in another work [34], by proposing a dimensionless packing parameter, thereby enhancing the procedure of the sphere's sequential placement. Using this improvement, Mueller generated packings of mono-sized spheres with much better approximation of the radial void fraction profile, even for cases of large N-beds. Magnico [47] has used a modified version of the Bennet method, which was improved based on the Mueller method [39] to account for wall effects, to generate random packings of spheres with N = 5.96 and 7.8. Basically, the distinct advantages of SD techniques are their low computational expenses as well as their intrinsic simplicities in terms of programming.

However, as a major disadvantage, it is very difficult to manage the porosity of the resulting structures even with highly complex deposition algorithms.

Collective Rearrangement (CR) algorithms form another category of packing simulation. CR is fundamentally regarded as a process whereby (i) the overlapping particles undergo a series of repetitive minor displacements so that all detected overlaps in the computational domain are removed (if the initial condition is overlapping), and (ii) the particles are migrated stochastically with the aim of decreasing the bulk porosity (if the initial condition is non-overlapping). Liu and Thompson [48] have proposed a CR algorithm to generate random packing structures of spheres. The authors have investigated the influence of different boundary conditions on the generated packing structures. Maier et al. [49] have used a hard-sphere Monte Carlo algorithm to synthesize random packings of mono-sized spheres. In this algorithm, spheres are initially arranged at the intersections of a cubic lattice within a cylindrical tube with periodic boundaries set at its ends. Each sphere is then migrated stochastically, where a displacement is allowable if it does not lead to overlap with another sphere or the wall. The investigators benchmarked the radial void fraction profiles obtained from three generated-structures with N > 10 against experimental data. Sobolev and Amirjanove [50] have proposed a similar CR algorithm, however their model benefits from a method allowing for a much denser initial arrangement of spheres in the container, thereby reducing the computational expenses significantly. The authors have shown that the density of simulated structures increases by repetition of the CR procedure, i.e. the number of packing trials. Freund et al. [5] have exercised a two-step Monte Carlo process based on the packing algorithm proposed by Soppe [11] The CR algorithm exerted starts with initial placement of spheres inside a cylindrical tube, and then the packing is compressed through rearranging the spheres with an increased possibility into the direction of gravity. The packing process is stopped using convergence criteria that take into account changes in potential energy as well as mechanical stability.

A subcategory of CR algorithms is the digital packing approach, which is based on 'pixelation' (2D), or 'voxelation' (3D) of both objects and packing space [20,31]. The basis of a code called DigiPac, which has been developed and improved by Caulkin et al. [20,31], is to allow random migration of particles, one grid for each time interval, on a cubic lattice. This random movement includes both directional and diffusive motions, imitating a random walk-based sedimentation model. In fact, the movement of particles over a grid facilitates the process of collision detection as it can be examined whether two particles occupy the same grid space at the same time. This interesting feature significantly reduces the computational expense of a typical run compared to other CR algorithms, whereby overlap detection is mostly

undertaken by further mathematical analysis [20]. One of the most important advantages of this algorithm is to use digitization for representing packing objects, allowing for synthetic generation of random packings of even non-spherical particles. The investigators have inspected the validity of DigiPac by comparing the radial void fraction profiles, extracted from a number of simulated packing structures of both solid and hollow cylinders with $7 < N < 16$, with their own experimental data. Baker and Tabor [51] have employed DigiPac to generate random packings of spheres including 160 particles with $N = 7.14$.

Fundamentally, CR algorithms have significant advantages compared to SD algorithms. For instance, the final bed porosity can be adjusted a priori, and a spatial correlation for particle size distribution as well as their initial placement can be prescribed. Nonetheless, the main disadvantage of such randomized particle packing algorithms is that they are neglecting the physical aspects of the packing process. Moreover, their computational demands are high due to the very slow process of convergence, particularly for very dense or very loose packings [48].

The third classification, i.e. Physics-based methods, embraces the whole procedure that realistically describes the interactions between pellets and between pellets and wall. The foundations of such procedures are rooted in Newtonian mechanics. Salvat et al. [15] have proposed a Physics-based approach in the form of a soft-sphere algorithm to generate a packed bed structure of mono-sized spheres in a cylindrical container. The algorithm allows some interpenetration between particles, but does not account for friction forces. The authors validated their model by comparing the predicted particle center distribution for $N = 7.99$ to experimental data by Mueller [52]. Dixon et al. [6] have employed an improved version of this algorithm using part of Mueller's algorithm [39] concerning the initial placement of spheres at the base of the cylindrical container. The authors have then validated their packing generation procedure, for models of more than 1000 spheres, with $N = 5.45$ and 7.44, by comparing the predicted radial void fraction profile to the literate data reported by Benenati and Brossilow [24]. In a similar work, Behnam et al. [7] have validated their packing generation model using the experimental data reported by Mueller [52]. Siiria and Yliruusi [16] have developed a program based on Newton's laws of motion to generate random packing of spheres. Their model accounts for all forces including gravity, collision forces and friction.

The Discrete Element Method (DEM) can be considered as a subcategory of physics-based methods. DEM (Cundall and Strack [53]) is conceptually related to molecular dynamics, in which the trajectories of individual particles are computed by evaluating all forces. Since the main emphasis of researchers in this area is to investigate dense granular flows, thereby generating the most packed particulate beds, most of investigators have thus implemented

time-driven (soft-sphere) class of DEM. Nowadays, DEM has become a common and reliable computational tool to either probe the dynamics of grains in a particulate bed,[54] or to be coupled with CFD tools to investigate the hydrodynamics of a packed bed [10,19,21,55,56]. For example, Theuerkauf et al. [57] used DEM to investigate the local and global bed properties in narrow tubular fixed beds. The investigators have introduced DEM as a robust tool for generating random packing structures of spheres with moderate to low tube-to-pellet diameter ratios. Bia et al. [19] have exercised a commercial DEM code, PFC[3D], to generate realistic random packings of spheres and cylinders with N ≤ 4 as a part of a CFD study of flow field and pressure drop in packed beds. The authors have highlighted the difficulties associated with simulation of non-spherical packing structures using DEM. Eppinger et al. [55] have exercised coupled DEM-CFD using a commercial CFD package, STAR-CD, to investigate the behavior of the flow field in DEM-generated packings of spheres with 3 ≤ N ≤ 10. The authors inspected the validity of their simulated models by comparing with published correlations concerning radial void fraction distribution. Yang et al. [58] have also employed the same DEM package as in the work of Bai et al. [19] to generate random packings of spheres with 3 < N ≤ 8, as a part of a CFD analysis of flow and thermal fields in packed beds. The investigators have shown satisfactory agreements between the radial void fraction data obtained from the models and published experimental data. In fact, DEM seems to be the most promising concept among the available methods for predicting both macroscopic and microscopic features of particulate flows. However, a particular challenge, not only in DEM but in every numerical approach, is the accurate incorporation of non-sphericity, convexity and non-convexity of packing objects, as frequently encountered in practical situations. Only a few studies have dealt with non-spherical DEM, investigating various strategies to model non-spherical objects and contact detection algorithms. For a detailed review on the application of DEM in non-spherical particulate system, we refer to the works of Lu et al. [22] and Zhong et al. [23]. These reviews have surveyed recent advances in 3D modelling of non-spherical objects, covering the main findings as well as the inherent difficulties concerned with non-spherical particulate systems using DEM.

The simplest non-spherical objects that have been incorporated into DEM are ellipses in 2D and ellipsoids in 3D, where a surrogate model of such particles can be simply represented by algebraic equations [59,60]. However, this method, i.e. modeling a non-spherical particle using algebraic equations, is restricted to particle shapes which can be expressed algebraically, as an (often relatively simple) equation. To date, one of the most frequent and straightforward approaches in non-spherical DEM is the so-called composite-sphere or glued-sphere method, in which the established framework of spherical DEM is applied to approximate non-spherical

particles and their collisions during the packing process. A number of researchers have addressed the hindrances associated with the application of DEM glued-sphere approach such as its sensitivity to the parameters and the need for calibration [61,62]. Wu et al. [33] have employed this approach to investigate the behavior of cubical particle packings. The authors have investigated the influence of vibration conditions on packing densification. Dong et al. [10] have implemented the same approach using a commercial DEM code, STAR-CD (using the methodology proposed by Eppinger et al. [55]) to generate random packings of steatite rings (with $d_o/d_i/h$ equal to 6.2/3.5/4.5 and 8/6/8 mm), as part of a CFD analysis of the flow field and heat transfer in pack beds. However, the main disadvantages of the composite-sphere method are: i) the computational expenses, which increase tremendously with the number of spheres required for 3D approximation of a non-spherical object, viz. the more realistic the geometry of a particle, the higher the number of spheres necessary per particle, and ii) the occurrence of multiple contact points, which is inherent in non-spherical particles, which may lead to inaccurate force calculation [22]. This has urged several researchers to improve the glued-sphere DEM method [62,77]. Furthermore, alternative approaches to model collisional contact between particles have recently been proposed and applied to different problems, addressing different issues for modelling non-spherical particles [22,78,79]. Notably, the Gilbert-Johnson-Keerthi (GJK) distance algorithm is a fast computational procedure that can be used to detect overlap between non-spherical particles, which has recently been combined with a soft-particle approach for the contact model [79]. Of course, a GJK contact detection algorithm could also be combined with a rigid body dynamics approach (discussed next), but a major disadvantage of the GJK approach is that it is inherently limited to convex particles, i.e particles without any holes and with only convex outer surfaces.

Despite the above seeds of research covering non-spherical pellets, there has been relatively little progress in this field. Several important modeling aspects, such as the contact detection procedure in such complicated systems, and the problem of force-torque coupling upon collision, require substantial research efforts.

The main purpose of this chapter is to address this complex problem, introducing a procedure of generating packings of non-spherical and even non-convex pellets. To this end, a physics-based packing algorithm based on rigid body dynamics (RBD) is developed and examined for generating random packings of catalyst pellets with different shapes, including spheres, equilateral solid cylinders and Raschig rings. The essential features of our algorithm are i) a realistic representation of non-spherical pellets using triangular face mesh, which allows for simulation of even non-convex pellets with sharp edges; ii) the exertion of a hard-body collisional model whereby avoiding the unphysically large overlap of particles that might be

caused by artificially lowered spring stiffness, frequently employed in DEM simulations to prevent unfeasibly small time steps in the treatment of particle collisions; and iii) an explicit way of modelling resting contacts between multiple particles based on relative velocities, which avoids artificial damping of linear and angular velocities. The fidelity of the approach in reproducing the topological properties of realistic packing arrangements is then discussed using comparisons between the predicted data obtained from computer-generated structures and published experimental and analytical data.

3.2. Numerical set-up and model formulations

3.2.1. Rigid Body Dynamics (RBD)

RBD is frequently used in the field of graphic design and simulation [63]. Fundamentally, it is an analytical scheme capable of simulating the dynamic behaviour of assemblies of arbitrarily shaped objects based on Newton's laws of motion and Lagrangian mechanics. The background of RBD has been thoroughly investigated by several authors [64,65]. The main hypothesis of this approach is to consider the objects as rigid bodies, thereby facilitating the analysis of their motion by describing the translation and rotation of reference frames attached to each rigid body. Furthermore, contrary to the widely-used time-driven DEM which benefits from the soft contact approach, RBD is more akin to hard contact methods, streamlining the process of collision analysis, particularly in a system of non-spherical objects, where any overlap between non-convex objects makes the detection of contact points/edges very problematic [22]. RBD has been frequently used as an appropriate middleware framework in computer graphics and animation software such as FlipBook by DigiCel, Blender by the Blender Foundation, Maya by Autodesk and Cinema 4D by Maxon. The application of RBD in the field of chemical reaction engineering has recently been introduced by Boccardo et al. [8], where the authors used the open-source code Blender (which uses the Bullet Physics Library) to synthesize packed beds of different pellet shapes such as spheres, cylinders and trilobes. Following this, Partopour and Dixon [66] proposed an integrated workflow for resolved-particle fixed bed models with non-spherical pellet shapes. The authors have also used the Bullet Physics Library for generating packing structures of spheres, cylinders, Raschig rings, and quadrilobes with five holes. In the Blender software, a simplified approach based on damping the translational and rotational velocities of each object is used to speed up the process of getting objects to the resting position (see Blender reference manual at www.blender.org and Partopour and Dixon [66]). This simplistic approach is pursued to avoid overshoot and jiggling of objects in the resting contact condition which accordingly leads to a more stable simulation and convergence. However, the damping of linear and angular velocities is implemented on each "active" object

during the simulation, i.e. at each time step, and causes a violation of the law of conservation of linear and angular momentum and energy over each time interval.

In this chapter we offer an alternative RBD-based packing algorithm in which no damping forces are applied to moving particles. Rather, the transition between moving and resting particles is controlled by a cutoff on the relative contact velocity followed by a detailed balance of constrained forces acting on each pellet to model the resting contact condition rigorously and to facilitate the stability of convergence in RBD simulations.

3.2.2. Description of a non-spherical pellet

In this work, a catalyst pellet is regarded as a non-deformable material, which is characterized by a translation vector $\mathbf{x}(t)$, indicative of the barycenter of a pellet in the *world space*, and a unit quaternion $\mathbf{q}(t) = [q_0(t), q_1(t), q_2(t), q_3(t)]$, with $q_0^2 + q_1^2 + q_2^2 + q_3^2 = 1$, which determines the orientation of a pellet around its center of mass in the world space. A rotation matrix $\mathbf{R}(t)$ that transforms the orientation of the particle from a body(-fixed) to the world space coordinate system, can be expressed in terms of quaternions as:

$$\mathbf{R}(t) = \begin{bmatrix} q_0^2 + q_1^2 - q_2^2 - q_3^2 & 2(q_1 q_2 - q_0 q_3) & 2(q_1 q_3 + q_0 q_3) \\ 2(q_1 q_2 + q_0 q_3) & q_0^2 - q_1^2 + q_2^2 - q_3^2 & 2(q_2 q_3 - q_0 q_1) \\ 2(q_1 q_3 - q_0 q_2) & 2(q_2 q_3 + q_0 q_1) & q_0^2 - q_1^2 - q_2^2 + q_3^2 \end{bmatrix} \tag{3.1}$$

Using the quaternion-based approach, we can circumvent singularities ("gimbal lock") inherent in the Euler angle method [67], and also diminish numerical drifts, and corresponding topological skewness, stemming from the direct exertion of rotational matrices in computing the orientation of a pellet during numerical simulation of the packing process. The other constant parameters describing the physio-mechanical properties of a catalyst pellet are its mass m, moment of inertia tensor $\mathbf{I}_b$ in the fixed body space, collisional dissipation measured by a coefficient of restitution COR, and surface friction factor μ_k. Lastly, the most important part of the preprocessing step in RBD-based simulations is the 3D modeling of the pellet shape, accomplished by describing the particle boundaries in the fixed body space. In order to model a surrogate for the pellets, a fast and simplified subdivision-based polygonal approach proposed by Loop [68] is adopted, by which the body surfaces of an object are approximated using triangular meshes. Having incorporated the general formula of packings such as sphere, equilateral solid cylinder and Raschig ring, into the Loop algorithm, the body space of surrogate geometries is modeled optimally and in the most smoothed fashion. Fig. 3.1 illustrates 3D models of the pellets investigated in this work.

(a)   (b)   (c)
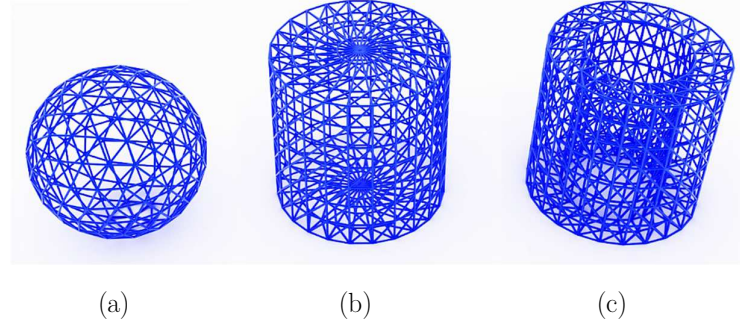
Fig. 3.1 3D models of catalyst pellets, represented by triangular face mesh; (a) sphere with d_p = 10mm, (b) equilateral solid cylinder with $d_p = h = 10$mm and (c) Raschig ring with $d_{po}/h/\delta$ = 10/10/2 mm.

3.2.3. Rigid body of equation of motion

The translational and rotational state of a moving object in the world space at time t is described here by a state vector, $\mathbf{X}(t)$, which is expressed as:

$$\mathbf{X}(t) = \begin{pmatrix} \mathbf{x}(t) \\ \mathbf{q}(t) \\ \mathbf{P}(t) \\ \mathbf{L}(t) \end{pmatrix} \tag{3.2}$$

where $\mathbf{x}(t)$ is the position of the center of mass in world space, $\mathbf{q}(t)$ is the unit quaternion describing the object orientation, and $\mathbf{P}(t)$ and $\mathbf{L}(t)$ are linear and angular momenta, respectively. The equation of motion, EOM, for an assembly of rigid pellets would hence be the derivative of the state vector at time t:

$$\dot{\mathbf{X}}_i(t) = \frac{d}{dt} \begin{pmatrix} \mathbf{x}_i(t) \\ \mathbf{q}_i(t) \\ \mathbf{P}_i(t) \\ \mathbf{L}_i(t) \end{pmatrix} = \begin{pmatrix} \mathbf{v}_i(t) \\ \frac{1}{2}\boldsymbol{\omega}_i(t)\mathbf{q}_i(t) \\ \mathbf{F}_i(t) \\ \boldsymbol{\tau}_i(t) \end{pmatrix} = \begin{pmatrix} \mathbf{P}_i(t)/m_i \\ \frac{1}{2}\mathbf{I}_i^{-1}(t)\mathbf{L}_i(t)\mathbf{q}_i(t) \\ \mathbf{F}_i(t) \\ \boldsymbol{\tau}_i(t) \end{pmatrix} \tag{3.3}$$

and

$$\mathbf{v}_i(t) = \dot{\mathbf{x}}_i(t) = \mathbf{P}_i(t)/m_i, \ \boldsymbol{\omega}_i(t) = \mathbf{I}_i^{-1}(t)\mathbf{L}_i(t), \ \mathbf{I}_i(t) = \mathbf{R}_i(t)\mathbf{I}_b\mathbf{R}_i(t)^T$$

where i=1, 2, ..., n_p denote the pellet index number, $\mathbf{v}_i(t)$ is the linear velocity of the center of mass of a pellet, $\boldsymbol{\omega}_i(t)$ the angular velocity around its center of mass, $\mathbf{F}_i(t)$ is the total external force acting on pellet i, $\boldsymbol{\tau}_i(t)$ is the torque on the object (around its center of mass), and $\mathbf{I}_i(t)$ is the moment of inertia tensor of pellet i, which can be simply computed from the body-fixed moment of inertia tensor $\mathbf{I}_b$ and the rotation matrix $\mathbf{R}_i(t)$. Note that both world space and

body space (local) coordinate systems are required to rigorously describe the rotational motion of a non-spherical pellet in the world space during numerical packing simulations (see Figure 3.2a). Transformation between these two reference frames is conveniently performed using the rotation matrix at each time step. To compute the rotational motion of pellets in the world space system, the vector transformation approach is applied, which has been demonstrated to be more computationally efficient compared to the tensor transformation approach [69].

To track the change of the state variables of the catalyst pellets over time, the EOM for each pellet, which is conceptually an initial value ODE problem, is resolved using a midpoint scheme. The reason behind adopting such a method to handle EOMs is the order of precision of $O(h^3)$, which alleviates skewing effects in the orientations of pellets stemming from numerical drift during the packing process. The algorithmic update for the ith pellet can be expressed as:

$$\mathbf{X}_i^{m+1} = \mathbf{X}_i^m + \Delta t^m \left(\frac{d\mathbf{X}_i}{dt} \right)^{m+1/2} \tag{3.4}$$

where

$$\left(\frac{d\mathbf{X}_i}{dt} \right)^{m+1/2} = \begin{pmatrix} \mathbf{v}_i(t_m + \Delta t^m / 2) \\ \frac{1}{2}\boldsymbol{\omega}_i(t)\mathbf{q}_i(t)\Big|_{t_m + \Delta t^m /2} \\ \mathbf{F}_i(t_m + \Delta t^m / 2) \end{pmatrix} = \begin{pmatrix} \mathbf{P}_i(t_m + \Delta t^m / 2)\big/ m_i \\ \frac{1}{2}\mathbf{I}^{-1}(t)\mathbf{L}_i(t)\mathbf{q}_i(t)\Big|_{t_m + \Delta t^m /2} \\ \mathbf{F}_i(t_m + \Delta t^m / 2) \\ \boldsymbol{\tau}_i(t_m + \Delta t^m / 2) \end{pmatrix} \tag{3.5}$$

where Δt^m is the time step at iteration m. To eliminate error accumulation in updating the orientation of a pellet, the quaternion of each pellet is re-normalized after each time interval [70].

3.2.3.1.   Implementation of force fields and torque

The total force acting on the ith pellet at time t, $\mathbf{F}_i(t)$ can be expressed as:

$$\mathbf{F}_i(t) = \mathbf{W}_i(t) + \mathbf{F}_{i,n}(t) + \mathbf{F}_{i,t}(t) \tag{3.6}$$

where $\mathbf{W}_i$ is a body force, in this case the weight acting on the center of mass of the pellet, causing it to accelerate at 9.81 ms^{-2} in the direction of gravity. This force is simply described as:

$$\mathbf{W}_i = -m_i g \hat{\mathbf{z}} \tag{3.7}$$

where $\hat{\mathbf{z}}$ is the unit vector in the direction of the z-axis in the world space coordinate system.

$\mathbf{F}_{i,n}(t)$ and $\mathbf{F}_{i,t}(t)$ describe the collision forces on pellet i due to its interaction with neighboring pellet or tube walls. In essence, for a typical oblique contact between two rigid objects, the contact force can be decomposed into normal and tangential directions. The normal contact force $\mathbf{F}_{i,n}(t)$ includes a repulsive force and viscous dissipation (associated with a certain coefficient of restitution). The tangential contact force $\mathbf{F}_{i,t}(t)$ is considered as a friction force. Fig. 3.2 shows a typical schematic of the forces acting on two colliding cylindrical pellets.
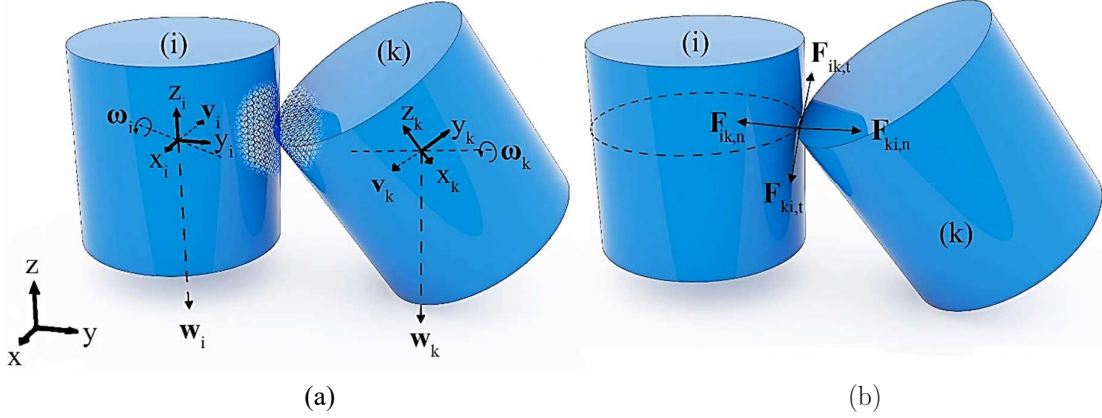
Fig. 3.2 Typical 3D-schematic of collision between two rigid cylinders, (a) spatial variables of colliding pellets, (b) normal and tangential forces acting on the contact point.

The total tangential force acting on the body of pellet i is expressed as:

$$\mathbf{F}_{i,t}(t) = \mathbf{F}_{iL,t}(t) + \mathbf{F}_{iB,t}(t) + \sum_{k} \mathbf{F}_{ik,t}(t) \tag{3.8}$$

where $\mathbf{F}_{iL,t}(t)$ and $\mathbf{F}_{iB,t}(t)$ are the tangential friction forces caused by lateral and bottom walls, respectively, and $\mathbf{F}_{ik,t}(t)$ is the tangential friction force due to collisional contact between the ith and k^{th} pellets. Fundamentally, the friction force between two objects resists sliding motion of two contacted surfaces against each other. Here, the Coulomb friction model is employed to describe the friction force at contact time t. This model can be represented for colliding contact between pellets i and k as:

$$\mathbf{F}_{ik,t}(t) = \mu_d f_{ik,n}(t) \widehat{\mathbf{t}}_{ik}(t) \tag{3.9}$$

$$\widehat{\mathbf{t}}_{ik}(t_c) = -\frac{(\widehat{\mathbf{n}}_{ik} \times \mathbf{v}_{pik}) \times \widehat{\mathbf{n}}_{ik}}{\left|(\widehat{\mathbf{n}}_{ik} \times \mathbf{v}_{pik}) \times \widehat{\mathbf{n}}_{ik}\right|} \tag{3.10}$$

and $\mathbf{v}_{pik}(t) = \mathbf{v}_{pi}(t) - \mathbf{v}_{pk}(t)$ $\hspace{2cm}$ (3.11)

where $f_{ik,n}(t)$ is the magnitude of the normal force at the contact point (discussed later), μ_d is the kinetic friction coefficient, $\widehat{\mathbf{t}}_{ik}(t)$ is the unit vector in the world space coordinate system

that friction force acts along, $\widehat{\mathbf{n}}_{ik}(t)$ is the normal unit vector of the cell face or plane to which the contact point $\mathbf{p}$ belongs, and $\mathbf{v}_{pi}(t)$ and $\mathbf{v}_{pk}(t)$ are the surface velocities at the contact points on the ith and k^{th} pellets, respectively, which can be mathematically expressed by:

$$\mathbf{v}_{pi}(t) = \mathbf{v}_i(t) + \boldsymbol{\omega}_i(t) \times \left(\mathbf{p}_i(t) - \mathbf{x}_i(t)\right) \tag{3.12}$$

$$\mathbf{v}_{pk}(t) = \mathbf{v}_k(t) + \boldsymbol{\omega}_k(t) \times \left(\mathbf{p}_k(t) - \mathbf{x}_k(t)\right) \tag{3.13}$$

In order to evaluate if dynamic friction should occur at the contact point, a threshold ε_f, based on the relative tangential velocity of the colliding pellets on the face cell or plane, i.e. $\left|\mathbf{v}_{pik}.\widehat{\mathbf{t}}_{ik}\right|$, is considered, thereby restricting the role of this force in the analysis when packings are being stabilized. It is worth remarking that both $\mathbf{F}_{iL,t}(t)$ and $\mathbf{F}_{iB,t}(t)$ can be computed using a simpler procedure by setting $\mathbf{v}_{pL} = \mathbf{v}_{pB} = 0$. Using the scalar $v_{pik,n}(t) = \mathbf{v}_{pik}(t).\widehat{\mathbf{n}}_{ik}(t)$, which describes the relative contact velocity in the direction of $\widehat{\mathbf{n}}_{ik}$, we can classify the behavior of collision, into three categories. Fundamentally, positive values of $v_{pik,n}(t)$, i.e. $v_{pik,n}(t) > \varepsilon_p$, mean that the pellets are separating and the contact point is vanishing after t_c. In this condition, the ODE solver can still continue the computational procedure. A zero value within a numerical threshold, $-\varepsilon_p < v_{pik,n}(t) < \varepsilon_p$, indicates that the pellets are neither approaching nor receding, which describes a situation called resting contact. This is a complicated condition for modelling support and counter forces at contact points (this is meticulously tackled in section 3.2.3.2). The last possibility, i.e. a negative value of this quantity, $v_{pik,n}(t) < -\varepsilon_p$, corresponds to the case of colliding contact. These alternative cases are illustrated in Fig. 3.3.
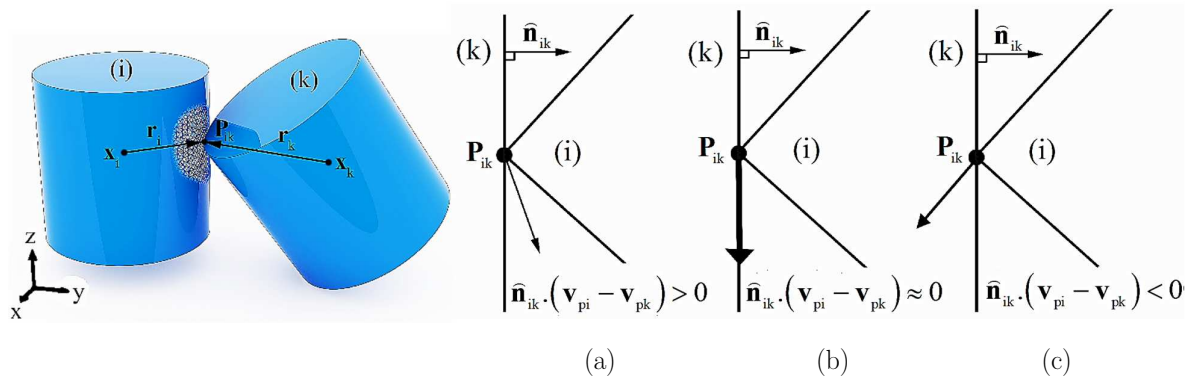
Fig. 3.3 The three alternatives for collision phenomena in a 2d vertex/face contact; (a) pellets are separating, (b) pellets are in resting contact, and (c) pellets are in colliding contact situation.

Similarly, the total normal force acting on the body of ith pellet, i.e. $\mathbf{F}_{i,n}(t)$, is described by the following relation:

$$\mathbf{F}_{i,n}(t) = \mathbf{F}_{iL,n}(t) + \mathbf{F}_{iB,n}(t) + \sum_k \mathbf{F}_{ik,n}(t) \tag{3.14}$$

where the first two terms in the right-hand side of Eq. (3.14) describe the normal force acting on the contact points of the ith pellet whilst in collisional contact with lateral and bottom walls, respectively, and the rightmost term, i.e. $\mathbf{F}_{ik,n}(t)$, is the normal force due to interaction between the ith and k^{th} pellets. Conceptually, $\mathbf{F}_{iL,n}(t)$ and $\mathbf{F}_{iB,n}(t)$ are always directed at the normal of the confining walls at the contact points and only affect the pellets, whilst $\mathbf{F}_{ik,n}(t)$ acts on the contact points in the direction of normal vector of either the cell face or the plane passing through the two crossed cell edges, whereat two pellets are colliding (the procedure of contact time/point evaluation is explained in section 3.2.4).

Conceptually, upon a collision the normal relative velocities of the colliding pellets are suddenly reversed in a discontinuous way so that the bodies do not interpenetrate. Such a situation would violate the assumption under which the ODE solver is able to work, namely a smooth variation of $\mathbf{X}_i(t)$ over the time intervals. Therefore, the ODE solver for the pellets engaged in collision conditions, whether it is colliding or resting contact, ought to be stopped, and another computational procedure should be pursued to trace the trajectories of the pellets. We note that this computational procedure is founded on the state vector of colliding objects at a time step before the contact time t_c, implicating that we assume that (i) the state vectors of colliding objects do not change during the collision period, i.e. $t_c \in [t_m, t_{m+1}]$, and that (ii) the state vectors of objects in collisional contact change discontinuously at the end of the collision period, i.e. at t_{m+1}.

In this study, we will work with the impulse due to a colliding contact when $v_{pik,n}(t) < -\varepsilon_p$. For such a collision, taken place at time t_c within the interval $[t_m, t_{m+1}]$, with the net impulse is defined as:

$$\mathbf{J}_i(t) = \int_{t_m}^{t_{m+1}} \mathbf{F}_i(t)dt = \Delta\mathbf{P}_i\Big|_{t_m}^{t_{m+1}} \tag{3.15}$$

The above equation is nothing but the statement that the total impulse of all collisional forces on pellet i corresponds to the difference in linear momentum of pellet i. As for the case of friction force, consider that two pellets i and k are in colliding contact at the vertex point p in their body spaces at time t_c, where $\mathbf{p}_i(t_c) = \mathbf{p}_k(t_c) = \mathbf{p}$. In this condition, the velocities of the collided objects need to instantly undergo a drastic change to prevent the bodies from interpenetration. The impulse, $\mathbf{J}_{ik}(t_c)$, for this case can be expressed by the following relation:

$$\mathbf{J}_{ik}(t_c) = \mathbf{J}_{ik,n}(t_c) + \mathbf{J}_{ik,t}(t_c) \tag{3.16}$$

and

$$\mathbf{J}_{ik,n}(t_c) = j_{ik,n}(t_c)\widehat{\mathbf{n}}_{ik}(t_c) \tag{3.17}$$

$$\mathbf{J}_{ik,t}(t_c) = j_{ik,t}(t_c)\widehat{\mathbf{t}}_{ik}(t_c) \tag{3.18}$$

where $j_{ik,n}$ and $j_{ik,t}$ are undetermined scalars representing the magnitude of impulse in normal and tangential directions with respect to the contact face, respectively. It is worth remarking that if the impulse of $\mathbf{J}_{ik}$ acts on pellet i, the body of pellet k would then be subjected to an equal but opposite impulse of $-\mathbf{J}_{ik}$ to satisfy the momentum conservation law. The impulse acting on pellet i (due to its collision with pellet k) produces an impulsive torque, $\boldsymbol{\tau}_{\mathbf{J},ik}$, which is expressed as:

$$\boldsymbol{\tau}_{\mathbf{J},ik}(t_c) = \left(\mathbf{p}_i(t_c) - \mathbf{x}_i(t_c)\right) \times \mathbf{J}_{ik}(t_c) \tag{3.19}$$

In order to evaluate the magnitude of the impulse in the normal direction, $j_{ik,n}$, an empirical model describing the colliding contact is used, where the relative normal velocities of the contact vertices before and after collision are connected by the coefficient of restitution, COR. This empirical law can be expressed as:

$$v^+_{pik,n} = -(\mathrm{COR})v^-_{pik,n} \tag{3.20}$$

where $v^-_{pik,n}$ and $v^+_{pik,n}$ are the relative velocities at the location of the contact in the $\widehat{\mathbf{n}}_{ik}(t_c)$ direction before and after the collision time $t_c \in [t_m, t_{m+1}]$, respectively. The coefficient of restitution lies between 0 and 1. When it is equal to 1, the collision is perfectly elastic and no kinetic energy is lost, whilst $\mathrm{COR} = 0$ results in $v^+_{pik,n} = 0$, corresponding to a plastic impact, where maximum kinetic energy is lost. Substitution of $v^-_{pik,n}$ and $v^+_{pik,n}$ in Eq. (3.20), together with a convenient mathematical procedure (see appendix A for a derivation), results in the following equation for the magnitude of normal impulse $j_{ik,n}$:

$$j_{ik,n} = \frac{-\left(1 + \mathrm{COR}\right)v^-_{pik,n}}{\widehat{\mathbf{n}}^T_{ik}\mathbf{K}_{ik,n}\widehat{\mathbf{n}}_{ik}} \tag{3.21}$$

and

$$\mathbf{K}_{ik,n} = \left(1/m_i + 1/m_k\right)\mathbf{I}_0 + \left[\mathbf{I}_i^{-1}(t_c)\left(\mathbf{r}_i \times \widehat{\mathbf{n}}_{ik}(t_c)\right)\right] \times \mathbf{r}_i + \left[\mathbf{I}_k^{-1}(t_c)\left(\mathbf{r}_k \times \widehat{\mathbf{n}}_{ik}(t_c)\right)\right] \times \mathbf{r}_k \tag{3.22}$$

$$\mathbf{r}_* = \mathbf{p}_* - \mathbf{x}_*$$

where $\mathbf{I}_0$ is the unit matrix and $\mathbf{K}_{ik,n}$ is a collision matrix for the colliding contact between pellets i and k. In case pellet i is in colliding contact with a confining wall, whether lateral or

bottom wall, the magnitude of impulse can be derived in a straightforward way. For example, $j_{iL,n}$, which describes $\mathbf{F}_{iL,n}(t_c)$, can be expressed by:

$$j_{iL,n} = \frac{-\left(1 + \mathrm{COR}\right)v_{pi,n}^{-}}{\widehat{\mathbf{n}}_{iL}^{\mathrm{T}}\mathbf{K}_{iL,n}\widehat{\mathbf{n}}_{iL}}$$

where

$$\mathbf{K}_{iL,n} = \left(1/m_i\right)\mathbf{I}_0 + \left[\mathbf{I}_i^{-1}(t_c)\left(\mathbf{r}_i \times \widehat{\mathbf{n}}_{iL}(t_c)\right)\right] \times \mathbf{r}_i$$

(3.23)

Suppose that the relative tangential velocity at the contact point $\mathbf{p}$, where the ith and kth pellets are in colliding contact, $v_{pik,t}^{-}(t) = v_{pik}^{-}(t).\widehat{\mathbf{t}}_{ik}(t)$ is non-zero. The magnitude of the tangential impulse $j_{ik,t}$ acting at contact time $t_c \in [t_m, t_{m+1}]$ is defined by the product of the dynamic friction coefficient μ_d and $j_{ik,n}$ using Coulomb's friction model as:

$$j_{ik,t} = \int_{t_m}^{t_{m+1}} \mu_d f_{ik,n}(t)dt = \mu_d j_{ik,n}$$

(3.24)

However, if $v_{pik,t}^{-}$ is very small, $j_{ik,t}$ calculated by Eq. (3.24) may reverse the sign of $v_{pik,t}^{+}$, resulting in unphysical motion. To circumvent such an incidence, we assume that $j_{ik,t} = 0$ if $v_{pik,t}^{-}v_{pik,t}^{+} \leq 0$.

Having computed the total impulse, $\mathbf{J}_{ik}(t_c)$, for a typical colliding contact between the ith and kth pellets, the discontinuous changes of linear and angular velocities of the pellets after collision can be expressed as:

$$\mathbf{v}_i^{+}(t_c) = \mathbf{v}_i^{-}(t_c) + \frac{\mathbf{J}_{ik}(t_c)}{m_i} = \mathbf{v}_i^{-}(t_c) + \frac{j_{ik,n}\left(\widehat{\mathbf{n}}_{ik}(t_c) + \mu_d\widehat{\mathbf{t}}_{ik}(t_c)\right)}{m_i}$$

(3.25)

$$\boldsymbol{\omega}_i^{+}(t_c) = \boldsymbol{\omega}_i^{-}(t_c) + \mathbf{I}_i^{-1}(t_c)\left(\mathbf{r}_i \times \mathbf{J}_{ik}(t_c)\right)$$

(3.26)

The same relations can also be written for the linear and angular velocity differences of pellet k by substituting $-\mathbf{J}_{ik}(t_c)$ in the above equations.

3.2.3.2. The problem of resting contact

One of the most problematic conditions occurring during the numerical simulation of the packing process is the resting contact, in which bodies are neither colliding nor detaching at their contact points, i.e. $-\varepsilon_p < v_{pik,n}(t) < \varepsilon_p$. This situation may cause a divergent number of collisions in a finite time span, which hence needs a specific procedure to handle the contacts, such that the pellets are kept fixed in their positions without any interpenetration. Consider a configuration of n contact points at which bodies are in resting contact (see Fig. 3.4). We assume that in rest there are no tangential forces, and therefore the resting contacts can be

resolved by specifying a set of forces acting normal to the contact surface, i.e. $\varphi_{ik}\hat{\mathbf{n}}_{ik}(t_c)$, chosen in such a way that they obey 3 constraints: (i) they should prevent the pellets from interpenetration, (ii) they should act repulsively in a way that holds the bodies together in contact, and (iii) they should become zero at the moment the bodies begin to detach again.
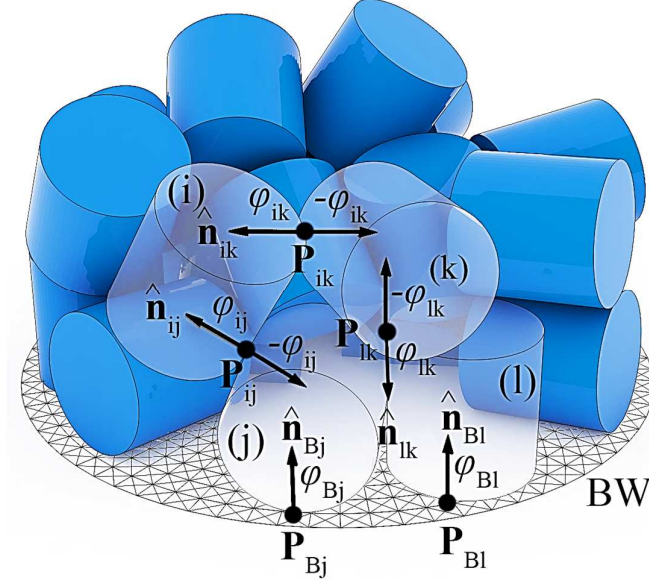
Fig. 3.4 Typical schematic of resting contact condition.

It is worth noting that all φ_{ik} need to be determined simultaneously, since a force acting on one contact point may influence objects involved on other contact points. To this end, we introduce a distance function, $d_{p,ik}(t)$, describing the distance between the resting contact points from two pellets i and k in the collision period. Considering the notations exercised before in describing colliding contacts, the distance function for a typical resting contact point $\mathbf{p}$ (whether it is a vertex/face or edge/edge contact), at the contact time $t_c \in [t_m, t_{m+1}]$, can be expressed by $d_{p,ik}(t_c)$:

$$d_{p,ik}(t_c) = \hat{\mathbf{n}}_{ik}(t_c).\Big[\mathbf{p}_i(t_c) - \mathbf{p}_k(t_c)\Big] \qquad (3.27)$$

The first constraint is to prevent bodies from interpenetration. Since both $d_{p,ik}(t_c)$ and $\dot{d}_{p,ik}(t_c)$, where the later describes the relative contact velocity in the direction of $\hat{\mathbf{n}}_{ik}$, $v_{pik,n}(t_c)$, are intrinsically zero (within the numerical threshold), we need to ensure that the second derivative of the distance function, measuring how two pellet surfaces accelerate towards each other at the contact point, to be equal to or greater than zero (within a numerical tolerance),

i.e. $\ddot{d}_{p,ik}(t_c) \geq 0$. The expression, describing $\ddot{d}_{p,ik}(t_c)$ can be simply derived by two times differentiating Eq. (3.27):

$$\ddot{d}_{p,ik}(t_c) = \hat{\mathbf{n}}_{ik}(t_c).\left[\dot{\mathbf{v}}_{pi}(t_c) - \dot{\mathbf{v}}_{pk}(t_c)\right] + 2\dot{\hat{\mathbf{n}}}_{ik}(t_c).\left[\mathbf{v}_{pi}(t_c) - \mathbf{v}_{pk}(t_c)\right] \tag{3.28}$$

$$\text{and} \quad \dot{\mathbf{v}}_{pi}(t_c) = \dot{\mathbf{v}}_i(t_c) + \dot{\boldsymbol{\omega}}_i(t_c) \times \mathbf{r}_i(t_c) + \boldsymbol{\omega}_i(t_c) \times \left(\boldsymbol{\omega}_i(t_c) \times \mathbf{r}_i(t_c)\right) \tag{3.29}$$

where $\dot{\mathbf{v}}_{pi}(t_c)$ and $\dot{\mathbf{v}}_{pk}(t_c)$ are the accelerations of the contact points in the world space coordinate system. It is worth remarking that if a pellet is in resting contact with the tube wall, Eq. (3.28) can be simplified by setting the rightmost term to zero, viz. $\dot{\hat{\mathbf{n}}}_{iL}(t_c) = \dot{\hat{\mathbf{n}}}_{iB}(t_c) = 0$.

Based on the second constraint, each of the contact forces needs to act outwardly which means that $\varphi_{ik} \geq 0$. The third constraint can simply be described in terms of φ_{ik} and $\ddot{d}_{p,ik}(t_c)$. Since the contact force must possess a value of zero if the resting contact starts breaking, it implies that $\varphi_{ik}(t_c)$ must be zero when a resting contact is broken. This constraint can be expressed by the following relation:

$$\varphi_{ik}(t_c)\ddot{d}_{p,ik}(t_c) = 0 \tag{3.30}$$

The magnitudes of $\varphi_{ik}(t_c)$ can thus be computed such that the mentioned constraints are satisfied for each contact point. Suppose that for a configuration of n (resting) contact points at $t_c \in [t_m, t_{m+1}]$, the distance acceleration for each of the contact points depends on the normal forces acting on all contact points together with some other constant forces and velocity-dependent terms related to the objects involved in that particular contact point at the pre-collision time step, t_m. In that case, we can express $\ddot{d}_{p,ik}(t_c)$ in terms of all unknown constraint forces, including those directly affecting the pellets i and k as:

$$\ddot{d}_{p,ik}(t_c) = \sum_j a_{ik,j}\varphi_{(i,k)j}(t_c) + b_{ik}(t_c) \tag{3.31}$$

where $a_{ik,j}$ describes how a unit change in $\varphi_{ij}(t_c)$, if pellet i is in direct contact with pellet j as well, can affect the contact point $\mathbf{p}_{ik}$. A more detailed derivation is given in Appendix B.

If we define $\ddot{\mathbf{D}}_p$ as the column vector of $\ddot{d}_{p,ik}(t_c)$ for n resting contact points, at time t_c, and $\boldsymbol{\psi}_N$ as the column vector of all constraint forces $\varphi_{ik}(t_c)$, then the problem of resting contact for n contact cases can be described in matrix form as:

$$\ddot{\mathbf{D}}_p = \mathbf{A}\boldsymbol{\psi}_N + \mathbf{B}$$
$$\text{where} \quad \ddot{\mathbf{D}}_p = \left[\ddot{d}_{p,ik}\right]_{n\times 1}, \quad \boldsymbol{\psi}_N = \left[\varphi_{ik,j}\right]_{n\times 1} \text{ and } \mathbf{A} = [a_{ik,j}]_{n\times n}, \quad \mathbf{B} = [b_{ik}]_{n\times 1} \tag{3.32}$$

with the following constrains:

(i) $\ddot{\mathbf{D}}_p \geq 0 \rightarrow \mathbf{A}\boldsymbol{\psi}_N + \mathbf{B} \geq 0$ $\hspace{4cm}$ (3.33)

(ii) $\boldsymbol{\psi}_N \geq 0$ $\hspace{7cm}$ (3.34)

(iii) $\boldsymbol{\psi}_N^T \ddot{\mathbf{D}}_p = 0 \rightarrow \boldsymbol{\psi}_N^T \left(\mathbf{A}\boldsymbol{\psi}_N + \mathbf{B} \right) = 0$ $\hspace{3cm}$ (3.35)

With the understanding that Eqs. (33) and (34) apply to each component of the column vectors. Eqs. (3.32-35) can be regarded as a quadratic programing problem, QP, in which we attempt to minimize the quadratic term $\boldsymbol{\psi}_N^T \ddot{\mathbf{D}}_p$ subject to the conditions $\boldsymbol{\psi}_N \geq 0$ and $\ddot{\mathbf{D}}_p \geq 0$. In this work, the procedures proposed by Baraff [71] is used to solve the problem, which has been proven as a reliable and fast solution algorithm.

3.3. Collision/Contact detection philosophy

The collision/contact detection procedure exerted here is based upon scrutinizing the proximities between body spaces of approaching rigid objects. This is implemented through a coherence-based two-layer search procedure, whereby the proximity between all pairs of face meshes are assessed to see if the minimum distance between their bounding volumes are lower than a preset threshold. The first layer of the search algorithm employs a series of criteria to narrow down the list of pairwise collision/contact possibilities at each time interval. These criteria are as follows:

For spheres :

$$\begin{cases} 2R_p \leq \left| \mathbf{x}_i(t) - \mathbf{x}_k(t) \right| \leq 2R_p + \lambda \\ R_p \leq \left| (L \text{ or } B) - \mathbf{x}_i(t) \right| \leq R_p + \lambda \end{cases} \text{ and } \text{sign}(\Delta \left| \mathbf{x}_{ik} \right|_{t_m}^{t_{m+1}}) = -1 \hspace{1cm} (3.36)$$

For cylinders and Raschig rings ($L_p = 2R_p$) :

$$\begin{cases} L_p \leq \left| \mathbf{x}_i(t) - \mathbf{x}_k(t) \right| \leq \sqrt{2}L_p + \lambda \\ \dfrac{L_p}{2} \leq \left| (L \text{ or } B) - \mathbf{x}_i(t) \right| \leq \dfrac{\sqrt{2}}{2}L_p + \lambda \end{cases} \text{ and } \text{sign}(\Delta \left| \mathbf{x}_{ik} \right|_{t_m}^{t_{m+1}}) = -1 \hspace{1cm} (3.37)$$

where $\lambda = 0.1R_p$ is a proximity threshold considered between two approaching objects and $\Delta \left| \mathbf{x}_{ik} \right|_{t_m}^{t_{m+1}}$ is the change of distance between barycenters of two objects in two successive time steps. The result of this search layer, in the form of a sorted list of pairs of pellets which are possibly colliding, is then be fed to a supplementary search engine, thereby determining the time of contact as well as details of intersections between the face meshes of collided objects. Henceforward, to avoid any probable interpenetrations of the pairs of pellets reported by the first search layer, the midpoint scheme is run using a much smaller time interval, δt_m. To estimate δt_m, let us consider two pellets i and k, detected by the first collision detection search

procedure, with a maximum relative surface velocity of $\left|\mathbf{v}_{ik}^{max}(t_m)\right|$. For the maximum allowable proximity of 0.2λ, the second collision search sub-algorithm can initiate at:

$$t_{m+1} = t_m + \delta t_m$$

$$\text{and } \delta t_m \leq \frac{0.2\lambda}{\left|\mathbf{v}_{ik}^{max}(t_m)\right|} \qquad (3.38)$$

Using this time interval hereafter, the inner search layer is executed in the form of a sweep/sort algorithm, by which a sorted list of data including the points and cell face with minimum distance to the body spaces of each pair of listed objects is created. The list is then scanned for either an overlap or a contact between two meshes, viz. vertex/cell face or edge/edge contacts. A simple penalty method based on the distance between the reported contact points and the center of mass of the pair of pellets in contact is then exercised to avoid any interpenetration. Following this, the algorithm returns to the latest pre-collision time, allowing the post-collision calculation to proceed by computing the collision responses based on the type of collision. Fig. 3.5 illustrates how the two-layer collision detection procedure works:

$$L_p \leq \left|\mathbf{x}_i(t) - \mathbf{x}_k(t)\right| \leq \sqrt{2}L_p + \lambda$$
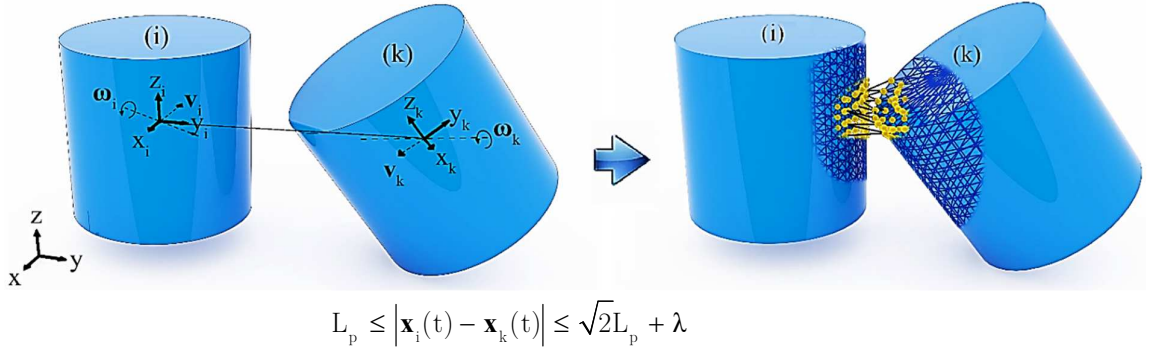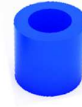
Fig. 3.5 Typical representation for two-layer collision search procedure.

3.4. Packing algorithm

The physics-based algorithm is founded on the equation of motion of rigid bodies as well as other auxiliary models describing collision phenomena. This algorithm can be described in four main stages: preprocessing, initialization, simulation and termination.

In the preprocessing stage, the details of rigid objects, i.e. catalyst pellets and container, including the physio-mechanical properties as well as their 3D models in the world space, are defined. This (preset) information is summarized in Table 3.1.

Table 3.1 The preset data in preprocessing stage

Objects		Size (mm)	Moments of Inertia (I_b) (kg.m^2)	Other preset data
Catalyst pellets		$d_p=10$	$I_{b,xx} = \frac{1}{10}Md_p^2$ $I_{b,yy} = \frac{1}{10}Md_p^2$ $I_{b,zz} = \frac{1}{10}Md_p^2$	**Mechanical data** 1. Pellet Density (ρ): 3.95 gr/cm^3 2. Gravitational acceleration: 9.81 m^2/s 3. Friction coefficient (μ_d): [0.05-0.95] 4. Surface Bounciness (COR): [0.05-0.95]
		$d_p=10$ $L_p=10$	$I_{b,xx} = \frac{1}{12}ML_p^2 + \frac{1}{16}Md_p^2$ $I_{b,yy} = \frac{1}{12}ML_p^2 + \frac{1}{16}Md_p^2$ $I_{b,zz} = \frac{1}{8}Md_p^2$	**3D Model data**
		$d_{pi}=6$ $d_{po}=10$ $L_p=10$	$I_{b,xx} = \frac{1}{12}M\left(\frac{3}{8}(d_{pi}^2 + d_{po}^2) + L_p^2\right)$ $I_{b,yy} = \frac{1}{12}M\left(\frac{3}{8}(d_{pi}^2 + d_{po}^2) + L_p^2\right)$ $I_{b,zz} = \frac{1}{8}M(d_{pi}^2 + d_{po}^2)$	1. General mathematical formula of pellet in world space 2. Vectors of vertex data on body space of each pellet 3. Vectors of center of mass for each pellet 4. Number of surface meshes generated for a pellet
Container	Size (mm)		Diameter: d_t is set to synthesize packings with $3.06 < N_{pv} < 9.16$ Height: H=120 mm	
	Other Data		1. Friction coefficient (μ_d) = 0.6 2. Surface bounciness (COR) = 0.6 3. Vectors of vertex data on body space of tube wall	

The initialization stage involves the initial placement of the pellets at the top of the tube as well as setting all thresholds for friction and collision/contact detection sub-algorithms. Having placed the pellets at the top of the container, we set the time interval Δt_m for the iterative calculation procedure (in our tests 1/40 sec) as well as the desired total simulation time. We can then proceed with the simulation, in which the ODE solver is run simultaneously with the collision search sub-algorithms to determine the trajectories of the barycenter and orientations of the pellets in the bed at each time step. To inspect whether dynamic equilibrium occurs, i.e. the termination stage, the work-energy theorem is exercised: a system of moving pellets reaches a dynamic equilibrium if the change in total kinetic energy of the system over

a typical time period approaches zero. The following flowchart exhibits the skeleton of the proposed packing algorithm.
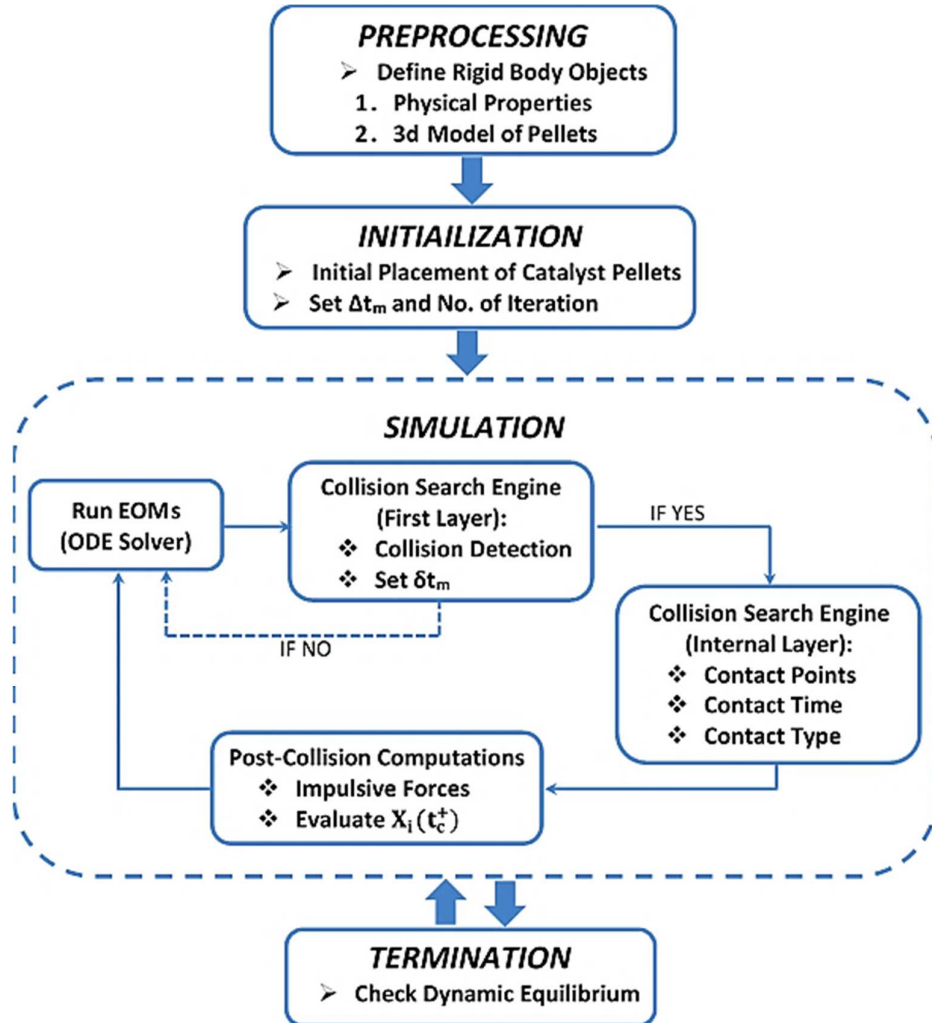
Fig. 3.6 Flowchart of packing algorithm

3.5. Results and discussion

Several series of packing simulations were conducted to assess the influence of preset parameters, i.e. physio-mechanical properties such as coefficient of restitution (COR) and surface friction factor, as well as initial placement of pellets at the top of the tube, on the structural properties of the packings. We investigated packing structures of spheres, solid cylinders and Raschig rings, with a tube-to-pellet diameter ratio, N, within the range of 3.06 to 9.16.

To inspect the fidelity and robustness of the proposed packing algorithm, the simulated packings have been scrutinized and benchmarked, first and foremost, in terms of bulk porosity

and radial void fraction distribution. To this end, the experimental and analytical data from [25,28,72] for bulk porosity and [24,26,27,52,73,74] for radial void fraction distribution were tested, which all together provide data for a wide range of tube-to-pellet diameter ratios, 1.7≤N≤27.95.

3.5.1. The role of loading methods and filling speed

The choice of initial placement of catalyst pellets, i.e. the loading method, in the setup of the packing simulations is of paramount importance as it may have a considerable influence on the dynamic behavior of the packing process and densification, and accordingly on the topological properties of the generated structures. The packing algorithm is set up based on the data given in Table 3.1, with COR $= 0.6$ and $\mu_d = 0.6$, to simulate random packings of spheres with three different loading strategies: 1) in the first scheme the pellets are introduced in a column in line with the tube axis; 2) in the second scheme the pellets are placed in two columns, equidistant from the tube axis; 3) in the third scheme the pellets are placed in 4 columns, equidistant from the tube axis. These scenarios (see Fig. 3.7) have been examined for two packings with tube-to-pellet diameter ratios of N $= 3.1$ and 6.1.
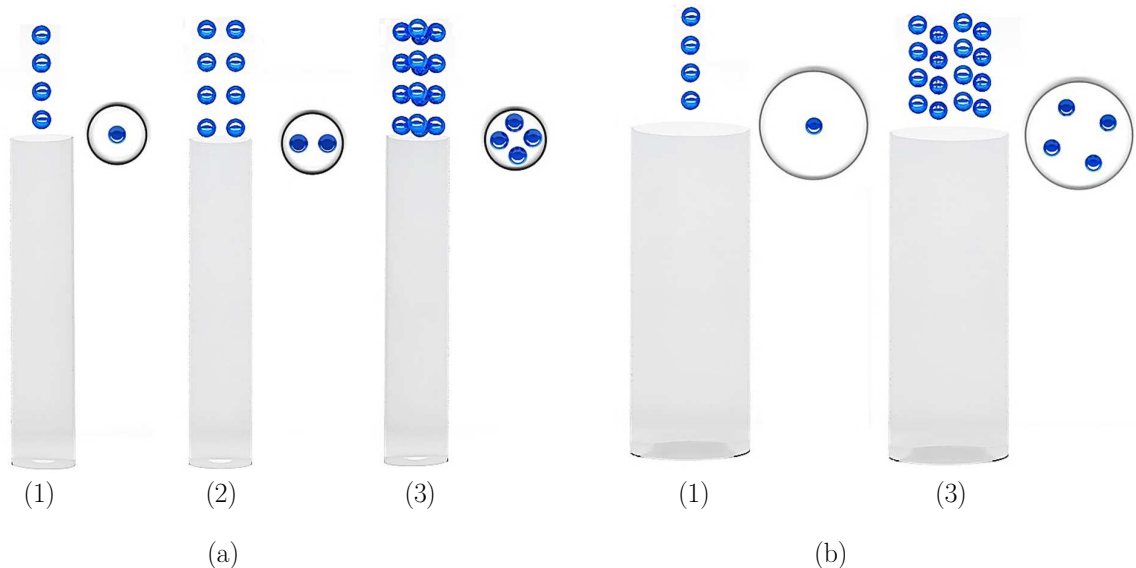
Fig. 3.7 Various scenarios considered for loading method; (a) spherical packing with N $= 3.1$, (b) spherical packing with N $= 6.1$

The simulated structures then were examined in terms of bulk voidage to determine which scenario would result in a denser structure. The mean voidage of the generated packings was computed precisely based on the mesh counts of catalyst pellets up to a packing altitude of H $= 100$ mm, and were benchmarked against empirical correlations proposed by Dixon [25] and Foumeny et al. [72]. The results are shown in the following bar plots.
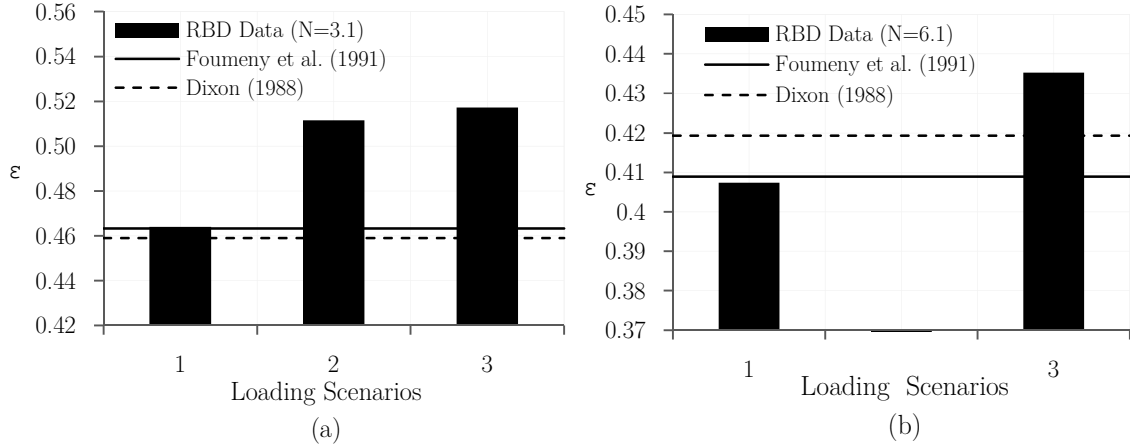
Fig. 3.8 The influence of different loading schemes on the bulk voidage of generated structures; (a) spherical packing with N = 3.1, (b) spherical packing with N = 6.1.

As demonstrated in Fig. 3.8, the first loading strategy not only results in denser packings among all test cases but is also in better agreement with empirical correlations. This can be attributed to the higher intensity of lateral displacements of the pellets for loading method 1, leading to a higher order of densification. The same analysis has been performed for packings of cylindrical pellets with N = 6.98; the results of the mean porosity analysis have confirmed the superiority of the first scenario, where the cylinders are placed obliquely with an angle of 45^0 with respect to the gravity direction. This leads to the densest structure for such narrow fixed beds and is in best agreement with published correlations. Similar results have been found by Fernengel et al. [75] for random packing of spheres with N = 6.25, where the authors investigated the influence of number of spheres per layer in the loading scheme on bulk voidage of simulated structures using LIGGGHTS® and Blender packages. It was also found that increasing the distance between successive pellets in their initial placement allows the tube to be a little more compacted.

In a second step, we imposed random translational and orientational disturbances on the pellets in the first scheme of loading, resulting in five extra loading schemes, to account for the influence of random pouring on the bulk voidage of RBD-simulated structures. This analysis was conducted for random packings of spheres (including translational disturbances) with N = 3.1 and 6.1 and cylinders (including both translational and orientational disturbances) with N = 3.55 and 6.98. Fig. 3.9 illustrates the imposed disturbances on the first loading scenario for packing of cylinders with N = 6.98.

(1)   (2)   (3)   (4)   (5)   (6)
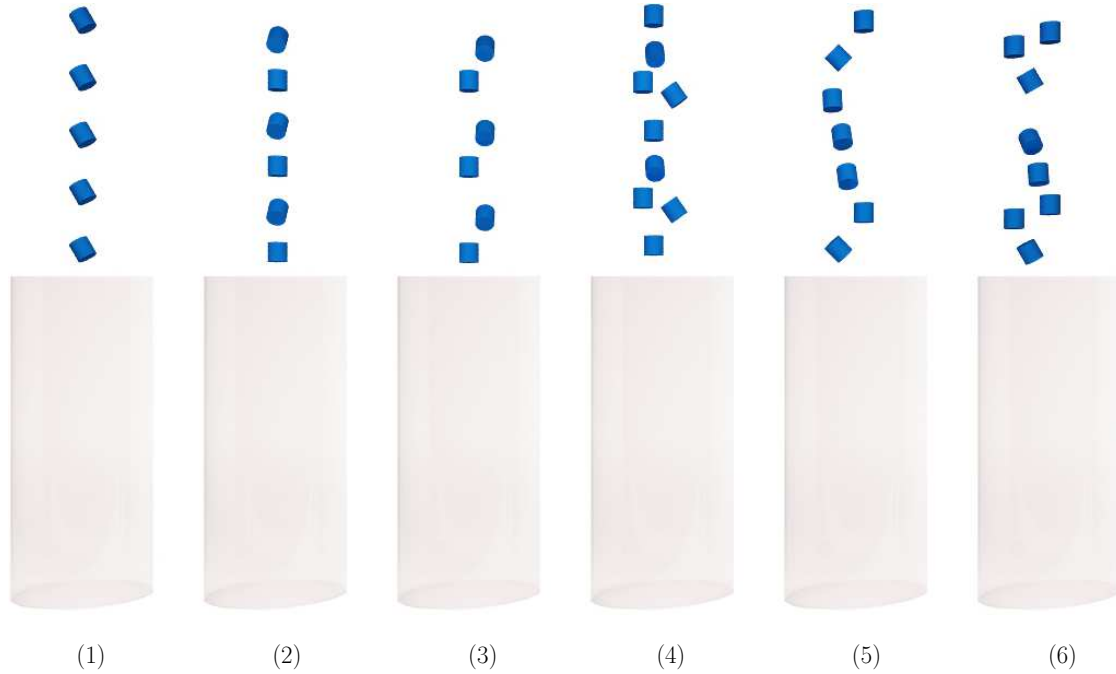
Fig. 3.9 Random disturbances imposed on the first loading scheme to mimic the influence of random pouring on bulk voidage in random packings of cylinders with N = 6.98.

Overall, the results show that denser structures can be synthesized using the original version of the first loading scheme for all cases. Here, for the sake of brevity, the result of comparison analysis for random packing of cylinders with N = 6.98 is presented in Table 3.2, where the bulk voidage obtained from the generated packings according to the loading schemes presented in Fig. 3.9 is compared with the empirical coloration by Dixon [25].

Table 3.2. Influence of imposing translational and orientational disturbances on the first loading scheme on the resulting bulk voidage for packing of cylinders with N = 6.98.

Loading Scenario	1	2	3	4	5	6
Bulk voidage (calculated)	0.405	0.410	0.419	0.416	0.420	0.425
Predicted voidage after Dixon (1988)	0.395	0.395	0.395	0.395	0.395	0.395
MER (%)	-2.4	-3.8	-6.1	-5.2	-6.2	-7.5

It is worth remarking that the aforementioned loading schemes were also implemented in our further analysis described in sections 3.5.2 and 3.5.3., where we have investigated the roles of restitution and friction factors in the bulk voidage of simulated structures. Similarly, our

results demonstrate that denser packing structure can be generally generated using the original version of first loading method for such narrow beds for all ranges of restitution and friction coefficients considered.

3.5.2.   The role of surface bounciness (Coefficient of Restitution)

The amount of surface bounciness, expressed as the coefficient of restitution, can substantially affect the subsequent chain of collisions, and therefore the final structures. Zhang et al. [76] investigated the influence of the coefficient of restitution on packing density, but their work was restricted to packings of spheres in large-N beds, say $N = 24$, where in the effect of container wall on the packing process and final bulk voidage cannot be elucidated. Since the impact of this physio-mechanical property on the packing densification has not yet been systematically investigated in low-N packings of (non-) spherical pellets, an effort is made here to monitor the role of this property on the bulk porosity of packings of shapes and cylinders. To this end, the packing algorithm is set up based on the data given in Table 3.1, to synthesize random packings of spheres with $N = 3.1$ and 6.1 and cylinders with $N = 3.55$ and 6.98. The friction factor is set to $\mu_d = 0.6$, whilst the restitution coefficient is set to 0.05, 0.15, 0.35, 0.55, 0.75 and 0.95, respectively, covering the whole range of collision behavior from semi-plastic to semi-elastic. The first loading scheme is applied. However, to generate statistically independent samples for averaging, random disturbances (with a maximum magnitude of $0.8d_p$ and maximum angle of 45^0) have been imposed to the initial pellet positions and orientations for each packing case (see Fig. 3.9). This was repeated 6 times for each case, leading to 144 generated test cases for spherical and cylindrical packings. Fig. 3.10 shows some typical results of generated packings.
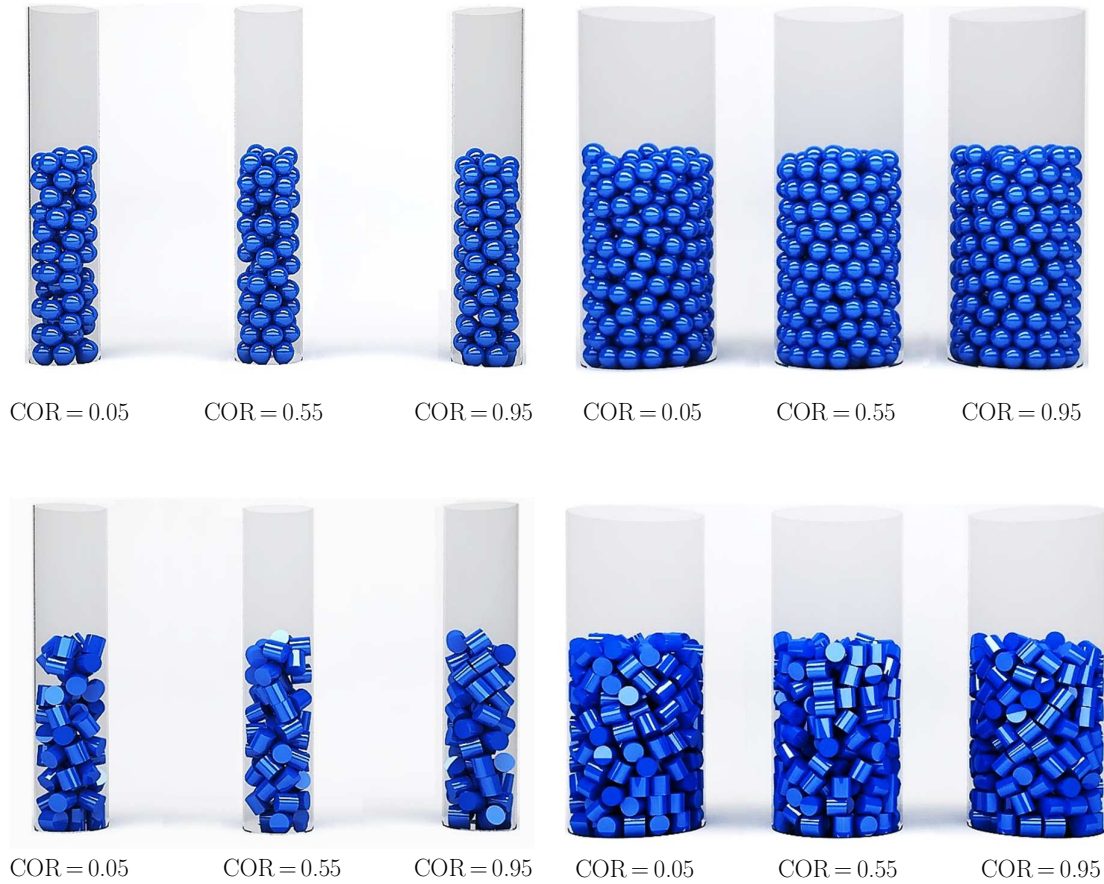
Fig. 3.10 The influence of COR on a number of samples simulated based on the first scenario of loading for packings of spheres (with N = 3.1 & 6.1) and cylinders (with N = 3.55 & 6.98).

The mean voidage of all test cases was then computed based on the number of pellets stacked within a tube up to the altitude of H = 120 mm and depicted versus COR in Fig. 3.11. Overall, the results of this analysis agree with the prevailing hypothesis on the influence of restitution coefficient, viz., higher values of COR generally result in denser packings, because with more elastic collisions, the probability of longer-lasting successive collision chains increases. This allows pellets to be further displaced laterally, and to be vibrated for a longer duration of time, allowing them to find their optimal positions. However, our results also show considerable variability of the mean porosity from sample to sample, in particular in narrower structures (see Fig. 3.11a-b), which can be reasonably attributed to the restrictive role of the tube wall. The trends in wider beds, as shown in Fig. 3.11c-d), demonstrate a lower amount of variability. Furthermore, the results demonstrate that the influence of COR on the resulting packing density is more discernable for COR values beyond 0.5, where it causes an intensive vibration of catalyst pellets in the bed.
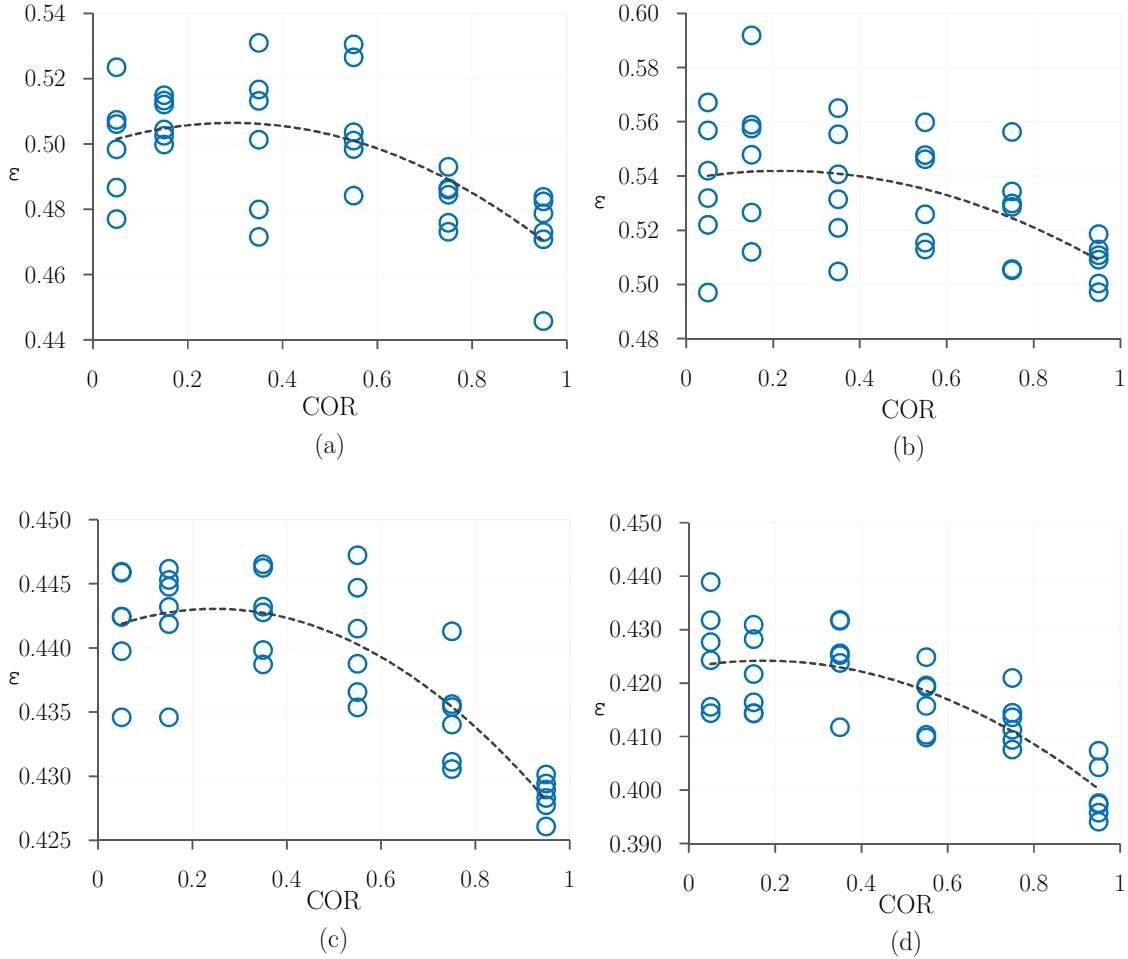
Fig. 3.11 Influence of coefficient of restitution (COR) of catalyst pellets on the bulk porosity of generated structures for packings of (a) spheres with $N = 3.1$, (b) cylinders with $N = 3.55$, (c) spheres with $N = 6.1$ and (d) cylinders with $N = 6.98$. Results of 6 independent simulations for each COR (with different random disturbances on the initial pellet positions and orientations) are shown, indicating the variability of the results. Dashed lines are trendlines based on the average of these independent simulations.

3.5.3. The role of surface roughness

The surface roughness of a pellet, which is fundamentally described by its friction coefficient, is another physio-mechanical property that can affect the process of packing. To assess the impact of this parameter on structural properties of random packings, the same procedure as for the role of COR is pursued. In this case, the pellet's COR is set to 0.6, whereas the surface friction coefficient is set to 0.05, 0.3, 0.5, 0.7 and 0.95, respectively, covering a large spectrum of dynamic friction coefficient. Fig. 3.12 shows some typical results of physical simulations.

$\mu_d = 0.05$ $\mu_d = 0.5$ $\mu_d = 0.95$ $\mu_d = 0.05$ $\mu_d = 0.5$ $\mu_d = 0.95$

$\mu_d = 0.05$ $\mu_d = 0.5$ $\mu_d = 0.95$ $\mu_d = 0.05$ $\mu_d = 0.5$ $\mu_d = 0.95$
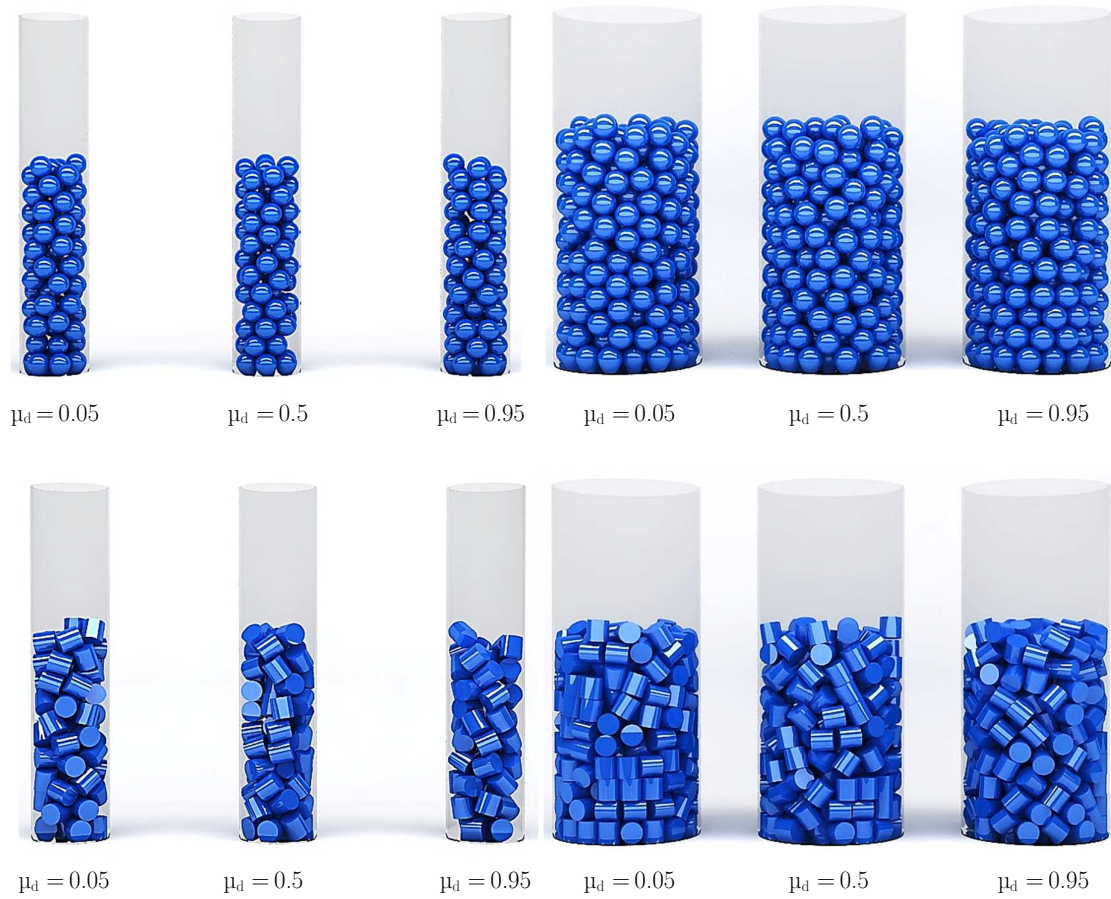
Fig. 3.12 The influence of pellets friction coefficient on a number of samples simulated based on the first loading scheme for packings of spheres (with N = 3.1 & 6.1) and cylinders (with N = 3.55 & 6.98).

The bulk porosity of all samples for each test case has been computed, and plotted against friction coefficient in Fig. 3.13.
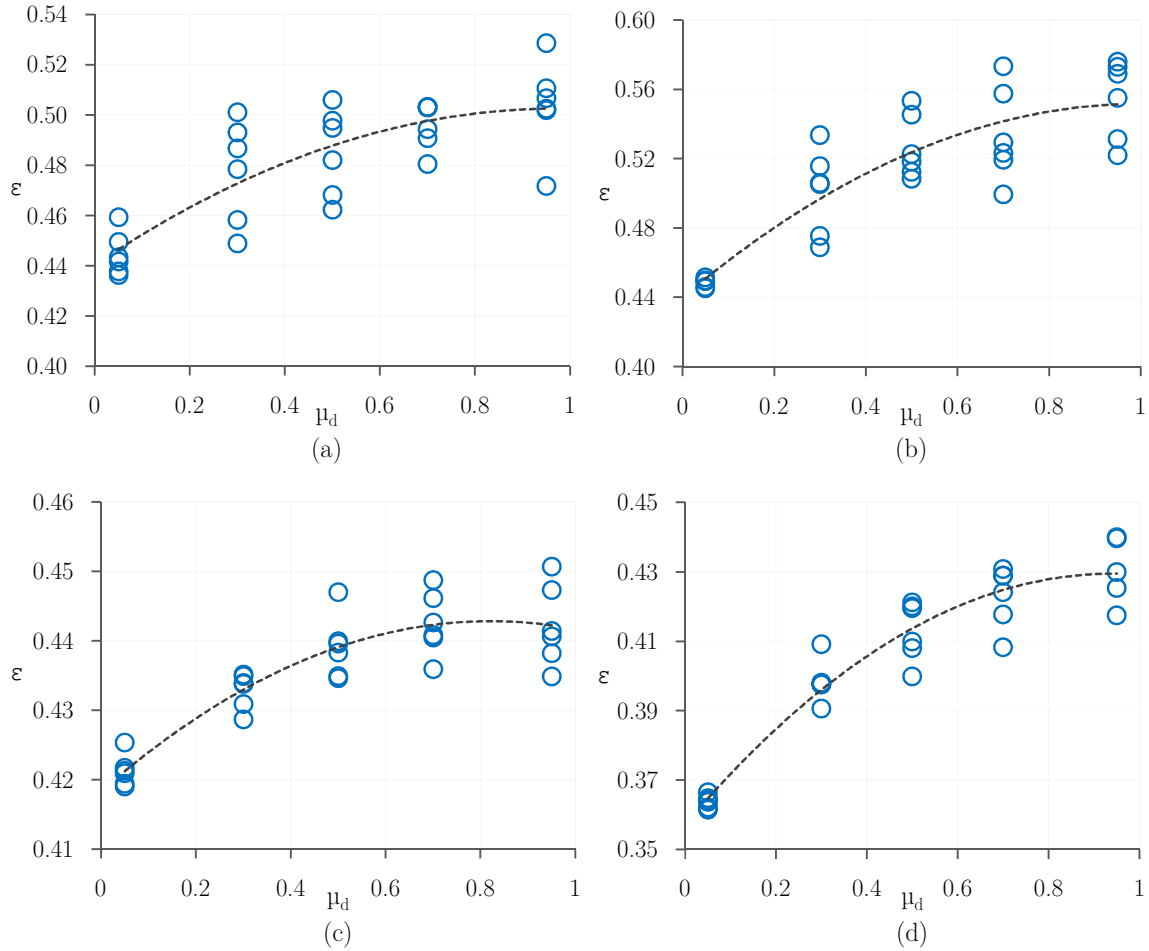
Fig. 3.13 Influence of friction factor of catalyst pellets on the bulk porosity of generated structures for packings of (a) spheres with $N = 3.1$, (b) cylinders with $N = 3.55$, (c) spheres with $N = 6.1$ and (d) cylinders with $N = 6.98$. Results of 6 independent simulations for each μ_d (with different random disturbances on the initial pellet positions and orientations) are shown, indicating the variability of the results. Dashed lines are trendlines based on the average of these independent simulations.

The results confirm the general understanding of the effect of surface friction on packing density: lower values of friction facilitate sliding of the contact surfaces relative to each other, leading to denser packing structures. In fact, the influence of friction factor on the packing density appears to be 1.5 times larger (in the studied range) than that of the COR, leading to an apparently lower variability between different samples.

3.5.4.   Validation study and postprocessing of the results

The main goal of this chapter is to introduce a new RBD methodology to synthesize realistic random packings of particles of any shape. We now present a detailed validation study, whereby the reliability of the RBD-algorithm in replicating structural properties of realistic packings is scrutinized. The specifications of the physical simulations (see Table 3.3) were

chosen to reproduce the experimental arrangements utilized in the works of Benenati and Brosilow [24], Roshani [73] and Mueller [52]. More simulation runs have been performed to generate random packings in the range $3.1 \leq N \leq 9.16$ to examine the restrictive role of confining walls on the predicted bulk porosity over a range of tube-to-pellet diameter ratios, and to benchmark the predicted radial porosity distribution against some of the most-frequently used empirical correlations. Table 3.3 addresses the specifications and data used in setup of RBD simulations.

Table 3.3 RBD simulation setup for validation study

Catalyst pellet		Bed environment	
No. of face mesh (per pellet)	Sphere: 3120	Bed Size:	Spherical beds: $d_t = 31$, 39.6, 41, 56, 59.6, 61 & 79.9 mm & Bed altitude: 120 mm
	Cylinder: 4400		cylindrical beds: d_t=33.65, 35.49, 45.79, 46.93, 69.83 & 91.58 mm & Bed altitude: 120 mm
	Raschig ring: 8008		Raschig ring beds: $d_t = 30.58$, 40.45, 60.18 & 79.91mm & Bed Altitude: 120 mm
Density: 8030 kg/m^3		Tube wall friction factor (dynamic): 0.6	
Surface friction factor (dynamic): 0.1		Tube wall surface bounciness (COR): 0.6	
Surface bounciness (COR): 0.9		Gravity acceleration: 9.81 ms^{-2}	

Fig. 3.14 illustrates the dynamic behavior of the random packing process, in four frames, for typical spherical, cylindrical and Raschig ring packings.
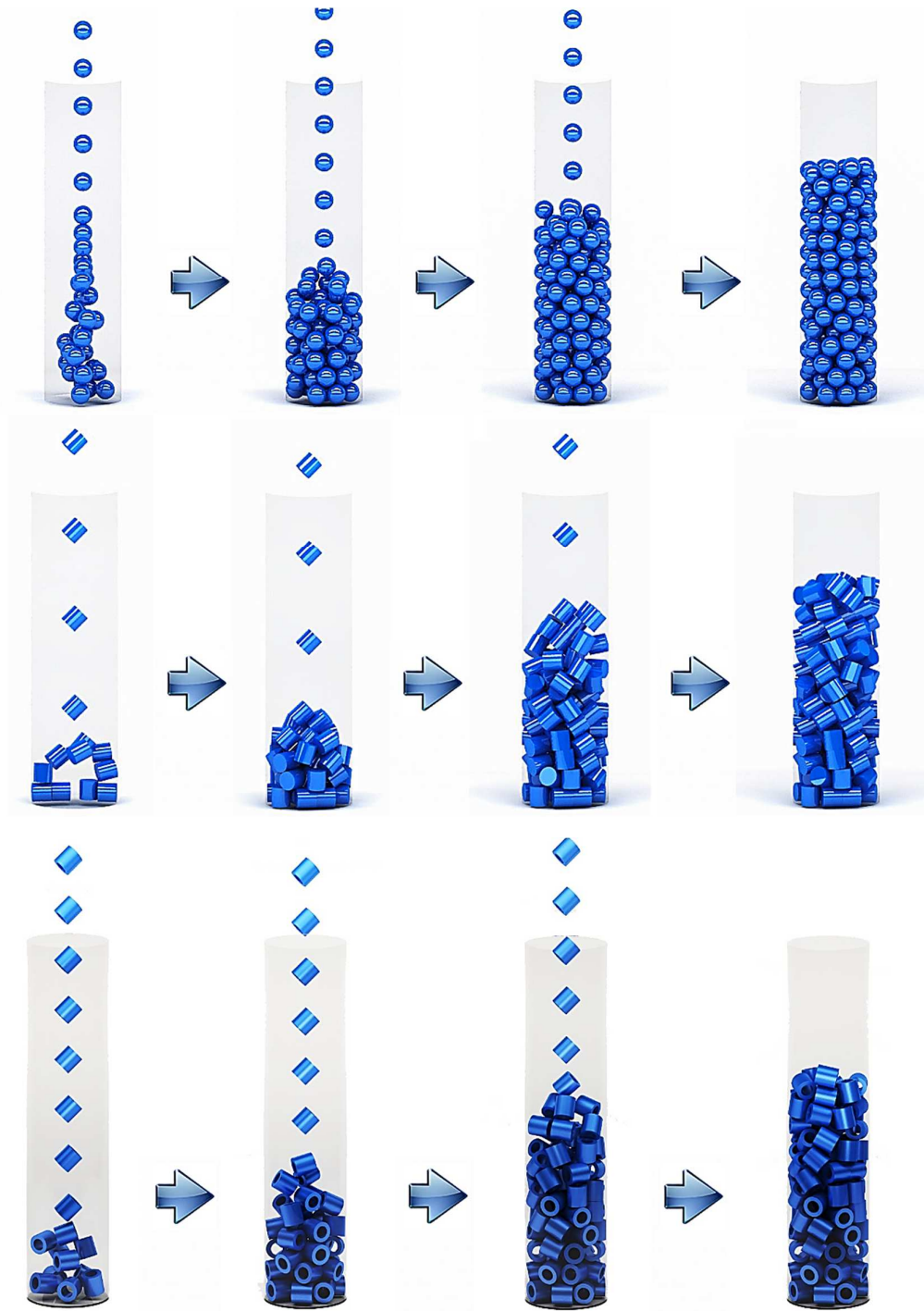
Fig. 3.14 The dynamics of packing process for packings of spheres, cylinders and Raschig rings with COR = 0.9 and μ_d = 0.1 in a tube with N = 4.1, 4.69 and 4.05 respectively.

Several packings have been generated, based on the specifications in the Table 3.3, including seven different tube-to-particle ratios for packings of spheres, five for packings of solid cylinders, and four for packings of Raching rings. Each case has been executed in triplo with slightly perturbed initial pellet positions to generate statistically independent data. Fig.

3.15 illustrates some typical results of RBD-simulated packings of spheres, cylinders and Raschig rings.

<center>N = 4.1   N = 4.69   N = 4.05</center>

<center>N = 8.1   N = 9.16   N = 7.99</center>

Fig. 3.15 Examples of RBD-simulated structures of spheres, cylinders and Raschig rings.

The bulk porosity of the generated structures has been computed based on the total amount of pellet material up to the altitude of 100 mm, and compared with well-known published correlations in Fig. 3.16.
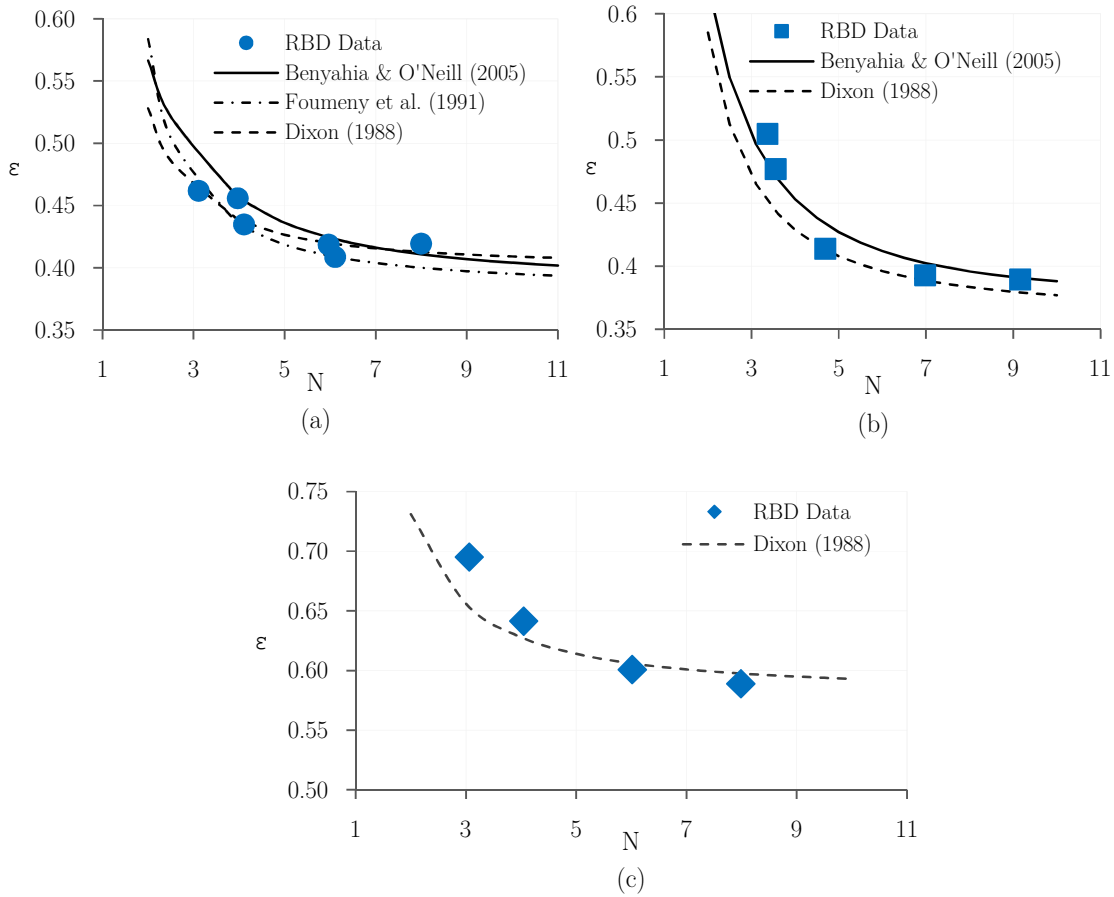
Fig. 3.16 Comparison between the mean porosity extracted from RBD simulations and empirical correlations for three types of pellets: (a) spheres, (b) equilateral solid cylinders, and (c) Raschig rings.

The RBD simulation results demonstrate satisfactory agreement with the empirical correlations for all cases, giving a maximum relative error (MRE) of 3.9%, 17.6% (relating to the narrowest bed case) and 6.6% for packings of spheres, cylinders and Raschig rings, respectively, based on the empirical correlation by Dixon [25].

The local structural properties of the RBD-simulated packings have also been examined. For this, the axially-averaged radial void fraction distribution of the RBD-simulated structures was extracted, and compered to published experimental and analytical data. To evaluate radial void fraction profiles, a planar mesh-based approach [10] was adopted, in which a packing structure is intersected with a series of concentric tubes with different diameters (see Fig. 3.17). The local void fraction at a specific radius can then be precisely computed by the following formula:

$$\varepsilon(r) = 1 - \frac{S_{int.}}{S_{total}} \tag{3.34}$$

where $S_{int.}$ is the intersecting area with pellets and S_{total} is the area of tube that intersects the packing at radius r.
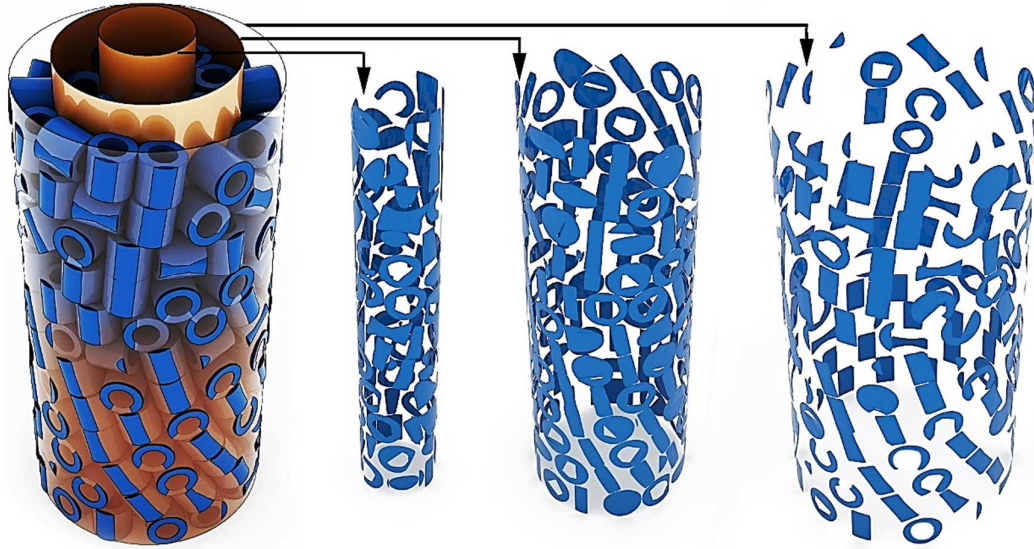
Fig. 3.17 Implementation of the planar mesh-based approach for evaluating axially-averaged radial void fraction data for RBD-simulated structure of Rachig ring with $N = 6.02$.

The radial void fraction profiles from the RBD-simulations versus the distance from the tube wall (made dimensionless by d_{pv}, the equivalent diameter of a sphere of the same volume) is shown in Fig. 3.18-19 for spheres and cylinders, respectively.
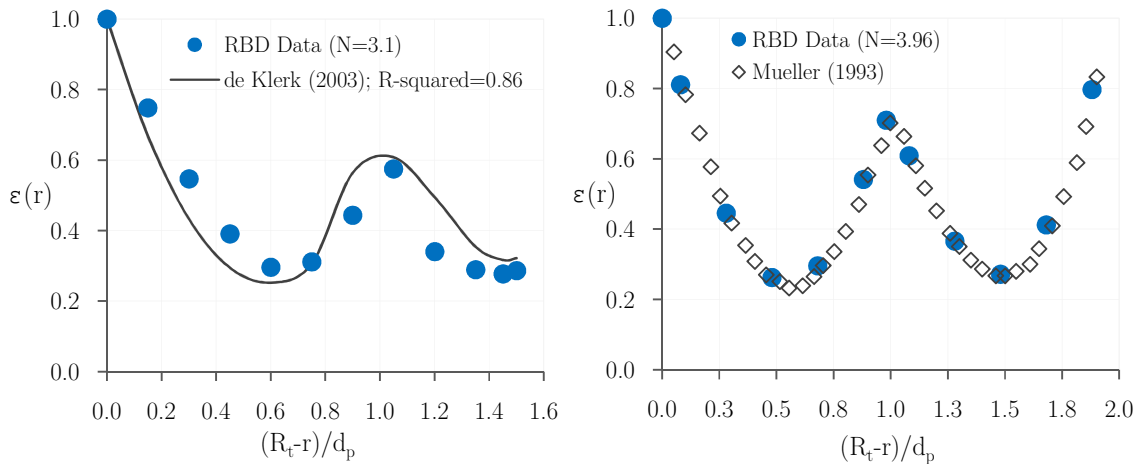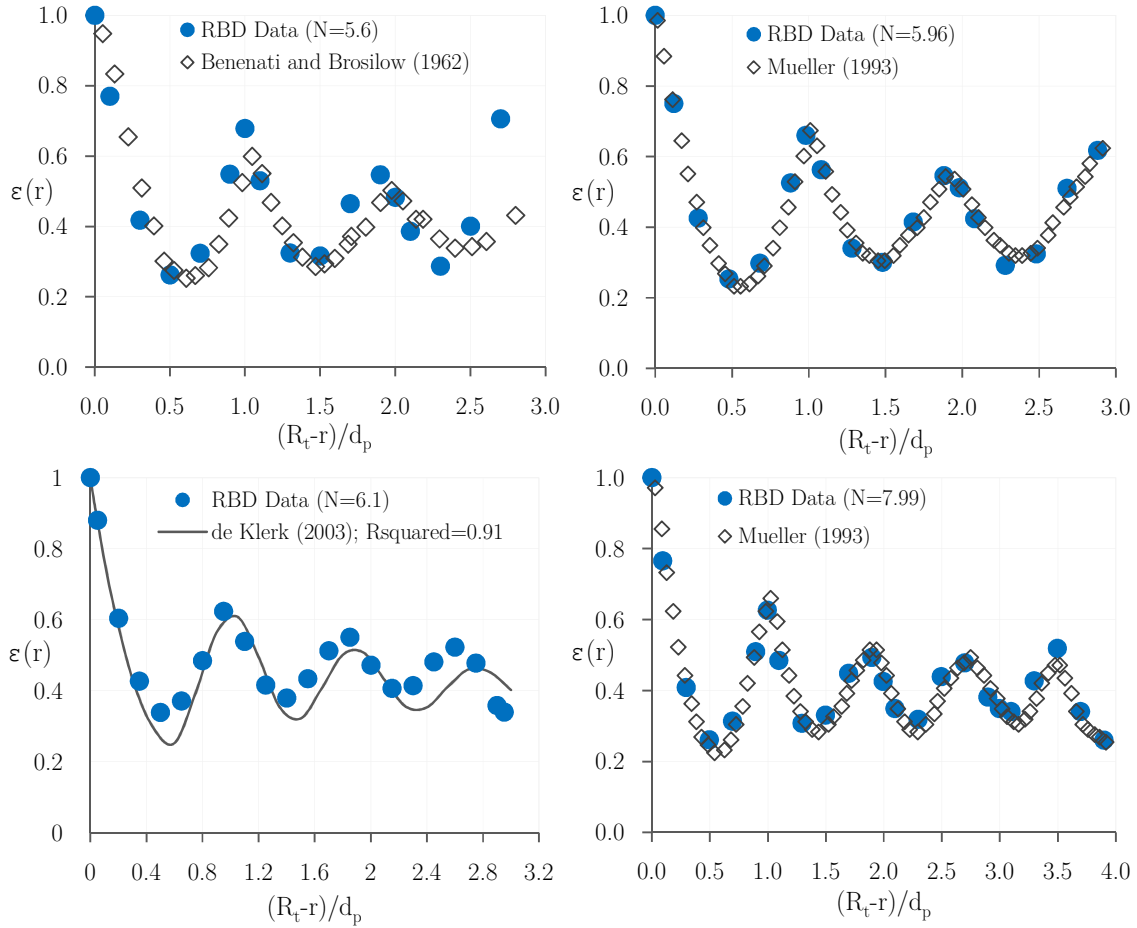
Fig. 3.18 Comparison between radial void fraction profiles obtained from RBD-simulations of sphere packings and literature data. The experimental data presented here are extracted with permission from [G.E. Mueller, Angular void fraction distributions in randomly packed fixed beds of uniformly sized spheres in cylindrical containers, Powder Technology. 77 (1993) 313–319, and R.F. Benenati, C.B. Brosilow, Void fraction distribution in beds of spheres, AIChE Journal. 8 (1962) 359–361].
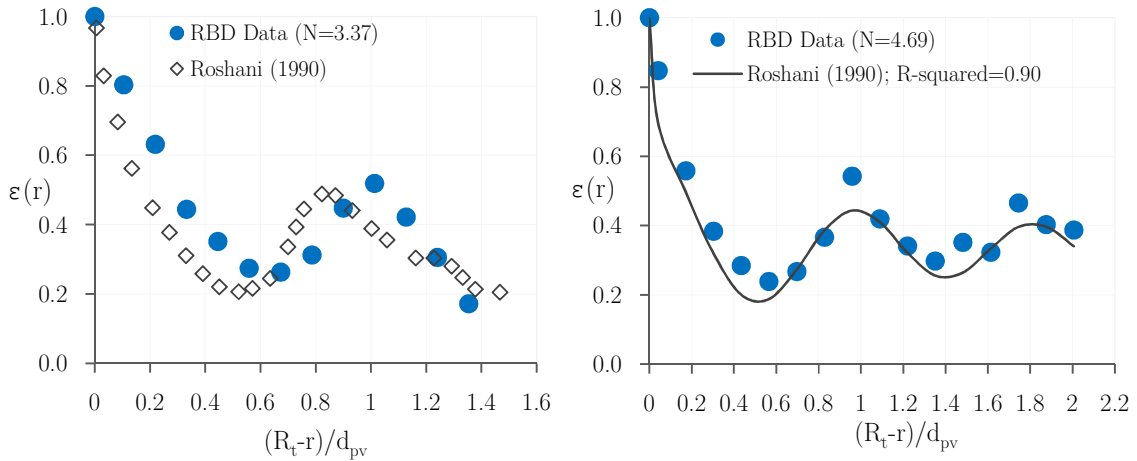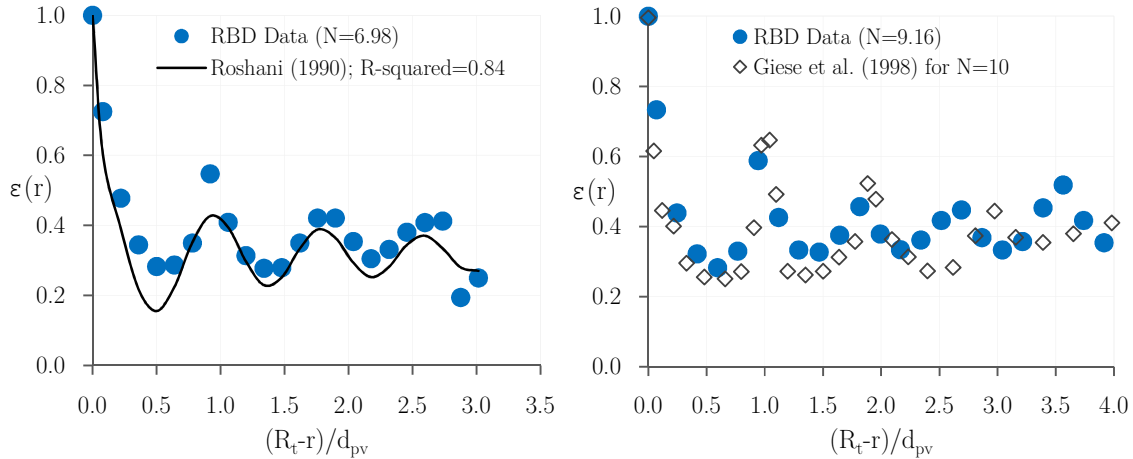
Fig. 3.19 Comparison between radial void fraction data obtained from RBD-simulations of packings of cylinders and analytical and experimental data by Roshani [73] and Giese et al. [74]. The experimental data presented here are extracted with permission from [S. Roshani, Elucidation of Local and Global Structural Prperties of Packed Bed configurations, The University of Leeds, (Thesis),(1990), and M. Giese, K. Rottschafer, D. Vortmeyer, Measured and modeled superficial flow profiles in packed beds with liquid flow, AIChE J. 44 (1998) 484–490].

Figs. 3.18-19 show a very good agreement between the radial void fraction profiles extracted from RBD-simulations and the corresponding experimental data by Mueller [52] for packings of spheres and Roshani [73] and Geise et al. [74] for packings of cylinders. The same conclusion can be made when comparing the RBD data with empirical correlations by de Klerk [27] and Roshani [73], giving R-squared and root mean square error values of more than 0.85 and lower than 0.08 for spheres, respectively, and more than 0.84 and lower than 0.07 for cylinders, respectively.

Overall, it can be concluded that the proposed packing algorithm is able to reasonably reproduce the essential features, including the oscillatory-damped behavior as well as amplitude and period of oscillations, of the most-frequently used experimental data.

We can now use the method to investigate the radial void fraction profile in packings of Raschig rings, as shown in Fig. 3.20.
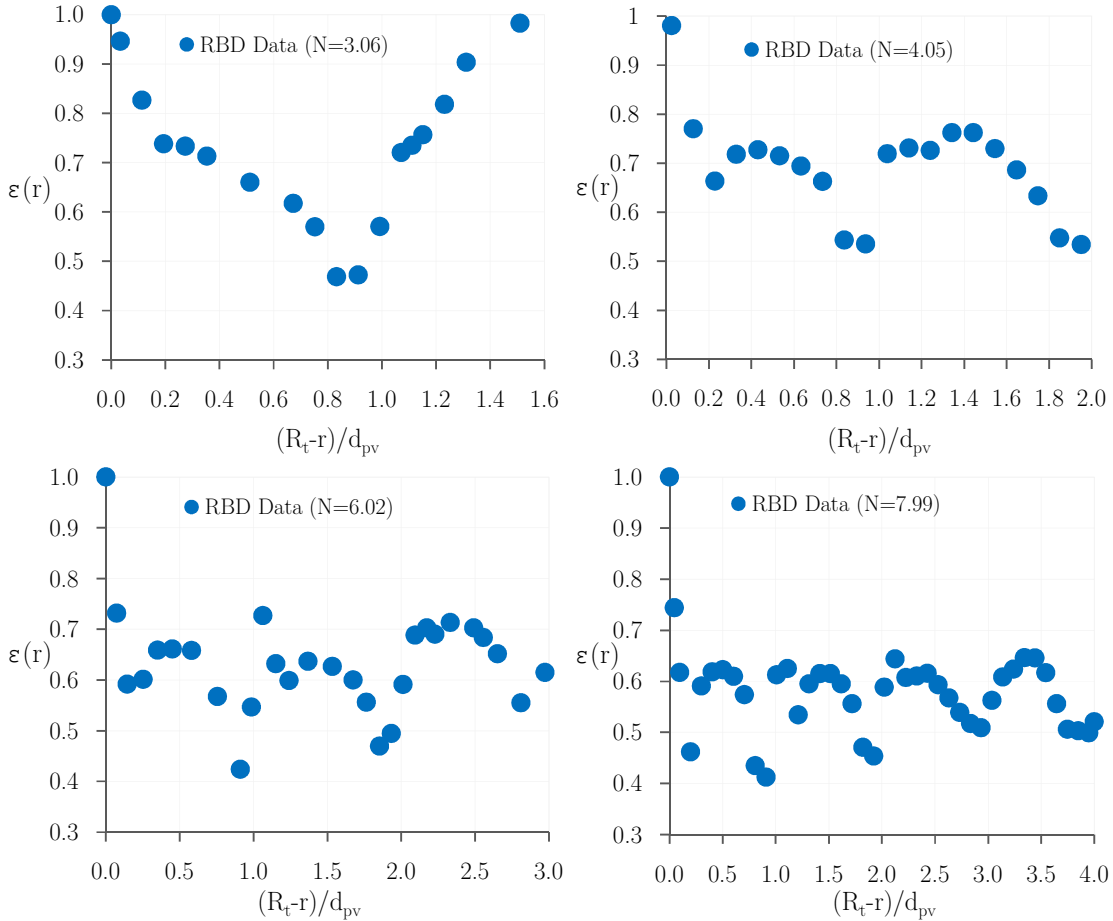
Fig. 3.20 Radial void fraction profiles obtained from RBD-simulations of packings of Raschig rings.

As depicted in Fig. 3.19, the behavior and pattern of the void fraction distribution over the dimensionless distance from the tube wall in Raschig ring packings is quite different compared to those known for sphere and cylinder packings. A similar trend has been reported by Giese et al. [74] (1998) for a Raschig ring bed with $N = 10$. This difference in packing has a large influence on the flow distribution, as we will show in the next chapter.

3.6. Conclusion

A novel physics-based packing algorithm, founded on the concepts of Rigid Body Dynamics (RBD), has been presented and validated. The algorithm enables us to synthesize random packing structures of non-spherical and non-convex shapes. The advantage of our approach, compared to popular computer graphics software such as Blender, is that we proposed a more rigorous and realistic approach to model the resting contact phenomenon, wherein the transition between moving and resting particles is controlled by a cut-off on the relative contact velocity followed by a detailed balance of constrained forces acting on each

pellet, facilitating the stability of convergence in RBD simulations. Our approach avoids the usage of artificial translational and angular momentum sinks on moving particles, and therefore exactly obeys the laws of conservation of linear and angular momentum.

We used our new approach to generate realistic random packings of spheres, cylinders and Raschig rings with a bed-to-pellet diameter ratio N ranging from 3 to 9.16, where the role of confining walls in the packing process is very important. The results of our validation study have demonstrated satisfactory agreement with literature data concerning bulk porosity and radial void fraction profiles, substantiating the merits of this approach in replicating the structural properties of realistic random packing geometries of non-spherical catalyst pellets. Furthermore, the influence of essential physio-mechanical properties of catalytic particles, such as surface roughness and bounciness, were studied for both spherical and cylindrical particulate beds.

A particular feature of this approach is that it can synthesize both loose and dense packing structures, depending on the precise loading scheme and physio-mechanical properties, thereby in a way mimicking both sock-loading and dense loading methods utilized in industrial practice.

The packing algorithm provides detailed information concerning the topological features of randomly packed fixed bed structures, e.g. the position and orientation of catalyst pellets in the bed. Therefore, it has the potential of being used as a supplementary tool to Lattice Boltzmann or Computational Fluid Dynamics simulations of reacting flows and heat and species transport characteristics of such complicated unit operations.

We finish our conclusions by noting that from the results presented in this work, we cannot yet make a statement about the possibly improved quality of the packing structures by our method relative to other methods such as Blender, DigiDEM and LIGGGHTS. We have shown that the packing structures are highly sensitive of pellet shape, physiomechanical properties, and loading methods. To trustfully show the differences between the different methods, it is therefore necessary to conduct a systematic comparison study, covering different pellet shapes with different ranges of physiomechanical properties and loading methods. We note that small but significant differences in the void fraction of sphere packings in cylindrical beds predicted by Blender, compared to DigiDEM and LIGGGHTS, have already been found in a recent paper by Fernengel et al. [75] (see their Fig. 2). At this point it is not certain whether such differences are caused by differences in handling the dynamics of the packing process (which for instance is influenced by the magnitudes of the translational and angular momentum damping terms) or by small differences in the contact model. Small differences in predicted voidage may even be acceptable for certain applications in view of the greatly enhanced

computational speed of Blender relative to these other packages. In any case, a careful and systematic comparison of these different methods is clearly needed, and will be the topic of our forthcoming contribution.

Nomenclature

A	a multiplier introduced in Eq. (31)	$[\text{kg}^{-1}]$
B	an acceleration source term introduced in Eq. (31)	$[\text{ms}^{-2}]$
COR	coefficient of restitution	[-]
d_p	pellet diameter	[m]
d_t	tube diameter	[m]
d_{pv}	Equivalent diameter of a sphere volume	[m]
f	The magnitude of normal force	[N]
$\mathbf{F}$	force vector	[N]
$\mathbf{g}$	gravity acceleration	$[\text{ms}^{-2}]$
$\mathbf{I}$	moment of inertia tensor	$[\text{kgm}^2]$
j	The magnitude of impulse	$[\text{kgms}^{-1}]$
$\mathbf{J}$	Impulse	$[\text{kgms}^{-1}]$
$\mathbf{K}$	collision matrix	$[\text{kg}^{-1}]$
$\mathbf{L}$	angular momentum	$[\text{kgm}^2\text{s}^{-1}]$
M	Mass of a pellet	[kg]
$\hat{\mathbf{n}}$	unit vector at the normal direction	[-]
N	Tube to pellet diameter ration	[-]
$\mathbf{p}$	Position of contact vertex at the surface of a pellet	[m]
$\mathbf{P}$	linear momentum	$[\text{kgms}^{-1}]$
$\mathbf{r}$	distance between a contact point and center of mass	[m]
R_t	tube radius	[m]
$\hat{\mathbf{t}}$	unit vector at the tangential direction	[-]
v	Linear velocity at specific direction	$[\text{ms}^{-1}]$
$\mathbf{v}$	Linear velocity	$[\text{ms}^{-1}]$
$\mathbf{W}$	weight force	[N]
$\mathbf{x}$	position of center of mass of a pellet	[m]
$\mathbf{X}$	state vector	[-]
$\hat{\mathbf{z}}$	unit vector at the direction of gravity	[-]

Greek Letters

ε	bulk porosity	[-]
$\varepsilon(r)$	radial porosity	[-]
ε_p	numerical threshold	[-]
μ_d	dynamic friction coefficient	[-]

| $\boldsymbol{\omega}$ | Angular velocity | $[s^{-1}]$ |
| φ | Normal force acting on resting a contact point | $[N]$ |

Subscripts

i	pellet i
j	pellet j
k	pellet k
n	normal
p	contact point
t	tangential

Bibliography

[1] M. Winterberg, E. Tsotsas, Correlations for effective heat transport coefficients in beds packed with cylindrical particles, Chemical Engineering Science. 55 (2000) 5937–5943. doi:10.1016/S0009-2509(00)00198-6.

[2] M. Nijemeisland, A.G. Dixon, Comparison of CFD simulations to experiment for convective heat transfer in a gas – solid fixed bed, Chemical Engineering Journal. 82 (2001) 231–246.

[3] A.G. Dixon, M. Nijemeisland, E.H. Stitt, Packed tubular reactor modeling and catalyst design using computational fluid dynamics, Advance in Chemical Engineering. 31 (2006) 307–389. doi:10.1016/S0065-2377(06)31005-8.

[4] M.E. Taskin, A.G. Dixon, M. Nijemeisland, E.H. Stitt, CFD Study of the Influence of Catalyst Particle Design on Steam Reforming Reaction Heat Effects in Narrow Packed Tubes, Industrial & Engineering Chemistry Research. (2008) 5966–5975.

[5] H. Freund, J. Bauer, T. Zeiser, G. Emig, Detailed simulation of transport processes in fixed-beds, Industrial & Engineering Chemistry Research. 44 (2005) 6423–6434. doi:10.1021/ie0489453.

[6] A.G. Dixon, G. Walls, H. Stanness, M. Nijemeisland, E.H. Stitt, Experimental validation of high Reynolds number CFD simulations of heat transfer in a pilot-scale fixed bed tube, Chemical Engineering Journal. 200–202 (2012) 344–356. doi:10.1016/j.cej.2012.06.065.

[7] M. Behnam, A.G. Dixon, M. Nijemeisland, E.H. Stitt, A New Approach to Fixed Bed Radial Heat Transfer Modeling Using Velocity Fields from Computational Fluid Dynamics Simulations BT - Industrial & Engineering Chemistry Research, Industrial and Engineering Chemistry Research. 52 (2013) 15244–15261. doi:10.1021/ie4000568.

[8] G. Boccardo, F. Augier, Y. Haroun, D. Ferre, D.L. Marchisio, Validation of a novel open-source work-flow for the simulation of packed-bed reactors, Chemical Engineering Journal. 279 (2015) 809–820. doi:10.1016/j.cej.2015.05.032.

[9] L. Pistocchini, S. Garone, M. Motta, Porosity and pressure drop in packed beds of spheres between narrow parallel walls, Chemical Engineering Journal. 284 (2016) 802–811. doi:10.1016/j.cej.2015.08.047.

[10] Y. Dong, B. Sosna, O. Korup, F. Rosowski, R. Horn, B. Sosna, O. Korup, F. Rosowski, R. Horn, Investigation of radial heat transfer in a fixed-bed reactor: CFD simulations and profile measurements, Chemical Engineering Journal. 317 (2017) 204–214. doi:10.1016/j.cej.2017.02.063.

[11] W. Soppe, Computer simulation of random packings of hard spheres, Powder Technology. 62 (1990) 189–197.

[12]   A.J. Sederman, P. Alexander, L.F. Gladden, Structure of packed beds probed by Magnetic Resonance Imaging, Powder Technology. 117 (2001) 255–269. doi:10.1016/S0032-5910(00)00374-0.

[13]   X.-H. Ren, S. Stapf, B. Blümich, Magnetic Resonance Visualisation of Flow and Pore Structure in Packed Beds with Low Aspect Ratio, Chemical Engineering & Technology. 28 (2005) 219–225. doi:10.1002/ceat.200407092.

[14]   M.J. Baker, P.G. Young, G.R. Tabor, Image based meshing of packed beds of cylinders at low aspect ratios using 3D MRI coupled with computational fluid dynamics, Computers and Chemical Engineering. 35 (2011) 1969–1977. doi:10.1016/j.compchemeng.2011.03.017.

[15]   W.I. Salvat, N.J. Mariani, G.F. Barreto, O.M. Martínez, An algorithm to simulate packing structure in cylindrical containers, in: Catalysis Today, 2005: pp. 513–519. doi:10.1016/j.cattod.2005.07.108.

[16]   S. Siiriä, J. Yliruusi, Particle packing simulations based on Newtonian mechanics, Powder Technology. 174 (2007) 82–92. doi:10.1016/j.powtec.2007.01.001.

[17]   G.E. Mueller, Radial porosity in packed beds of spheres, Powder Technology. 203 (2010) 626–633. doi:10.1016/j.powtec.2010.07.007.

[18]   L.Y. Yi, K.J. Dong, R.P. Zou, A.B. Yu, Coordination number of the packing of ternary mixtures of spheres: Dem simulations versus measurements, Industrial and Engineering Chemistry Research. 50 (2011) 8773–8785. doi:10.1021/ie200765h.

[19]   H. Bai, P.A. Gillis, P.M. Witt, A Coupled DEM and CFD Simulation of Flow Field and Pressure Drop in Fixed Bed Reactor with Randomly Packed Catalyst Particles, Ind. Eng. Chem. Res. 48 (2009) 4060–4074.

[20]   R. Caulkin, A. Ahmad, M. Fairweather, X. Jia, R.A. Williams, Digital predictions of complex cylinder packed columns, Computers & Chemical Engineering. 33 (2009) 10–21. doi:10.1016/j.compchemeng.2008.06.001.

[21]   G.D. Wehinger, T. Eppinger, M. Kraume, Evaluating catalytic fixed-bed reactors for dry reforming of methane with detailed CFD, Chemie-Ingenieur-Technik. 87 (2015). doi:10.1002/cite.201400153.

[22]   G. Lu, J.R. Third, C.R. Müller, Discrete element models for non-spherical particle systems: From theoretical developments to applications, Chemical Engineering Science. 127 (2015) 425–465. doi:10.1016/j.ces.2014.11.050.

[23]   W. Zhong, A. Yu, X. Liu, Z. Tong, H. Zhang, DEM/CFD-DEM Modelling of Non-spherical Particulate Systems: Theoretical Developments and Applications, Powder Technology. 302 (2016) 108–152. doi:10.1016/j.powtec.2016.07.010.

[24]   R.F. Benenati, C.B. Brosilow, Void fraction distribution in beds of spheres, AIChE

Journal. 8 (1962) 359–361. doi:10.1002/aic.690080319.

[25]   A.G. Dixon, Correlations for wall and particle shape effects on fixed bed bulk voidage, The Canadian Journal of Chemical Engineering. 66 (1988) 705–708. doi:10.1002/cjce.5450660501.

[26]   E.A. Foumeny, S. Roshani, Mean voidage of packed beds of cylindrical particles, Chemical Engrnerrmg Science. 46 (1991) 2363–2364. doi:10.1080/19447012408661000.

[27]   A. De Klerk, Voidage variation in packed beds at small column to particle diameter ratio, AIChE Journal. 49 (2003) 2022–2029. doi:10.1002/aic.690490812.

[28]   F. Benyahia, K.E. O'Neill, Enhanced Voidage Correlations for Packed Beds of Various Particle Shapes and Sizes, Particulate Science and Technology. 23 (2005) 169–177. doi:10.1080/02726350590922242.

[29]   W. Zhang, K.E. Thompson, A.H. Reed, L. Beenken, equilateral cylindrical particles, Chemical Engineering Science. 61 (2006) 8060–8074. doi:10.1016/j.

[30]   C.G. du Toit, Radial variation in porosity in annular packed beds, Nuclear Engineering and Design. 238 (2008) 3073–3079. doi:10.1016/j.nucengdes.2007.12.018.

[31]   R. Caulkin, A. Ahmad, M. Fairweather, X. Jia, R.A. Williams, An investigation of sphere packed shell-side columns using a digital packing algorithm, Computers and Chemical Engineering. 31 (2007) 1715–1724. doi:10.1016/j.compchemeng.2007.03.014.

[32]   N. Zobel, T. Eppinger, F. Behrendt, M. Kraume, Influence of the wall structure on the void fraction distribution in packed beds, Chemical Engineering Science. 71 (2012) 212–219. doi:10.1016/j.ces.2011.12.029.

[33]   Y. Wu, X. An, A.B. Yu, DEM simulation of cubical particle packing under mechanical vibration, Powder Technology. 314 (2017) 89–101. doi:10.1016/j.powtec.2016.09.029.

[34]   G.E. Mueller, Numerically packing spheres in cylinders, Powder Technology. 159 (2005) 105–110. doi:10.1016/j.powtec.2005.06.002.

[35]   R. Caulkin, M. Fairweather, X. Jia, N. Gopinathan, R.A. Williams, An investigation of packed columns using a digital packing algorithm, Computers & Chemical Engineering. 30 (2006) 1178–1188. doi:10.1016/j.compchemeng.2006.02.019.

[36]   K.E. Thompson, C.S. Willson, W. Zhang, Quantitative computer reconstruction of particulate materials from microtomography images, Powder Technology. 163 (2006) 169–182.

[37]   P. Richard, P. Philippe, F. Barbe, S. Bourlès, X. Thibault, D. Bideau, Analysis by x-ray microtomography of a granular packing undergoing compaction., Physical Review E. 68 (2003) 020301. doi:10.1103/PhysRevE.68.020301.

[38]   T. Aste, M. Saadatfar, A. Sakellariou, T.J. Senden, Investigating the geometrical structure of disordered sphere packings, 339 (2004) 16–23.

doi:10.1016/j.physa.2004.03.034.

[39]   G.E. Mueller, Numerical simulation of packed beds with monosized spheres in cylindrical containers, Powder Technology. 92 (1997) 179–183. doi:10.1016/S0032-5910(97)03207-5.

[40]   S.K. Chan, K.M. Ng, Geometrical characteristics of a computer-generated three-dimensional packed column of equal and unequal sized spheres—with special reference to wall effects, Chemical Engineering Communications. 48 (1986) 215–236. doi:10.1080/00986448608911788.

[41]   P.L. Spedding, R.M. Spencer, Simulation of packing density and liquid flow in fixed beds, Computers and Chemical Engineering. 19 (1995) 43–73. doi:10.1016/0098-1354(94)E0036-M.

[42]   M.J. Powell, Computer-simulated random packing of spheres, Powder Technology. 25 (1980) 45–52. doi:10.1016/0032-5910(80)87007-0.

[43]   D. Coelho, J.F. Thovert, P.M. Adler, Geometrical and Transport Properties of Random Packings of Speres and Aspherical Particles, Physical Review E. 55 (1997) 1959. https://journals.aps.org/pre/abstract/10.1103/PhysRevE.55.1959 (accessed December 23, 2017).

[44]   T. Atmakidis, E.Y. Kenig, CFD-based analysis of the wall effect on the pressure drop in packed beds with moderate tube/particle diameter ratios in the laminar flow regime, Chemical Engineering Journal. 155 (2009) 404–410. doi:10.1016/j.cej.2009.07.057.

[45]   M.E. Kainourgiakis, E.S. Kikkinides, A.K. Stubos, Diffusion and flow in porous domains constructed using process-based and stochastic techniques, Journal of Porous Materials. 9 (2002) 141–154.

[46]   C.H. Bennett, Serially deposited amorphous aggregates of hard spheres, Journal of Applied Physics. 43 (1972) 2727–2734.

[47]   P. Magnico, Hydrodynamic and transport properties of packed beds in small tube-to-sphere diameter ratio: pore scale simulation using an Eulerian and a Lagrangian approach, Chemical Engineering Science. 58 (2003) 5005–5024. doi:10.1016/S0009-2509(03)00282-3.

[48]   G. Liu, K.E. Thompson, Influence of computational domain boundaries on internal structure in low-porosity sphere packings, Powder Technology. 113 (2000) 185–196. doi:10.1016/S0032-5910(00)00255-2.

[49]   R.S. Maier, D.M. Kroll, R.S. Bernard, S.E. Howington, J.F. Peters, H.T. Davis, Hydrodynamic dispersion in confined packed beds, Physics of Fluids. 15 (2003) 3795–3815.

[50]   K. Sobolev, A. Amirjanov, The development of a simulation model of the dense packing

of large particulate assemblies, Powder Technology. 141 (2004) 155–160.

[51]   M.J. Baker, G.R. Tabor, Computational analysis of transitional air flow through packed columns of spheres using the finite volume technique, Computers & Chemical Engineering. 34 (2010) 878–885. doi:10.1016/j.compchemeng.2009.10.013.

[52]   G.E. Mueller, Angular void fraction distributions in randomly packed fixed beds of uniformly sized spheres in cylindrical containers, Powder Technology. 77 (1993) 313–319. doi:10.1016/0032-5910(93)85023-3.

[53]   P.A. Cundall, O.D.L. Strack, A discrete numerical model for granular assemblies, Géotechnique. 29 (1979) 47–65. doi:10.1680/geot.1979.29.1.47.

[54]   J.E. Hilton, P.W. Cleary, Raceway formation in laterally gas-driven particle beds, Chemical Engineering Science. 80 (2012) 306–316. doi:10.1016/J.CES.2012.06.044.

[55]   T. Eppinger, K. Seidler, M. Kraume, DEM-CFD simulations of fixed bed reactors with small tube to particle diameter ratios, Chemical Engineering Journal. 166 (2011) 324–331. doi:10.1016/j.cej.2010.10.053.

[56]   G.D. Wehinger, C. Fu, M. Kraume, Contact Modi fi cations for CFD Simulations of Fixed-Bed Reactors : Cylindrical Particles, Industrial & Engineering Chemistry Research. (2017). doi:10.1021/acs.iecr.6b03596.

[57]   J. Theuerkauf, P. Witt, D. Schwesig, Analysis of particle porosity distribution in fixed beds using the discrete element method, Powder Technology. 165 (2006) 92–99. doi:10.1016/j.powtec.2006.03.022.

[58]   J. Yang, J. Wu, L. Zhou, Q. Wang, Computational study of fluid flow and heat transfer in composite packed beds of spheres with low tube to particle diameter ratio, Nuclear Engineering and Design. 300 (2016) 85–96. doi:10.1016/j.nucengdes.2015.10.030.

[59]   R.M. Baram, P.G. Lind, Deposition of general ellipsoidal particles, Physical Review E. 85 (2012) 41301.

[60]   Q.J. Zheng, Z.Y. Zhou, A.B. Yu, Contact forces between viscoelastic ellipsoidal particles, Powder Technology. 248 (2013) 25–33.

[61]   M. Marigo, E.H. Stitt, Discrete element method (DEM) for industrial applications: Comments on calibration and validation for the modelling of cylindrical pellets, KONA Powder & Particle Journal. 32 (2015) 236–252.

[62]   Z. Yan, S.K. Wilkinson, E.H. Stitt, M. Marigo, Discrete element modelling (DEM) input parameters: understanding their impact on model predictions using statistical analysis, Computational Particle Mechanics. 2 (2015) 283–299.

[63]   D. Maggiorini, L.A. Ripamonti, F. Sauro, Unifying rigid and soft bodies representation: the Sulfur physics engine, International Journal of Computer Games Technology. 2014 (2014) 6.

[64]   B.N. Rao, D. Jeyakumar, K.K. Biswas, S. Swaminathan, E. Janardhana, Rigid body separation dynamics for space launch vehicles, The Aeronautical Journal. 110 (2006) 289–302.

[65]   W.B. Heard, Rigid Body Mechanics : Mathematics, Physics and Applications. John Wiley & Sons, 2008.

[66]   B. Partopour, A.G. Dixon, An integrated workflow for resolved-particle packed bed models with complex particle shapes, Powder Technology. 322 (2017) 258–272. doi:10.1016/j.powtec.2017.09.009.

[67]   H. Goldstein, C.P. Poole, J.L. Safko, Classical mechanics, Addison Wesley, 2002.

[68]   C. Loop, Smooth subdivision surfaces based on triangles, The University of Utah, (Thesis) 1987.

[69]   M. Kremmer, J.F. Favier, Calculating rotational motion in discrete element modelling of arbitrary shaped model objects, Engineering Computations. 17 (2000) 703–714.

[70]   P.A. Langston, M.A. Al-Awamleh, F.Y. Fraige, B.N. Asmar, Distinct element modelling of non-spherical frictionless particle flow, Chemical Engineering Science. 59 (2004) 425–435.

[71]   D. Baraff, Fast contact force computation for nonpenetrating rigid bodies, in: Proceedings of the 21st Annual Conference on Computer Graphics and Interactive Techniques, ACM, 1994: pp. 23–34. doi:10.1145/192161.192168.

[72]   E.A. Foumeny, H.A. Moallemi, C. Mcgreavy, J.A.A. Castro, Elucidation of mean voidage in packed beds, The Canadian Journal of Chemical Engineering. 69 (1991) 1010–1015. doi:10.1002/cjce.5450690425.

[73]   S. Roshani, Elucidation of Local and Global Structural Prperties of Packed Bed configurations, The University of Leeds, (Thesis),1990.

[74]   M. Giese, K. Rottschafer, D. Vortmeyer, Measured and modeled superficial flow profiles in packed beds with liquid flow, AIChE J. 44 (1998) 484–490. doi:10.1002/aic.690440225.

[75]   J. Fernengel, J. von Seckendorff, O. Hinrichsen, Influence of Cylinder-to-Particle Diameter Ratio and Filling Speed on Bed Porosity of Random Packed Beds of Spheres, in: Computer Aided Chemical Engineering, Elsevier Masson SAS, 2018: pp. 97–102. doi:10.1016/B978-0-444-64235-6.50019-X.

[76]   Z.P. Zhang, L.F. Liu, Y.D. Yuan, A.B. Yu, A simulation study of the effects of dynamic variables on the packing of spheres, Powder Technology. 116 (2001) 23–32. doi:10.1016/S0032-5910(00)00356-9.

[77]   A.D. Rakotonirina, J.-Y. Delenne, F. Radjai, A. Wachs, Grains3D, a flexible DEM approach for particles of arbitrary convex shape—Part III: extension to non-convex

particles modelled as glued convex particles, Computational Particle Mechanics. 324 (2018) 1–30. https://doi.org/10.1007/s40571-018-0198-3)

[78] A.D. Rakotonirina, A. Wachs, Grains3D, a flexible DEM approach for particles of arbitrary convex shape - Part II: Parallel implementation and scalable performance, Powder Technology. 324 (2018) 18–35. doi:10.1016/j.powtec.2017.10.033.

[79] L.J.H. Seelen, J.T. Padding, J.A.M. Kuipers, A granular Discrete Element Method for arbitrary convex particle shapes: Method and packing generation, Chemical Engineering Science. 189 (2018) 84–101. doi:10.1016/j.ces.2018.05.034.

Chapter 4

RBD-CFD Simulation of Fluid Flow and Heat Transfer: Preprocessing, Setup and Validation Study

Abstract

A novel and efficient workflow to predict the hydrodynamics and heat transfer in fixed beds containing non-spherical pellets is presented. The workflow consists of a sequential Rigid Body Dynamics and Computational Fluid Dynamics (RBD-CFD) approach. The RBD is founded on the physics-based hard-body packing algorithm presented in Chapter 3. The methodology is benchmarked for simulation of hydrodynamics and heat transfer in laminar, transient and turbulent regimes, for $5 \leq Re_p \leq 3,000$, in random packings of spheres, cylinders and Raschig rings with tube-to-pellet diameter ratios ranging from 2.29 to 6.1. Using a combination of patch conforming and patch independent meshing approaches, implemented by an ad-hoc Python-based script in ANSYS Workbench v.16.2, an inflationary volume mesh topology is created in the random packing structures. This meshing approach provides a high-quality mesh to appropriately capture phenomena at the contact regions, and immensely facilitates solution convergence in the turbulent region, without the need to manipulate the under-relaxation factors. Both verification and validation studies are performed. For verification, the mesh refinement analysis is conducted, resulting in an optimum size of mesh with a numerical error of 1.77% and 1.74% for bed pressure drop and azimuthal-averaged temperature profile, respectively, based on the Richardson extrapolation method. For validation, the CFD results of velocity and temperature fields are benchmarked against published data, concerning azimuthally-averaged axial velocity, bed pressure drop and interphase heat transfer Nusselt number.

4.1. Introduction

Fixed bed unit operations have found extensive applications, particularly in reaction engineering, where they are used as the process workhorse in various chemical and process industries to handle highly exothermic and endothermic reactions. Such reactions require specific thermal management to prevent runaway reaction conditions. For this reason, narrow-to-moderate tubular fixed bed configurations are regularly employed, with tube-to-pellet diameter ratios N in the range of 2 to 10. The design of such reactors is predominantly performed on the basis of pseudo-continuum models, wherein the essential role of topological non-uniformities and local flow mal-distribution are neglected. This leads to failure of pseudo-homogeneous models in accurate prediction of the transport scalars at the pellet scale [1–5]. These inadequacies have led to numerous experimental and analytical research efforts to incorporate the effects of bed structure, in particular the wall effect, into these models. Several investigators have employed non-invasive experimental techniques, e.g. McGreavy et al. [6], Bey and Eigenberger [7], Giese et al. [8] and Krischke [9] used Laser Doppler Velocimetry (LDV), and Sederman et al. [10], Suekane et al. [11], Ren et al. [12], Baker et al. [13] used Magnetic Resonance Imaging (MRI) to investigate the flow field. Both methods are of limited coverage due to intrinsic restrictions connected to these non-invasive methods, as addressed

by Dixon et al. [5]. A number of researchers has been inspired by the void fraction distribution over the bed radius, and tried to explain the radial inhomogeneities in the velocity field by flow channeling occurring near the wall region where the local porosity approaches unity. This observation has resulted in a simplified version of the radially dependent axial velocity profile, $v_z(r)$, from a modified momentum balance, e.g. [7], or a form of the Brinkman-Forcheimer-extended Darcy (BFD) equation, e.g. [8], with pseudo-homogeneous models to account for the wall-effect in low-N fixed beds. Using such velocity-based pseudo-continuum models, e.g. $\Lambda_r(r)$ model, several reactor studies have attained better agreement with experiments [14–16]. However, even these more sophisticated models are still based upon lumped (effective) properties, e.g. effective transport parameters. These lumped properties not only obscure the physical premise of the model, but also are very questionable for modeling low-N tubular fixed beds, where the cross-section contains only a few catalyst pellets, and thus azimuthal symmetry cannot be reasonably expected [4,5,17]. In fact, a spatially resolved 3D simulation of the reactor system needs to be performed, so that the velocity, thermal and species concentration fields are thoroughly addressed [4,18,19]. Over the last decades, advances in computer performance and computational techniques have allowed researchers to conduct comprehensive 3D simulations of flow fields and transport scalars within tubular fixed beds containing several hundred particles using Computational Fluid Dynamics (CFD) and Lattice Boltzmann methods (LBM), e.g. [17–36]. However, majority of the prevailing efforts has concentrated on spherical packing structures, whilst application of catalyst pellets of non-spherical shape such as cylinders, Raschig rings, trilobe, quadrulobe, hollow extrudates, etc. is common in industry because of their potential to enhance transport processes (e.g. Raschig rings are used in ethylene epoxidation, and multi-hole shaped catalyst pellets are used in methane steam reforming units). The dominance of spherical packing studies can be attributed to the cumbersome and complicated strategies needed to generate a 3D surrogate model for packing structures of non-spherical pellets, which is an essential prerequisite for CFD simulations. The orientational freedom of non-spherical particles makes the procedure of packing simulations very problematic, both in terms of modeling the collision phenomena and computational expense. Some researchers use the Discrete Element Method (DEM) to synthesize random packings of non-spherical pellets [26–28,37]. The most frequent approach in non-spherical DEM is the so-called multi- or composite-sphere method (Lu et al. [38]), in which the established framework of soft-sphere DEM is applied to model shaped particles and their collisions during the loading process (see Fig. 4.1).

(a)   (b)
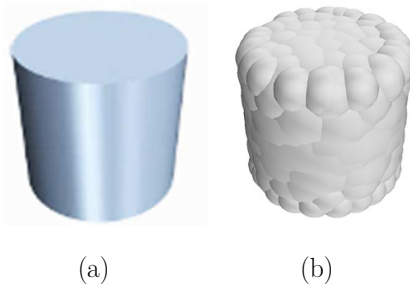
Fig. 4.1 (a) Actual CAD particle shape, (b) approximated by 100 DEM spheres; extracted from Wehinger et al. [27].

The approximation of non-spherical pellets by the composite-sphere method can lead to inaccurate contact force computations, particularly when collisions occur [38,39]. Nevertheless, some research groups have employed this approach in a CFD analysis of the local flow and transport properties in narrow-tube fixed beds of cylinder and Raschig ring pellets [26,28].

Wehinger et al. [26] have assessed the performance of the dry reforming of methane (DRM) process over three different pellets, including spheres, cylinders and Raschig rings, with N = 4.5, 3.6 and 3.6, respectively, using a sequential DEM and CFD method. The authors used a composite-sphere approach to generate random packings of solid cylinders, and used a post-treatment in CAD software to replace solid cylinders with hollow cylinders, thus generating a Raschig ring packing structure. Even though interpenetration between Raschig rings during the packing process, due to the presence of an axial hole in the pellet's topology, is basically omitted using this strategy, the computed bulk porosity was in accordance with literature data. This may be caused in part by the inherently soft interactions used in DEM, allowing for a finite amount of overlap. The authors have discussed the behavior of the flow field and species transport inside the mentioned structures in the laminar flow regime. In another study, Wehinger et al. [27] dealt with the role of contact point treatment in CFD simulations of heat transfer in a tube stacked with cylindrical pellets. They used a multi-sphere model consisting of 100 DEM spheres as a surrogate model for a solid cylinder to synthesize a packing structure of cylinders with N = 4.17. Their analysis covers three flow conditions with particle Reynolds number Re_p = 191, 382 and 763, corresponding to the experimental work of Bey and Eigenberger [7]. Dong et al. [28] investigated the behavior of radial heat transfer in tubular fixed beds of glass spheres (N = 7) and steatite rings (N = 3.39) using a sequential DEM and CFD approach in the laminar flow regime, where Re_p was in the range of 60 to 100. The investigators pursued the same approach as Wehinger et al. [26] to generate a geometrical model for steatite rings, and validated their CFD results of heat transfer by comparing radial temperature profiles extracted from CFD results to their own experimental data.

Other approaches than DEM have also been tried. For example, Boccardo et al. [40] have employed an open-source work-flow, based on Blender, which is a graphics and animation software released by the Blender Foundation, to generate random packings of spheres, cylinders and trilobes with N = 16.1, 27 and 23.3, respectively. The investigators then utilized the packing geometries for a CFD analysis of the flow field and pressure drop using Open-FOAM CFD code. Even though there is no access to the basic algorithms and concepts used for the modelling collision phenomena and handling of resting contacts in such a real time simulator, e.g. Blender software, a few works with the subject of fixed beds of shaped particles have recently been published, e.g. [29].

Overall, progress in fixed bed modeling is hampered by the complexities associated with the construction of realistic non-spherical packings. The main aim of this contribution is to introduce a novel and efficient workflow to investigate the in-situ behavior of hydrodynamics and wall-to-bed heat transfer in fixed beds containing non-spherical pellets. The workflow consists of a sequential Rigid Body Dynamics and Computational Fluid Dynamics (RBD-CFD) approach. The RBD is founded on the physics-based hard-body packing algorithm, presented in Chapter 3. The results of this workflow will be assessed in terms of both verification and validation using the published empirical and analytical data. However, before dealing with the details of the workflow, a concise review over the CFD studies of hydrodynamics and heat transfer in fixed beds is given. The review will address the prevailing classifications, progress, advantages and restrictions concerning the application of CFD tools for modeling hydrodynamics and heat transfer in such a complicated topology.

4.1.1. Literature review on CFD studies in fixed beds

The applications of CFD approach has been extended to the field of chemical engineering from 1990s, with the introduction of specially tailored fluid mixing program (Nijemeisland and Dixon [18]; Dixon and Nijmemeisland [19]). Fundamentally, the approach makes it realizable to numerically solve the momentum, mass and energy balances together with other auxiliary models, accounting for the turbulent flow regime, radiation mechanisms, etc., in complicated structures, such as fixed beds. The methodologies referred to by the term "CFD" in the field of fixed bed modeling can be classified into two main categories. In the first, a tortuous structure is modelled as an effective porous medium, with effective lumped parameters for dispersion and heat transfer [41]. Here the velocity field is coupled with the heat and species transport models using an azimuthally-averaged axial velocity field obtained from simplistic models e.g. those proposed by Bey and Eigenberger [7] and Giese et al. [8]. The inadequacy of

this simplified version of CFD approach has been profoundly addressed in Chapter 2 within the context of advances in pseudo-continuum models.

The second type of CFD simulations in fixed beds accounts for the topological complexities of a real random packing structure instead of an effective porous medium. This, more rigorous "discrete particle" CFD, would provide a detailed insight into local flow structure as well as the propagation of heat and species at the pellet scale within a reactor. Earlier efforts on discrete pellet simulations of fixed beds has been surveyed by several researchers, e.g. [5,19]. Sørensen and Stewart [42] studied interphase transfer under creeping flow in a 3D cubic array of spheres. Dalman et al. [43] dealt with the flow structure in an axisymmetric radial plane with two spheres, presenting a first insight into flow patterns at the pellet scale. The authors showed that eddies could form between the spheres, resulting in a region with poor heat transfer. In a similar work, Lloyd and Boehm [44] performed a CFD simulation, however with eight instead of two spheres in line. The investigators dealt with the influence of the sphere spacing on the drag coefficients. McKenna et al. [45] studied the effect of pellet size on pellet-to-fluid heat transfer using a 2D CFD simulation of small clusters of particles and a single catalyst sphere close to a wall. Logtenberg and Dixon [46,47] studied the heat transfer in an eight-sphere model, including two layers of four spheres perpendicular to the flow in the tube with a tube-to-particle diameter ratio, $N = 2.43$. Logtenberg et al. [48] used a 3D 10-sphere model with $N = 2.68$ to obtain the effective heat transfer parameters from CFD simulations of wall-to-bed heat transfer.

Nijemiesland and Dixon [18] studied heat transfer in an ordered packing structure consisting 44 spheres in a tube with $N = 2$. The geometry used was a 3D surrogate model of their experimental setup. The authors showed very good quantitative and qualitative agreement between the simulation results and the measured temperature profile. Calis et al. [49] investigated the flow field and pressure drop in Composite Structured Packing (CSP) models with the channel-to-sphere diameter ratios of 1 and 2. The authors validated their CFD simulations with comparing the predicted velocity profiles and the in-situ velocity field measured with LDV. In a similar work, Romkes et al. [50] investigated the particle-to-fluid heat and mass transfer in CSP models with channel-to-sphere diameter ratios between 1 and 5, and for a wide range of particles Reynolds numbers. Basically, the majority of CFD studies in 2000s decade has been performed on a small clusters of ordered packing geometries or a periodic wall segment model, which consists of a 120^0 slice of the bed cross-sectional area of a few layers of pellets, addressing flow field and heat transfer, e.g. Dixon and coworkers [5,31,32,51,52] and Guardo and coworkers [35,53–55]. The former research group showed that the velocity and the temperature fields predicted in a 120^0 periodic wall segment model matches

well with those obtained from an ordered full-packed bed model of spheres with six particles layers for $N = 4$. However, they found these results based on an ordered packing model, where the angular and axial symmetries are one of the main features of the ordered packing structures. A number of researches have exercised computer-generated random packings for CFD simulation of flow and transport scalers in fixed beds, [17,20,21,22,26,28, 29,33,34,36,40, 56–58].

Magnico [33] studied the influence of radial heterogeneities of the granular structures on the local flow and radial mass transfer in packed tubes of $N = 5.96$, 7.8 at low to moderate Re_p range, say 7 to 200. In a similar work, Freund et al. [4,34] have used Lattice Boltzmann method to investigate the hydrodynamics and mass transfer in a packed tube of spheres with $N = 5.96$ at $Re_p \leq 100$. Similarly, Reddy and Joshi [59], Jafari et al. [36], Atmakidis and Kenig [57], Bai et al. [60] and Baker and Tabor [61] have used computer-generated random packings of spheres in CFD studies of hydrodynamics in a wide range of Re_p. These studies have specifically focused on the influence of wall-effect on the bed pressure drop. Evidently, the majority of CFD studies, including random packings as geometrical domains, have only dealt with flow or dispersion of mass, in which the solid particles need not to be meshed, thereby reducing the size of the CFD computations. Very few efforts have considered heat transfer, which requires meshing inside the pellets as well, e.g. Augier et al. [20–23,28,62]. Therefore, it seems that there are two main obstacles towards CFD study of a reacting flow in fixed beds, first the inherent difficulties concerning the computer-generated model of random packings of non-spherical pellets as tersely indicated in the introduction (a detailed review is given in Chapter 3), and second is the computational cost imposed by the creation of mesh inside pellets, which is essential in study of heat transfer. Therefore, the aim of this chapter is to introduce and validate a novel and efficient workflow to predict the hydrodynamics and heat transfer in fixed beds containing non-spherical pellets.

4.2. Workflow

4.2.1. Step 1: discrete pellet modelling of random packing structures

The first essential step in the numerical simulation of hydrodynamics and heat transfer through random packing structures is to generate a realistic 3D model of the packing topology. For this step, the physics-based Rigid Body Dynamics (RBD) algorithm presented in Chapter 3 is employed to synthesize random packings of spheres, solid cylinders and Raschig rings. The RBD-based packing procedure can handle any non-spherical, even non-convex, pellet shape. Details and validation of the algorithm have been presented in Chapter 3. The essential features of RBD are (i) that each pellet is described by a triangular face mesh in a global coordinate

system (see Fig. 4.2), and (ii) that collisional contacts are handled as hard-body collisions, instead of the soft-particle approach used in DEM. The former feature allows for simulation of pellets with sharp edges. The latter feature avoids unphysically large overlap of particles caused by artificially lowered spring stiffness, frequently employed in DEM simulations to prevent unfeasibly small time steps in the treatment of particle collisions. As illustrated in Fig. 2.4, the sharp edges of the cylindrical pellet are well-reproduced by the polygonal modeling used in the physics-based packing algorithm. In contrast, the composite-sphere method leads to a poor approximation of the edges (see Fig. 4.1), which can result in imprecise prediction of contact forces, and accordingly erroneous packing structures.

(a)

(b)
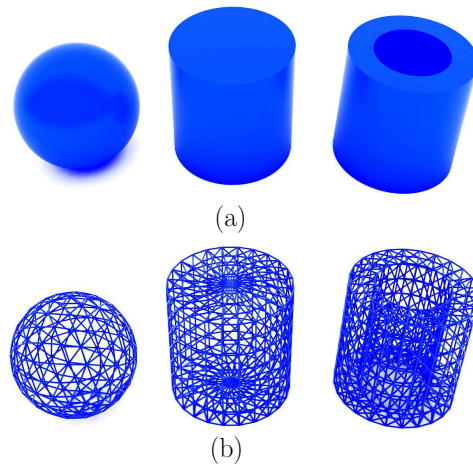
Fig. 4.2 3D model of a sphere ($d_p = 10$ mm), a cylinder ($l=d_p = 10$mm) and a Raschig ring ($d_{po}/d_{pi}/l = 10/6/10$ mm). (a) The exact 3D model of pellets built in ANSYS Workbench 16.2; (b) The model described by a face mesh for the RBD algorithm.

Table 4.1 Specification of RBD-simulated packing structures to be exercised in a supplementary CFD study

Pellet shape	Pellet size (mm)	Tube diameter (mm) (H=120 mm)	N (d_t/d_p)	Particle count up to H=100 mm
Sphere	$d_p = 10$	31	3.1	73
		41	4.1	131
		61	6.1	319
Cylinder	$d_p = l = 10$	22.9	2.29	48*
	$d_{pv} = 11.45$	35.5	3.55	63
	$d_{ps} = 10$	45.8	4.58	126
Raschig ring	$d_{po} = l = 10$	30.6	3.1	51
	$d_{pi} = 6$	40.5	4.1	100
	$d_{pv}/d_{ps} = 9.87/5$	60.2	6.1	251

* This particle count is up to a height of H=200 mm.

The physical dimensions used to synthesize realistic random packings of spheres, cylinders and Rascig rings are given in Table 4.1.

After the pellets have settled in the container, information about the simulated packings, in particular bulk porosity and radial porosity profiles, is generated using a post-processing mesh-based analysis, as elaborated in Chapter 3. Typical results of computer-generated packings to be employed in our CFD simulations are illustrated in Fig 4.3.

(a)   (b)   (c)   (a)   (b)   (c)
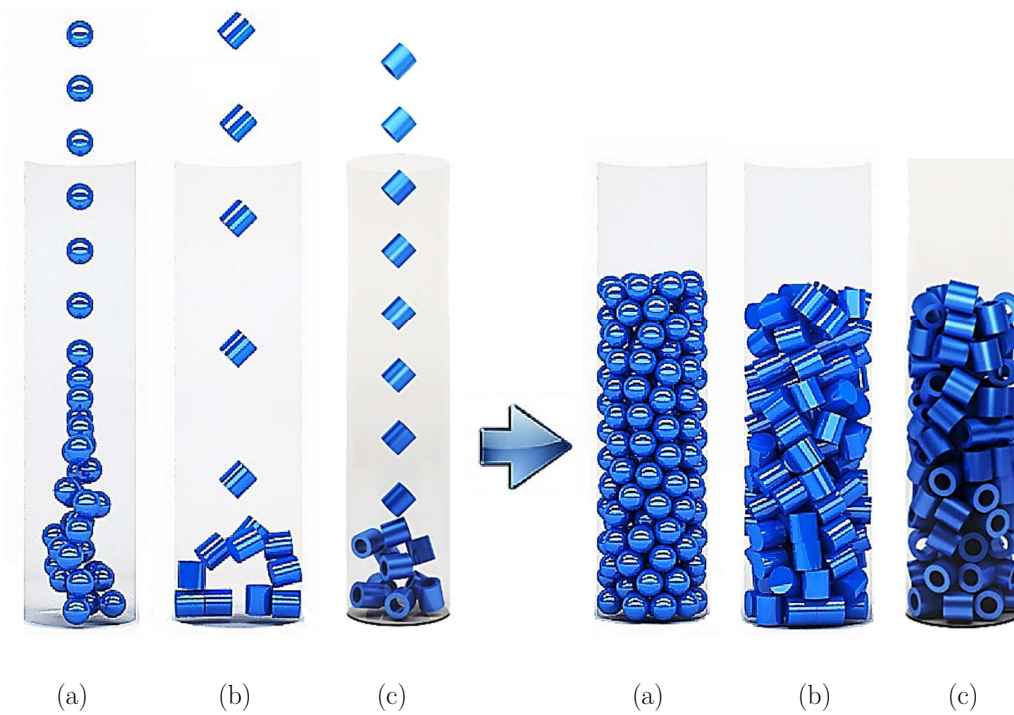
Fig. 4.3 Typical results of RBD-simulated random packings; (a) spherical packing with $N = 4.1$, (b) cylindrical packing with $N = 4.69$ and (c) Raschig rings packing with $N = 4.05$.

4.2.2. Step 2: Contact point treatment

The second step in the workflow is to transfer details of the packing structure, i.e. the position and orientation of each non-spherical pellet, to a mesh developer software. To this end, the face mesh data of each pellet is extracted with the format of an "stl" file and imported into ANSYS Workbench 16.2 to produce a CAD model of the packing structure. One of the most important issues before meshing such a complicated topology is to deal with the contact points. Near contact points, the computational cells are in danger of becoming exceedingly skewed, meaning that some of their surfaces can be much larger than others, which can result in convergence problems in the turbulent flow regime. A detailed assessment of the prevailing

97

alternative treatments for the contact point problem in fixed beds of spheres was performed by Dixon et al. [21,63]. Local treatment methods, such as the so-called bridge and cap methods, cannot be generally applied to non-spherical packings because of the complexities arising from the probable edge-edge or face-face contacts, which make the creation of a bridge or a cap at the contact regions very difficult. Therefore, here the global gap approach is necessarily implemented. Based on this method, all pellets in the reconstructed packing model in ANSYS Workbench software are locally shrunk by 0.5% of their nominal diameter around their respective centers of mass, resulting in an interstice at each contact region. Imposing such a small interstitial space can resolve the convergence problem by creating a computational mesh with appropriate skewness and orthogonal quality in such regions (see step 3). The shrinking factor should be kept sufficiently small to have a negligible effect on the bulk porosity of the packings, and to prevent jet formation in the gap regions at high Re_p conditions [5,18,63]. The former researchers have performed a detailed sensitivity study to determine the allowable gap size between spherical particles, and it was deduced that a gap of 1% of the particle radius does not adversely affect the velocity field at low to moderate range of Re_p. Fig. 4.4 shows the reconstructed (CAD) models of spherical and cylindrical packings including contact point refinement.

(a)   (b)
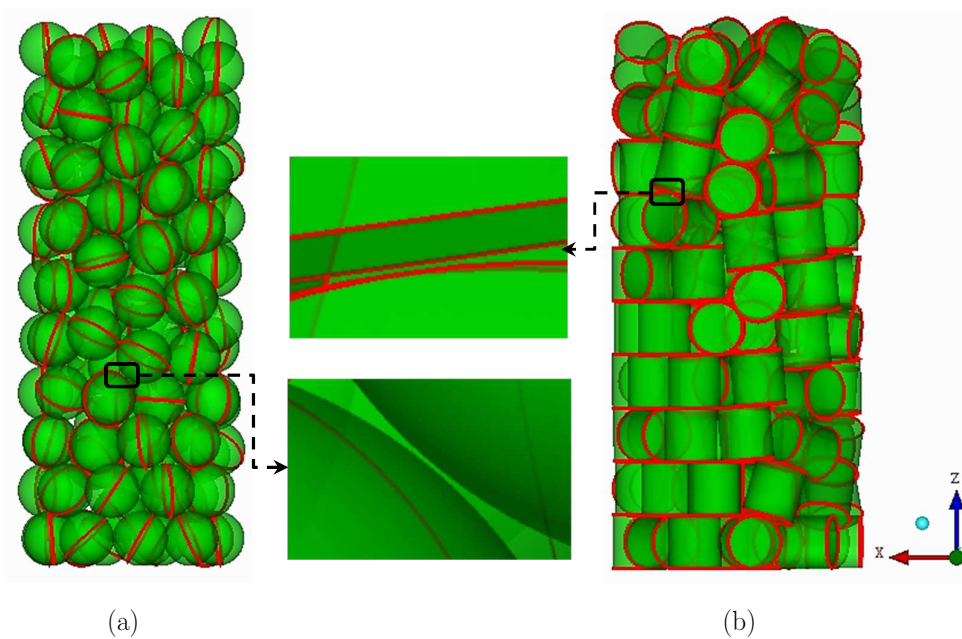
Fig. 4.4 Reconstructed models of the RBD-generated packings in ANSYS Workbench 16.2 with $0.005d_p$ gap; (a) spherical packing with N = 4.1, (b) cylindrical packing with N = 4.58. Red lines indicate the sharp edges of the cylinders (and a random equator for the spheres).

4.2.3. Step 3: mesh generation

The third step in the workflow deals with generating a high-quality mesh for CFD simulations. Conceptually, the quality of the mesh plays a crucial role in the accuracy and stability of a numerical computation. As always, there is a compromise between the mesh quality, i.e. fine or coarse, and the accuracy and computational expense. In fact, a coarse mesh results in an oversimplified velocity and temperature fields, conceivably obscuring substantial flow and thermal characteristics within the system, and may lead to a non-converging iteration process, whilst, a very fine mesh leads to a larger computational domain, resulting in a huge computational demand. Therefore, to determine an optimal mesh topology for a geometry, a trial and error process so-called mesh-independency study needs to be performed. Based on this analysis, we obtain a specific threshold for the mesh size, where more refinement of the mesh increases the model size without displaying a more detailed data for flow or temperature fields in a solution domain. Fig. 4.5 illustrates a general sketch of the geometry and mesh processing for a typical CFD study.
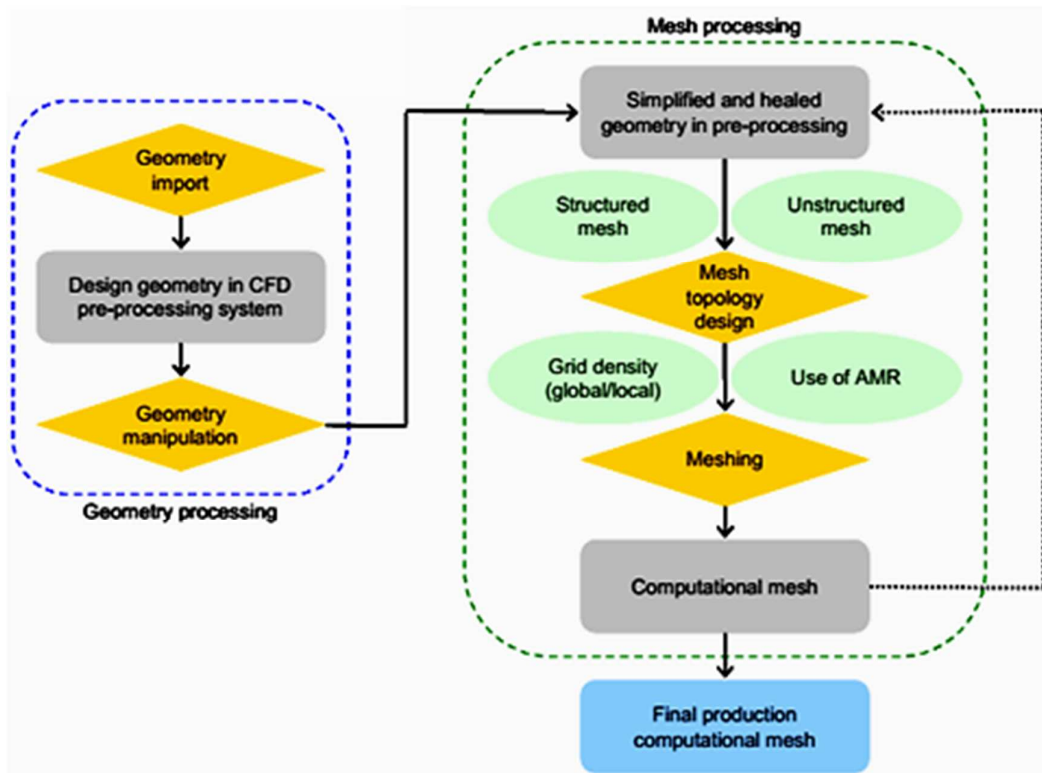
Fig. 4.5 A general sketch of CFD pre-processing steps.

In this work an advanced meshing approach, based on a combination of patch-independent and patch-conforming mesh methods, is implemented to generate a graded mesh topology for a random packing structure. This meshing approach is founded on a top-down meshing method to create an inflationary face mesh topology. This is controlled by an *ad hoc* Python-based

script in ANSYS Workbench. Following this, a bottom-up meshing method based on the Quick (Delaunay) technique is applied to create a graded volume mesh in the void spaces. This procedure is applied to generate a graded mesh topology for packing structures of spheres and cylinders.

We note that in a recent release of ICEM CFD V.18.2, an algorithm has been introduced by which the mesh can be automatically refined based on geometry curvature and proximity. Similar to our *ad hoc* meshing procedure in ANSYS Workbench, this algorithm can create an inflationary meshing scheme in a random packing consisting a pre-defined gap between pellets, with large elements on flat planar surfaces and smaller elements in areas of high curvature or within small gaps. Therefore, the graded volume mesh topologies for case studies including Raschig ring packings have been generated automatically via ICEM CFD 18.2, which is favorable due to its simplicity and lower computational time. Furthermore, to achieve a precise prediction of the velocity field in the near wall region, which depends on reliable prediction of wall-bounded turbulent flows, a number of prismatic layers needs to be implemented on the solid surfaces, i.e. both tube wall and pellets [32,49,50,64]. This would be realizable provided that the y^+ criterion (the thickness of near-wall cell layer) for a particular wall function (e.g. standard, non-equilibrium, enhanced wall treatment), which is coupled with the Reynolds averaged turbulence models (RANS), is satisfied. However, several researchers have reported that the y^+ criterion is hardly satisfied, e.g. [5,32,49,53,64]. This can be explained by the limited allowable values of cell size due to the need for squeezing grids in the gap regions, resulting in y^+ values being too small (say $y^+ <<1$). In this work, the thickness of prismatic layers, δ_{BL}, is chosen based on the estimated thickness of the momentum boundary layer (Dhole et al. [65]). The authors presented a correlation for the thickness of momentum boundary layer, $\delta_{BL,u}$, at the forward stagnation point for spheres:

$$\frac{\delta_{BL,u}}{d_p} = 1.13 \, Re_p^{-0.5} \tag{4.1}$$

As an initial approximation, we assumed to hold this thickness for the entire pellet. It is worth mentioning that the thermal boundary layer is a little thicker in our study, because $\delta_{BL,T} = Pr^{-1/3} \delta_{BL,u}$.

To this end, after several trials based on the medium mesh level (see Table 4.3), our boundary-layer treatment for the flow simulations in the turbulent regime consisted of 6 layers of prisms with an initial height of 2.5×10^{-6} m, and a growth factor of 1.2, leading to a total prism depth of 2.48×10^{-5} m. This allows the laminar sub-layer to be resolved for the highest inlet Re_p by obtaining the dimensionless distance parameter, i.e. y^+ between 0.5 - 2, as

recommended by Dixon et al. [63]. Figs. 4.6 to 4.8 show how the proposed inflationary meshing scheme results in finer grids at the contact regions of packings of different shapes.

(a)   (b)
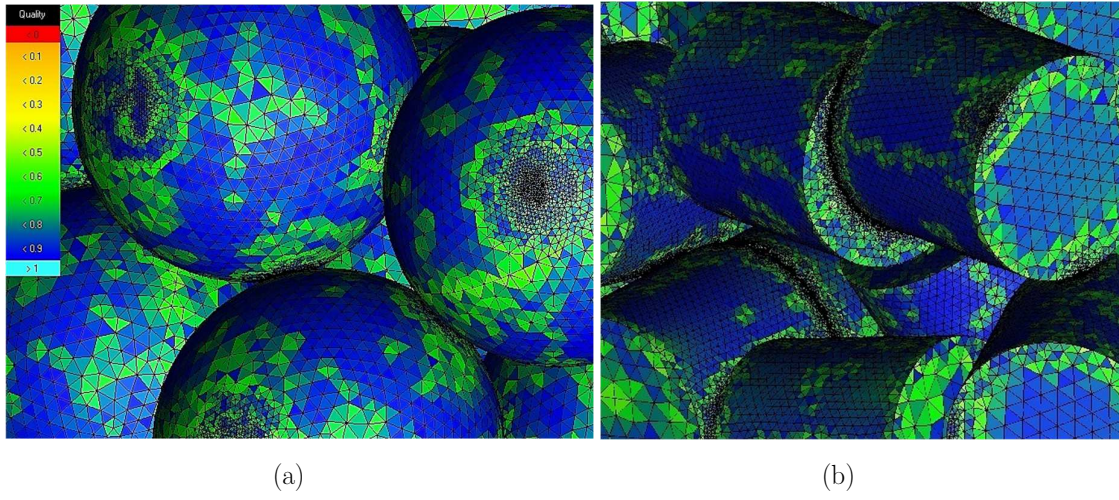
Fig. 4.6 The face mesh quality on pellet surfaces based on a medium mesh size (see Table 4.3); (a) spheres (b) cylinders.

(a)   (b)
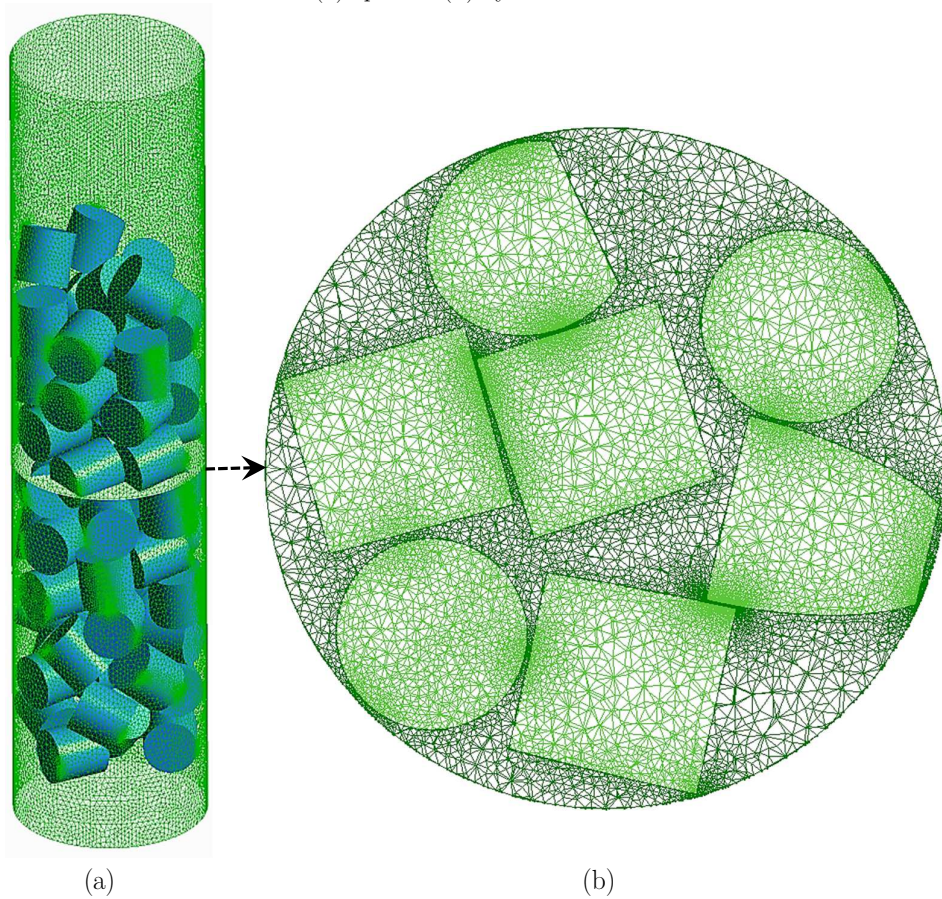
Fig. 4.7 Graded mesh topology in random packing of cylinders with $N = 3.55$ based on a medium mesh level (see Table 4.3); (a) face mesh on the tube wall, (b) a cut plane of the volume mesh at height $z = 6d_p$.

(a)   (b)
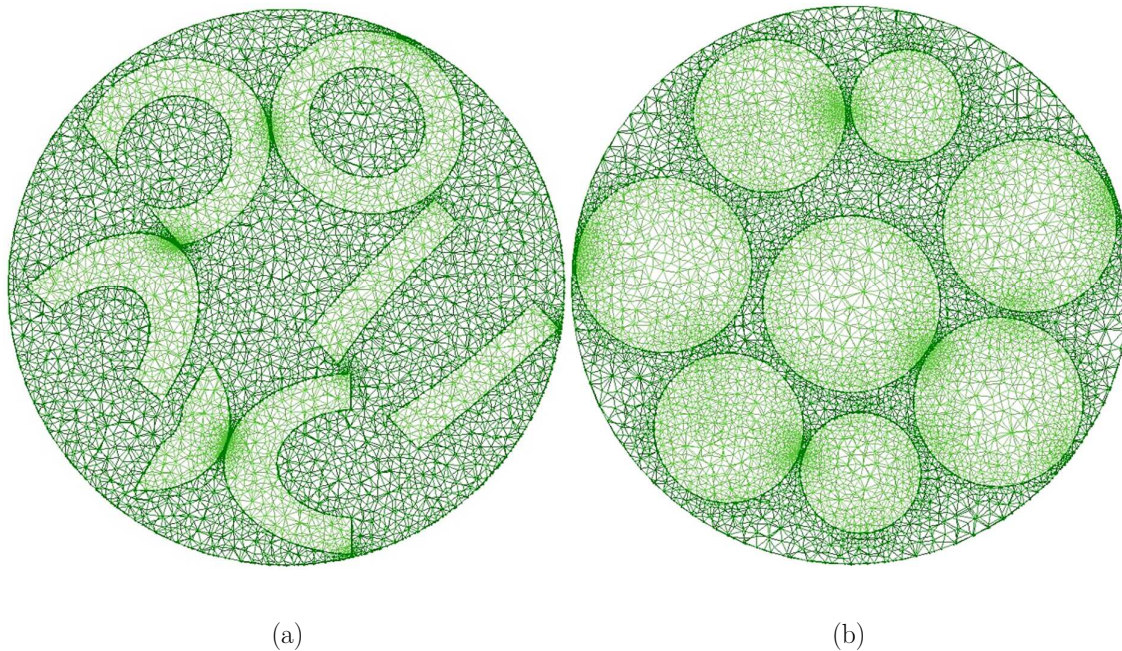
Fig. 4.8 Cut planes of the graded volume mesh generated based on a medium mesh level (see Table 4.3) at cross section of $z = 5d_p$ for random packings of (a) Raschig rings with $N = 3.05$, (b) spheres with $N = 3.1$

4.3. CFD setup

4.3.1. Problem description and boundary conditions

CFD simulations of fluid flow and heat transfer are performed for the random packing models addressed in Table 4.1 in the laminar, transitional and turbulent flow regimes, using the finite volume code ANSYS Fluent 16.2. The fluid phase is assumed to be incompressible and non-isothermal with the physical properties of air, which is available in the database of ANSYS Fluent 16.2. Furthermore, ideal gas law and Sutherland's law are used to account for density- and viscosity-temperature dependencies, respectively. The solid phase is consisted of the entire pellets within a tube with the specifications, i.e. size, shape and number, summarized in Table 4.1. To investigate the influence of catalyst pellets of different thermal conductivities on the lateral heat transfer inside a fixed bed, the thermal conductivity of solid phase is set as 1.01, 16.27 and 40 W/mK, corresponding to glass, steel and alumina catalyst materials.

The air at the total pressure of 1.01325 bar and temperature of 298K, which gives the physical properties of ρ=1.225 kg/m^3, cp=1006.43 J/kgK, k_f=0.0242 W/mK, μ=1.7894×10^{-5} Pa.s (yielding the molecular Prandtl number of 0.74) enters from the bottom of the packed column with a unidirectional and uniform velocity and temperature to provide a consistent basis for further comparison. The inlet air velocities are chosen in accordance to the desired

particle Reynolds number Re_p (based on the volume-equivalent pellet diameters) ranging from 5 to 3000. These inlet flow conditions also cover the flow conditions used in the experimental work of Krischke [9]. To provide a consistent basis for comparisons, the initial inlet turbulence intensity (for $Re_p \geq 200$) is computed based on the formula $I = 0.1\,Re^{-1/8}$.

The thermal boundary condition at tube wall is considered as constant temperature ($T_w = 700K$ for $Re_p \leq 200$ and $T_w = 1500K$ for $Re_p \geq 400$). No-slip boundary conditions are applied to the column wall and pellet surfaces, i.e. at fluid/solid interfaces. Furthermore, the coupled heat transfer boundary condition is applied to the fluid/pellets interfaces to account for the conjugate heat transfer. ANSYS Fluent uses a discrete form of Fourier's law (Eq. 4.2) to compute fluid/solid film heat transfer at a pellet surface in laminar flow regime. However, for turbulent flow, the law-of-the-wall (defined by a wall function, which here is Enhanced Wall Treatment) together with the analogy between heat and momentum transfer is applied.

$$q_w = h_{fs}\left(\frac{\partial T}{\partial n}\right)_{\text{pellet surface}} \tag{4.2}$$

where n is the local coordinate normal to a pellet surface.

For the bed outlet, a pressure-outlet boundary condition, which is substantially a "free" boundary condition for an unconfined flow, is defined. Moreover, to minimize boundary effects at the column inlet and outlet, the bed entry and exit are extended by 1 and 6 particle diameters, respectively. A schematic overview of the flow model and boundary conditions is given in Fig. 4.9.

It is worth mentioning that several researchers applied the transitional periodic boundary condition, which is basically exercised when the physical geometry of interest and the expected pattern of the flow/thermal solution have a periodically repeating nature e.g. [31–33,66,67]. This allows a pressure drop occurring across the translational periodic boundaries, and accordingly enables the modeling of "fully-developed" periodic flow. However, using such a boundary condition, specifically in narrow tubular fixed beds, is arguable, as it omits the longitudinal heterogeneity inherent in such low-N structures. In fact, both the lateral and longitudinal distribution of catalyst pellets in narrow-tube packing structures cannot be described by a periodically repeating nature applied for a small segment of a packed bed, although this approach can accelerate the convergence of computations. For this reason, we implemented a "real" boundary condition, as described earlier, in our CFD simulations.
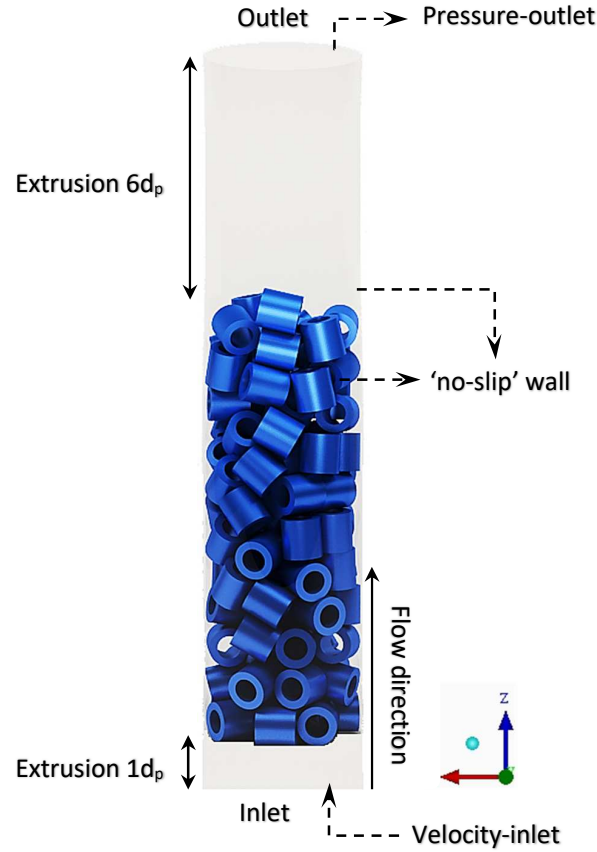
Fig. 4.9 Schematic overview of a Raschig ring packing model and boundary conditions used in the CFD simulations; N = 4.05.

4.3.2.   Governing equations and computational procedures

The governing equations for CFD simulations of hydrodynamics and heat transfer include the equations of conservation of total mass (continuity), momentum and energy. The equation used for the continuity equation can be expressed as:

$$\frac{\partial \rho}{\partial t} + \frac{\partial \rho u_i}{\partial x_i} = S_m \tag{4.3}$$

where summation over the same indices appearing twice is implied (Einstein convention). The source term S_m covers the mass added through phase changes or user-defined sources. This generalized form of the continuity equation can be even more reduced for our case studies, where no source term is present and a constant density is assumed:

$$\frac{\partial \rho u_i}{\partial x_i} = 0 \tag{4.4}$$

The equation for conservation of momentum in the direction i is expressed by

$$\frac{\partial(\rho u_i)}{\partial t} + \frac{\partial \rho u_i u_j}{\partial x_j} = \frac{\partial p}{\partial x_i} + \frac{\partial \tau_{ij}}{\partial x_j} + \rho g_i + F_i$$

$$\text{and} \quad \tau_{ij} = \mu\left(\frac{\partial u_i}{\partial x_j} + \frac{\partial u_j}{\partial x_i}\right) - \frac{2}{3}\mu \frac{\partial u_i}{\partial x_i}\delta_{ij}$$

$$(4.5)$$

where μ is the molecular viscosity, p is the static pressure, τ_{ij} is the stress tensor, ρg_i is the gravitational body force in direction i. F_i represents external body force in direction i which is zero for the present work.

The energy equation is solved with the following form:

$$\frac{\partial(\rho h)}{\partial t} + \frac{\partial \rho u_i h}{\partial x_j} = \frac{\partial}{\partial x_i}\left(k\frac{\partial T}{\partial x_i}\right) + \frac{\partial \sum_j h_j J_j}{\partial x_i} + \frac{Dp}{Dt} + \tau_{ik}\frac{\partial u_i}{\partial x_k} + S_k \tag{4.6}$$

where h is the sensible enthalpy and S_k includes heat of chemical reaction, any inter-phase exchange of heat, and any other user defined volumetric heat sources.

The above equations, i.e. Eqs. 4.3-4.6, are solved for the laminar flow regime ($Re_p \leq 100$). For fully-turbulent flow, i.e., $Re_p \geq 600$, a Reynolds-Averaged Navier-Stokes (RANS) model is employed. Reynolds-averaged turbulence modeling remains the most widely-used method for describing turbulence in the engineering domain. Fundamentally, in Reynolds averaging, the solution variables in the instantaneous (exact) Navier-Stokes equations are decomposed into the mean (ensemble-averaged or time-averaged), $\bar{u}_i$ and fluctuating, u'_i components, and then integrated over an interval of time large compared to the small-scale fluctuations. This way, the Cartesian tensor form Reynolds averaged Navier–Stokes (RANS) equation can be written as:

$$\frac{\partial(\rho \bar{u}_i)}{\partial t} + \frac{\partial \rho \bar{u}_i \bar{u}_j}{\partial x_j} = \frac{\partial \bar{p}}{\partial x_i} + \frac{\partial}{\partial x_j}\left(\mu\left(\frac{\partial \bar{u}_i}{\partial x_j} + \frac{\partial \bar{u}_j}{\partial x_i}\right) - \left(\frac{2}{3}\mu\frac{\partial \bar{u}_l}{\partial x_l}\right)\right) + \frac{\partial(-\rho \overline{u'_i u'_j})}{\partial x_j} \tag{4.7}$$

In fact, the velocities and other solution variables are thus described by ensemble-averaged values, and the effects of turbulence are represented by the Reynolds stresses, $-\rho \overline{u'_i u'_j}$. Several approaches have been proposed to represent the influence of the Reynolds stresses in terms of time-averaged flow quantities, e.g. the Boussinesq approach and Reynolds Stress Transport models, resulting in a variety of Reynolds-averaged-based turbulence models, e.g. Spalart-Allmaras model, k-ε family models, k-ω family models, and RSM models. A detailed description of these models is available in standard references, e.g. [41,68]. Several researchers have examined different forms of RANS models in CFD simulations of fixed beds, e.g. [21,35,54,64]. In this work, for fully-turbulent flow, i.e., $Re_p \geq 600$, a Reynolds-Averaged

Navier-Stokes (RANS) model is adopted, using the realizable k-ε model (Shih et al. [69]) with an Enhanced-Wall-Treatment (EWT) to model the turbulence. Compared to the standard k-ε model (Launder and Spalding [70]), this model has an improved modeling of the turbulent energy dissipation rate (ε) and applies a variable C_μ instead of a constant value, offering a more sophisticated approach for simulation of flow fields with strong streamlines curvature, vortices and rotations, as typically found in random packing structures [68]. Furthermore, Enhanced-Wall-Treatment (EWT) was proposed by ANSYS Fluent which is described by blending the linear (laminar) and logarithmic (turbulent) law-of-the-wall using a function suggested by Kader [71]. Details of this method are described in the theory guide of ANSYS Fluent 12. In the transitional flow regime, where $100 < \mathrm{Re_p} < 600$, both the (laminar) Navier-Stokes equations and the realizable k-ε model were examined.

To solve the governing equations, a pressure-based solver with the SIMPLE scheme (Van Doormaal and Raithby [72]) for pressure-velocity coupling was utilized. Moreover, the PRESTO! (PREssure STaggering Option) method (Patankar [68]) was adopted as the interpolation scheme for computing cell-face pressures, which is fundamentally devised for strongly curved domains. A second-order upwind interpolation scheme was applied for both the convection and diffusion terms to interpolate the field variables (stored at cell centers) to the faces of a control volume. Furthermore, the gradients of solution variables at cell centers were determined using a Green-Gauss Node-Based method to minimize false diffusion. The CFD runs were initially set under isothermal conditions with only momentum and turbulence activated. Having established a converged flow field throughout the geometrical domain, the heat transfer simulations are run by setting the thermal boundary conditions and the temperature-dependent properties of the flowing fluid. Contrary to previous works, e.g. [21,32,63,73], convergence can be properly achieved without a need for manipulating the under-relaxation factors, due to our high-quality mesh topology. Convergence was monitored by the common residuals as well as the computed drag coefficient on the packings and vertex value of axial velocity in a predefined point behind the packing section (at the position 0,0,125 mm). Furthermore, the overall mass balance of the system was checked for accurate conservation for all flow field results.

4.4.   Results and discussion

4.4.1.   Mesh verification study

To investigate mesh convergence, three mesh sizes were compared for the cylinder packing with N = 2.29. Details of the mesh, including the cell size and total cell count, are given in Table 4.2.

Table 4.2 Specification of the mesh refinement study, based on the cylindrical packing with N=2.29.

Description	Fine	Medium	Coarse
Mesh size range (mm)	0.05-0.4 (d_p/25)	0.05-0.55 (d_p/18.2)	0.05-0.8 (d_p/12.5)
Fluid Cell ($\times 10^6$)	15.29	10.87	6.80
Total cell ($\times 10^6$)	23.27	17.70	10.04

The three mesh levels are compared based on the CFD results of flow and heat transfer in Fig. 4.10-12. Fig. 4.10 shows the comparison results for axial velocity component along a typical line, (passing through the points (-0.011496,0,0.11 m) and (0.011496,0,0.11 m)) at bed height z = 100 mm at Re_p = 10000. Figs. 4.11 and 4.12 show the azimuthally-averaged temperature profile at different bed cross sections together with the local temperature along the bed axis for very high (Re_p = 10000) and very low (Re_p = 10) flow rates, where the convective and the conductive heat transfer mechanisms are dominant, respectively. Overall, the results demonstrate very good agreement between the medium and fine mesh levels for both the computed axial velocity and temperature profiles. The inadequacy of the coarse mesh can be distinctly recognized for predicting the temperature profile (see Fig. 4.11), where the convection is the dominant mechanism, and the axial velocity at the wall region (see Fig. 4.10), where the gradients are essentially steeper, at a very high Re_p.
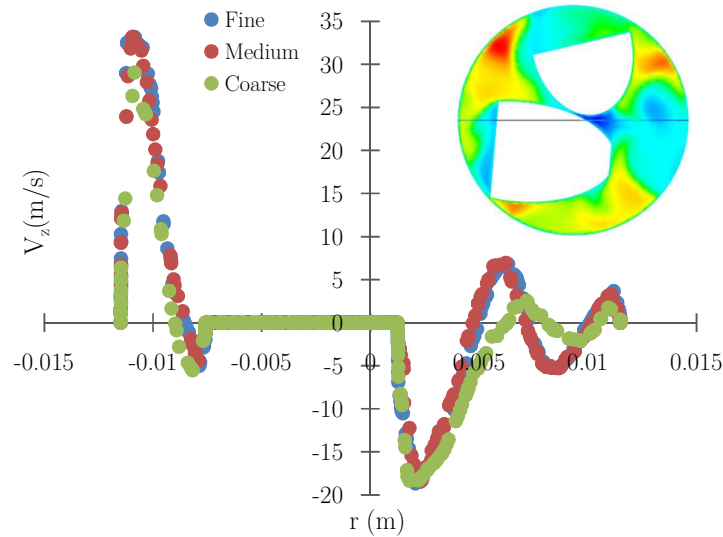
Fig. 4.10 Comparison between the computed axial velocity profiles obtained from three mesh levels at a typical line located at bed height $z=100$ in a cylindrical packing with $N=2.29$ at $Re_p=10000$.
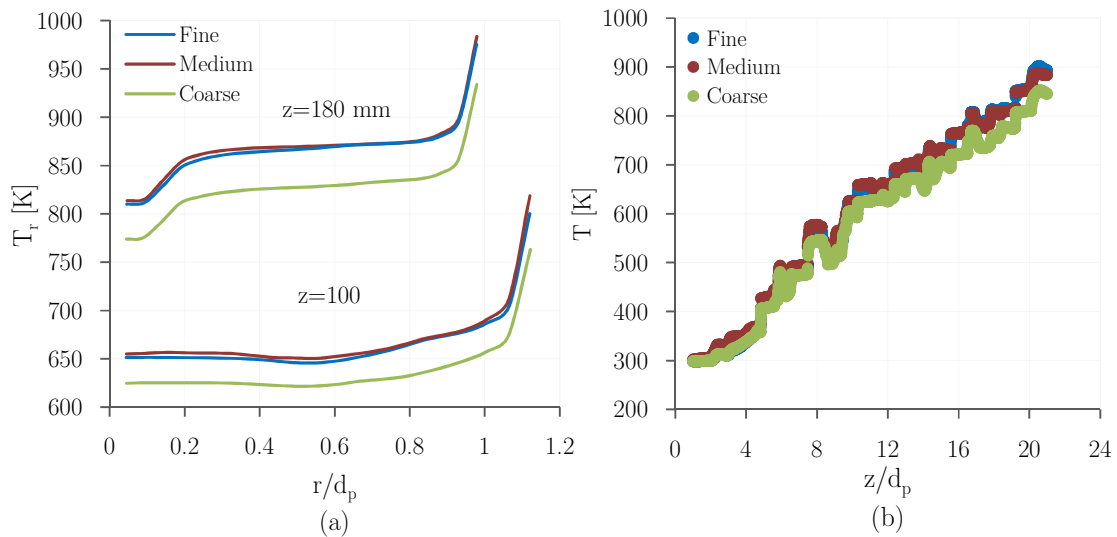
Fig. 4.11 Comparison between the computed temperature profile obtained from three mesh levels in a cylindrical packing with $N=2.29$ at $Re_p=10000$; (a) azimuthally-averaged temperature profile at $z=100$ and 180 mm, (b) local temperature data along the bed axis.
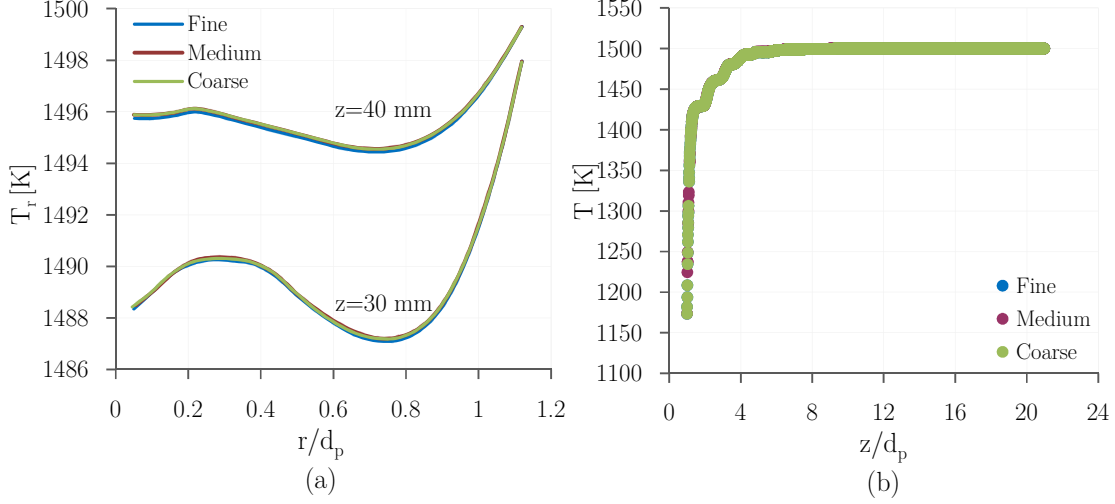
Fig. 4.12 Comparison between the computed temperature profile obtained from three mesh levels in a cylindrical packing with $N = 2.29$ at $Re_p = 10$; (a) azimuthally-averaged temperature profile at $z = 30$ and 40 mm, (b) local temperature data along the bed axis.

However, as shown in Fig 4.12, the difference between the coarse mesh profile and the profiles from the fine and medium meshes is negligible, suggesting that when using such a graded meshing scheme, even the course mesh is fine enough to show mesh independence for the conductive mode of heat transfer in the fluid phase.

The Richardson extrapolation (RE) approach (Roache [74]) was used to assess the discretization error of the medium mesh level for the computed velocity and temperature fields. The RE method uses the field variables from the medium mesh, φ_m, and the fine mesh, φ_f, to compute the values that would theoretically be obtained at zero mesh size, φ_∞, using the following formula:

$$\varphi_\infty = \varphi_f + \frac{\varphi_f - \varphi_m}{r_g^2 - 1} \tag{4.8}$$

$$\text{and } r_g = \sqrt{\frac{N_f}{N_m}} \tag{4.9}$$

where N_f and N_m are the mesh sizes of the fine and medium meshes, respectively. This formula assumes a second order discretization error. The extrapolated relative error (ERE) for the medium mesh is given by:

$$\text{ERE} = \left| \frac{\varphi_\infty - \varphi_m}{\varphi_\infty} \right| \tag{4.10}$$

This approach was applied to the CFD results of pressure drop at $Re_p = 10,000$ and azimuthally-averaged temperature profile, according to Fig. 4.10a, for fine and medium mesh levels to predict the value of the bed pressure drop and temperature profile at zero grid size, i.e. Δp_∞, $T_{r,\infty}$. Using this method, the numerical error was computed as 1.77% for pressure drop and the average errors for radial temperature profiles at $z = 100$ and 180 mm were estimated as 1.74% and 1.03%, respectively. Since the highest Reynolds numbers present the most challenging conditions, this shows the medium mesh to be at the appropriate level for all remaining CFD simulations.

4.4.2.   Validation study

To validate the CFD results of the flow field, the computed bed pressure drops and axial velocity profiles are compared with literature data. For the pressure drop, the correlations by Eisfield and Schnitzlein [75] and Cheng [76], which properly account for the wall effects in low N-packings, are used. The former authors have performed a detailed analysis based on several thousands of experimental results to improve the correlation proposed by Reichelt [77] for different types of packings. Here, a dimensionless form of these correlations, the so-called pore-based friction factor, Ψ_W, is used for the analysis. To this end, we used Eq. (2.7-2.8) to compute the pore-based friction factor based on the predicted pressure drop from CFD simulations. Furthermore, the parameters and further details of the correlations by Eisfield and Schnitzlein [75] and Cheng [76] are given in Table 2.3.
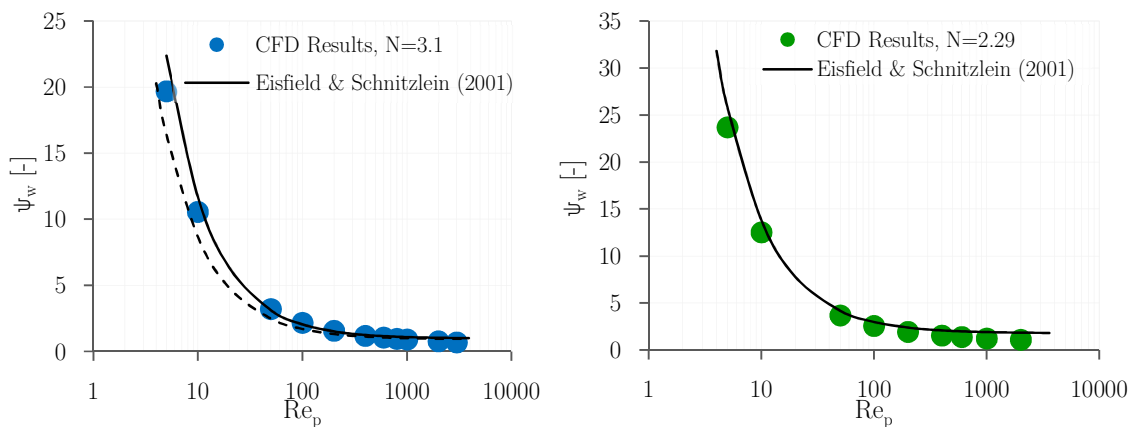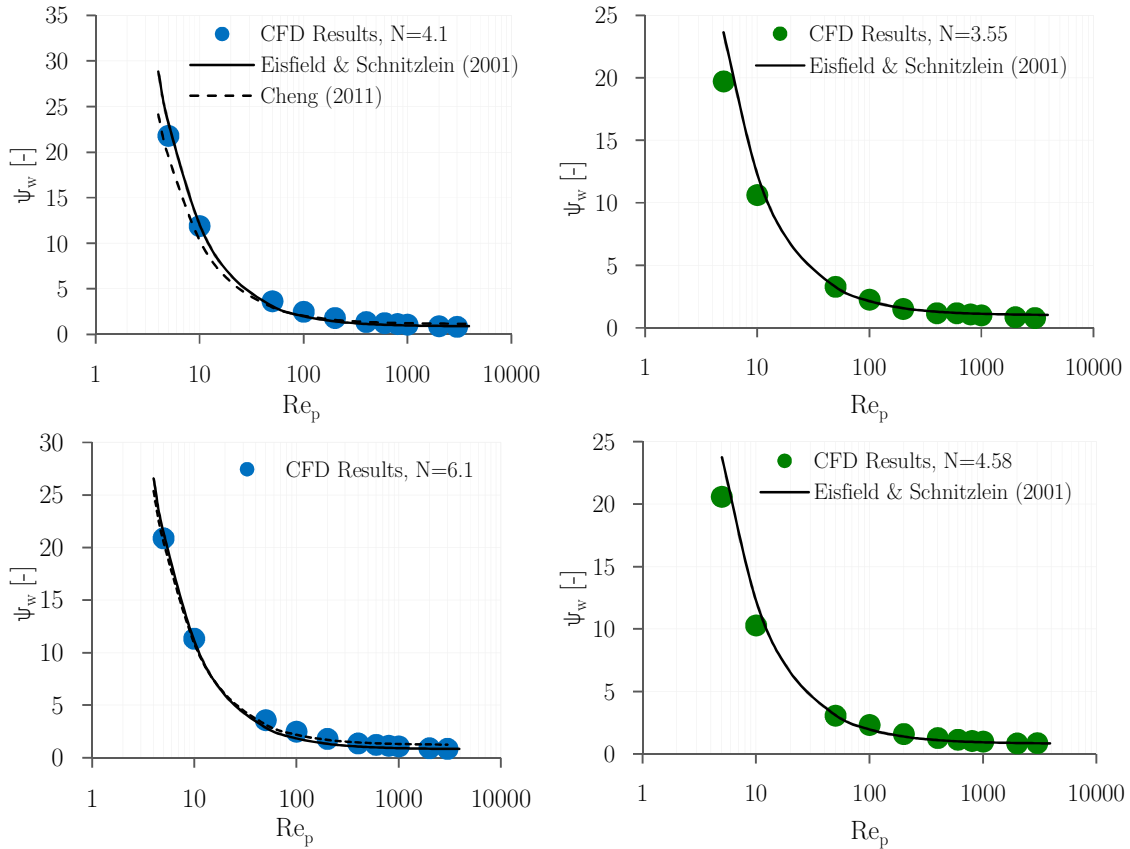
Fig. 4.13 Comparison between dimensionless pressure drops obtained from the CFD results and empirical correlations for packings of spheres (left) and cylinders (right).

As shown in Fig. 4.13, the computed dimensionless pressure drops and the correlation results are in very good agreement in all flow regimes for both spherical and cylindrical packings. It is noteworthy that the maximum deviation found from the correlation of Eisfield and Schnitzlein [75] is 17% for the cylindrical packing with $N = 3.55$ at $Re_p = 5$, which is reasonably justified by the range of experimental errors reported by the authors.

The validity of local flow distribution was also investigated based on the experimental data from Krischke [9]. The author has conducted LDV measurements to probe the axial velocity distribution inside random packings of glass spheres with $N = 4$ and 6.15 at different Re_p.
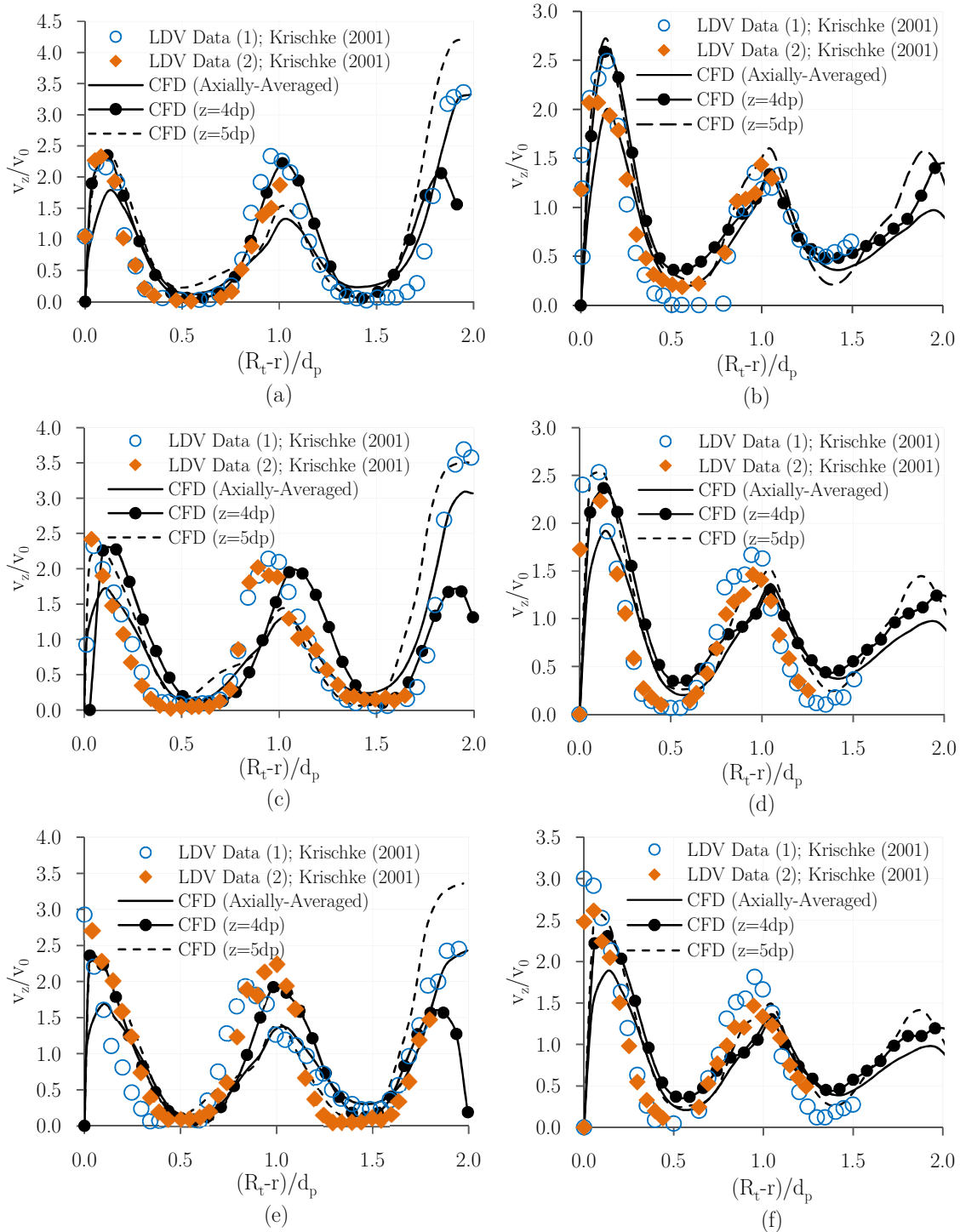
Fig. 4.14 Comparison between simulated azimuthally-averaged axial velocity profiles and the experimental (LDV) data from Krischke [9] for random packings of spheres with N = 4.1 at (a) Re_p = 50; (c) Re_p = 450, (e) Re_p = 1000, and with N = 6.1 at (b) Re_p = 50; (d) Re_p = 350, (f) Re_p = 670.

In Fig. 4.14, the empirical (LDV) data of the azimuthally-averaged and bed volume-averaged axial velocity profiles, measured by Krischke [9], have been compared with the CFD results of azimuthally-averaged axial velocity profiles, obtained from two cross sections at the

bed heights of $4d_p$ and $5d_p$, as well as the 2D axially (bed volume)-averaged z-velocity profiles. Overall, the results are in reasonable agreement with the experimental data for both packing structures and for all Re_p cases, as the typical oscillatory behavior of the radially varying axial velocity profiles are appropriately predicted both near the wall and in the inner bed regions. This oscillatory flow behavior has also been observed and described by Bey and Eigenberger [7] and Giese et al. [8]. It is worth mentioning that for $N = 4$ both CFD results and LDV data indicate the presence of a channel in the bed center, as the velocity increases significantly in this region. This feature of the random packings of spheres with $N \approx 4$ has previously been observed in Chapter 3, where the local porosity at the center of the bed increases tremendously. Such a behavior has also been observed by several other researchers, e.g. [17,22,78].

To inspect the validity of our CFD results with regards to the wall-to-bed heat transfer, the computed fluid-to-solid film heat transfer, represented by Nusselt number, Nu_{fs} was benchmarked against published correlations. To this end, the correlations by Gupta et al. [79], Gunn [80] and Wakao et al. [81] have been used (see Table 4.3) which covers a wide range of bed porosity and flow conditions.

Table 4.3 Predictive formulas for fluid/solid film heat transfer coefficient (Nu_{fs})

Author	Fluid/Solid Nusselt Number (Nu_{fs})	Application range	Re_p
Gupta et al. [79]	$Nu_{fs} = \dfrac{Pr^{1/3}}{\varepsilon} Re_p \left(0.0108 + \dfrac{0.929}{Re_P^{0.58} - 0.483}\right)$	$0.26 < \varepsilon < 0.78$	$10-0000$
Gunn [80]	$Nu_{fs} = (7 - 10\varepsilon + 5\varepsilon^2)(1 + 0.7\,Re_P^{0.2}\,Pr^{1/3})$ $+ (1.33 - 2.4\varepsilon + 1.2\varepsilon^2)(Re_P^{0.7}\,Pr^{1/3})$	$0.35 < \varepsilon < 1$	$20-10^5$
Wakao et al. [81]	$Nu_{fs} = 2 + 1.1 Re_P^{0.6}\,Pr^{1/3}$	$2 < N < 107.6$	$15-500$

To obtain h_{fs} from the CFD results, the facet-averaged value of total heat flux for the solid phase, q'_{fs}, is computed and then divided by the difference between mass-weighted average of fluid phase temperature, $T_{f,b}$ and the facet-averaged values of pellets' wall temperature, $T_{p,w}$.

$$h_{fs} = \frac{q'_{fs}}{T_{f,b} - T_{p,w}} \text{ and } Nu_{fs} = \frac{h_{fs} d_{pv}}{k_f} \tag{4-11}$$

$$\varphi = \frac{\sum_{i=1}^{n} \varphi_i}{n} \text{ where } \varphi : q'_{fs} \text{ and } T_{p,w} \tag{4-12}$$

$$T_{f,b} = \frac{\sum_{i=1}^{n} T_{f,i} \rho_i \left| \mathbf{v}_i . \mathbf{A}_i \right|}{\sum_{i=1}^{n} \rho_i \left| \mathbf{v}_i . \mathbf{A}_i \right|} \tag{4-13}$$

where $\mathbf{v}$ and $\mathbf{A}$ are the momentum and facet area vectors.

Furthermore, correlations were also defined as custom field functions in ANSYS Fluent, thereby accounting for the mass-weighted average of Re_p and Pr from the fluid phase.

As shown in Fig. 4.15, the computed fluid/solid film heat transfer Nusselt number and the correlation results are in good agreement in all flow regimes for packings of spheres with N = 3.1, 6.1. The same results were also found for other packing models. (not shown here for sake of brevity).
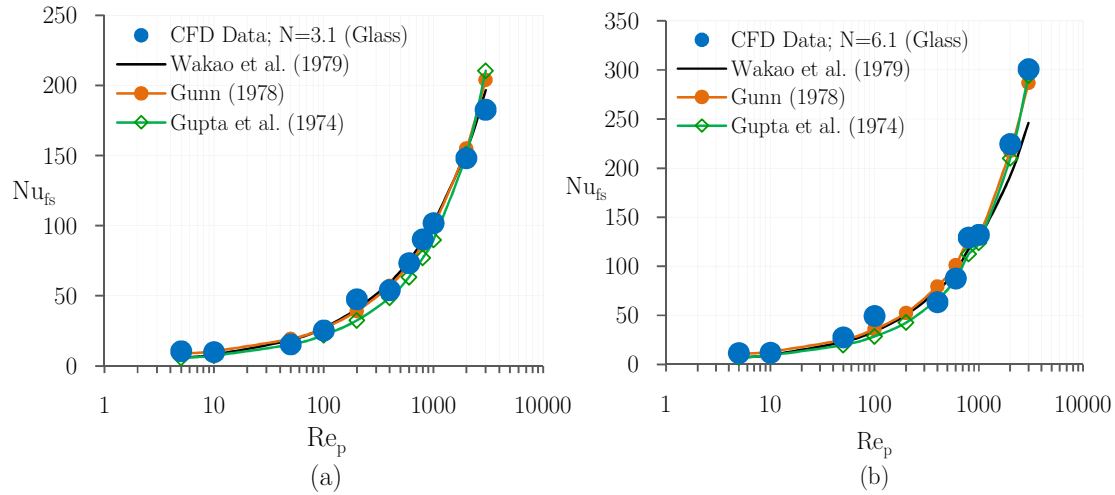
Fig. 4.15 Comparison between computed fluid-to-solid film Nusselt number and the published correlations for packing models of glass spheres with glass particles; (a) N = 3.1, (b) N = 6.1.

4.5. Conclusions

A novel and efficient workflow was introduced to simulate the hydrodynamic sand heat transfer in fixed beds containing non-spherical pellets. The workflow, entitled the RBD-CFD approach, consists of three main sequences, starting with physical simulation of random packings using the RBD-based packing algorithm presented in Chapter 3, followed by a contact point treatment in the computer-generated structures, and creation of an inflationary volume

mesh topology using an *ad-hoc* python-based script in ANSYS Workbench 16.2. The methodology was implemented and validated for a CFD study (using ANSYS Fluent 16.2) of the velocity field, pressure drop and fluid-to particle heat transfer in both spherical and cylindrical packing structures with tube-to-pellet diameter ratio N ranging from 2.29 to 6.1.

The distinct advantages of the RBD simulation of a packing structure, over more conventional composite-sphere DEM approaches, are a better representation of the sharp edges of the particles and avoidance of any particle overlap. Therefore, the algorithm can provide a realistic packing structure for a supplementary "discrete particle" CFD study of flow and transport scalars within the reactor.

The inflationary meshing scheme has been applied to random packing structures using a combination of patch conforming and patch independent approaches. This approach does not only provide a fine mesh to appropriately capture details of the phenomena occurring at the contact regions, but it also facilitates the solution convergence in the turbulent flow regime without any need for manipulating the under-relaxation factors, which is a routine method contrived by most other researchers to resolve the convergence problem in such complicated flow domains.

The CFD results of the hydrodynamics were validated by comparing the pressure drop as well as azimuthally-averaged axial velocity profiles to published empirical data. Furthermore, to confirm the validity of the computed temperature fields, the interphase Nusselt number obtained from CFD simulations were compared with published correlations.

This chapter, with the aid of validated data, offers the RBD-CFD method as a reliable methodology for understanding the in-situ behavior of hydrodynamics and thermal field at the pellet scale of non-spherical fixed beds. The post-processing of the validated CFD results will be presented in Chapter 5.

Nomenclature

d_p	Pellet diameter	[m]
d_{pv}	Diameter of a sphere of equal volume	[m]
d_{ps}	Diameter of a sphere of equal specific surface area	[m]
d_t	Tube or bed diameter	[m]
I	Turbulence intensity	[-]
L	Bed length	[m]
N	Tube-to-pellet diameter ratio	[-]
N_{pv}	Tube-to-pellet diameter ratio based on d_{pv}	[-]
Nu	Nusselt number: $\left(hd_{ps}\big/k_f\right)$	[-]
R_t	Bed radius	[m]
Re_p	Reynolds number based on d_{pv}: $\rho u_s d_{pv}\big/\mu$	[-]
u_s	Superficial velocity	[m/s]
v_o	Inlet velocity	[m/s]
v_z	Azimuthally-averaged axial velocity	[m/s]
Δp	Pressure drops	[kg.m^{-1}s^{-2}]
r	Radial Coordinate	[m]
z	Axial Coordinate	[m]

Greek letters

ε	Bulk porosity	[-]
$\varepsilon(r)$	Radial porosity profile	[-]
μ	Fluid dynamic viscosity	[kg/(ms)]
ρ_f	Fluid phase density	[kg/m^3]
Ψ	Pore-based friction factor	[-]

Bibliography

[1]   D. Vortmeyer, E. Haidegger, Discrimination of three approaches to evaluate heat fluxes for wall-cooled fixed bed chemical reactors, Chemical Engineering Science. 46 (1991) 2651–2660. doi:10.1016/0009-2509(91)80058-7.

[2]   M.G. Freiwald, W.R. Paterson, Accuracy of model predictions and reliability of experimental data for heat transfer in packed beds, Chemical Engineering Science. 47 (1992) 1545–1560. doi:10.1016/0009-2509(92)85003-T.

[3]   J.N. Papageorgiou, G.F. Froment, Simulation models accounting for radial voidage profiles in fixed-bed reactors, Chemical Engineering Science. 50 (1995) 3043–3056. doi:10.1016/0009-2509(95)00138-U.

[4]   H. Freund, T. Zeiser, F. Huber, E. Klemm, G. Brenner, F. Durst, G. Emig, Numerical simulations of single phase reacting flows in randomly packed fixed-bed reactors and experimental validation, Chemical Engineering Science. 58 (2003) 903–910. doi:10.1016/S0009-2509(02)00622-X.

[5]   A.G. Dixon, M. Nijemeisland, E.H. Stitt, Packed tubular reactor modeling and catalyst design using computational fluid dynamics, Advance in Chemical Engineering. 31 (2006) 307–389. doi:10.1016/S0065-2377(06)31005-8.

[6]   C. McGreavy, E. Foumeny, K.J.-C.E. Science, undefined 1986, Characterization of transport properties for fixed bed in terms of local bed structure and flow distribution, Elsevier. (n.d.). https://www.sciencedirect.com/science/article/pii/0009250986871597 (accessed January 31, 2018).

[7]   O. Bey, G. Eigenberger, Fluid flow through catalyst filled tubes, Chemical Engineering Science. 52 (1997) 1365–1376.

[8]   M. Giese, K. Rottschafer, D. Vortmeyer, Measured and modeled superficial flow profiles in packed beds with liquid flow, AIChE J. 44 (1998) 484–490. doi:10.1002/aic.690440225.

[9]   A.M. Krischke, Modellierung und experimentelle Untersuchung von Transportprozessen in durchstromten Schuttungen, VDI VERLAG, 2001.

[10]   A.J. Sederman, M.L. Johns, P. Alexander, L.F. Gladden, Structure-flow correlations in packed beds, Chemical Engineering Science. 53 (1998) 2117–2128.

[11]   T. Suekane, Y. Yokouchi, S. Hirai, Inertial flow structures in a simple-packed bed of spheres, AIChE Journal. 49 (2003) 10–17.

[12]   X. Ren, S. Stapf, B. Blümich, Magnetic resonance visualisation of flow and pore structure in packed beds with low aspect ratio, Chemical Engineering and Technology. 28 (2005) 219–225. doi:10.1002/ceat.200407092.

[13]   M.J. Baker, P.G. Young, G.R. Tabor, Image based meshing of packed beds of cylinders at low aspect ratios using 3D MRI coupled with computational fluid dynamics,

Computers and Chemical Engineering. 35 (2011) 1969–1977. doi:10.1016/j.compchemeng.2011.03.017.

[14] O. Bey, G. Eigenberger, Gas flow and heat transfer through catalyst filled tubes, International Journal of Thermal Sciences. 40 (2001) 152–164. doi:10.1016/S1290-0729(00)01204-7.

[15] M. Winterberg, E. Tsotsas, Modelling of heat transport in beds packed with spherical particles for various bed geometries and/or thermal boundary conditions, International Journal of Thermal Sciences. 39 (2000) 556–570. doi:10.1016/S1290-0729(00)00251-9.

[16] M. Winterberg, E. Tsotsas, A. Krischke, D. Vortmeyer, A simple and coherent set of coefficients for modelling of heat and mass transport with and without chemical reaction in tubes filled with spheres, Chemical Engineering Science. 55 (2000) 967–979. doi:10.1016/S0009-2509(99)00379-6.

[17] T. Eppinger, K. Seidler, M. Kraume, DEM-CFD simulations of fixed bed reactors with small tube to particle diameter ratios, Chemical Engineering Journal. 166 (2011) 324–331. doi:10.1016/j.cej.2010.10.053.

[18] M. Nijemeisland, A.G. Dixon, Comparison of CFD simulations to experiment for convective heat transfer in a gas-solid fixed bed, Chemical Engineering Journal. 82 (2001) 231–246. doi:10.1016/S1385-8947(00)00360-0.

[19] A.G. Dixon, M. Nijemeisland, CFD as a design tool for fixed-bed reactors, in: Industrial and Engineering Chemistry Research, 2001: pp. 5246–5254. doi:10.1021/ie001035a.

[20] F. Augier, F. Idoux, J.Y. Delenne, Numerical simulations of transfer and transport properties inside packed beds of spherical particles, Chemical Engineering Science. 65 (2010) 1055–1064. doi:10.1016/j.ces.2009.09.059.

[21] A.G. Dixon, G. Walls, H. Stanness, M. Nijemeisland, E.H. Stitt, Experimental validation of high Reynolds number CFD simulations of heat transfer in a pilot-scale fixed bed tube, Chemical Engineering Journal. 200–202 (2012) 344–356. doi:10.1016/j.cej.2012.06.065.

[22] M. Behnam, A.G. Dixon, M. Nijemeisland, E.H. Stitt, A New Approach to Fixed Bed Radial Heat Transfer Modeling Using Velocity Fields from Computational Fluid Dynamics Simulations BT - Industrial & Engineering Chemistry Research, Industrial and Engineering Chemistry Research. 52 (2013) 15244–15261. doi:10.1021/ie4000568.

[23] M. V Tabib, S.T. Johansen, S. Amini, A 3D CFD-DEM methodology for simulating industrial scale packed bed chemical looping combustion reactors, Industrial and Engineering Chemistry Research. 52 (2013) 12041–12058. doi:10.1021/ie302028s.

[24] L. Pistocchini, S. Garone, M. Motta, Porosity and pressure drop in packed beds of spheres between narrow parallel walls, Chemical Engineering Journal. 284 (2016) 802–811. doi:10.1016/j.cej.2015.08.047.

[25]   A. Singhal, S. Cloete, S. Radl, R. Quinta-Ferreira, S. Amini, Heat transfer to a gas from densely packed beds of cylindrical particles, Chemical Engineering Science. 172 (2017) 1–12. doi:10.1016/j.ces.2017.06.003.

[26]   G.D. Wehinger, T. Eppinger, M. Kraume, Evaluating catalytic fixed-bed reactors for dry reforming of methane with detailed CFD, Chemie-Ingenieur-Technik. 87 (2015). doi:10.1002/cite.201400153.

[27]   G.D. Wehinger, C. Füterer, M. Kraume, Contact modifications for CFD simulations of fixed-bed reactors: Cylindrical particles, Industrial and Engineering Chemistry Research. 56 (2017) 87–99. doi:10.1021/acs.iecr.6b03596.

[28]   Y. Dong, B. Sosna, O. Korup, F. Rosowski, R. Horn, Investigation of radial heat transfer in a fixed-bed reactor: CFD simulations and profile measurements, Chemical Engineering Journal. 317 (2017) 204–214. doi:10.1016/j.cej.2017.02.063.

[29]   B. Partopour, A.G. Dixon, An integrated workflow for resolved-particle packed bed models with complex particle shapes, Powder Technology. 322 (2017) 258–272. doi:10.1016/j.powtec.2017.09.009.

[30]   M. Nijemeisland, A.G. Dixon, CFD Study of Fluid Flow and Wall Heat Transfer in a Fixed Bed of Spheres, AIChE Journal. 50 (2004) 906–921. doi:10.1002/aic.10089.

[31]   A.G. Dixon, M. Ertan Taskin, M. Nijemeisland, E.H. Stitt, Wall-to-particle heat transfer in steam reformer tubes: CFD comparison of catalyst particles, Chemical Engineering Science. 63 (2008) 2219–2224. doi:10.1016/j.ces.2008.01.017.

[32]   M.E. Taskin, A.G. Dixon, M. Nijemeisland, E.H. Stitt, CFD Study of the Influence of Catalyst Particle Design on Steam Reforming Reaction Heat Effects in Narrow Packed Tubes, (2008) 5966–5975.

[33]   P. Magnico, Hydrodynamic and transport properties of packed beds in small tube-to-sphere diameter ratio: pore scale simulation using an Eulerian and a Lagrangian approach, Chemical Engineering Science. 58 (2003) 5005–5024. doi:10.1016/S0009-2509(03)00282-3.

[34]   H. Freund, J. Bauer, T. Zeiser, G. Emig, Detailed simulation of transport processes in fixed-beds, Industrial and Engineering Chemistry Research. 44 (2005) 6423–6434. doi:10.1021/ie0489453.

[35]   M. Coussirat, A. Guardo, B. Mateos, E. Egusquiza, Performance of stress-transport models in the prediction of particle-to-fluid heat transfer in packed beds, Chemical Engineering Science. 62 (2007) 6897–6907. doi:10.1016/j.ces.2007.08.071.

[36]   A. Jafari, P. Zamankhan, S.M. Mousavi, K. Pietarinen, Modeling and CFD simulation of flow behavior and dispersivity through randomly packed bed reactors, Chemical Engineering Journal. 144 (2008) 476–482. doi:10.1016/j.cej.2008.07.033.

[37] Y. Wu, X. An, A.B. Yu, DEM simulation of cubical particle packing under mechanical vibration, Powder Technology. 314 (2017) 89–101. doi:10.1016/j.powtec.2016.09.029.

[38] G. Lu, J.R. Third, C.R. Müller, Discrete element models for non-spherical particle systems: From theoretical developments to applications, Chemical Engineering Science. 127 (2015) 425–465. doi:10.1016/j.ces.2014.11.050.

[39] M. Marigo, E.H. Stitt, Discrete element method (DEM) for industrial applications: Comments on calibration and validation for the modelling of cylindrical pellets, KONA Powder and Particle Journal. 32 (2015) 236–252.

[40] G. Boccardo, F. Augier, Y. Haroun, D. Ferre, D.L. Marchisio, Validation of a novel open-source work-flow for the simulation of packed-bed reactors, Chemical Engineering Journal. 279 (2015) 809–820. doi:10.1016/j.cej.2015.05.032.

[41] V. V Ranade, Computational flow modeling for chemical reactor engineering, Academic press, 2001.

[42] J.P. Sørensen, W.E. Stewart, Computation of forced convection in slow flow through ducts and packed beds—III. Heat and mass transfer in a simple cubic array of spheres, Chemical Engineering Science. 29 (1974) 827–832.

[43] M.T. Dalman, J.H. Merkin, C. McGreavy, Fluid flow and heat transfer past two spheres in a cylindrical tube, Computers & Fluids. 14 (1986) 267–281.

[44] B. Lloyd, R. Boehm, Flow and heat transfer around a linear array of spheres, Numerical Heat Transfer, Part A Applications. 26 (1994) 237–252.

[45] T.F. McKenna, R. Spitz, D. Cokljat, Heat transfer from catalysts with computational fluid dynamics, AIChE Journal. 45 (1999) 2392–2410. doi:10.1002/aic.690451113.

[46] S. Logtenberg, A.G. Dixon, Computational fluid dynamics studies of fixed bed heat transfer, Chemical Engineering and Processing: Process Intensification. 37 (1998) 7–21. doi:10.1016/S0255-2701(97)00032-9.

[47] S.A. Logtenberg, A.G. Dixon, Computational Fluid Dynamics Studies of the Effects of Temperature-Dependent Physical Properties on Fixed-Bed Heat Transfer, Society. 5885 (1998) 739–747.

[48] S.A. Logtenberg, M. Nijemeisland, A.G. Dixon, Computational fluid dynamics simulations of fluid flow and heat transfer at the wall-particle contact points in a fixed-bed reactor, Chemical Engineering Science. 54 (1999) 2433–2439. doi:10.1016/S0009-2509(98)00445-X.

[49] H.P.A. Calis, J. Nijenhuis, B.C. Paikert, F.M. Dautzenberg, C.M. Van Den Bleek, CFD modeling and experimental validation of pressure drop and flow profile in a novel structured catalytic reactor packing, Chemical Engineering Science. 56 (2001) 1713–1720. doi:10.1016/S0009-2509(00)00400-0.

[50]   S.J.. Romkes, F.. Dautzenberg, C.. van den Bleek, H.P.. Calis, CFD modelling and experimental validation of particle-to-fluid mass and heat transfer in a packed bed at very low channel to particle diameter ratio, Chemical Engineering Journal. 96 (2003) 3–13. doi:10.1016/j.cej.2003.08.026.

[51]   M. Nijemeisland, A.G. Dixon, E.H. Stitt, Catalyst design by CFD for heat transfer and reaction in steam reforming, in: Chemical Engineering Science, 2004: pp. 5185–5191. doi:10.1016/j.ces.2004.07.088.

[52]   A.G. Dixon, M. Nijemeisland, E.H. Stitt, CFD Study of Heat Transfer near and at the Wall of a Fixed Bed Reactor Tube : Effect of Wall Conduction, Ind. Eng. Chem. Res. 44 (2005) 6342–6353.

[53]   A. Guardo, M. Coussirat, M.A. Larrayoz, F. Recasens, E. Egusquiza, CFD Flow and Heat Transfer in Nonregular Packings for Fixed Bed Equipment Design, Ind. Eng. Chem. Res. 43 (2004) 7049–7056.

[54]   A. Guardo, M. Coussirat, M.A. Larrayoz, F. Recasens, E. Egusquiza, Influence of the turbulence model in CFD modeling of wall-to-fluid heat transfer in packed beds, Chemical Engineering Science. 60 (2005) 1733–1742. doi:10.1016/j.ces.2004.10.034.

[55]   A. Guardo, M. Coussirat, F. Recasens, M.A. Larrayoz, X. Escaler, CFD studies on particle-to-fluid mass and heat transfer in packed beds: Free convection effects in supercritical fluids, Chemical Engineering Science. 62 (2007) 5503–5511. doi:10.1016/j.ces.2007.02.040.

[56]   A. Torkkeli, Droplet microfluidics on a planar surface, VTT Publications. 55 (2003) 3–194. doi:10.1002/aic.

[57]   T. Atmakidis, E.Y. Kenig, CFD-based analysis of the wall effect on the pressure drop in packed beds with moderate tube/particle diameter ratios in the laminar flow regime, Chemical Engineering Journal. 155 (2009) 404–410. doi:10.1016/j.cej.2009.07.057.

[58]   G.W. Koning, Heat and Mass Transport in Tubular Packed Bed Reactors at Reacting and Non-Reacting Conditions, Measurement. 48 (2002) 272.

[59]   R.K. Reddy, J.B. Joshi, CFD modeling of pressure drop and drag coefficient in fixed and expanded beds, Chemical Engineering Research and Design. 86 (2008) 444–453. doi:10.1016/j.cherd.2007.12.007.

[60]   H. Bai, J. Theuerkauf, P.A. Gillis, P.M. Witt, A coupled DEM and CFD simulation of flow field and pressure drop in fixed bed reactor with randomly packed catalyst particles, Industrial & Engineering Chemistry Research. 48 (2009) 4060–4074.

[61]   M.J. Baker, G.R. Tabor, Computational analysis of transitional air flow through packed columns of spheres using the finite volume technique, Computers & Chemical Engineering. 34 (2010) 878–885. doi:10.1016/j.compchemeng.2009.10.013.

[62]   G.D. Wehinger, T. Eppinger, M. Kraume, Detailed numerical simulations of catalytic fixed-bed reactors: Heterogeneous dry reforming of methane, Chemical Engineering Science. 122 (2015) 197–209. doi:10.1016/j.ces.2014.09.007.

[63]   A.G. Dixon, M. Nijemeisland, E.H. Stitt, Systematic mesh development for 3D CFD simulation of fixed beds: Contact points study, Computers & Chemical Engineering. 48 (2013) 135–153. doi:10.1016/j.compchemeng.2012.08.011.

[64]   A.G. Dixon, M. Ertan Taskin, M. Nijemeisland, H.H. Stitt, Systematic mesh development for 3D CFD simulation of fixed beds: Single sphere study, Computers and Chemical Engineering. 35 (2011) 1171–1185. doi:10.1016/j.compchemeng.2010.12.006.

[65]   S.D. Dhole, R.P. Chhabra, V. Eswaran, A numerical study on the forced convection heat transfer from an isothermal and isoflux sphere in the steady symmetric flow regime, International Journal of Heat and Mass Transfer. 49 (2006) 984–994.

[66]   P. Magnico, Pore-scale simulations of unsteady flow and heat transfer in tubular fixed beds, AIChE Journal. 55 (2009) 849–867.

[67]   P.R. Gunjal, V. V. Ranade, R. V. Chaudhari, Computational study of a single-phase flow in packed beds of spheres, AIChE Journal. 51 (2005) 365–378. doi:10.1002/aic.10314.

[68]   S. Patankar, Numerical heat transfer and fluid flow, CRC press, 1980.

[69]   T.-H. Shih, W.W. Liou, A. Shabbir, Z. Yang, J. Zhu, A new k-ϵ eddy viscosity model for high reynolds number turbulent flows, Computers & Fluids. 24 (1995) 227–238.

[70]   B.E. Launder, D.B. Spalding, The numerical computation of turbulent flows, in: Numerical Prediction of Flow, Heat Transfer, Turbulence and Combustion, Elsevier, 1983: pp. 96–116.

[71]   B.A. Kader, Temperature and concentration profiles in fully turbulent boundary layers, International Journal of Heat and Mass Transfer. 24 (1981) 1541–1544.

[72]   J.P. Van Doormaal, G.D. Raithby, Enhancements of the SIMPLE method for predicting incompressible fluid flows, Numerical Heat Transfer. 7 (1984) 147–163.

[73]   A. Guardo, M. Coussirat, F. Recasens, M.A. Larrayoz, X. Escaler, CFD study on particle-to-fluid heat transfer in fixed bed reactors: Convective heat transfer at low and high pressure, Chemical Engineering Science. 61 (2006) 4341–4353. doi:10.1016/j.ces.2006.02.011.

[74]   P.J. Roache, Verification of codes and calculations, AIAA Journal. 36 (1998) 696–702.

[75]   B. Eisfeld, K. Schnitzlein, The influence of confining walls on the pressure drop in packed beds, Chemical Engineering Science. 56 (2001) 4321–4329.

[76]   N. Cheng, Wall effect on pressure drop in packed beds, Powder Technology. 210 (2011) 261–266. doi:10.1016/j.powtec.2011.03.026.

[77]   W. Reichelt, Zur Berechnung des Druckverlustes einphasig durchströmter Kugel-und Zylinderschüttungen, Chemie Ingenieur Technik. 0 (1972) 1068–1071. doi:10.1002/cite.330441806.

[78]   G.E. Mueller, Angular void fraction distributions in randomly packed fixed beds of uniformly sized spheres in cylindrical containers, Powder Technology. 77 (1993) 313–319. doi:10.1016/0032-5910(93)85023-3.

[79]   S.N. Gupta, R.B. Chaube, S.N. Upadhyay, Fluid-particle and heat transfer beds, Chemical Engineering. 29 (1974) 839–843.

[80]   D.J. Gunn, Transfer of heat or mass to particles in fixed and fluidised beds, International Journal of Heat and Mass Transfer. 21 (1978) 467–476.

[81]   N. Wakao, S. Kaguei, T. Funazkri, Effect of fluid dispersion coefficients on particle-to-fluid heat transfer coefficients in packed beds: correlation of Nusselt numbers, Chemical Engineering Science. 34 (1979) 325–336.

Chapter 5

RBD-CFD Simulation of Fluid Flow and Heat Transfer: Importance of Heterogeneities and Inadequacy of Pseudo-Continuum Approaches
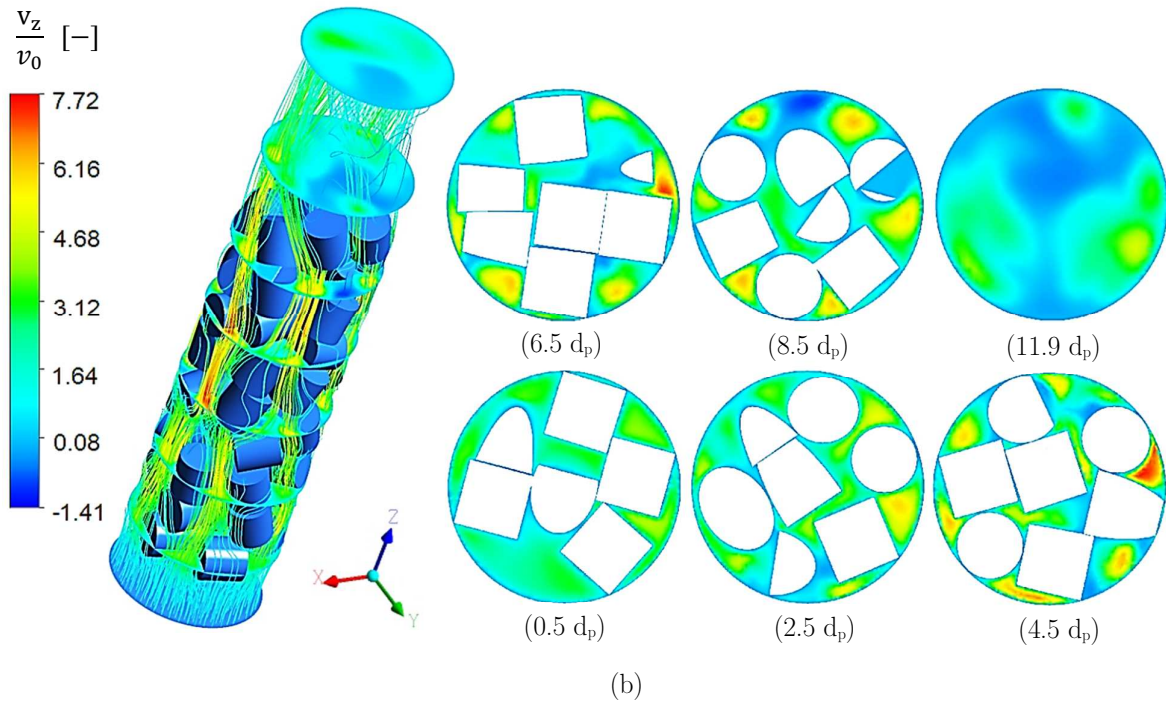
Abstract

The in-situ behavior of velocity and thermal fields in random packings of spheres, cylinders and Raschig rings were meticulously analyzed by postprocessing the results of RBD-CFD simulations, described in chapter 4. The results reveal a tremendous influence of local structure on the velocity and temperature distributions at the pellet scale, particularly in narrower packings, where the spatial heterogeneity of the structure is very strong along the bed axis. Compared to random packings of spheres, in random packings of cylinders and Raschig rings more intense inhomogeneities in local velocity and temperature fields were observed. This can be ascribed to the role of sharp edges of such pellets in imposing stronger curvatures of the flow streamlines along the packing. Furthermore, the results show that the azimuthal averaging of velocity and temperature fields result in the under-estimation of local velocity and temperature values by more than 400% and 50 K, respectively. This explains the inadequacy of even modified versions of pseudo-continuum approaches in predicting the radial heat transfer in tubular fixed bed reactors. The results of this chapter suggest the RBD-CFD methodology as a robust and reliable tool, providing detailed information on the "pellet-scale" behavior of transport processes in fixed bed reactors of non-spherical pellets.

5.1. Hydrodynamic results

5.1.1. 3D structure of flow fields

Having a detailed knowledge of the flow distribution inside fixed bed reactors is crucial for the design because it strongly influences local propagation of transport scalars and thus the reactor performance.

Fig. 5.1 exhibits three examples of the 3D structure of flow fields, in the form of contour plots of the axial velocity normalized by the inlet velocity for several cross sections, together with flow streamlines colored by the local axial velocity, for packings of spheres, cylinders and Raschig rings at $Re_p = 100$. The contour plots of normalized axial velocities at different bed cross sections demonstrate a tremendous inhomogeneity in the velocity distribution, which directly arises from the structural features of the randomly-packed fixed bed arrangements.

(6.5 d$_p$)   (8.5 d$_p$)   (11 d$_p$)

(0.5 d$_p$)   (2.5 d$_p$)   (4.5 d$_p$)

(a)

(6.5 d$_p$)   (8.5 d$_p$)   (11.9 d$_p$)

(0.5 d$_p$)   (2.5 d$_p$)   (4.5 d$_p$)

(b)
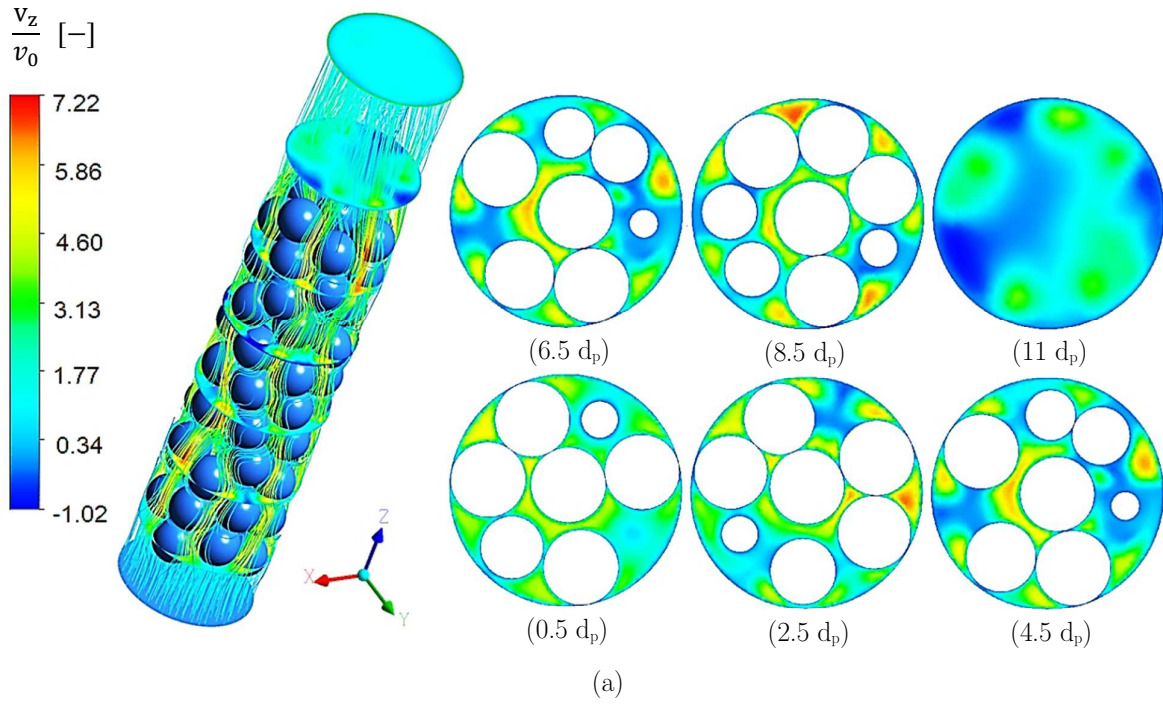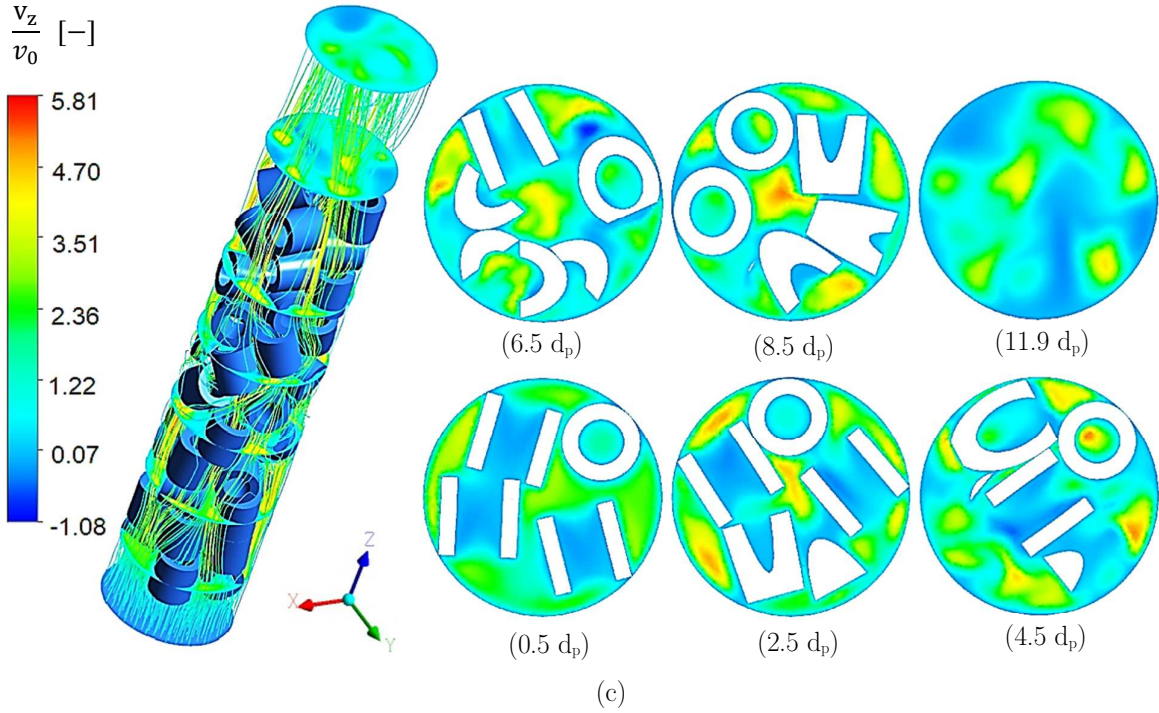
Fig. 5.1 Examples of 3D flow fields using streamlines and contour plots of normalized axial velocity at different cross sections at axial positions $0.5d_P$, $2.5d_P$, $4.5d_P$, $6.5d_P$, $8.5d_P$ and $+0.5d_P$ behind the packing section, for packings of (a) spheres, (b) cylinders and (c) Raschig rings, with $N_{pv} = 3.1$ at $Re_p = 100$.

This inhomogeneity can be much more pronounced in packings of cylinders and Raschig rings, where the sharp edges of the cylinders at each crosscut impose stronger curvatures of the streamlines along the packing. Besides, as shown in 5.1c, the presence of an internal hole in the Raschig ring pellets leads to even a higher level of heterogeneity in the flow field, specifically when a Raschig ring is situated perpendicular to the flow direction. Furthermore, the contours reveal a local increase of axial velocity up to factors of 7.24, 7.72 and 5.81 for packings of spheres, cylinders and Raschig rings, respectively, for $N_{pv} = 3.1$ and $Re_p = 100$. The lower local increase of axial velocity in the packing of Raschig rings compared to spheres and cylinders can be ascribed to the shape of such pellets, where the existence of an axial hole inside the particle increases the local porosity. The high velocity "hotspots" are found predominantly near the wall region and also partially in the inner regions of the packing structures. The latter phenomenon can be more clearly observed in the contours of axial velocity at the central plane (XZ plane) of the packings, as shown in Fig. 5.2.

(a)

(b)

$$\frac{\mathbf{v_z}}{v_0} \ \ [-]$$

(c)
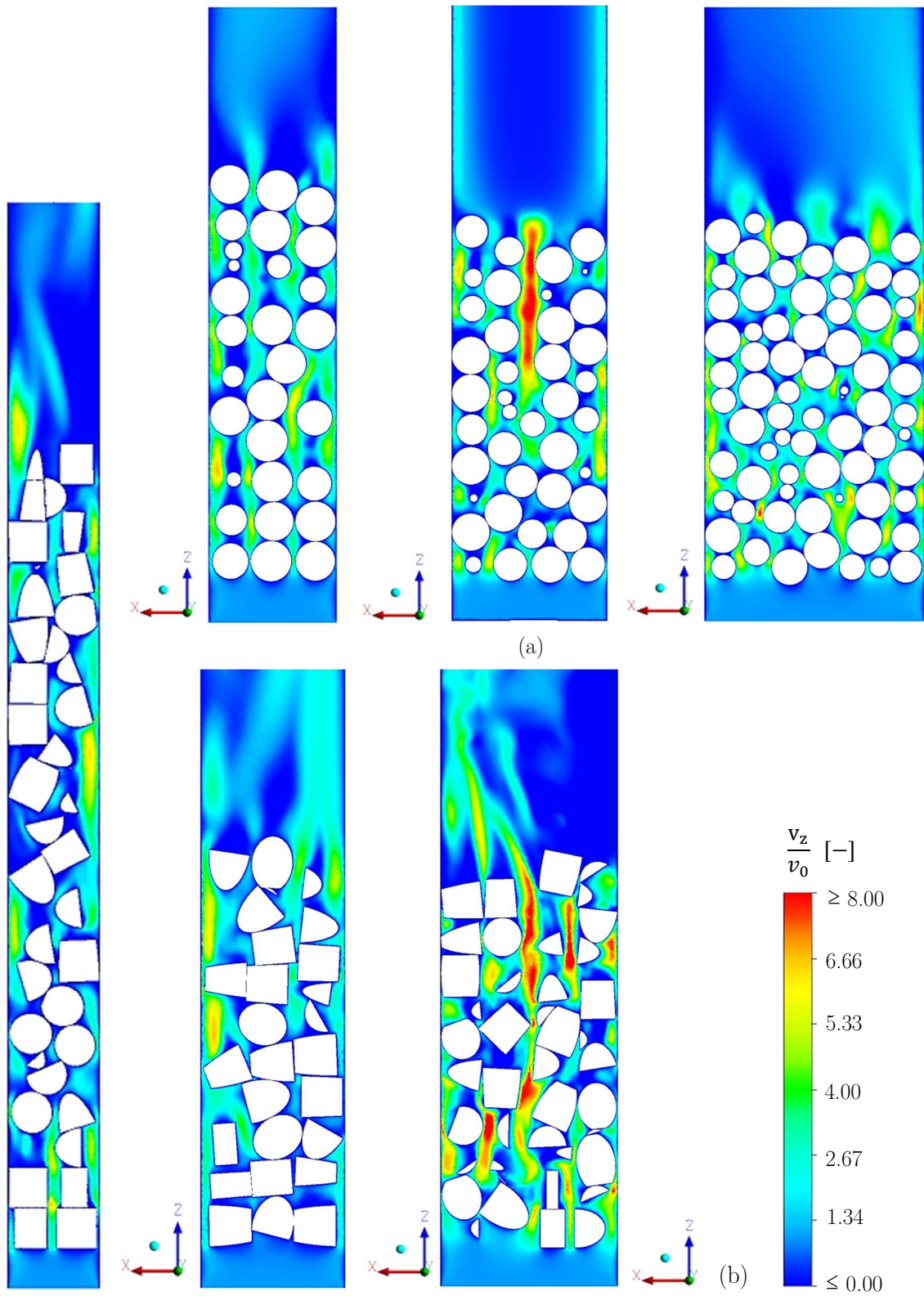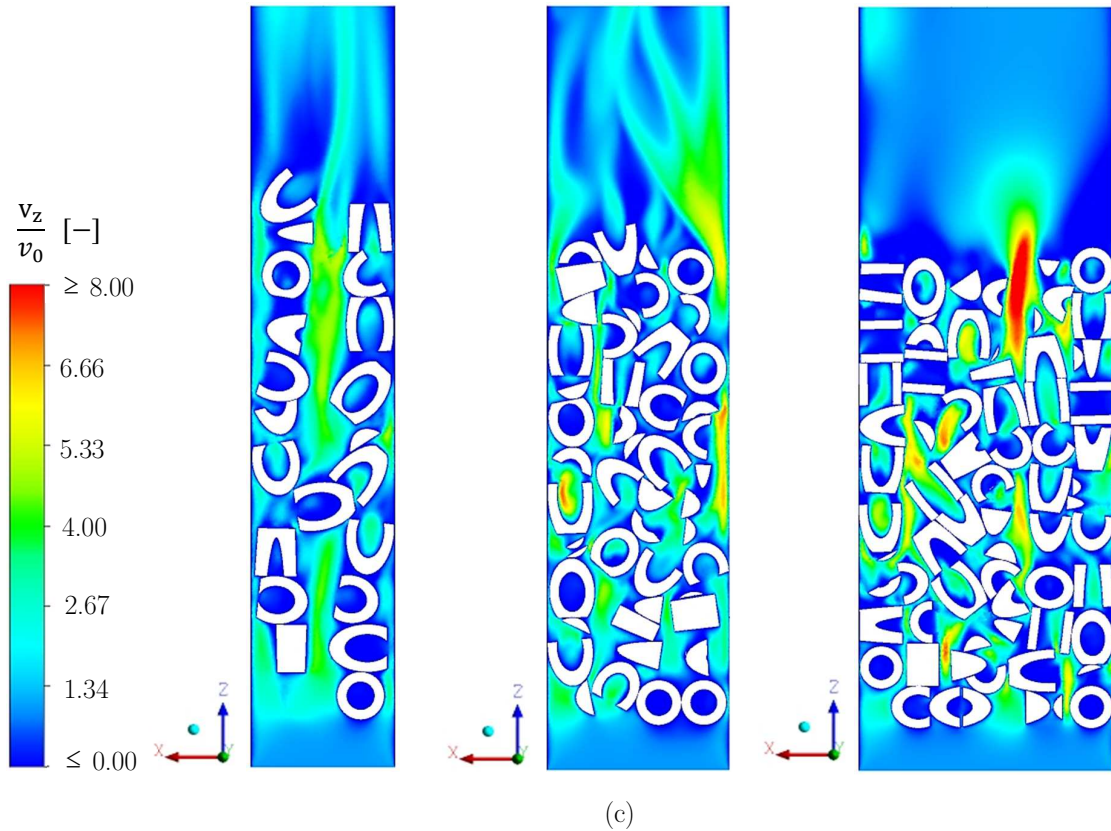
Fig. 5.2 Contour plots of normalized axial velocity at the central plane (XZ) of different random packings at $Re_p = 100$; (a) spheres with $N = 3.1$, 4.1 and 6.1; (b) cylinders with $N = 2.29$, 3.55 and 4.58; (c) Raschig rings with $N = 3.06$, 4.05 and 6.02.

As illustrated in the contour plots, a local increase in axial velocity mostly occurs in areas where the structure is not so dense, such as the near-wall region (the so-called wall channeling phenomenon) and connected axial interstices. However, it is evident that for some packings the maximum axial velocities occur at the center of the packing geometry, which originates from the high local porosity near the tube center in such packing structures. Conceptually, such flow characteristics can be a priori anticipated from the radial porosity profiles of these packing structures (see Figs. 3.17-19). Several researchers have reported similar observations, albeit only for packing of spheres with N around 4, e.g. [1–3]. Our CFD results demonstrate that maximum axial velocities also appear in the center of cylindrical packings with N slightly larger than 4 and Raschig ring packings with N around 3 (see Fig. 5.2b-c). Furthermore, the contour maps of v_z/v_0 show that the local rise in axial velocity increases with N at specific Re_p, which can be explained by the decreasing the bulk porosity with increasing N. Similar results were fond for the magnitude of negative z-velocity (not shown here). Moreover, the contour plots reveal that areas with stagnant and backflow velocity fields, i.e. vortices, are emerging in

the wakes of pellets (and also inside the internal holes of Raschig rings, see Fig. 5.3) and behind the packing sections. As illustrated in Fig. 5.3, such regions become increasingly common with increasing Re_p. Our CFD results show that the magnitude of negative axial velocity increases with the increase of Re_p, viz. v_z/v_0 = -0.13, -2.76 and -2.81 at Re_p = 10, 100 and 1000, respectively, for Raschig rings packing with N = 4.05.
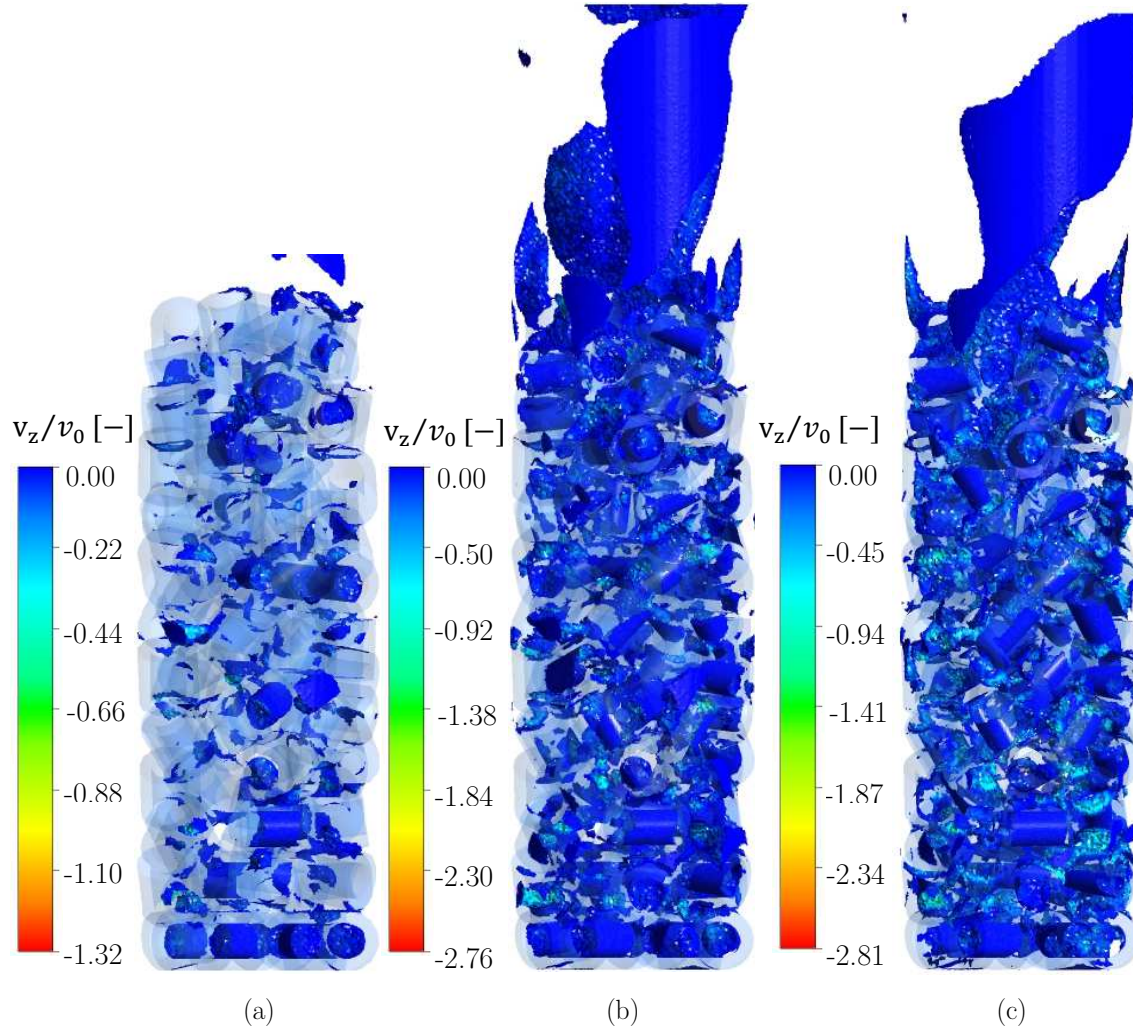
Fig. 5.3 Regions with stagnant and backflow velocity fields in a random packing of Raschig rings with N = 4.05; (a) Re_p = 10, (b) Re_p = 100 and (c) Re_p = 1000.

5.1.2.   Azimuthally-averaged velocity profile

Because of the important role of flow maldistribution in lateral heat and species transport in fixed bed reactors, several researchers have tried to describe the hydrodynamic features of such tortuous structures using a simplified radially-varying axial velocity profile. Therefore, this section deals with the behavior of the 2D (azimuthally-averaged, axial and radial position-dependent) axial velocity profile in different packing structures.

Fig. 5.4 shows the azimuthally-averaged axial velocity distributions, extracted from two different bed heights, and the axially-and-azimuthally-averaged profile, for all packing models at Re_p=1000. The plots show the occurrence of the first maxima adjacent to the tube wall, which varies between 1.5 and 3 times the inlet superficial velocity. Furthermore, the position of the first minimum occurs approximately at $0.5d_p$ from the tube wall in packings of spheres, while this position shifts to around $0.65d_{pv}$ and $0.85d_{pv}$ from the tube wall for cylindrical and Raschig ring packings, respectively, all corresponding to the minimum in local porosity profiles shown in Fig. 5.5. Nonetheless, a distinct difference between the local (azimuthally-averaged) and the global (axially-and-azimuthally-averaged) v_z/v_0 profiles can be found, specifically at the points where the local porosity has its extreme values. For example, the local (azimuthally-averaged) velocity ratio, i.e. $v_z(r,z)$ shows a maximum local deviation about 76% of v_0 (with the average deviation of 18% for z- velocity obtained profile from $z = 3.5d_p$), up to 95% (with the average deviation of 27% for z-velocity profile obtained from $z = 3.5d_p$) and up to 89% (with the average deviation of 28% for z-velocity profile obtained from $z = 3.5d_p$) from its global (axially-and-azimuthally averaged) values for packings of spheres with N = 6.1, cylinders with N = 2.29 and Raschig rings with N = 6.02, respectively, at $Re_p = 1000$. These local deviations culminate in narrower packing structures, e.g. $N_{pv} = 2$ and 3.1, where the azimuthal symmetry basically cannot be fulfilled, resulting in large heterogeneity in the radial velocity profiles along the bed axis. It is worth remarking that a higher local deviation between azimuthally-averaged and axially-and-azimuthally averaged z-velocities in the Raschig ring packing with N = 6.02 compared to spherical packing with N = 6.1 implies a higher level of circumferential asymmetry even in larger N-beds of such non-convex pellets. Furthermore, considerable differences between the local and global values of v_z/v_0 can be observed in the vicinity of the tube wall in all packings. These observations are very important, because of the important role of convective mechanisms in the wall-to-bed heat transfer. In the literature, global axially-and-azimuthally-averaged v_z/v_0 profiles, which can also be predicted from a modified version of the Navier-Stokes equations, e.g. [4], are regularly used to improve pseudo-continuum heat transfer models. Our results suggest that using such global v_z/v_0 profiles can lead to erroneous predictions of transport properties in this region, specifically for low N fixed bed reactors.
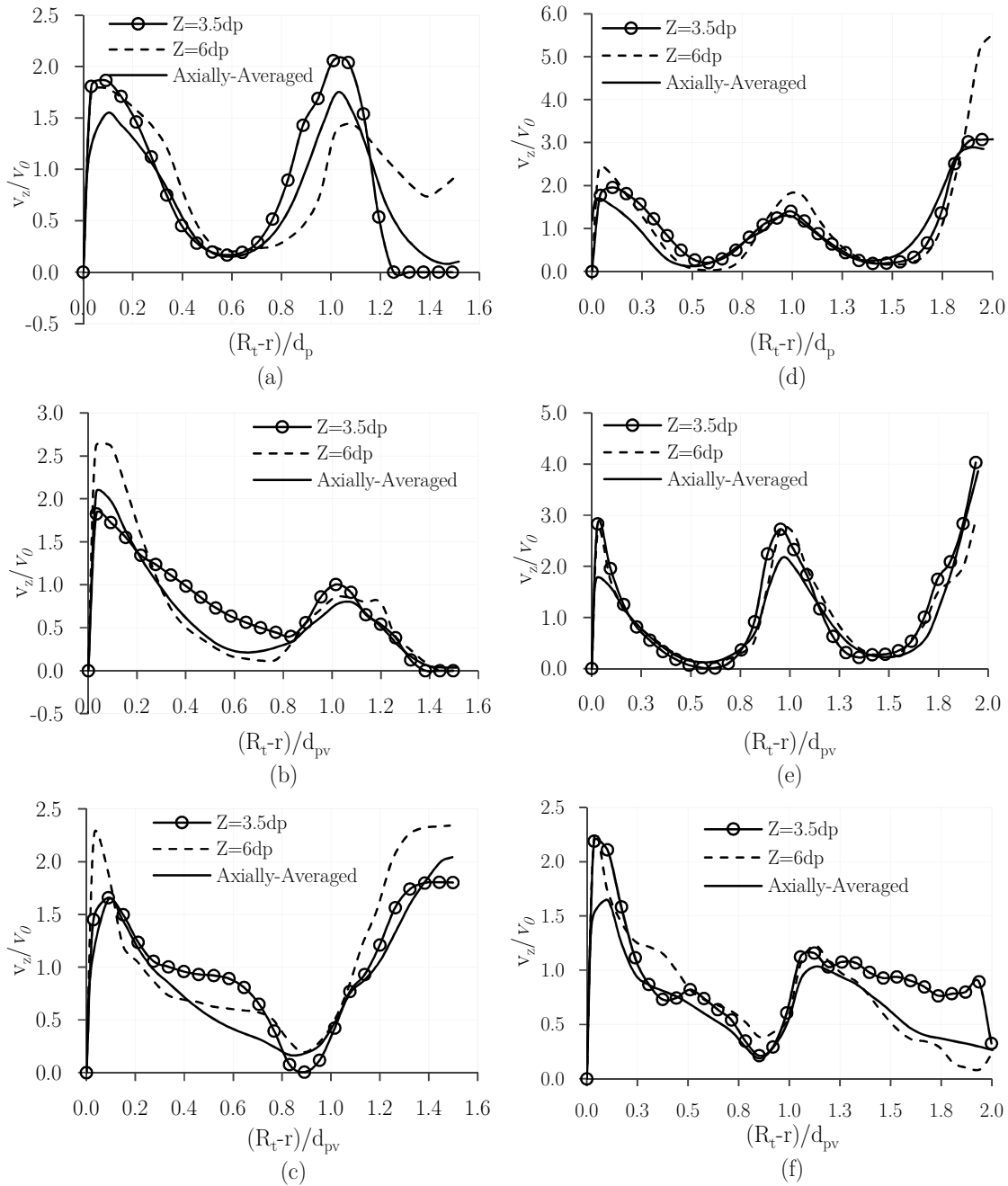
Fig. 5.4 Azimuthally–averaged axial velocity profiles at the cross sections z = 3.5d_p, 6d_p and axially-averaged profile at Re$_p$ = 1000 for packings of (a) spheres with N = 3.1, (b) cylinders with N = 3.55 (c) Raschig rings with N = 3.06, (d) spheres with N = 4.1, (e) cylinders with N = 4.58, and (f) Raschig rings with N = 4.05.

In Fig. 5.5a-c, the axial-and-azimuthally-averaged axial velocity profiles at Re$_p$=1000 are plotted together with the radial porosity distribution against dimensionless distance from tube wall for all packing structures. Fig. 5.5d compares the normalized axial-and-azimuthally-averaged axial velocity profiles between the packings of spheres, cylinders and Raschig rings

with $N = 3.1$ at $Re_p = 100$. Furthermore, we show the artificial axial velocity profile proposed by Bey and Eigenbereger [4,5] for cylindrical and Raschig ring packings at $Re_p = 1000$ (Fig. 5.5e).

(a)

(b)
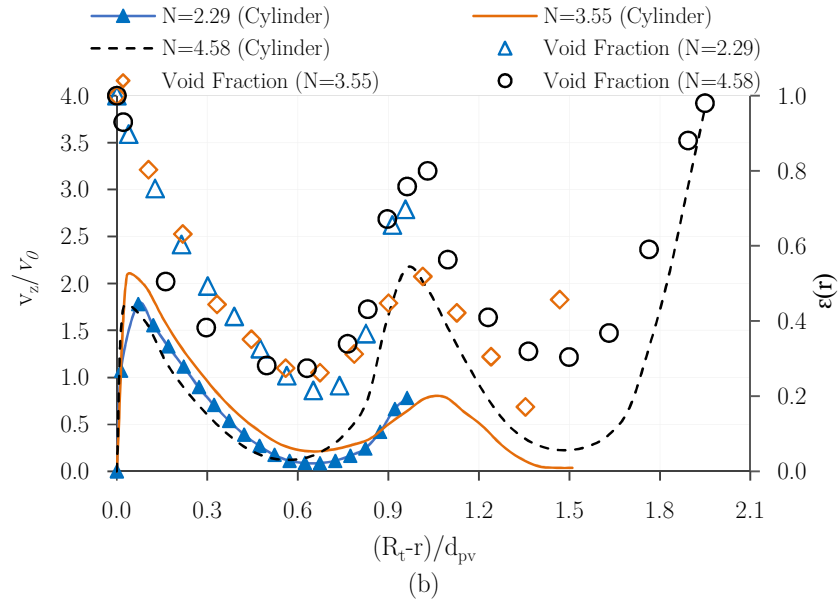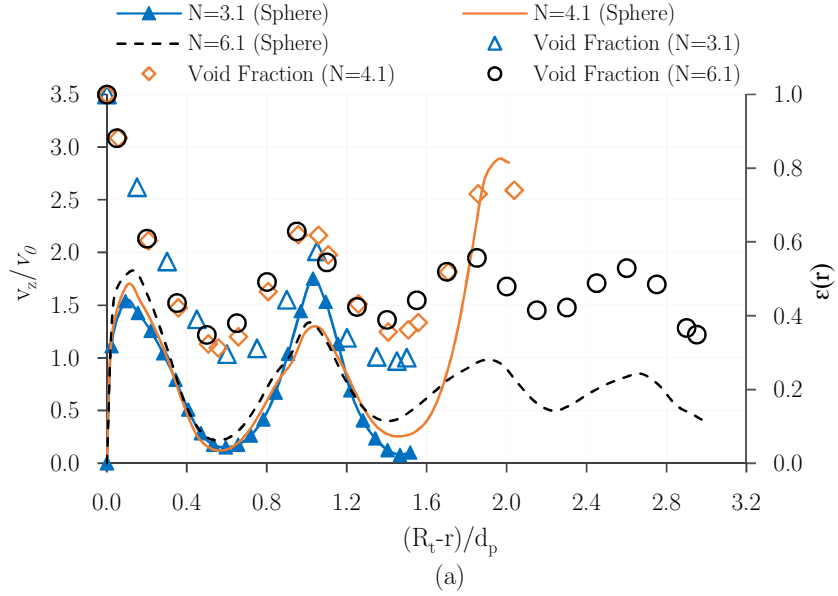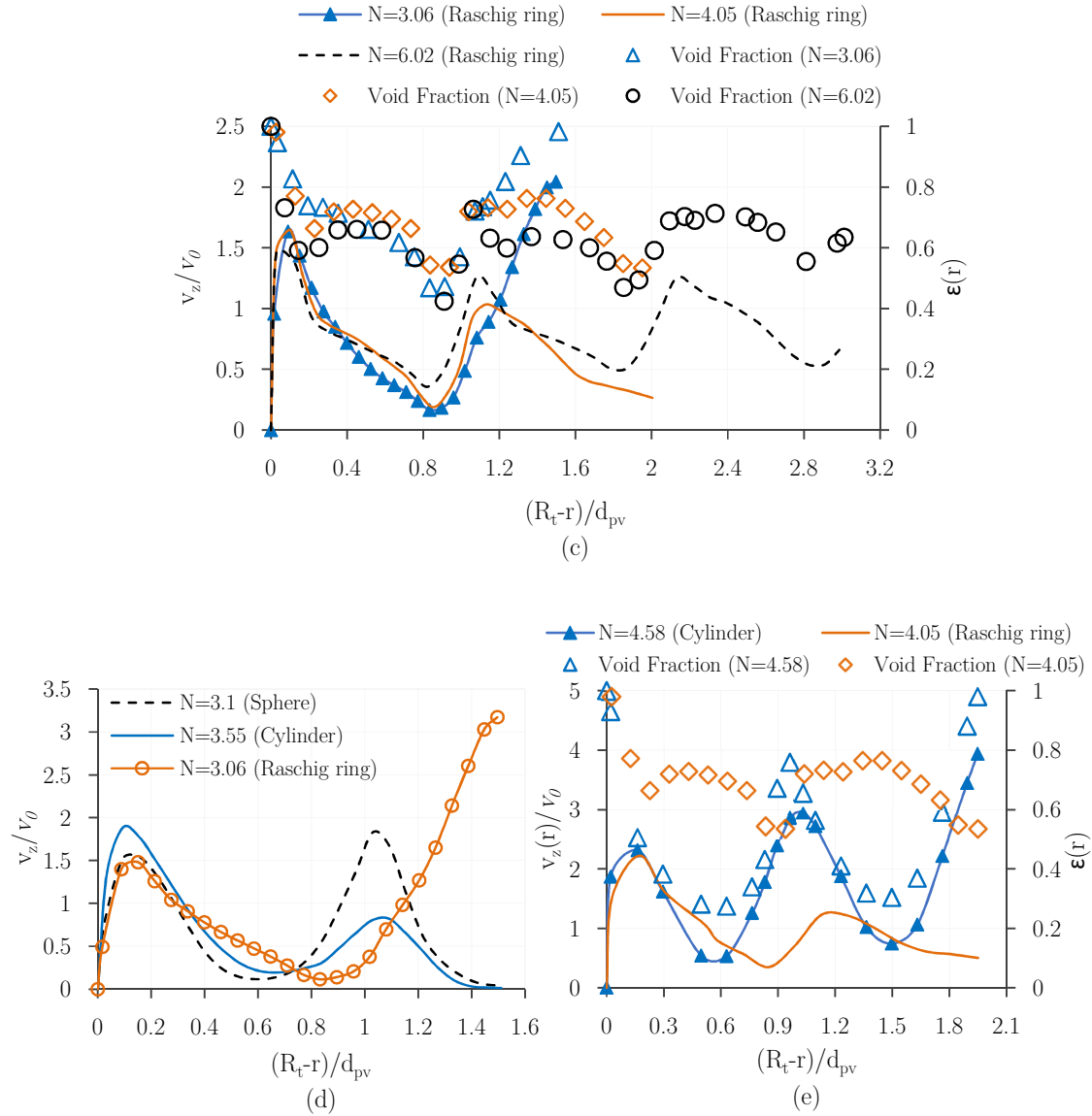
Fig. 5.5 (axial-and-azimuthally-averaged) axial velocity distribution, together with the porosity profiles at $Re_p = 1000$ for random packings of (a) spheres (b) cylinders and (c) Raschig rings; (d) axial-and-azimuthally-averaged axial velocity profiles for all packings with $N_{pv} = 3.1$ at $Re_p = 100$; (e) the artificial normalized axial velocity profile after Bey and Eigenberger [4] at $Re_p = 1000$

Overall, the results demonstrate a meaningful harmony between the axially-and-azimuthally averaged bed topology data, i.e. radial porosity distribution, and axially-and-azimuthally averaged axial velocity profile in spherical and cylindrical cases, in the sense that the oscillatory pattern in the radial porosity distribution is closely reflected by the radial-dependent axial velocity profile, whereas such a harmony can hardly be realized in packings of Raschig rings. Moreover, the normalized artificial z-velocity profiles (Fig. 5.5e) show peaks in the velocity ratio between 2 and 3 near the wall region, which is in agreement with the

measurements of Vortmeyer and coworkers [6] and Bey and Eigenbereger [4,5]. Nonetheless, the above averaged axial velocities are basically positive for every Re_p, which implies the inadequacy of such flow information in reflecting the appearance of vortex regions, i.e. backflow as well as stagnant flow fields. This is also exemplified by the fact that there is a noticeable deviation (more than 400%) between the azimuthally-averaged values of axial velocities (see Fig. 5.5d), even when obtained for a specific bed cross section and the local normalized axial velocity values shown by the contour plots in Fig. 5.1, for typical packings of spheres, cylinders and Raschig rings with $N_{pv} = 3.1$ at $Re_p = 100$. This elucidates to what extent the averaging of velocity fields (or the exertion of artificial velocity profiles based on averaged porosity data) in modeling fixed beds neglects the localized phenomena at the pellet scale, which can lead to erroneous predictions of the behavior of transport scalars inside the reactors

5.2. Heat transfer results

5.2.1. Contour maps of thermal field

The analysis of heat transfer in tubular fixed beds is essential as it can strongly influence the reactor performance in terms of the product yield and selectivity. In lower N-beds, say N<10, as discussed in chapter 3, the reactor wall induces a radial heterogeneity in the local packing structure. The consequence of such a topological feature, as explained in the previous sections, is the occurrence of a tremendous local inhomogeneity in the velocity fields. In this section we are going to address the influence of (bed-related) local flow maldistribution in such complicated structures on the temperature field. Following this, the role of pellet shape and tube-to-pellet diameter ratio on temperature field is investigated at the pellet scale.

Fig. 5.6 shows three examples of the pellet-scale temperature fields in both fluid and solid (i.e. catalyst) phases, in the form of contour maps of temperature for several cross sections together with the pellets surface temperature, for the packings of spheres, cylinders and Raschig rings at $Re_p = 100$.

T [K]

298 365 432 492 566 633 700

(6.5 d$_p$)   (8.5 d$_p$)   (11 d$_p$)

(0.5 d$_p$)   (2.5 d$_p$)   (4.5 d$_p$)

(a)

T [K]

298 365 342 492 566 633 700

(6.5 d$_p$)   (8.5 d$_p$)   (11.9 d$_p$)

(0.5 d$_p$)   (2.5 d$_p$)   (4.5 d$_p$)

(b)
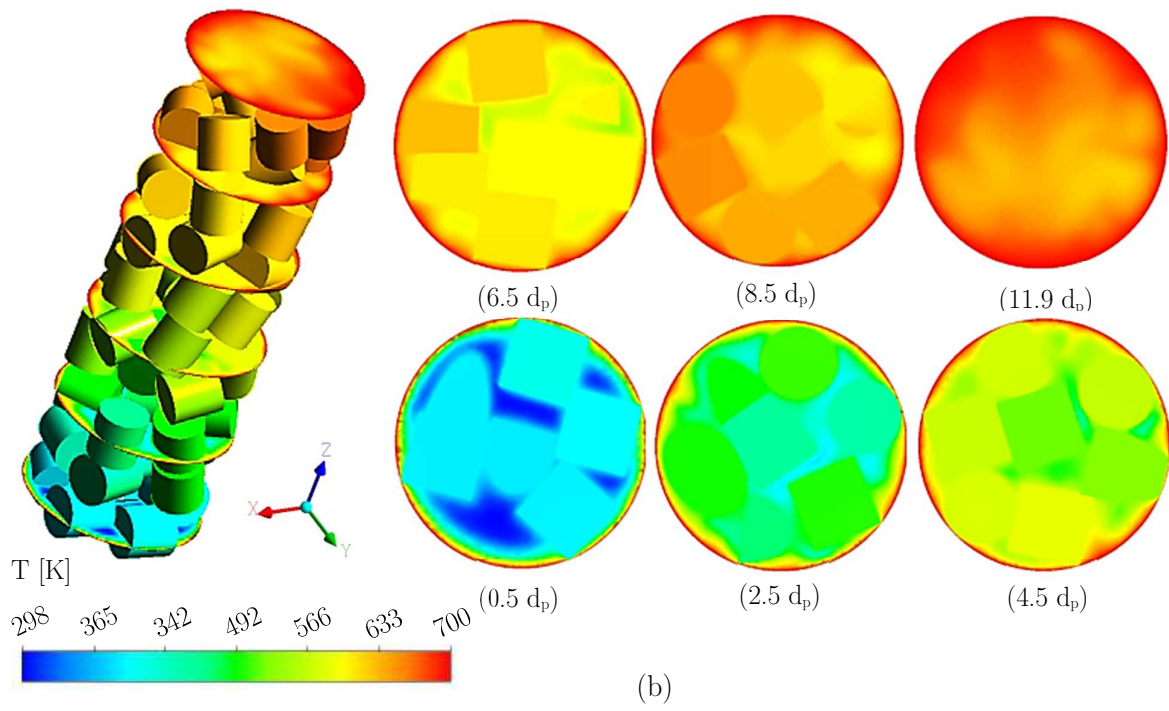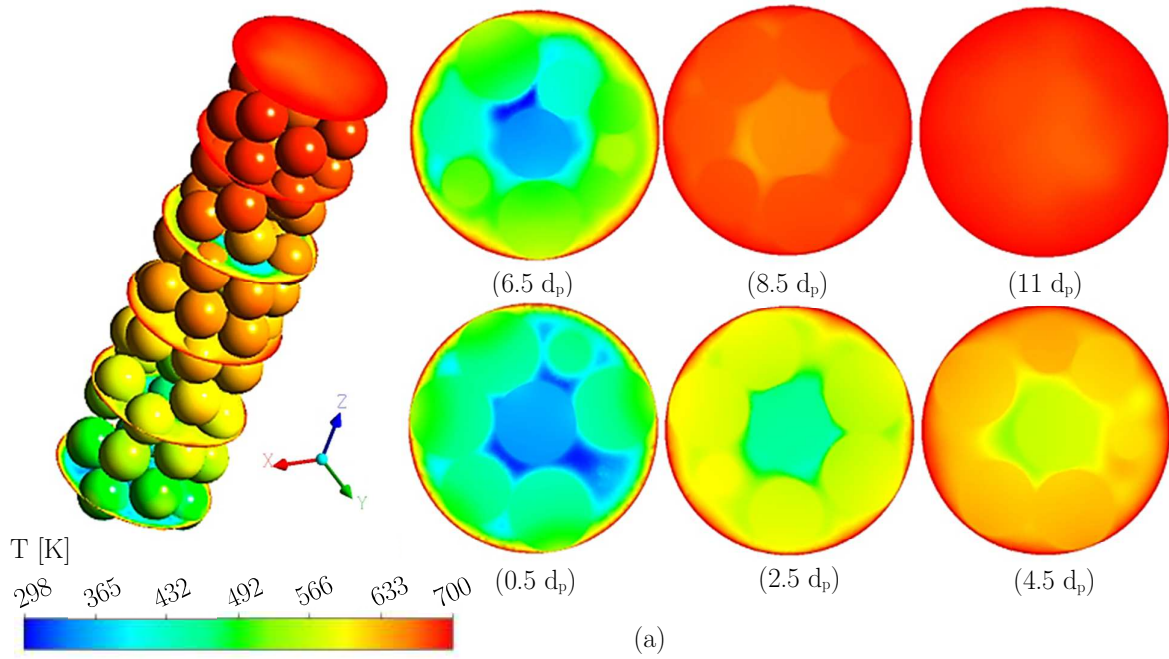
Fig. 5.6 Contour plots of temperature field on the surface of pellets and at different cross sections at axial positions $0.5d_P$, $2.5d_P$, $4.5d_P$, $6.5d_P$, $8.5d_P$ and $+0.5d_P$ behind the packing section, for packings of alumina pellets; (a) spheres, (b) cylinders and (c) Raschig rings, with $N_{pv} = 3.1$ at $Re_p = 100$.

The contour plots of temperature fields at different bed cross sections demonstrate a tremendous inhomogeneity in the temperature distribution along the packing depth, which directly arises from the local flow maldistribution in such narrow-fixed bed arrangements. This inhomogeneity is much more discernable in packings of cylinders and Raschig rings (see Fig. 5.6b-c), closely connected to the role of topological features of such shaped pellets in the local velocity distribution. Furthermore, the temperature contour maps at each cross section substantiate that there is no azimuthal symmetry in temperature distribution, which is caused by the extreme radial and angular heterogeneity inherent in the low-N fixed bed structures. This observation can also explain why a 120^0 wall-segment model proposed by Dixon and coworkers [7–9] cannot be adequate for analysis of flow and heat transfer in a full fixed bed.

To investigate the influence of N on the temperature distribution, contour maps of temperature fields at different cross sections are depicted for random packings of spheres and Raschig rings with $N_{pv} = 3.1, 4.1$ and 6.1 in Figs. 5.7 and 5.8, respectively.

(a)

(b)
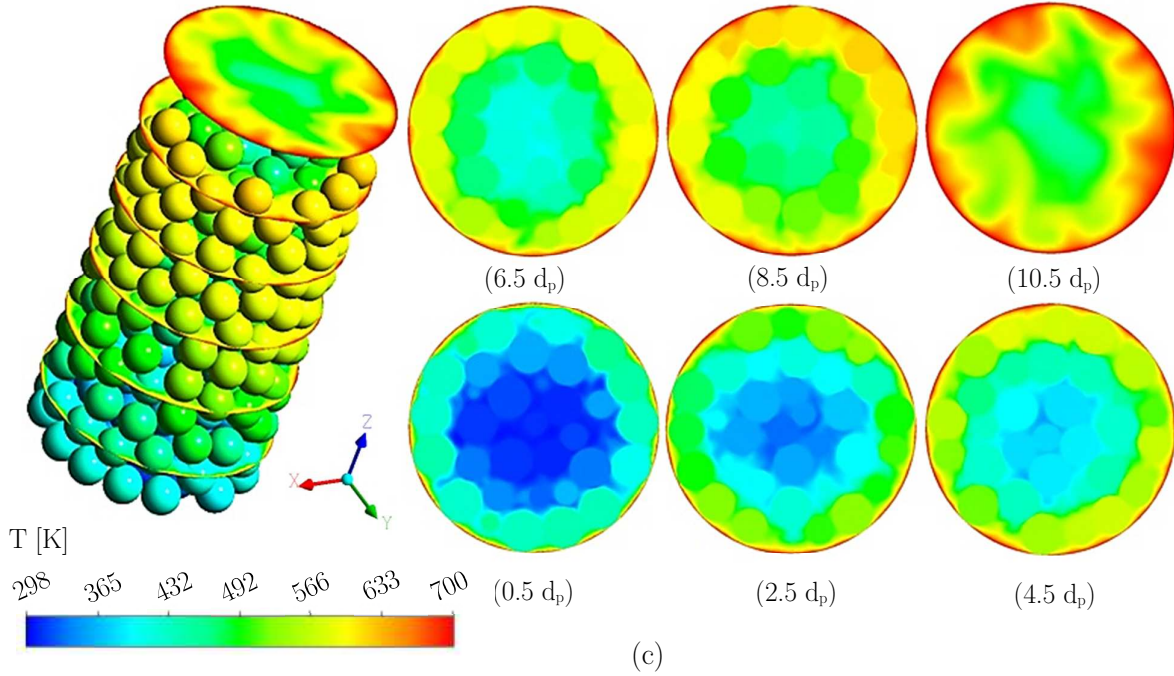
Fig. 5.7 Contour plots of temperature field on the surface of pellets and at different cross sections at axial positions 0.5d$_P$, 2.5d$_P$, 4.5d$_P$, 6.5d$_P$, 8.5d$_P$ and +0.5d$_P$ behind the packing section, for packings of alumina spheres; (a) N = 3.1, (b) N = 4.1 and (c) N = 6.1 at Re$_p$ = 100.

(b)

(c)

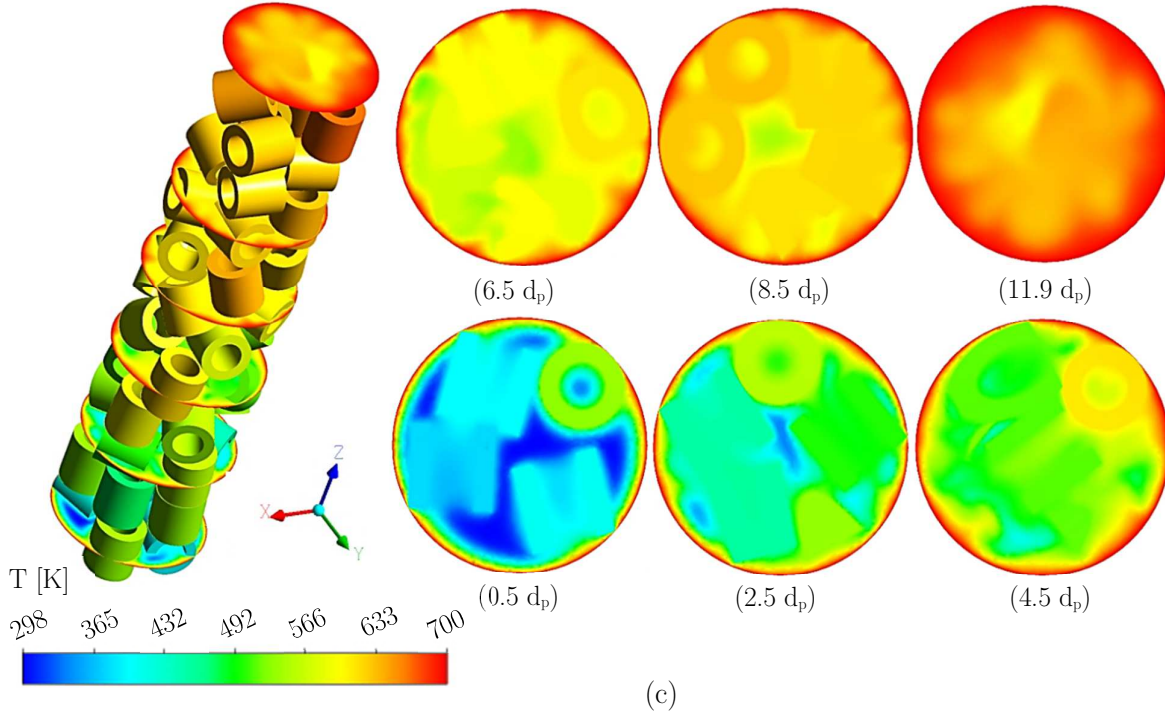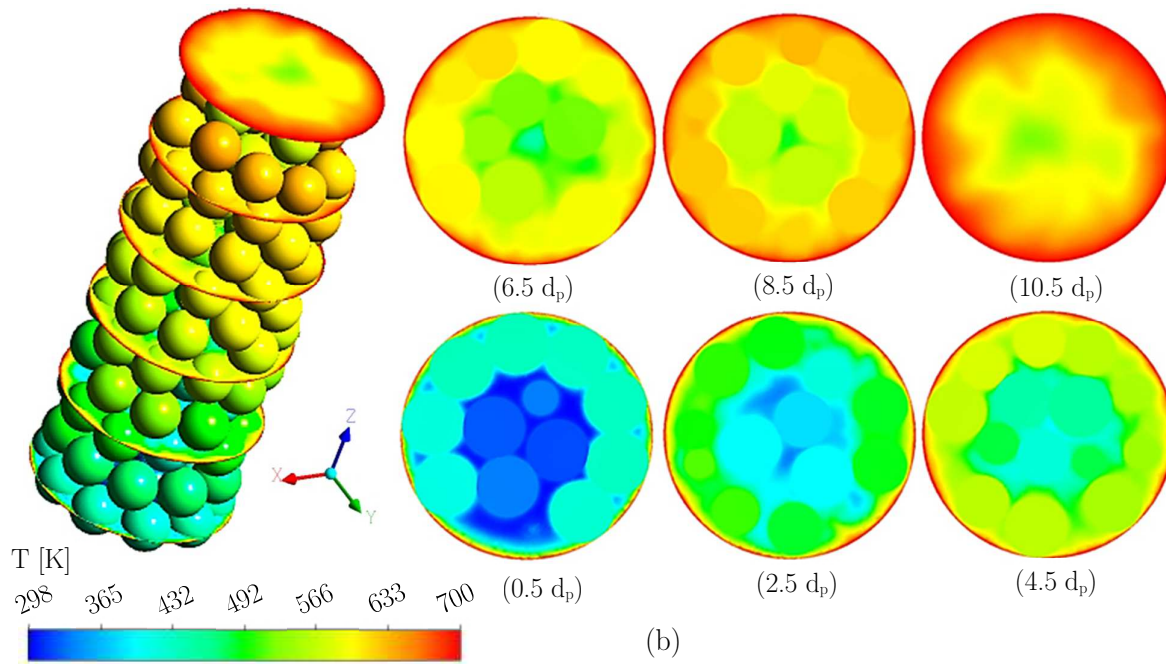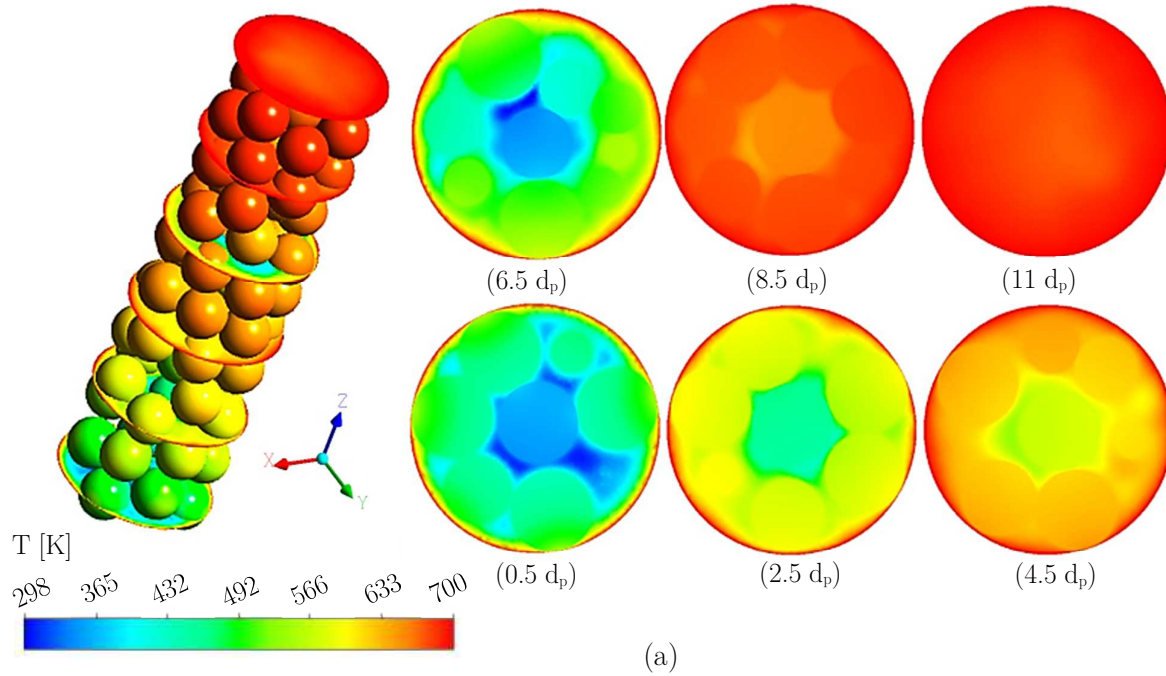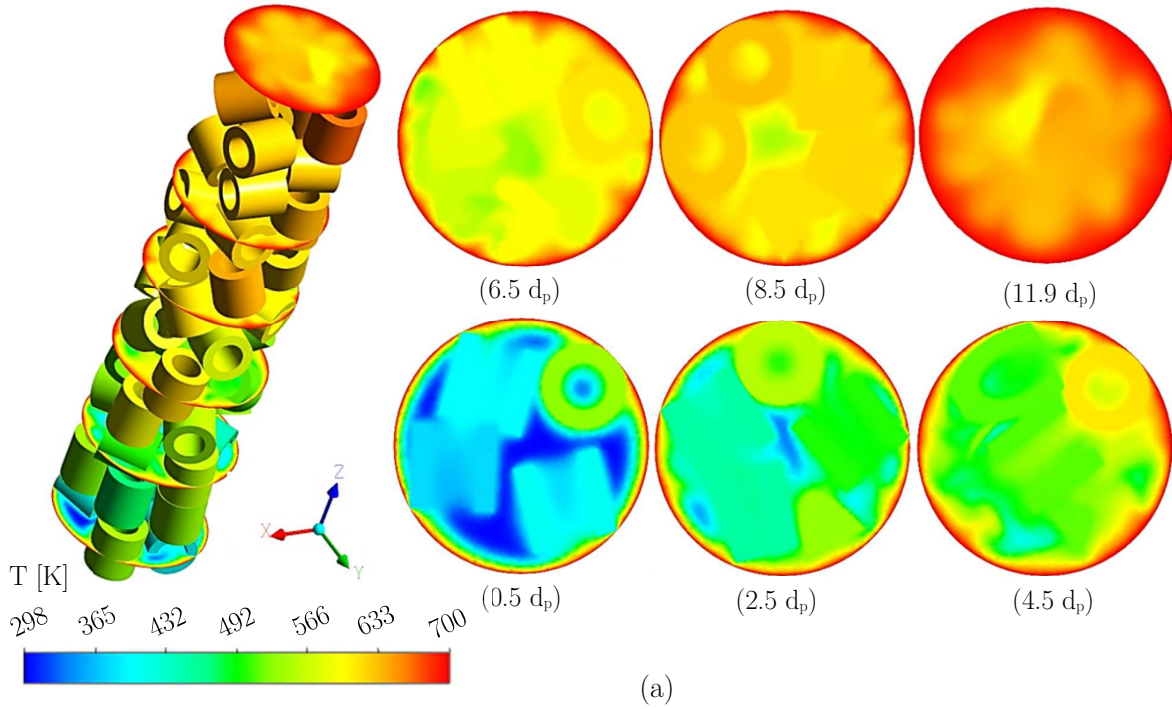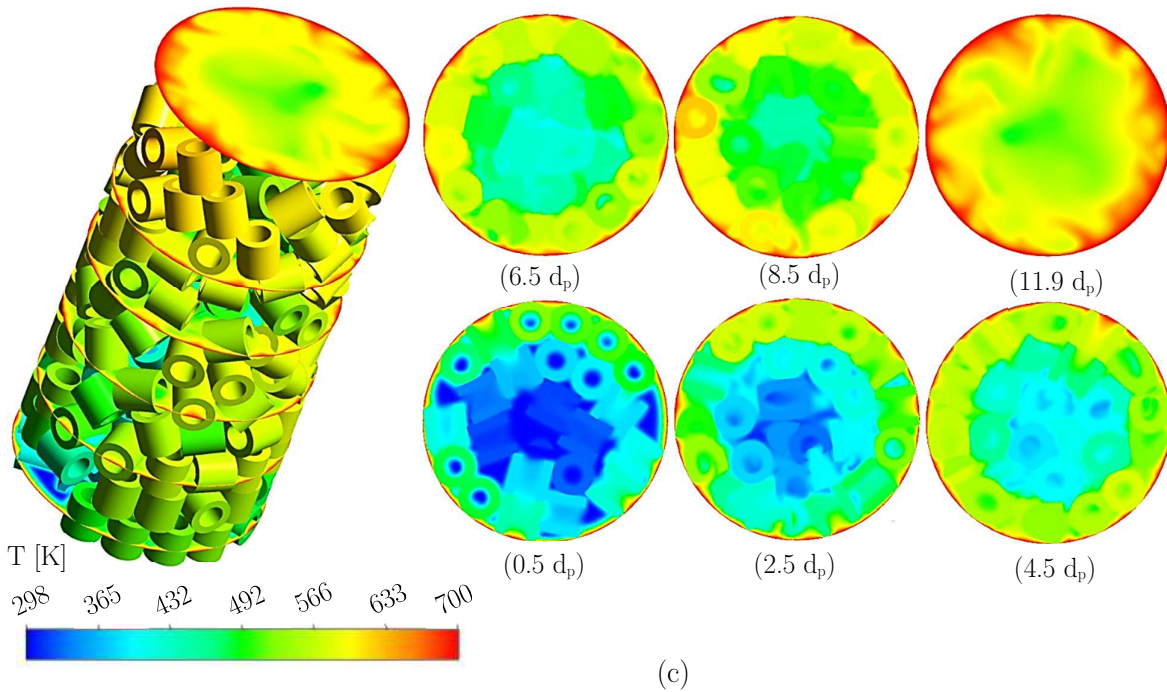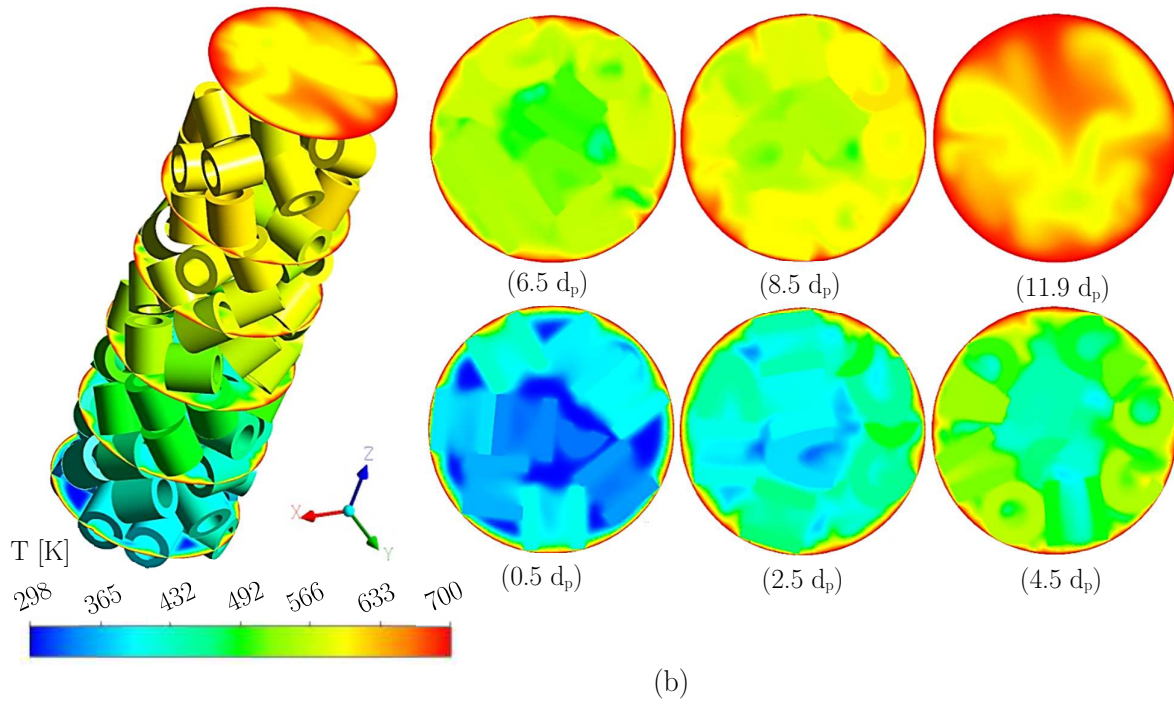Fig. 5.8 Contour plots of temperature field on the surface of pellets and at different cross sections at axial positions 0.5d$_P$, 2.5d$_P$, 4.5d$_P$, 6.5d$_P$, 8.5d$_P$ and +0.5d$_P$ behind the packing section, for packings of alumina Raschig rings; (a) N = 3.1, (b) N = 4.1 and (c) N = 6.1 at Re$_P$ = 100.

As shown in Figs. 5.7-8, a considerable inhomogeneity in the temperature fields can be observed in wider packing structures as well. This behavior is more pronounced in packed tubes of Raschig rings (see Figs. 5.7c and 5.8c), where the presence of an internal hole in such pellets causes even a much sharper temperature gradient along a typical azimuth at each crosscut. This thermal heterogeneity can be clearly discerned near the wall region, where the sharpest temperature gradients in both fluid and catalyst phases exist. Overall, Figs. 5.6-8 demonstrate a large difference between the fluid and catalyst phases' temperature along the azimuthal direction at each cross section. This implies that azimuthal-averaging of the temperature field in tubular fixed beds can lead to underestimation of the wall-to-bed heat transport in a wall-heated tubular fixed bed reactor. This is shown more quantitatively in Fig. 5.9.
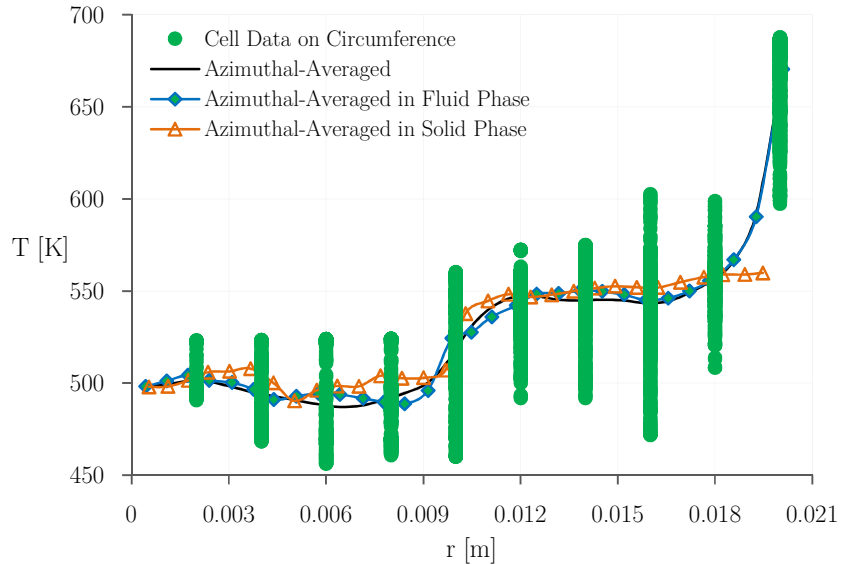
Fig. 5.9 Temperature field data at different azimuthal positions together with the azimuthally-averaged temperature profiles at cross section $z = 6d_p$ for packings of alumina Raschig rings with $N = 4.05$ at $Re_p = 100$.

Fig. 5.9 suggests the maximum deviation between the local and the azimuthally-averaged temperature data is more than 50 K, occurring at a distance of around $0.5d_p$ from the tube wall for this case.

Furthermore, using the contour maps of temperature field, we can shed light on the properties of the thermal boundary layer near the tube wall. A closer look at the wall region in the contour plots of the temperature fields at different cross sections shows that the thermal wall boundary layer is broken by the presence of catalyst pellets in this region, i.e. contacts between tube wall and particles. This observation substantiates that the thermal boundary layer introduced by pseudo-continuum models are rather artificial and do not represent the in-

situ or pellet-scale temperature field data. The same conclusion can be deduced for the velocity boundary layer at the tube wall.

5.2.2. Radial temperature profile

In Fig. 5.10, the azimuthally-averaged dimensionless temperature profile is compared for packings of spheres, cylinders and Raschig rings with $N_{pv} = 3.1$ at packing height $z = 6d_p$ and for different pellet conductivities (corresponding to alumina and glass particles, respectively).
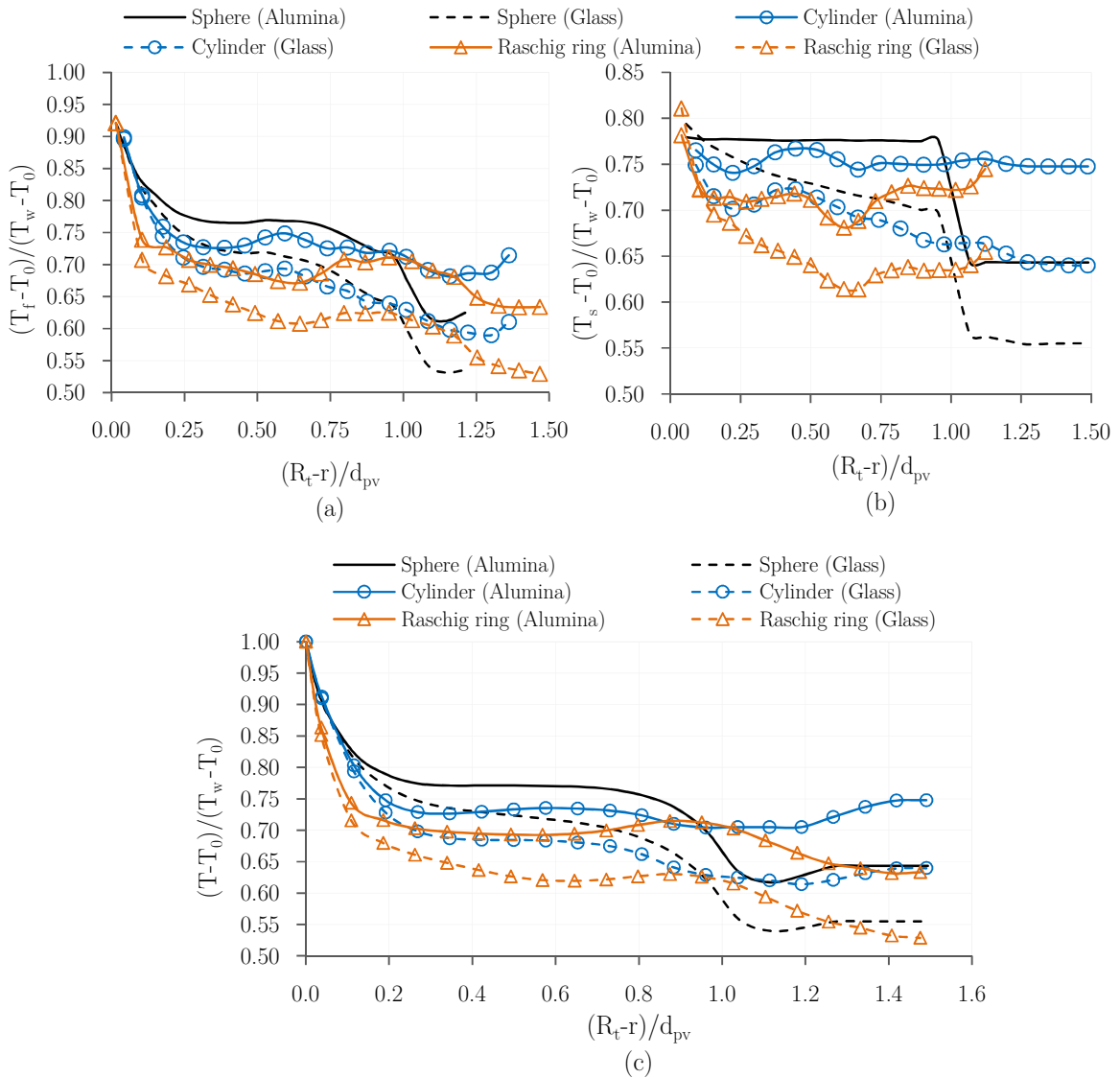
Fig. 5.10 Azimuthally-averaged temperature profile for packings of spheres, cylinders and Raschig rings with $N_{pv} = 3.1$, at the packing depth $z = 6d_p$ for glass and alumina pellets at $Re_p = 100$; (a) azimuthally-averaged fluid phase temperature, (b) azimuthally-averaged pellet phase temperature, (c) azimuthally-averaged temperature of all phases.

Overall, as shown in Fig. 5.10, the temperature profiles in packings of cylinders and Raschig rings are much smoother than for spheres for both fluid and pellet phases, evidencing a more efficient radial heat dispersion in such packing structures. Furthermore, the graphs demonstrate a considerable influence of the exact value of the thermal conductivity of the catalyst pellets on the radial temperature profiles in the individual phases, and accordingly on the azimuthally-averaged temperature profile. This observation, i.e. the influence of thermal conductivity of catalyst phase on the fluid phase bulk temperature, can explain why the correlations proposed by Singhal et al. [10,11] under-predict the fluid/pellet Nusselt number. The authors have neglected the role of solid phase in their heat transfer simulations, where they just set a constant temperature at the surface of pellets as the thermal boundary condition to analyze fluid/solid film heat transfer (characterized by the Nusselt number).

The behavior of the azimuthally-averaged temperature profiles suggests two different thermal regions along the tube radius: first is the near wall region with a thickness of around $0.2d_p$ from the tube wall for low-N packings, where a large temperature gradient exists, and second, the core region in the remaining radius. Such a differentiation is in agreement with experimental observations by Froment and coworkers [12,13] and, more recently, by Dong et al. [14]. It is worth remarking that the sharpest temperature gradient at the wall region occurs within the distance of $0.2d_p$ from the tube wall, where the axial velocity peaks appear (see Figs. 5.4-5). Since the local porosity at the location of axial velocity peaks in the wall region is larger than 0.75, the contribution of the fluid phase temperature is considerable in the azimuthally-averaged temperature profile. This observation can also explain the influence of the wall-channeling phenomenon on the radial temperature profile.

Fig. 5.11. illustrates the 2D (azimuthally-averaged) temperature profiles in the packings of spheres, cylinders and Raschig rings with $N_{pv} = 3.1$ at different cross sections for $Re_p = 100$.

(a)

(b)

(c)
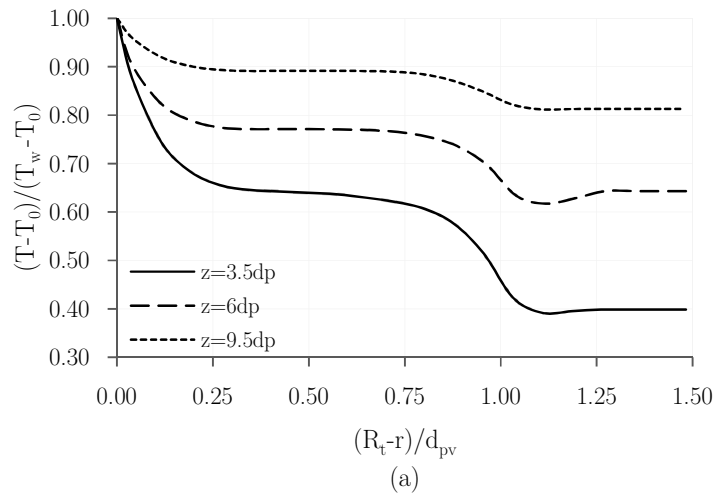
Fig. 5.11 Azimuthally-averaged temperature profiles for packings of alumina pellets with $N_{pv} = 3.1$, at the packing depth $z = 3.5d_p$, $6d_p$ and $9.5d_p$ at $Re_p = 100$; (a) spheres, (b) cylinders, and (c) Raschig rings.

Contrary to the azimuthally-averaged axial velocity profiles, which show local fluctuations along the tube radius at different cross sections (see Fig. 5.4), the azimuthally-averaged temperature profiles show a stable pattern at different cross sections. Furthermore, the temperature profiles in Figs. 5.10-11 demonstrate the presence of a "hump" at a distance of around $0.8d_{pv}$ to $1d_{pv}$ from the tube wall in all packings with $N_{pv} = 3$. This behavior can be explained by the appearance of a very sharp temperature gradient at the surface of the pellets adjacent to the tube wall. The humps appear to be a little smoother in packings of cylinders and Raschig rings. It is worth noting that these features, i.e. the presence of a hump or shoulder in the 2D temperature profile, have been previously addressed by several researchers, e.g. [14–17]. Fig. 5.11 shows that the position of the observed hump does not change along the bed height, although it seems to be smoothened or even disappear as the local temperature in fluid

and the catalyst phases approaches thermal equilibrium conditions. Moreover, our CFD results demonstrate independence of the radial position of the observed humps with changing Re_p (not shown). It is noteworthy that the presence of a low temperature gradient field over a large fraction of the tube radius, say $0.2 < (R_t-r)/d_{pv} < 0.8d_{pv}$, in low-N packings, can explain why the effective radial thermal conductivity, k_{er} is enormously high in narrow-tube fixed bed reactors. Such a region emerges due to the higher contribution of the catalyst phase temperature in the azimuthally-averaged temperature profile, where the thermal gradient is quite low, particularly for alumina pellets (see Fig. 5.10b).

Fig. 5.12 illustrates the azimuthally-averaged temperature profile in packing of spheres, cylinders and Raschig rings with different N at cross section $z = 6d_p$ and $Re_p = 100$.
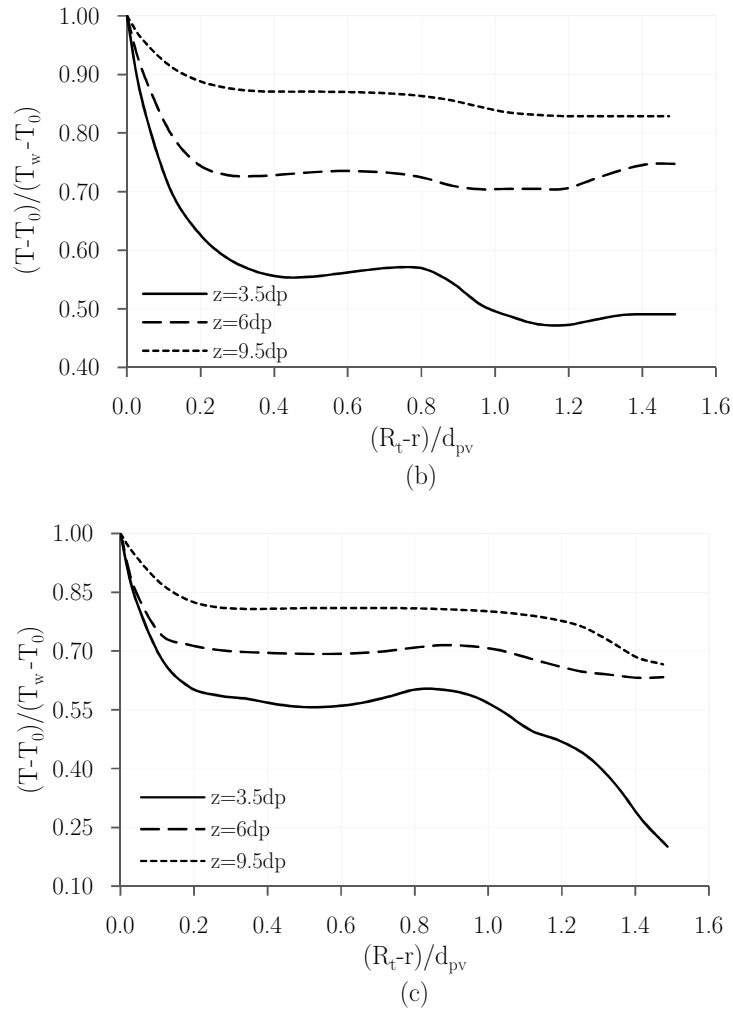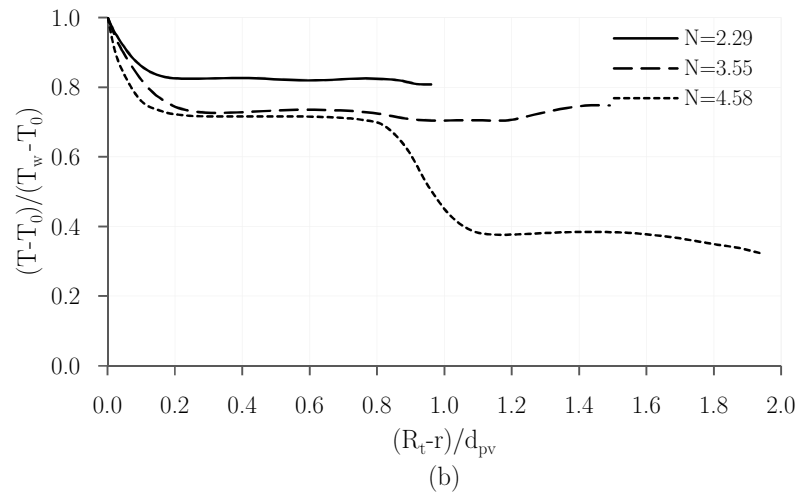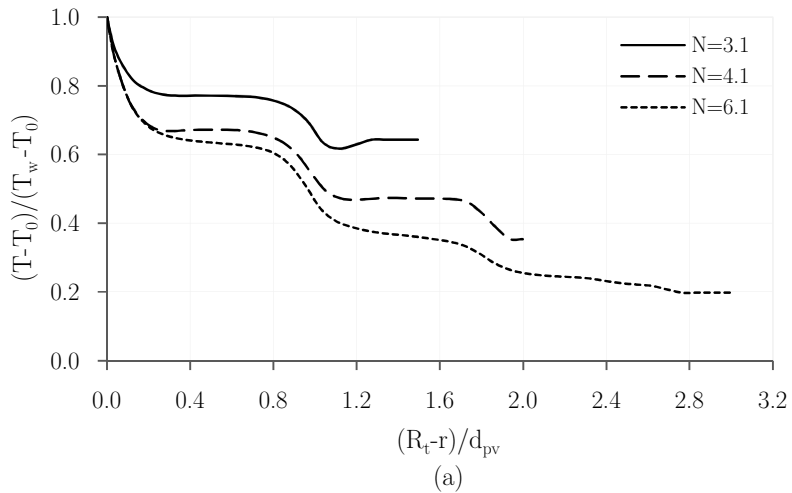

(a)

(b)

(c)
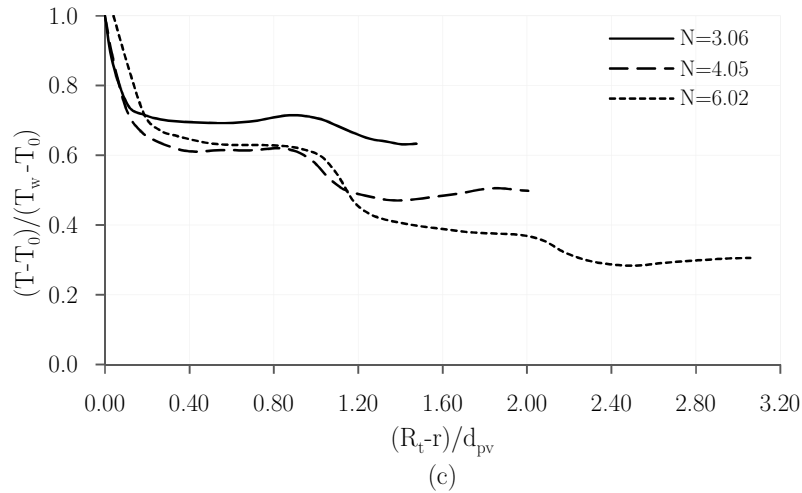
Fig. 5.12 Azimuthal-averaged temperature profiles for packings of alumina pellets with $N_{pv} = 3.1$, at the packing depth $z = 3.5d_p$, $6d_p$ and $9.5d_p$ at $Re_p = 100$; (a) spheres, (b) cylinders, and (c) Raschig rings.

Fig. 5.12 reveals the presence of a second hump in wider beds at a distance of around $1.6d_{pv}$ to $2d_{pv}$ from the tube wall, although it is clearly much smoother than the first hump. It can also be deduced that the presence of a hole at the middle of the packing structures of spheres and cylinders with $N_{pv} = 4$, leads to a poor radial heat transfer compared to the packing of Raschig rings with $N_{pv} = 4.1$. Furthermore, Fig. 5.12 shows much smoother temperature profiles in packings of cylinders and Raschig rings, even for wider tubes.

5.3.   Conclusions

This chapter presented the post-processing results of RBD-CFD simulations in order to obtain characteristics of the fluid flow and wall-to-bed heat transfer in packed beds of different types of non-spherical pellets. The RBD-CFD approach can provide detailed information, which in terms of resolution and precision is not only comparable to the results of advanced experimental techniques, but often very difficult to obtain using methods such as PIV, MRI, 3D CT, etc. This way, the RBD-CFD method can be regarded as a novel design philosophy within the context of "Numerical Experiments", which enables a deep understanding of complex physio-chemical phenomena in fixed bed reactors of non-spherical pellets.

The 3D flow field results reveal a remarkable influence of local structure on the velocity distribution at the pellet scale, where the presence of wall effects, i.e. flow channeling, across the entire tube radius can be clearly observed in the contour plots of the velocity field in narrow tubular fixed beds. These results demonstrate large inhomogeneities in the velocity field, particularly in random packing of cylinders and Raschig rings, where sharp edges in such pellets impose stronger curvatures of the flow streamlines along the packing. It is also shown that

azimuthal averaging of the 3D velocity field along the bed, which has been an advancement in plug flow idealization in classical modelling, cannot reflect the vortex regions (areas with negative axial velocities) inside the structure, and underestimate the local velocity values by more than 400%.

The contour maps of the temperature fields also show substantial inhomogeneities in the temperature distribution along the packing depth, which is attributed to the role of (bed-related) local flow mal-distribution in low-N fixed beds. This inhomogeneity is even more discernable in Raschig ring packings, where the presence of an internal hole in such pellets leads to a sharper temperature gradient along the azimuthal direction. This result suggests inadequacy of the 120^0 wall-segment model proposed by Dixon and coworkers [7,9] for analysis of heat transfer in a full fixed bed. Moreover, the temperature field results also show a remarkable influence of the solid catalyst phase thermal conductivity on the fluid phase local and bulk temperatures. This observation can explain why the correlations proposed by Singhal et al. [10,11] under-predict fluid/film Nusselt number.

The azimuthally averaged temperature field shows deviations of more than 50 K from the local temperature data, at a distance of around $0.5d_p$ from the tube wall for the case studied. Azimuthal averaging of the temperature field reveals the occurrence of humps in the radial profile at a distance of around $0.8d_{pv}$ to $1d_{pv}$ from the tube wall, implying a sharp temperature gradient at the surface of pellets adjacent to the tube wall.

In summary, the observed deviations caused by azimuthal averaging of velocity and thermal fields, particularly in tubular fixed beds of non-spherical pellets, can explain the inadequacy of even modified versions of pseudo-continuum approaches in predicting the radial heat transfer in fixed bed reactors.

Nomenclature

d_p	Pellet diameter	[m]
d_{pv}	Diameter of a sphere of equal volume	[m]
d_t	Tube or bed diameter	[m]
L	Bed length	[m]
N	Tube-to-pellet diameter ratio	[-]
N_{pv}	Tube-to-pellet diameter ratio based on d_{pv}	[-]
R_t	Bed radius	[m]
Re_p	Reynolds number based on d_{pv}: $\rho u_s d_{pv}/\mu$	[-]
T	Temperature	[K]
v_o	Inlet velocity	[m/s]
v_z	Azimuthally-averaged axial velocity	[m/s]
$v_z(r)$	Artificial velocity after Bey and Eigenberger [4]	[m/s]
R	Radial Coordinate	[m]
Z	Axial Coordinate	[m]

Greek Letters

ε	Bulk porosity	[-]
$\varepsilon(r)$	Radial porosity profile	[-]

Bibliography

[1]   G.E. Mueller, Angular void fraction distributions in randomly packed fixed beds of uniformly sized spheres in cylindrical containers, Powder Technology. 77 (1993) 313–319. doi:10.1016/0032-5910(93)85023-3.

[2]   T. Eppinger, K. Seidler, M. Kraume, DEM-CFD simulations of fixed bed reactors with small tube to particle diameter ratios, Chemical Engineering Journal. 166 (2011) 324–331. doi:10.1016/j.cej.2010.10.053.

[3]   M. Behnam, A.G. Dixon, M. Nijemeisland, E.H. Stitt, A New Approach to Fixed Bed Radial Heat Transfer Modeling Using Velocity Fields from Computational Fluid Dynamics Simulations BT - Industrial & Engineering Chemistry Research, Industrial and Engineering Chemistry Research. 52 (2013) 15244–15261. doi:10.1021/ie4000568.

[4]   O. Bey, G. Eigenberger, Fluid flow through catalyst filled tubes, Chemical Engineering Science. 52 (1997) 1365–1376.

[5]   O. Bey, G. Eigenberger, Gas flow and heat transfer through catalyst filled tubes, International Journal of Thermal Sciences. 40 (2001) 152–164. doi:10.1016/S1290-0729(00)01204-7.

[6]   M. Giese, K. Rottschafer, D. Vortmeyer, Measured and modeled superficial flow profiles in packed beds with liquid flow, AIChE J. 44 (1998) 484–490. doi:10.1002/aic.690440225.

[7]   A.G. Dixon, M. Nijemeisland, E.H. Stitt, Packed tubular reactor modeling and catalyst design using computational fluid dynamics, Advance in Chemical Engineering. 31 (2006) 307–389. doi:10.1016/S0065-2377(06)31005-8.

[8]   A.G. Dixon, M. Ertan Taskin, M. Nijemeisland, E.H. Stitt, Wall-to-particle heat transfer in steam reformer tubes: CFD comparison of catalyst particles, Chemical Engineering Science. 63 (2008) 2219–2224. doi:10.1016/j.ces.2008.01.017.

[9]   M.E. Taskin, A.G. Dixon, M. Nijemeisland, E.H. Stitt, CFD Study of the Influence of Catalyst Particle Design on Steam Reforming Reaction Heat Effects in Narrow Packed Tubes, (2008) 5966–5975.

[10]   A. Singhal, S. Cloete, S. Radl, R. Quinta-Ferreira, S. Amini, Heat transfer to a gas from densely packed beds of monodisperse spherical particles, Chemical Engineering Journal. 314 (2017) 27–37. doi:10.1016/j.cej.2016.12.124.

[11]   A. Singhal, S. Cloete, S. Radl, R. Quinta-Ferreira, S. Amini, Heat transfer to a gas from densely packed beds of cylindrical particles, Chemical Engineering Science. 172 (2017) 1–12. doi:10.1016/j.ces.2017.06.003.

[12]   A.P. de Wasch, G.F. Froment, Heat transfer in packed beds, Chemical Engineering Science. 27 (1972) 567–576. doi:10.1016/0009-2509(72)87012-X.

[13]   J.J. Lerou, G.F. Froment, Velocity, temperature and conversion profiles in fixed bed

catalytic reactors, Chemical Engineering Science. 32 (1977) 853–861. doi:10.1016/0009-2509(77)80071-7.

[14]   Y. Dong, B. Sosna, O. Korup, F. Rosowski, R. Horn, B. Sosna, O. Korup, F. Rosowski, R. Horn, Investigation of radial heat transfer in a fixed-bed reactor: CFD simulations and profile measurements, Chemical Engineering Journal. 317 (2017) 204–214. doi:10.1016/j.cej.2017.02.063.

[15]   F. Froment, J. Lerou, Short Communication- Estimation of heat transfer parameters in packed beds from radial temperature profiles, Chemical Engineering Journal. 15 (1978) 233–237.

[16]   M.G. Freiwald, W.R. Paterson, Accuracy of model predictions and reliability of experimental data for heat transfer in packed beds, Chemical Engineering Science. 47 (1992) 1545–1560. doi:10.1016/0009-2509(92)85003-T.

[17]   P. Magnico, Pore-scale simulations of unsteady flow and heat transfer in tubular fixed beds, AIChE Journal. 55 (2009) 849–867.

Chapter 6

Evaluation of Effective Heat Transfer Parameters in Tubular Fixed Beds of Non-Spherical Pellets

Abstract

Chapter 5 showed the inadequacy of azimuthal averaging of the thermal fields in tubular fixed bed reactors. Still, from a point of view of design and control, it is very desirable to have simple pseudo-homogenous models available for such reactors. In this chapter, we perform numerical experiments to elucidate the effective heat transfer parameters introduced in classical k_{er}-h_w pseudo-homogenous model. The results demonstrate that the reactor length-dependency of the values of k_{er} and h_w is basically inherent in such effective thermal parameters and originates from the evolutionary trend of the thermal equilibrium in fluid and catalyst phases along the bed length. Furthermore, we show that the procedures suggested in the review paper by Dixon (2012) do not solve the length-effect problem. We conducted a detailed sensitivity analysis of the influences of the pellet shape and thermal conductivity, as well as tube-to-pellet diameter ratio, on the effective heat transfer parameters. The results provide an intuitive picture of the contributions of the different transport mechanisms to the effective thermal properties. The most promising literature correlations for Pe_{er} and Nu_w are examined to predict the radial temperature profile using the k_{er} - h_w pseudo-homogenous model and then compared with the azimuthally-averaged temperature data obtained from RBD-CFD simulation results for random packing of spheres with $N = 6.1$. It is concluded that the models of Specchia/Baldi/Gianetto/Sicardi for all flow regimes and of Martin/Nilles for the turbulent regime can be recommended for practical use for spherical particles. The results of this chapter suggest that the RBD-CFD methodology can be used as a tool to tune simplistic pseudo continuum models to improve their reliability.

6.1.   Introduction

The prediction of wall-to-bed heat transfer rate in fixed bed reactors is a topic of continuing interest for reactor design [1–11]. Of particular concern is the case of low-N tubular fixed bed reactors due to their inherent advantage of enhanced wall-to-bed heat transport, which is essential for handling highly exothermic and endothermic reactions. Despite the intrinsic inadequacies connected with pseudo-continuum models with respect to the prediction of radial heat transfer, there is a continued interest in the use of classical pseudo-homogenous k_{er}-h_w models (see e.g. [12–15]). Such models are suitable for fast and repetitive computations for selected features of the 2D (axial-radial) temperature field, allowing for fast design, optimization, and control of such reactors. Nonetheless, our results in Chapter 5 demonstrated how azimuthal-averaging of the temperature field leads to noticeable deviations from local temperature data, particularly in low-N tubular fixed beds with non-spherical pellets, where the influence of local structure on both the velocity and temperature fields is substantial. Similar remarks are made in relatively recent review papers (e.g. [9,16]). Our review of the problem of radial heat transfer in Chapter 2 showed a large disagreement between the predicted values and literature correlations for the effective radial Peclet number, Pe_{er}, and the apparent

wall Nusselt number, Nu_w, versus particle Reynolds number, Re_p. The reasons for such discrepancies can be sought in experimental errors, e.g. insulation problem, and in the neglect of essential features such as the role of tube-to-pellet diameter ratio, shape and thermal conductivity of pellets that can strongly affect the local transport processes.

Another major problem associated with the evaluation of effective heat transfer parameters Pe_{er} and Nu_w is their dependence on the bed height. Several research groups have noticed that using a 2D-PF heat transfer model as the fitting model, both k_{er} and h_w evaluated from the temperature profiles show a bed length dependency. Paterson and Carberry [1] demonstrated that the disagreement between observed and computed hot spots may be attributed to either neglecting the axial heat dispersion term in the modeling or to the use of length-dependent parameters in the descriptive heat transfer models. In fact, the authors suggested the use of a 2D-ADPF model instead of a 2D-PF model to overcome length dependency problem. Earlier researches, e.g. by Gunn and Khalid [17] and Dixon et al. [18], have shown that when the 2D-ADPF model with three parameters, i.e. k_{ea}, k_{er} and h_w, is fitted to the thermal data for different bed lengths, the results do not reveal any length dependency. However, the values of k_{ea} were poorly overestimated, being larger than any realistic values by an order of magnitude. This observation has resulted in a debate about the use of k_{ea} as one of the three fitted parameters in the 2D-ADPF model [1,19]. Following these studies, Dixon [20] investigated the influence of bed length on the effective parameters using several heat transfer experiments. The author confirmed that k_{er} and h_w decrease to asymptotic values along the bed depth even when the 2D-ADPF model with a fixed predefined k_{ea} is used as a fitting model. The Author also claimed that this observation stems from experimental errors, and thus presented some recommendations for heat transfer experiments to overcome the length effects. He noticed that the heat conduction along the length of the tube wall from the heated test section to the unheated calming section leads to preheating of the inlet gas (see Fig. 6.1) and therefore a radially varying temperature profile at the bed inlet instead of a constant temperature, thereby leading to the so-called "length effect" in k_{er} and h_w.

Similar conclusions were also reached by Freiwald and Paterson [21] and Borkink and Westerterp [22]. They found that the length dependence effect could be eliminated by using the 2D-ADPF model instead of the 2D-PF model, provided that the heat loss from the calming

section and thermocouple cross are either effectively avoided or taken into account in the modelling by improving the inlet temperature boundary condition.
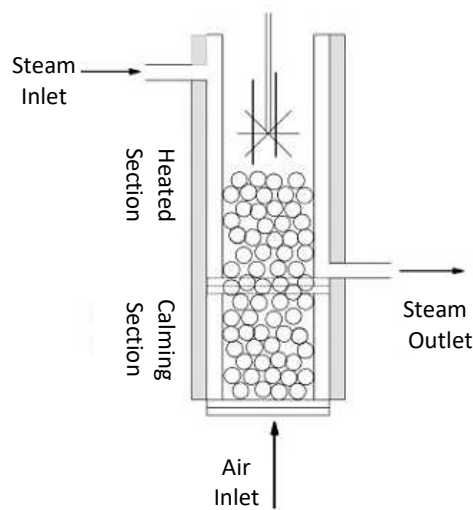
Fig. 6.1 Schematic of a generic laboratory heat transfer experiment for steam heating of a flowing gas through a bed of particles, with radial temperature measurement by a thermocouple cross (Dixon [23]).

Nonetheless, Wen and Ding [24] and Liu et al. [25] have demonstrated the appearance of a reactor length dependency on the effective transport parameters, although they have pursued the procedures suggested by Dixon [20] and Freiwald and Paterson [21] to reduce experimental sources of error. The first authors claimed that, based on the analogy to an empty tube, this phenomenon might be caused by an entrance length, over which the flow and temperature profiles become fully-developed. Furthermore, the authors noted that the configurations used in their experimental setup is more realistic in terms of industrial applications, where there is no calming section to obtain an artificially fully developed velocity field.

In essence, the reactor length dependency, in addition to the observed dichotomy in literature correlations for the effective parameters, have led to ambiguities which are not very helpful to designers of fixed bed reactors in selecting appropriate predictive correlations. This situation effectively forces designers to seek validation of their design calculations through supplementary experimental studies, thereby imposing large additional expenses to a project. However, using the concept of Numerical Experiments introduced and elaborated in Chapters 4 and 5, in this chapter we will shed some light on the prevailing ambiguities associated with the effective heat transfer parameters introduced by the classical pseudo-homogenous k_{er}-h_w model. The RBD-CFD methodology is able to provide a deeper insight into such "lumped" transport properties because it can methodically address the roles of flow regime (typified by

Re_p), tube-to-pellet ratio N, bed length, pellet shape, and pellet material (typified by thermal conductivity).

6.2. Parameter estimation problem

Parameter estimation is a key problem in the development of process models, and thus an important issue in both process design and control. In fact, parameter estimation plays a critical role in accurate description of the behavior of complex systems through mathematical models such as statistical probability distribution functions, parametric dynamic models, etc.

Fundamentally, using pseudo-homogenous models such as the 2D-PF or 2D-ADPF heat transfer models, we translate the transport processes taking place in a 3D two-phase gas-solid system into a 2D one-homogenous phase system. This requires "effective" parameters that reflect the underlying transport mechanisms occurring in a real two-phase system. These parameters are obtained by resorting to the inverse problem using pseudo-homogeneous heat transfer models to predict observed (and suitably averaged) temperature field data. In essence, the objective of an inverse problem is to find the best model, Ω, such that $E \approx O(\Omega)$, where O is an operator representing the governing equations that relate the model parameters with the observed data, E.

In this study, a 2D-ADPF model, Eq. (6.1), is considered as the fitting model and the temperature fields obtained from RBD-CFD results of heat transfer, i.e. numerical experiments, form the observed data. The objective of our analysis is to compute the effective radial thermal conductivity, k_{er}, and apparent wall heat transfer coefficient, h_w, for an entire fixed bed of a certain length, using an optimization process so that the best fit between the model results and observed RBD-CFD data is achieved. The 2D-ADPF heat transfer model is presented in the following dimensionless form:

$$\frac{\partial \theta}{\partial \zeta} = \frac{1}{Pe_{er}} \left(\frac{2}{N} \right) \left(\frac{\partial^2 \theta}{\partial \omega^2} + \frac{1}{\omega} \frac{\partial \theta}{\partial \omega} \right) + \frac{1}{Pe_{ea}} \left(\frac{2}{N} \right) \left(\frac{\partial^2 \theta}{\partial \zeta^2} \right) \tag{6.1}$$

with the following boundary conditions:

$$\text{for } \zeta = 0 \quad \rightarrow \quad \theta = 1 \tag{6.2}$$

$$\text{for } \omega = 0 \quad \rightarrow \quad \frac{\partial \theta}{\partial \omega} = 0 \tag{6.3}$$

$$\text{for } \omega = 1 \quad \rightarrow \quad \frac{\partial \theta}{\partial \omega} + Bi\theta = \begin{cases} Bi & (\zeta > 0) \\ 0 & (\zeta < 0) \end{cases} \tag{6.4}$$

Here $\zeta = z/R_t$ is the dimensionless axial position and $\omega = r/R_t$ the dimensionless radial position, non-dimensionalized by the tube radius R_t, and $\theta = (T_w - T)/(T_w - T_0)$ is the

dimensionless temperature, non-dimensionalized by the difference between wall and inlet gas temperatures T_w and T_0. The radial and axial heat dispersion is characterized by the effective radial and axial Peclet numbers $Pe_{er} = Gc_p d_{pv}/k_{er}$ and $Pe_{ea} = Gc_p d_{pv}/k_{ea}$, with $G = \rho v$ the mass flux. The wall-to-bed heat transfer is characterized by the Biot number $Bi = h_w R_t/k_{er}$. As explained in Chapter 2, this one-phase model describes the overall heat transfer resistance by an effective radial thermal conductivity, k_{er}, lumping together all heat transfer mechanisms in the radial direction, and an apparent wall heat transfer coefficient, h_w, which is postulated to account for the temperature jump near the wall region. The 2D-ADPF heat transfer model has an analytical solution in terms of an infinite series of Bessel functions, which can be obtained using the Fourier method. Several researchers report the analytical solution of this model, e.g. [17,26], which can be represented in the following dimensionless form:

$$\frac{T_w - T(\zeta,\omega)}{T_w - T_0} = \theta(\zeta,\omega) = 2\sum_{i=1}^{\infty} \frac{J_0(\lambda_i\omega)\exp(-\lambda_i^2\gamma)}{\lambda_i\left[1 + (\lambda_i/Bi)^2\right]J_1(\lambda_i)} \tag{6.5}$$

where

$$\gamma = \frac{4\zeta\dfrac{1}{Pe_{er}}\dfrac{1}{N}}{1 + \sqrt{1 + 16\lambda_i^2\dfrac{1}{Pe_{er}}\dfrac{1}{Pe_{ea}}\dfrac{1}{N}}} \tag{6.6}$$

and the eigenvalues λ_i are the roots of the characteristic equation:

$$\lambda_i J_1(\lambda_i) - Bi J_0(\lambda_i) = 0 \tag{6.7}$$

To examine if the procedures proposed by Dixon [20,23] and Borkink and Westerterp [22,27,28] are able to resolve the problem of length-dependency, the inlet gas temperature that is needed to make a dimensionless temperature profile is computed based on two methods: (i) the mass weighted-average of temperature at the bed inlet, which is calculated by Eq. (6.8), and (ii) the azimuthally-averaged radial temperature profile at the bed inlet, i.e. $T_0(\omega)$.

$$\overline{T}_0 = \frac{\int T\rho\left|v.dA\right|}{\int \rho\left|v.dA\right|} = \frac{\sum_{i=1}^{n} T_i\rho_i\left|v_i.dA_i\right|}{\sum_{i=1}^{n} \rho_i\left|v_i.dA_i\right|} \tag{6.8}$$

The observed data to be employed in our parameter estimation problem includes the azimuthally-averaged temperature profile obtained from the RBD-CFD simulations for all case studies presented in Chapter 4 (Table 4.1). This allows access to an extensive data pool of temperature fields in packing structures of spheres, cylinders and Raschig rings with different tube-to-pellet ratios N, and for a wide range of particle Reynolds numbers, $5 \leq Re_p \leq 3000$. Furthermore, to investigate the influence of bed length on k_{er} and h_w, azimuthally-averaged temperature data at different bed cross sections $z = 1d_p$, $3d_p$, $5d_p$, $7dv$, $9d_p$, $10d_p$ to $11d_p$

(representing the end of the packing section) and $+2d_p$ behind the packing section are utilized to solve the parameter estimation problem. This way the temperature field data at different cross sections can be translated into 2D radial temperature profiles, which can be compared with the pattern predicted by Eqs. (6.5-7). It is important to note that in our optimization procedure we do not aim to determine local effective parameters. Rather, for each specific cross-section we aim to determine the set of global (volume-averaged) effective parameters which, when applied to the entire volume from the entrance of the fixed bed to that specific cross section, yields the same azimuthally-averaged (radial) temperature profile as in the RBD-CFD simulations. Fig. 6.2 illustrates a general schematic of our procedure to obtain an azimuthally-averaged temperature profile from the CFD results.

Before proceeding to the solution, it is essential to deliberate on the role of the axial Peclet number, Pe_{ea}. Wakao et al. [29] demonstrated that the influence of Pe_{ea} on the minimum error obtained from their model optimization is negligible. Note that this explains why it is possible that some literature values for k_{ea} are larger than any realistic value by an order of magnitude. Overall, there are no severe comments found in the literature that address any shortcomings or discrepancies on the published correlations for the axial heat transfer Peclet number. Therefore, in this work, Pe_{ea} is kept constant and computed from the empirical correlation proposed by Dixon and Cresswell [30], assuming $Pe_{af(\infty)} = 2$, and using the correlation presented by Zehner and Schlünder [31] for the effective solid conductivity.

$$\frac{1}{Pe_{ea}} = \frac{1}{Pe_{af(\infty)}} + \frac{k_{as}}{k_f} \frac{1}{Re_p \, Pr} \tag{6.9}$$

Where

$$\frac{k_{as}}{k_f} = 1 - \sqrt{1-\varepsilon} + \frac{2\sqrt{1-\varepsilon}}{(1-\frac{k_f B}{k_p})} \left[\frac{(1-\frac{k_f}{k_p})B}{(1-\frac{k_f B}{k_p})^2} \ln\left(\frac{k_p}{k_f B}\right) - \frac{B+1}{2} - \frac{B-1}{(1-\frac{k_f B}{k_p})} \right] \tag{6.10}$$

with $\quad B = C\left(\frac{1-\varepsilon}{\varepsilon}\right)^{10/9}$

and C is 1.25, 2.5, $2.5(1+(d_i/d_o)^2)$ and 1.4 for spheres, solid cylinders, and hollow cylinder, respectively. In Eq. (6.9), Pr is the Prandtl number defined as $\mu c_p/k_f$.
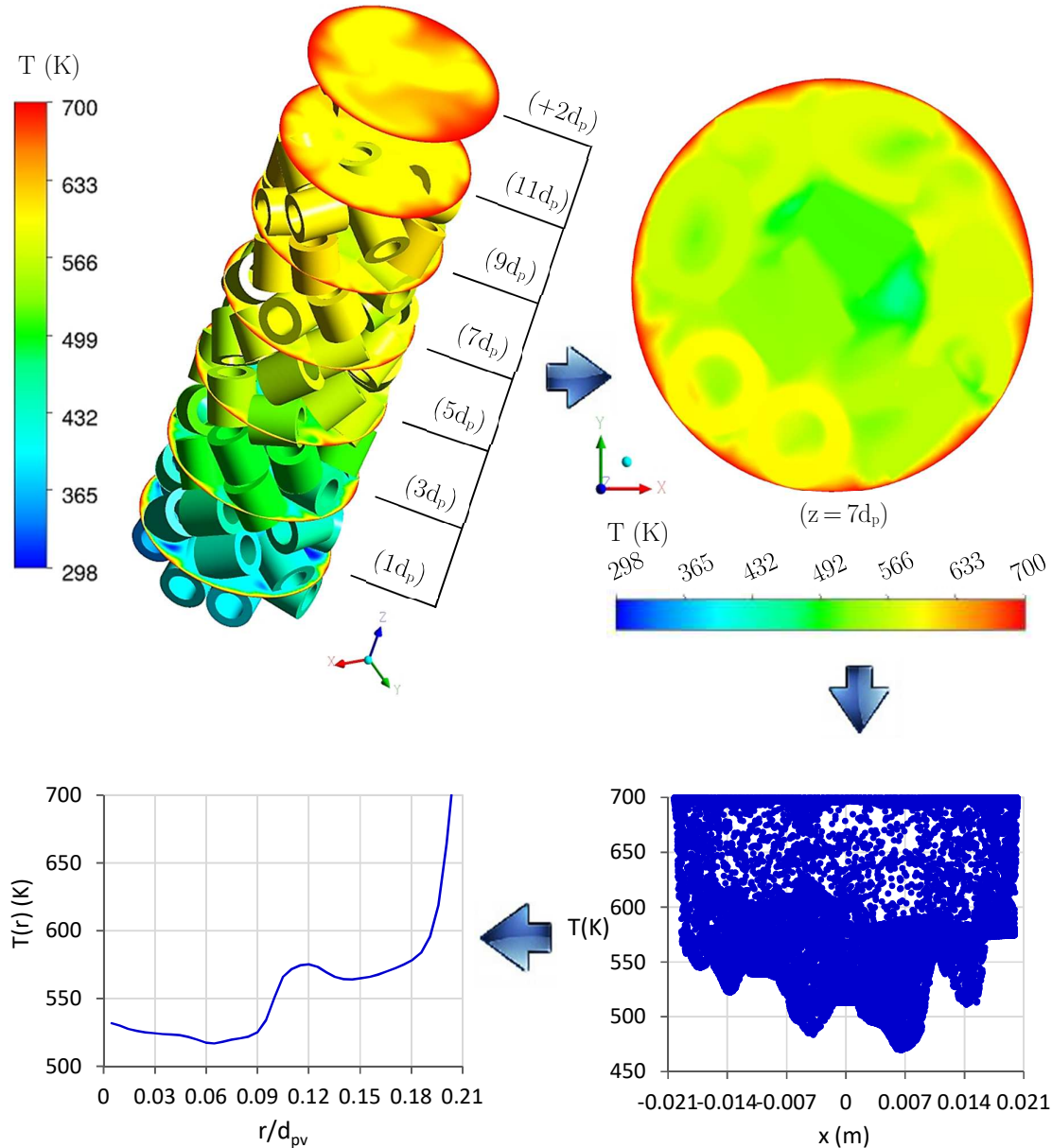
Fig. 6.2 General sequence pursued to obtain azimuthally-averaged temperature distribution at different cross sections for random packings of alumina Raschig rings with N = 4.05 at $Re_p = 100$. In this example, we focus on the cross section at axial position $z = 7d_p$. Bottom right: individual temperature measurements as a function of x-coordinate. Bottom left: azimuthally averaged radial temperature profile.

6.2.1.   Multi-variable optimization method

Accurate solution of a multi-variable parameter estimation problem necessitates a robust and rigorous optimization method, which allows computing the most dependable parameters, resulting in the best achievable fit between predictions and measurements. In this work, a nonlinear least squares (NLLS) method is applied to compute Pe_{er} and Bi. The approach uses

an initial guess for the effective parameters, whereby the radial temperature profile is predicted using Eqs. (6.1-10) at locations corresponding to the measurements, i.e. at a specific cross section where the azimuthal-averaged temperature data is obtained, and a sum of squares of the differences is accordingly formed. The parameters are then altered using a multi-variable optimization approach to minimize the sum of squares of the differences, giving the best-fit parameter estimates. The objective function in this optimization problem is therefore an error function, which is the root of the mean square error between the predictions and measurements.

$$\text{Error} = \left[\frac{1}{n} \sum (T_{Pre} - T_{CFD})^2 \right]^{1/2} \qquad (6.11)$$

where T_{Pre} and T_{CFD} are the predicted and measured temperatures, respectively, and n is the total number of points of comparison at the specified cross section. The variation of different effective parameters will result in an error map in which the minimum can be located, and the effective parameters corresponding to the minimum error represent the best that predict the measured temperatures, i.e. azimuthally-averaged temperature profile obtained from the CFD results. To obtain the global minimum, a robust optimization function, FMINCON, available in Matlab software is used, which enables us to compute a constrained minimum of a scalar function of several variables starting at an initial guess. A detailed description as well as the background of this nonlinear optimization function can be found in standard references [32–34]. It mentions that such an optimization routine is adopted because, first, our problem includes functions with strong nonlinear dependencies on the variables, and secondly, both of the P_{er} and Bi conceptually possess a limited range of values, enabling the optimization solver to narrow down the search regions, and accordingly reduce the computational expenses.

Appendix C supplies the Matlab M-file code for solving our two-parameter estimation problem. The code uses the empirical correlations proposed by Melanson and Dixon [35] and Dixon et al. [18] to make a reasonable initial guess for Pe_{er} and Bi, respectively. Despite the observed scattering of the predicted values of Pe_{er} and Nu_w versus Re_p based on different literature correlations (as discussed in Chapter 2), these parameters appear to vary within certain ranges. To this end, we assume the values of Pe_{er} and $Bi(d_p/R_t)$ should be within the ranges [0.1-15] and [1-10], respectively. Furthermore, the physical properties of air are calculated at the average temperature at a specific cross section. To ensure that the computed values by the FMINCON function addresses the global minimum of our objective function, we also examined another nonlinear least-squares solver programmed in Matlab, LSQNONLIN, which solves nonlinear least-squares cure fitting problems. The background of this algorithm is elaborated in Coleman et al. [32].

6.3. Results and discussion

The optimization code was run for 168 case studies, including the packing structures of spheres, cylinders and Raschig rings with different N to investigate the effect of bed length on the effective 2D-ADPF heat transfer model parameters, i.e. k_{er} and h_w. The analysis of the results allows us to shed light on the influences of pellets of different shapes and thermal conductivities and also different tube-to-pellet diameter ratios on the effective heat transfer parameters.

6.3.1. Verification study

To assure that the FMINCON optimization results reflect the global minimum of the objective function, we have first compared its prediction with LSQNONLIN. The computed values of Pe_{er} and Bi based on the both solvers are very comparable: the difference is of the order of the third decimal digit. Furthermore, to measure the accuracy of the optimization results, the observed temperature data, i.e. azimuthally-averaged temperature profiles obtained from the RBD-CFD heat transfer results, are compared with the radial temperature profiles predicted by the 2D-ADPF heat transfer model, based on the optimum values of Pe_{er} and Bi in Fig. 6.3. The Figure shows the comparison at different bed cross sections in random packings of alumina Raschig rings with N = 4.05 and 6.02 at Re_p = 100. The good agreement between the azimuthally-averaged temperature profiles and the radial temperature profiles predicted by 2D-ADPF at different bed cross sections substantiate the reliability of the optimization results. At the same time, it is also evident that the pseudo-continuum 2D-ADPF model cannot predict the presence of the observed hump in the temperature profile. This can be ascribed to the simplifying assumptions, i.e. plug flow idealization (implying neglect of granularity on the pellet scale) and thermal equilibrium between catalyst and fluid phases.
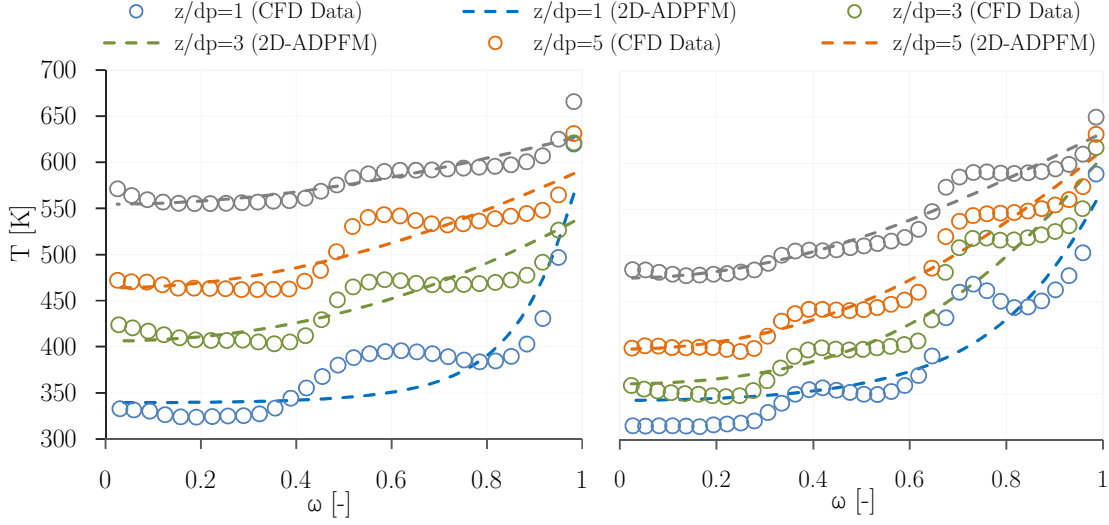
Fig. 6.3 Comparison between the azimuthally-averaged temperature profiles obtained from RBD-CFD results and the radial temperature profile predicted by the 2D-ADPF heat transfer model at cross sections $z = 1d_p$, $3d_p$, $5d_p$ and $9d_p$ in random packings of alumina Raschig rings with (a) $N = 4.05$ and (b) 6.02, at $Re_p = 100$.

Furthermore, the results demonstrate that when the two phases approach thermal equilibrium, as can be realized at $z = 9d_p$, a better prediction of the radial temperature profile is possible by the 2D-ADPF model. Nevertheless, we remind the reader of the inadequacy of a 2D radial temperature profile for estimating the wall-to-bed heat transfer rate, caused by the granularity of the flow field as was discussed in Chapter 5 (Fig. 5.9).

6.3.2. Influence of the inlet temperature profile

Here we explore whether the suggestion by Dixon [23] and Borkink and Westerterp [22,27,28], i.e. to use a radially dependent inlet temperature profile $T_0(\omega)$ in Eqs. (6.1-7) instead of a flat inlet temperature profile, can explain the reactor length effect. To this end, we performed several optimization runs using both a mass-weighted average (flat profile) inlet temperature and radially dependent inlet temperature $T_0(\omega)$ for a case study including random packing of alumina spheres with $N = 3.1$ at $Re_p = 10,100$ and 1000. Here, for the sake of brevity, only the results at $Re_p = 100$ are presented in Fig. 6.4, where the computed values of Pe_{er} are compared and benchmarked against the predictive correlation by Melanson and Dixon [35].

Fig. 6.4 Comparison between computed Pe_{er} based on different inlet temperature profiles for random packing of alumina sphere with $N = 3.1$ at $Re_p = 100$.

As shown in Fig. 6.4, no matter by which method, i.e. mass-weighted average or radially-varying profile, the inlet temperature in the 2D-ADPF model is introduced, the results still show the length dependency of Pe_{er}. Furth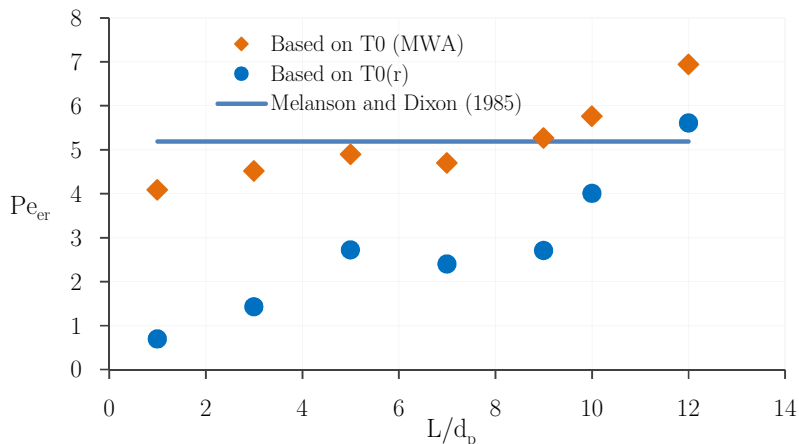ermore, applying $T_0(\omega)$ leads to an underestimation of Pe_{er} by around 200% compared to the predicted values by the Melanson-Dixon correlation. Similar results have been found for Bi and also for both Pe_{er} and Bi at $Re_p = 1000$. This means that the length-dependency of the effective heat transfer parameters cannot be explained or circumvented by using $T_0(\omega)$ instead of a flat temperature profile, and conceptually does not stem from experimental errors per se. It is worth remarking that the predicted values of Pe_{er} and Bi at $Re_p = 10$ are the same between the two approaches, which is explained by the fact that the radially dependent temperature profile approaches a flat profile as $Re_p \rightarrow 0$.

6.3.3. The influence of pellet shape and tube-to-pellet size ratio

The behavior of the volume-averaged k_{er} and h_w as a function of bed length is elucidated in Figs. 6.5-6, respectively, for all packing structures at three values of Re_p, representative for laminar, transient and turbulent flow regimes. Overall, the graphs demonstrate that the computed values of k_{er} and h_w vary with bed length, and this length-dependent behavior does not pertain to pellets shapes, thermal conductivity (see Fig. 6.9-10 for the role of thermal conductivity) and tube-to-pellet diameter ratio. The length-dependency is observed, despite the fact that the observed data has been obtained from our RBD-CFD simulations, thereby completely avoiding the prevailing shortcomings connected to conventional experimental analysis, i.e. heat leaks into calming sections as well as heat losses from thermometers, as addressed by Dixon [20]. This result again demonstrates that the procedures suggested by Dixon [20,23] and Borkink and Westerterp [22,27,28] cannot unravel and solve the problem of the bed length-effect.

As shown in Fig. 6.5, the graphs exhibit different patterns concerning the behavior of k_{er} versus the length of packing section. In the laminar flow regime, k_{er} shows a decreasing trend as a function of bed length progression, and eventually approaches an asymptotic value (see Fig. 6.5 for plots at $Re_p = 10$ as a representative of laminar flow regime). Similar trends have been found for all cases at $Re_p < 100$. This result is in agreement with the observations by De Wasch and Froment [36], Gunn and Khalid [17], Dixon et al. [18] and Dixon [20]. In the transient flow regime, which is expected to occur at Re_p in the range of 100 or 200 to 600 (although it seemingly depends on N), the behavior of k_{er} as a function of bed length does not reach a discernable trend (see Fig. 6.5 for plots at $Re_p = 100$ as a representative of the transient regime). This behavior can be attributed to the formation of local vortices, which partially emerge along the packing section, resulting in scattering of the k_{er} data with an untraceable trend. For Re_p higher than 600, i.e. in the fully turbulent regime, k_{er} is shown to increase to an asymptotic value as the bed length increases (see Fig. 6.5 for plots at $Re_p = 1000$ as a representative of the turbulent regime).
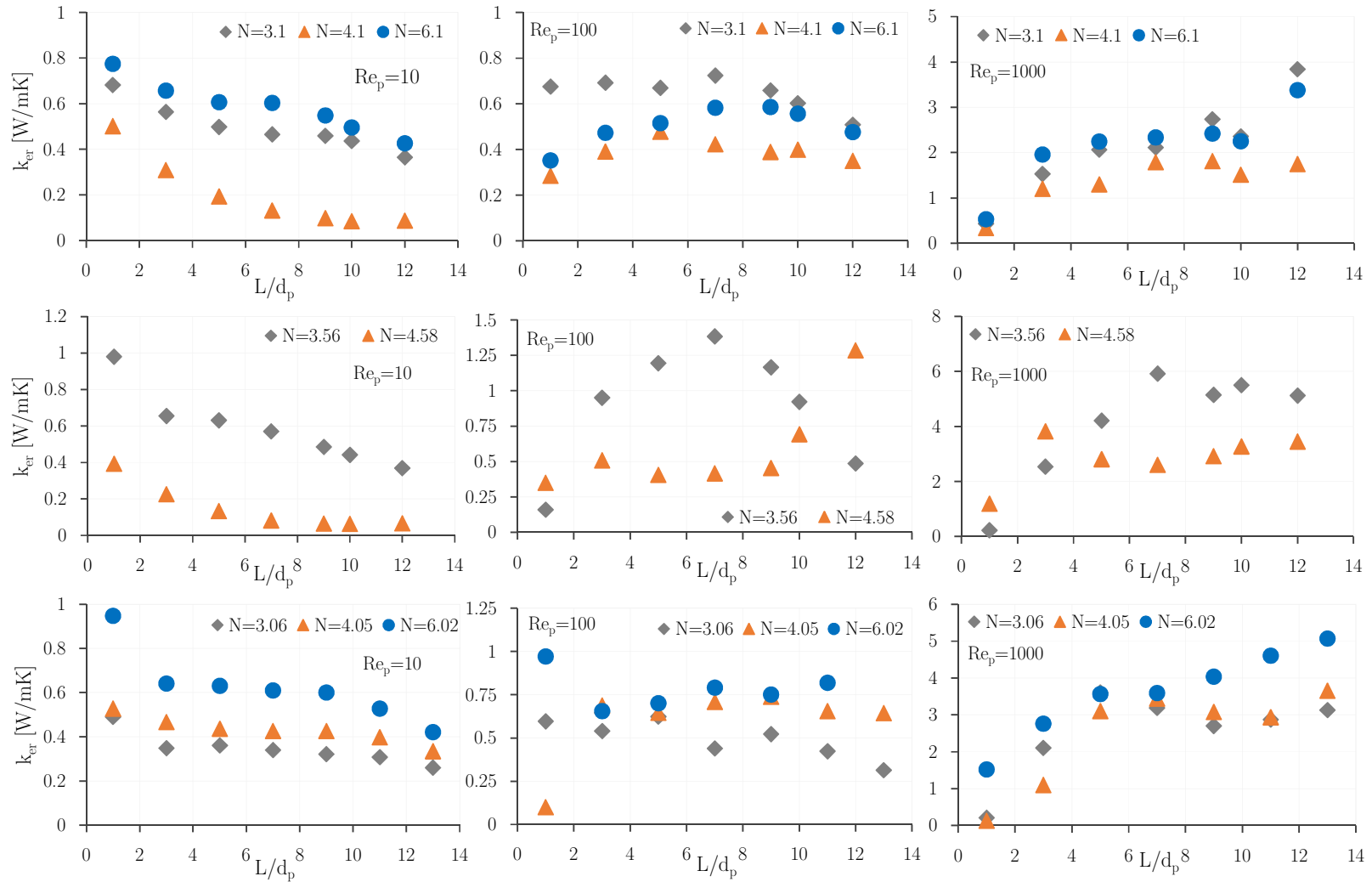
Fig. 6.5 The influence of bed height and N on k_{er} in random packings of spheres (first row), cylinders (second row) and Raschig rings (third row).
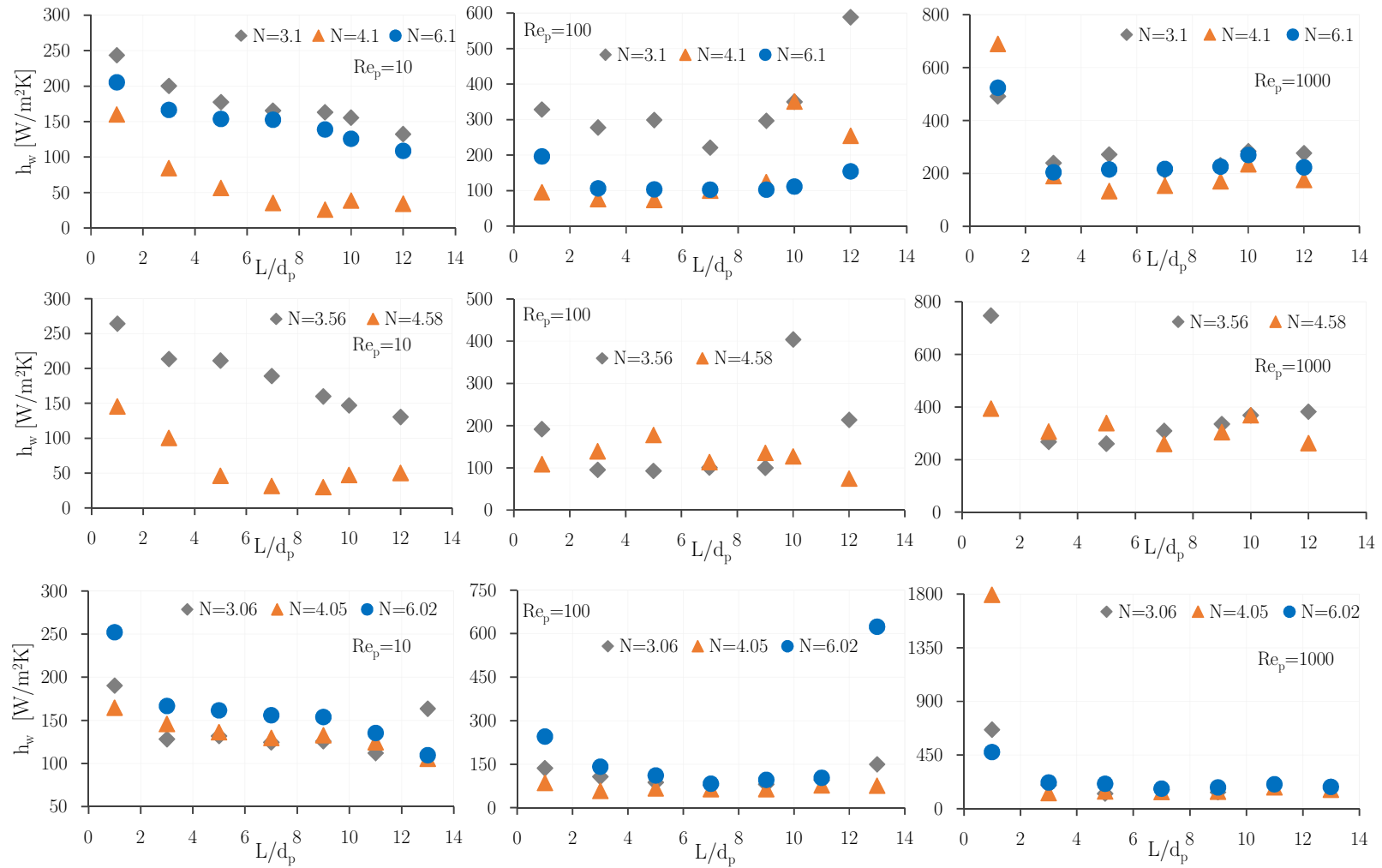
Fig. 6.6 The influence of bed height and N on h_w in random packings of spheres (first row), cylinders (second row) and Raschig rings (third row).

This increasing trend can be explained by the increasing role of eddy transport along the bed, which can be represented by the change of turbulent intensity and/or turbulent kinetic energy along the bed (see Fig. 6.7).
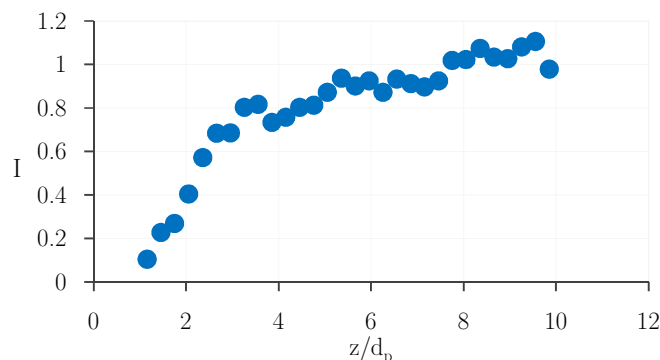
Fig. 6.7 Averaged axial turbulent intensity profile as a function of axial position in a random packing of alumina Raschig rings with $N = 4.05$ at $Re_p = 1000$.

Nonetheless, a reliable interpretation regarding the trend of k_{er} for the turbulent flow regime requires much longer beds, so that the residence time of the flowing fluid is high enough to allow both phases to reach thermal equilibrium.

The results depicted in Fig. 6.5 demonstrate a very poor radial heat transfer in the packing structures that include an axial hole, e.g. packing of spheres, cylinders and Raschig rings with $N = 4.1$, 4.58 and 4.05, respectively, where the computed values of k_{er} are clearly lower than for other cases. Neglecting such structures from our window of analysis, the results generally show that k_{er} increases as N increases in the laminar flow regime (see Fig. 6.5 for $Re_p = 10$ as a representative), whilst in the transient and turbulent regimes, the computed values for k_{er} are comparable making it difficult to find a correlation between k_{er} and N. As shown in Chapter 2 (Table 2.4), the number of published correlations that account for the influence of N of k_{er} at low Re_p is very scarce.

The results shown in Fig 6.5 can also confirm our previous observation in Chapter 5 concerning the advantage of shaped pellets for improving the wall-to-bed heat transfer rate. We find higher computed values of k_{er} for packings of cylinders and Raschig rings compared to packing of spheres.

Fig. 6.6 shows that, in general, h_w decreases as a function of bed length, apparently approaching an asymptotic value, with much smoother trends compared to k_{er}. Several other researchers have reported similar patterns for h_w based on their experimental and theoretical analyses, e.g. [17,18,20,36]. To explain the length-dependent behavior of the apparent wall heat transfer coefficient, we look into the trend of wall heat flux along the bed depth. The results

of circumferential-averaged wall heat flux are depicted as a function of axial position in Fig. 6.8 for random packing of alumina Raschig rings with N = 4.05 at Re_p = 10, 100 and 1000.
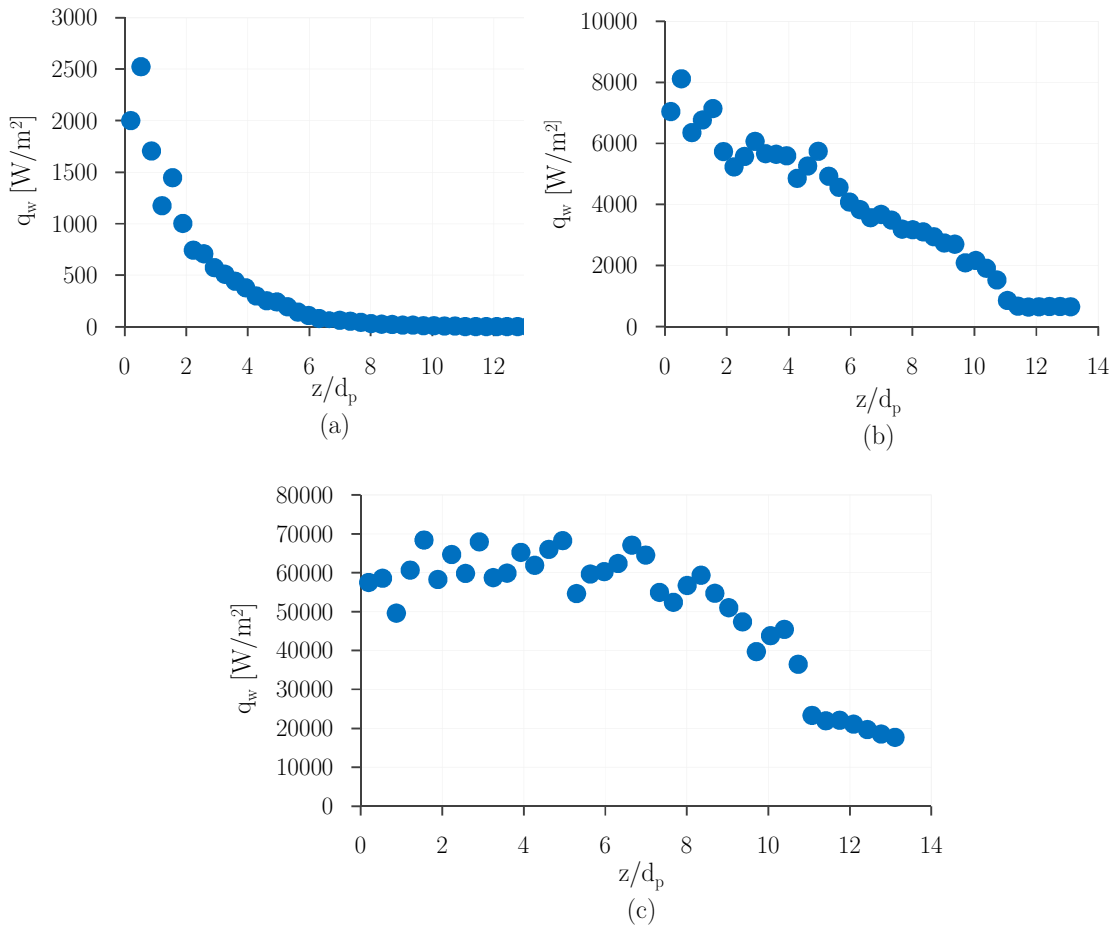
Fig. 6.8 Azimuthally-averaged axial profile of wall heat flux in a random packing of alumina Raschig rings with N = 4.05; (a) Re_p = 10, (b) Re_p = 100 and (c) Re_p = 1000.

Overall, the results show that the apparent wall heat transfer coefficient as a function of bed length emanates from the axial trend of the wall heat flux in conjunction with the trend of radial heat dispersion along the bed. This can be expressed through the boundary condition of heat transfer at the tube wall, i.e. Eq. (6.4), wherein the apparent wall heat transfer coefficient plays the role of a thermal resistance to account for the so-called "temperature jump". This equation can be rewritten in dimensional form as:

$$q_w = h_w (T_w - T) = k_{er} \frac{\partial T}{\partial r} \tag{6.12}$$

Fundamentally, the fluid and catalyst solid phases approach thermal equilibrium for sufficiently long beds, i.e. $T_f \rightarrow T_s \rightarrow T_w$ as $z \rightarrow \infty$, thereby reducing the wall heat flux to the bed, as shown in Fig. 6.8. This explains why for example in the laminar flow regime both h_w

and k_{er} decrease along the bed depth. In this case, the reduction of k_{er} as a function of bed length implies that the decreasing rate in the wall heat flux would have been higher than the decreasing rate of the radial temperature gradient, i.e. $\partial T/\partial r$, and accordingly (T_w-T) along the bed, thereby causing a decreasing trend for h_w along the packing length. It is consequently evident that in turbulent and transient flow regimes, the behavior of h_w as a function of bed length would also be governed by the simultaneous behavior of the effective radial thermal conductivity and wall heat flux. Since there is an intense connection between the rate of wall heat flux and the thermal equilibrium condition at a specific axial position in the bed, it can be deduced that the length-effect phenomenon stems from the trend of temperature non-equilibrium along the bed length. Reiterating that the pseudo homogenous models are based on the thermal equilibrium assumption between fluid and catalyst solid phases, the effective thermal parameters thus need to capture effectively how far the two phases are from local thermal equilibrium, as well as the radial heterogeneity in the bed structure and local flow mal-distribution.

Furthermore, as in the case of k_{er}, the presence of a channel near the center of the some of the packing structures leads to a poor heat transfer rate in the wall region. This is reflected in Fig. 6.6 by the lower fitted values of the apparent wall heat transfer coefficient for random packings of spheres, cylinders and Rachig rings with N = 4.1, 4.58 and 3.06, respectively, in all flow regimes. As explained in Chapter 5, the presence of a flow channel reduces the radial dispersion in a packed column, thereby reducing the radial heat transfer rate, which is quantitatively evidenced here by the lower values of k_{er} and h_w. Based on these results, we cannot find a correlation between h_w and N which is in conformity with the published correlations, because none of the known correlations account for the role of N.

It is remarkable that the results depicted in Fig. 6.6 do not show a major influence of the pellet shape on h_w (contrary to the results found for k_{er}), which means that the rate of heat transfer at the wall region cannot be improved by the use of non-spherical pellets. This observation can be explained by the high local porosity at the wall region, which implies a dominance of convection mechanisms in this region.

6.3.4. The influence of pellet thermal conductivity

To investigate the role of pellet thermal conductivity on the effective heat transfer parameters, we now turn to fixed beds with pellets of different thermal conductivities, namely of alumina and glass. We investigate different shapes with N_{pv} = 3.1 at Re_p = 10, 100 and 1000. The results for k_{er} and h_w are depicted as a function of bed length in Figs. 6.9 and 6.10, respectively.

Generally, the results show a large influence of the pellet's thermal conductivity on the effective radial thermal conductivity in all flow regimes (see Fig 6.9), while the influence on the apparent wall heat transfer coefficient can only be recognized at low Re_p (see Fig 6.10). The first observation highlights how remarkably important is the role of stagnant contributions to k_{er}, even for transient and turbulent regimes. This reflects the sizeable contribution of radial conduction within the catalyst solid phase to the radial heat dispersion. The second observation is in agreement with the presence of a high local porosity in the wall region, which suggests dominance of convective mechanisms. This justifies our observation that at higher Re_p h_w does not depend on the pellet's thermal conductivity at high Re_p, say $Re_p > 100$. Nonetheless, it seems that at low Re_p the role of conductive transport at the wall region becomes important (see Fig. 6.10 for $Re_p = 10$).

Fig. 6.9 The influence of pellet thermal conductivity and bed length on k_{er} in random packing of spheres (first row), cylinders (second row) and Raschig rings (third row) with $N_{pv} = 3.1$ at $Re_p = 10$ (first column), 100 (second column) and 1000 (third column).
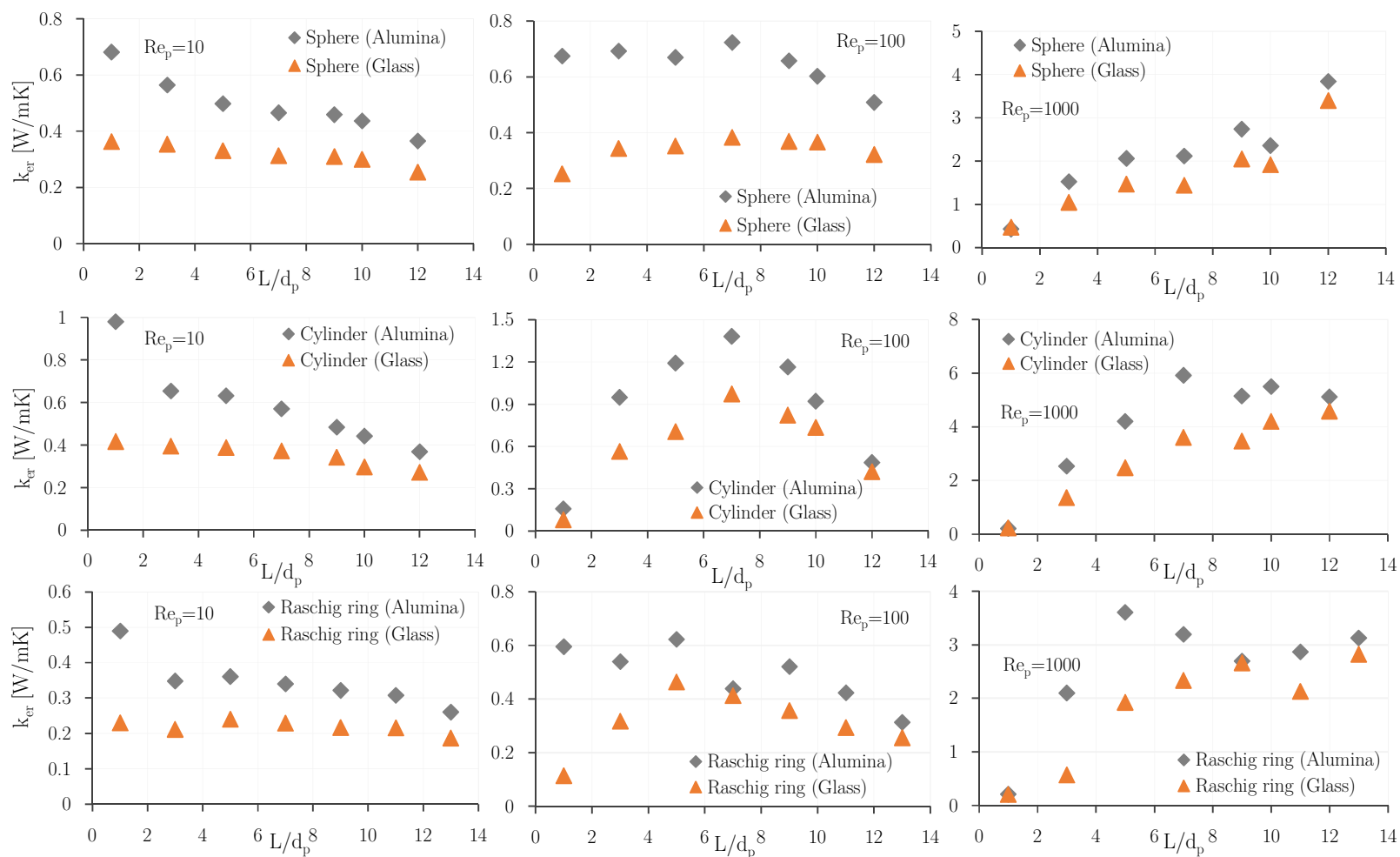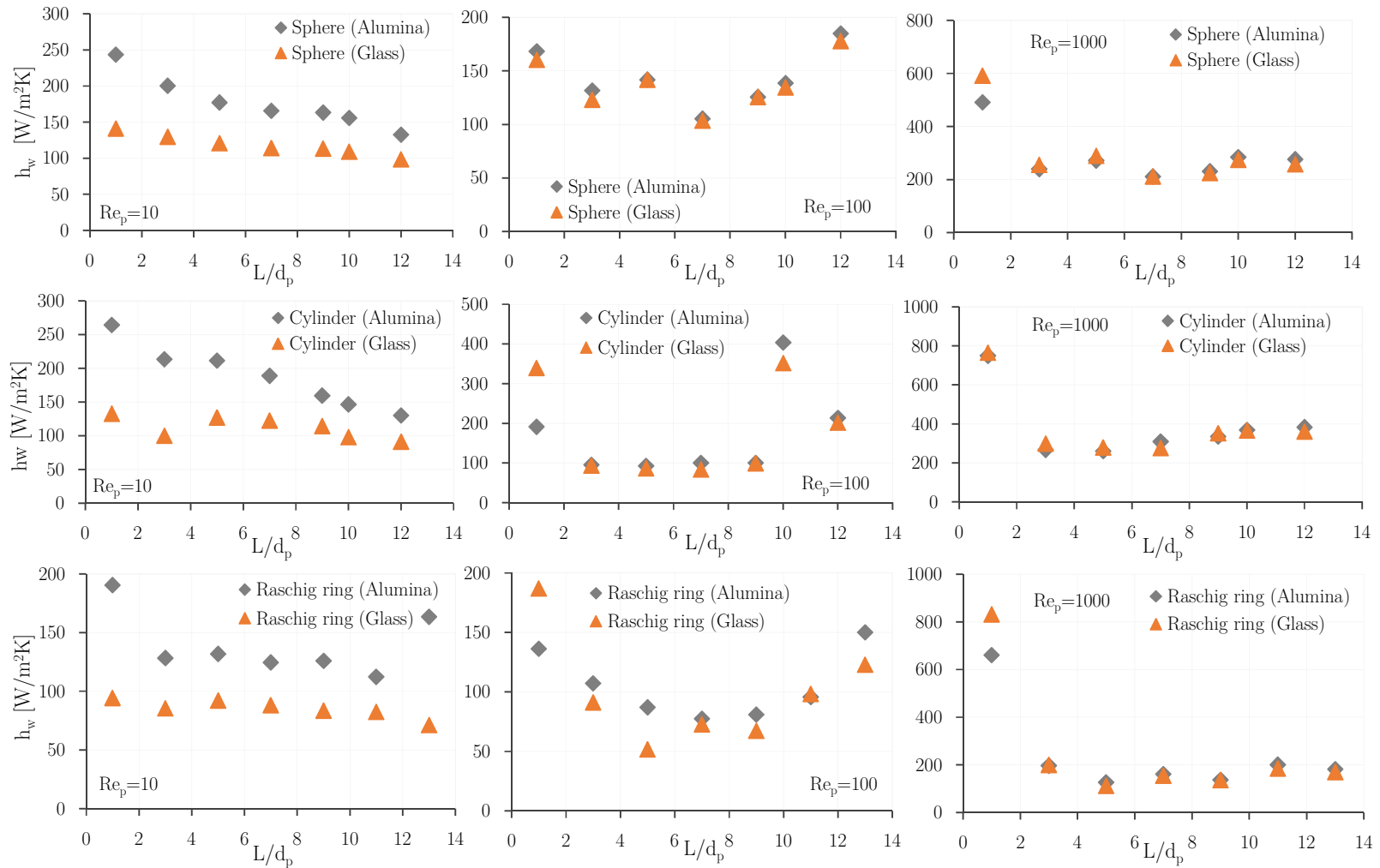
Fig. 6.10 The influence of pellet thermal conductivity and bed length on h_w in random packing of spheres (first row), cylinders (second row) and Raschig rings (third row) with $N_{pv} = 3.1$ at $Re_p = 10$ (first column), 100 (second column) and 1000 (third column)

6.3.5. Reliability and accuracy of literature correlations

In this section we deal with the accuracy and dependability of classical k_{er}-h_w heat transfer models in terms of anticipating the wall-to bed heat transfer rate. To this end, the radial temperature profiles predicted by the 2D-ADPF heat transfer model based on different sets of literature correlations are compared to the azimuthally-averaged temperature data from RBD-CFD simulation results. In spite of a multiplicity of choices with evidently conflicting results, we have employed the often-cited correlations used in design computations, embracing those proposed by the "schools" of Yagi/Kunii/Wakao [37–39], Zehner/Bauer/Hennecke/Schlünder [31,40–42], Specchia/Baldi/Gianetto/Sicardi [43,44], Cresswell/Dixon/Paterson [2,18,30,35,45] and Martin/Nilles [46–48]. A summary of these correlations was given in Chapter 2 (Tables 2.4-5). Since most of these researchers have focused on fixed beds of spherical pellets, our comparisons and analyses are thus conducted based on the heat transfer results in random packing of spheres with N = 6.1. A comparison between the azimuthally-averaged temperature profile at cross section z =9d$_p$ and the radial temperature profiles predicted by the 2D-ADPF model based on different correlations is shown in Fig. 6.11 for different Re$_p$. Overall, a detailed comparisons of radial temperature profiles demonstrates that the model of Specchia/Baldi/Gianetto/Sicardi [43,44] for all flow regimes and of Martin/Nilles [46–48] for the turbulent regime agree reasonably with the RBD-CFD simulation results for the case investigated. It is worth remarking that the deviation observed for the other models, e.g. Yagi and Wakao [38] and Dixon [2], in our typical case study, together with the inherent deviations which arise from the azimuthal-averaging of the 3D temperature field (as addressed in Chapter 5) can cause erroneous predictions of hotspot zones in tubular fixed bed reactors.

The accuracy of the model of Specchia/Baldi/Gianetto/Sicardi [43,44] is further examined in Fig. 6.12 in terms of predicting the radial temperature profile at different axial positions along the bed.
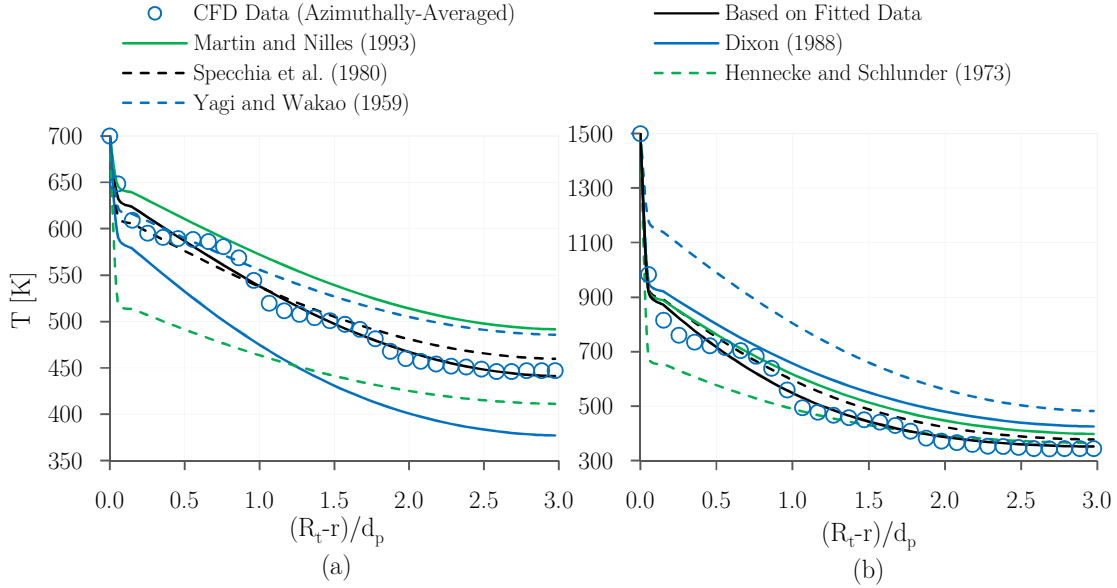
Fig. 6.11 Comparisons between azimuthally-averaged temperature profile and the radial temperature profile predicated by 2D-ADPF model based on different correlations at the bed cross section $z = 9d_p$ in random packing of spheres with $N = 6.1$; (a) $Re_p = 100$ and (b) $Re_p = 1000$.
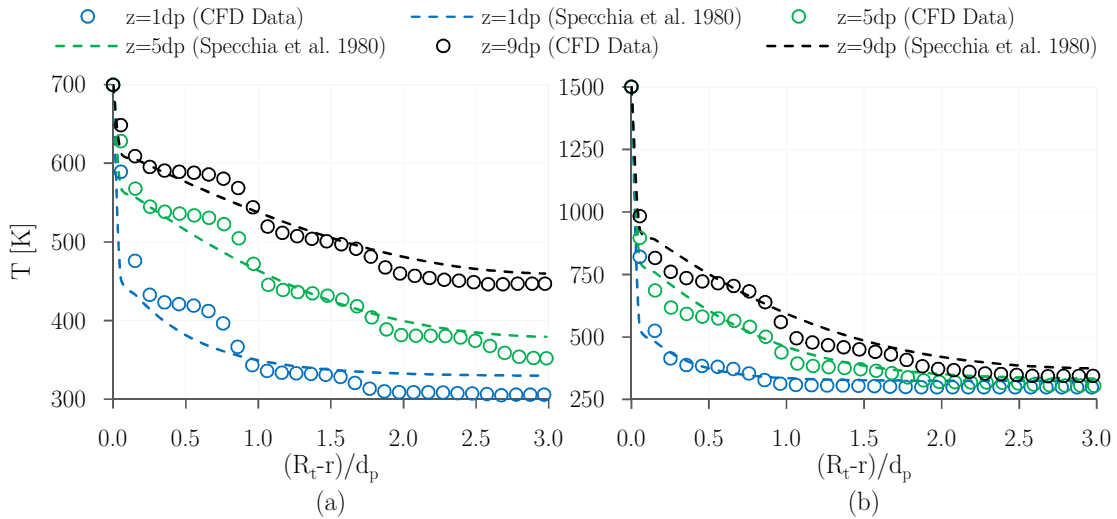
Fig. 6.12 Comparisons between azimuthally-averaged temperature profile and the radial temperature profile predicated based on the model of Specchia et al. (1980) at different cross sections in random packing of spheres with $N = 6.1$; (a) $Re_p = 100$ and (b) $Re_p = 1000$

As shown in Fig. 6.12, using the model of Specchia/Baldi/Gianetto/Sicardi [43,44], results in a reasonable prediction of the radial temperature profile at different bed cross sections. However, it is evident that such a simplistic model cannot reproduce the trend of radial temperature distribution close to the wall, which, as explained before, is due to the presence of a high thermal disequilibrium between the two phases in this region.

6.4. Conclusion

The effect of bed length on the volume-averaged effective heat transfer parameters used in the 2D-ADPF heat transfer model, i.e. k_{er} and h_w, is thoroughly investigated by fitting the model prediction to our RBD-CFD simulation results.

Most previous researches explained the so-called length-effects as a cause of either the experimental error arisen from the poor/inadequate insulation of the calming section or thermocouple's cross (Dixon, [20,23]; Freiwald and Paterson [21], to name a few) or the under-developed velocity and thermal fields to be extended over a specific bed length after the bed entrance (Li and Finlayson [49]; Paterson and Carberry [1]; Wen and Ding [24]). The results of this study demonstrated that this phenomenon actually originates from the evolutionary trend of thermal (non-)equilibrium between the fluid and catalyst solid phases along the bed. The results of this Chapter have also shown that the procedures suggested by Dixon [20] and Borkink and Westertrep [22,27,28] cannot resolve the problem of the length-effect.

A detailed sensitivity analysis is performed, whereby the influences of shape and thermal conductivity of catalyst pellets as well as the tube-to-pellet diameter ratio on both k_{er} and h_w are investigated. The results give appropriate insight into the contribution of the different transport mechanisms in the effective thermal properties. The performances of the most promising theoretical- and empirical-based literature correlations for Pe_{er} and Nu_w were investigated in a comparison of the azimuthally-averaged temperature data obtained from RBD-CFD simulation results. It is concluded that the models of Specchia/Baldi/Gianetto/ Sicardi [43,44] for all flow regimes and of Martin/Nilles [46–48] for the turbulent regime can be recommended for practical use for spherical particles.

Overall, in spite of the severe shortcomings inherent in the pseudo-continuum models for predicting the thermal behavior of a fixed bed reactor, we have shown that the RBD-CFD methodology can be used as a design tool to tune such simplistic approaches to improve the reliability of the model results.

Bibliography

[1]   W.R. Paterson, J.J. Carberry, Fixed bed catalytic reactor modelling: The heat transfer problem, Chemical Engineering Science. 38 (1983) 175–180. doi:10.1016/0009-2509(83)80149-3.

[2]   A.G. Dixon, Wall and particle-shape effects on heat transfer in packed beds, Chemical Engineering Communications. 71 (1988) 217–237. doi:10.1080/00986448808940426.

[3]   G.D. Wehinger, C. Fu, M. Kraume, Contact Modi fi cations for CFD Simulations of Fixed-Bed Reactors : Cylindrical Particles, (2017). doi:10.1021/acs.iecr.6b03596.

[4]   H. Dixon, A G, Tsotsas, E and Martin, Letters to the editor- Thermal Conductivity of Packed Beds, Chemical Engineering and Processing: Process Intensification. 24 (1988) 177–179. doi:10.1097/01.JAA.0000451871.48448.1f.

[5]   A.G. Dixon, J.H. Van Dongeren, The influence of the tube and particle diameters at constant ratio on heat transfer in packed beds 1, Chemical Engineering and Processing: Process Intensification. 37 (1998) 23–32.

[6]   O. Bey, G. Eigenberger, Gas flow and heat transfer through catalyst filled tubes, International Journal of Thermal Sciences. 40 (2001) 152–164. doi:10.1016/S1290-0729(00)01204-7.

[7]   S.J. Romkes, F.. Dautzenberg, C.. van den Bleek, H.P.. Calis, CFD modelling and experimental validation of particle-to-fluid mass and heat transfer in a packed bed at very low channel to particle diameter ratio, Chemical Engineering Journal. 96 (2003) 3–13. doi:10.1016/j.cej.2003.08.026.

[8]   M.E. Taskin, A.G. Dixon, M. Nijemeisland, E.H. Stitt, CFD Study of the Influence of Catalyst Particle Design on Steam Reforming Reaction Heat Effects in Narrow Packed Tubes, (2008) 5966–5975.

[9]   P. Magnico, Pore-scale simulations of unsteady flow and heat transfer in tubular fixed beds, AIChE Journal. 55 (2009) 849–866. doi:10.1002/aic.11806.

[10]   M. Behnam, A.G. Dixon, M. Nijemeisland, E.H. Stitt, A New Approach to Fixed Bed Radial Heat Transfer Modeling Using Velocity Fields from Computational Fluid Dynamics Simulations BT - Industrial & Engineering Chemistry Research, Industrial and Engineering Chemistry Research. 52 (2013) 15244–15261. doi:10.1021/ie4000568.

[11]   Y. Dong, B. Sosna, O. Korup, F. Rosowski, R. Horn, B. Sosna, O. Korup, F. Rosowski, R. Horn, Investigation of radial heat transfer in a fixed-bed reactor: CFD simulations and profile measurements, Chemical Engineering Journal. 317 (2017) 204–214. doi:10.1016/j.cej.2017.02.063.

[12]   O. Nekhamkina, M. Sheintuch, Approximate characteristics of a moving temperature front in a fixed-bed catalytic reactor: Effect of mass dispersion, Chemical Engineering

Journal. 154 (2009) 115–119. doi:10.1016/j.cej.2009.04.043.

[13]   L. Obalová, K. Jirátová, K. Karásková, Ž. Chromčáková, N 2 O catalytic decomposition–From laboratory experiment to industry reactor, Catalysis Today. 191 (2012) 116–120.

[14]   D. Schlereth, O. Hinrichsen, A fixed-bed reactor modeling study on the methanation of CO_2, Chemical Engineering Research and Design. 92 (2014) 702–712.

[15]   X.P. Dai, P.Z. Liu, Y. Shi, J. Xu, W.S. Wei, Fischer–Tropsch synthesis in a bench-scale two-stage multitubular fixed-bed reactor: Simulation and enhancement in conversion and diesel selectivity, Chemical Engineering Science. 105 (2014) 1–11.

[16]   A.G. Dixon, G. Walls, H. Stanness, M. Nijemeisland, E.H. Stitt, Experimental validation of high Reynolds number CFD simulations of heat transfer in a pilot-scale fixed bed tube, Chemical Engineering Journal. 200–202 (2012) 344–356. doi:10.1016/j.cej.2012.06.065.

[17]   D.J. Gunn, M. KHALID, Thermal Dispersion and Wall Effect in Packed Beds, Chemical Engineering Science. 30 (1975) 261–267.

[18]   A.G. Dixon, D.L. Cresswell, W.R. Paterson, Heat Transfer in Packed Beds of Low TubejParticle Diameter Ratio, Edinburgh, 1978. http://www.worldcat.org/title/heat-transfer-in-packed-beds-of-low-tubeparticle-diameter-ratio/oclc/638440257 (accessed December 15, 2017).

[19]   B.A. Li, Chi-Hsiung; and Finlyson, Heat transfer in packed beds-a reevaluation, Chemical Engineering Transaction. 32 (1976) 1055–1066.

[20]   A.G. Dixon, The Length Effect on Packed Bed Effective Heat Transfer Parameters, Chemical Engineering Journal. 31 (1985) 163–173.

[21]   M.G. Freiwald, W.R. Paterson, Accuracy of model predictions and reliability of experimental data for heat transfer in packed beds, Chemical Engineering Science. 47 (1992) 1545–1560. doi:10.1016/0009-2509(92)85003-T.

[22]   J.G.H. Borkink, K.R. Westerterp, Determination of Effective Heta Transport Coefficients for Wall-Cooled Packed Beds, Chemical Engineering Science. 47 (1992) 2337–2342.

[23]   A.G. Dixon, Fixed bed catalytic reactor modelling—the radial heat transfer problem, The Canadian Journal of Chemical Engineering. 90 (2012) 507–527.

[24]   D. Wen, Y. Ding, Heat transfer of gas flow through a packed bed, Chemical Engineering Science. 61 (2006) 3532–3542. doi:10.1016/j.ces.2005.12.027.

[25]   G.B. Liu, K.T. Yu, X.G. Yuan, C.J. Liu, A computational transport model for wall-cooled catalytic reactor, Industrial and Engineering Chemistry Research. 47 (2008) 2656–2665. doi:10.1021/ie070737y.

[26] N. Wakao, S. Kaguei, T. Funazkri, Effect of fluid dispersion coefficients on particle-to-fluid heat transfer coefficients in packed beds: correlation of Nusselt numbers, Chemical Engineering Science. 34 (1979) 325–336.

[27] J.G. H.Borkink, K.R. Westerterp, Influence of tube and aprticle diameter on heat transport in packed beds, AIChE Journal. 38 (1992) 703–716.

[28] J.G.H. Borkink, W. K.R., Significance of the radial porosity profile for the description of heat transport in wall-cooled packed beds, Chemical Engineering Science. 49 (1994) 863–876. doi:10.1016/0009-2509(94)80023-5.

[29] N. Wakao, S. Kaguei, H. Nagai, Effective diffusion coefficients for fluid species reacting with first order kinetics in packed bed reactors and discussion on evaluation of catalyst effectiveness factors, Chemical Engineering Science. 33 (1978) 183–187.

[30] A. Dixon, D. Cresswell, Theoretical prediction of effective heat transfer parameters in packed beds, AIChE Journal. 25 (1979) 663–676. doi:10.1002/aic.690250413.

[31] P. Zehner, E.U. Schlünder, Die effektive Wärmeleitfähigkeit durchströmter Kugelschüttungen bei mäßigen und hohen Temperaturen, Chemie Ingenieur Technik. 45 (1973) 272–276.

[32] T.F. Coleman, Y. Li, An interior trust region approach for nonlinear minimization subject to bounds, SIAM Journal on Optimization. 6 (1996) 418–445.

[33] R.H. Byrd, J.C. Gilbert, J. Nocedal, A trust region method based on interior point techniques for nonlinear programming, Mathematical Programming. 89 (2000) 149–185.

[34] R.A. Waltz, J.L. Morales, J. Nocedal, D. Orban, An interior algorithm for nonlinear optimization that combines line search and trust region steps, Mathematical Programming. 107 (2006) 391–408.

[35] M.M. Melanson, A.G. Dixon, Solid conduction in low dt/dp beds of spheres, pellets and rings, International Journal of Heat and Mass Transfer. 28 (1985) 383–394. doi:10.1016/0017-9310(85)90071-7.

[36] A.P. de Wasch, G.F. Froment, Heat transfer in packed beds, Chemical Engineering Science. 27 (1972) 567–576. doi:10.1016/0009-2509(72)87012-X.

[37] S. Yagi, D. Kunii, Studies on effective thermal conductivities in packed beds, AIChE Journal. 3 (1957) 373–381. doi:10.1002/aic.690030317.

[38] S. Yagi, N. Wakao, Heat and mass transfer from wall to fluid in packed beds, AIChE Journal. 5 (1959) 79–85.

[39] S. Yagi, D. Kund, Heat transfer in packed beds through which, 7 (1964) 333–339.

[40] P. Zehner, E.U. Schlünder, Wärmeleitfähigkeit von Schüttungen bei mäßigen Temperaturen, Chemie Ingenieur Technik. 42 (1970) 933–941.

[41]   R. Bauer, E.U. Schlunder, Effective Radial Thermal-Conductivity of Packings in Gas-Flow. 2. Thermal-Conductivity of Packing Fraction without Gas-Flow, International Chemical Engineering. 18 (1978) 189–204.

[42]   F.W. Hennecke, E.U. Schlünder, Wärmeübergang in beheizten oder gekühlten Rohren mit Schüttungen aus Kugeln, Zylindern und Raschig-Ringen, Chemie Ingenieur Technik. 45 (1973) 277–284. doi:10.1002/cite.330450510.

[43]   V. Specchia, G. Baldi, A. Gianetto, Solid-Liquid Mass Transfer in Concurrent Two-Phase Flow through Packed Beds, 17 (1978) 362–367.

[44]   V. Specchia, G. Baldi, S. Sicardi, Heat Transfer in Packed Bed Reactors With One Phase Flow, Chemical Engineering Communications. 4 (1980) 361–380. doi:10.1080/00986448008935916.

[45]   a. G. Dixon, D.L. Cresswell, Effective heat transfer parameters for transient packed-bed models, AIChE Journal. 32 (1986) 809–819. doi:10.1002/aic.690320511.

[46]   H. Martin, Low Peclet number particle-to-fluid heat and mass transfer in packed beds, Chemical Engineering Science. 33 (1978) 913–919.

[47]   H. Martin, Thermal Conductivity of Packed Beds : A Review, (1987) 19–37.

[48]   H. Martin, M. Nilles, Radiale Warmeleitung in durchstromten Schuttungsrohren, Chemie Ingenieur Technik. 65 (1993) 1468–1477.

[49]   B.A. Finlayson, Packed bed reactor analysis by orthogonal collocation, Chemical Engineering Science. 26 (1971) 1081–1091.

Chapter 7

Conclusions and Recommendations

7.1. Conclusions

The research described in this thesis has dealt with several important topics in the field of fixed bed reactor modelling and design, namely the development of a Rigid Body Dynamics algorithm for generating random packing structures of non-spherical and non-convex pellets, an efficient and integrated workflow for predicting the in-situ or "pellet-scale" behaviour of hydrodynamics and heat transfer within realistic fixed-bed reactors, and to address and explain the prevailing ambiguities and shortcomings connected with classical macroscopic design procedures. Our research road-map is summarized in the following flowchart.
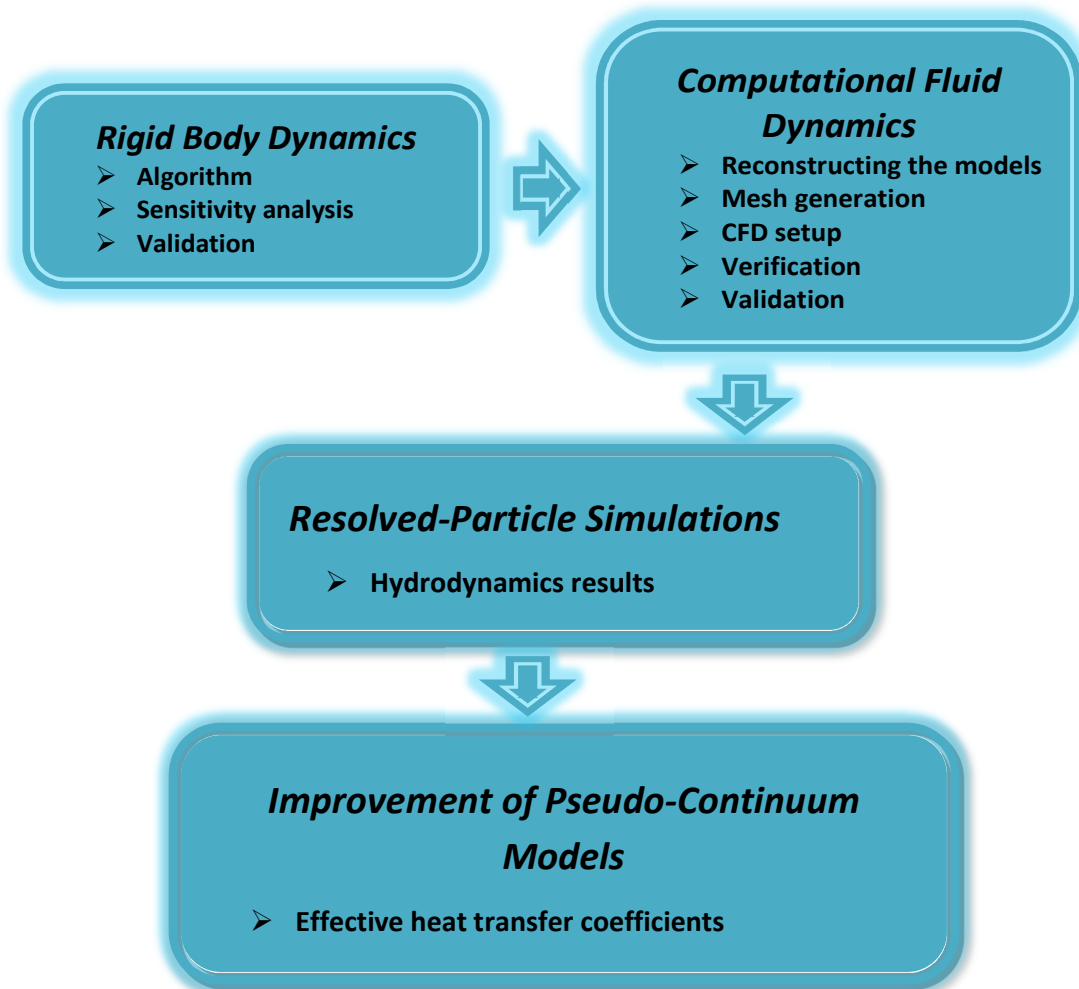

Fig. 7.1 The research road-map.

In the first step we have dealt with the structural feature of fixed bed reactors, as it plays a crucial role in the design of such a complicated unit operation. A novel physics-based algorithm founded on the concepts of Rigid Body Dynamics (RBD) was developed to

synthesize realistic packing structures of non-spherical and non-convex pellets. The proposed RBD algorithm benefits from a hard-body approach to detect the collision/contact incidence and employs impulse theory in conjunction with a quadratic optimization routine to model different collisional contact situations. The RBD algorithm was used to generate random packings of spheres, equilateral solid cylinders and Raschig rings with tube-to-pellet diameter ratios ranging from 3 to 9.16. These conceptual models were then examined and validated in terms of bulk porosity and radial void fraction distribution, finding satisfactory agreement with the literature data for both global and local bed properties. The advantage of our approach, compared to popular computer graphics software such as Blender, is that we are explicit about the treatment of binary collisions and frictional forces, and explicit about the transition to and treatment of multi-particle assemblies in resting contact. We also conducted a thorough analysis concerning the influence of physio-mechanical properties of catalyst pellets on packing densification. The results demonstrated that denser packing structures can be generated with restitution coefficients closer to one, and friction factors closer to zero. This finding shows the capability of our algorithm to generate packing structures of non-spherical pellets with a wide range of packing densities, which mimics both loose and dense packing topologies.

In the second step, we employed RBD-generated structures in a supplementary Computational Fluid Dynamics (CFD) study to probe the pellet-scale behavior of flow and thermal fields inside packing structures of spheres, cylinders and Raschig rings. To this end, we devised an efficient and integrated workflow, consisting of a sequential RBD-CFD approach. To facilitate convergence in the turbulence regime and to optimize the computational expenses of our "Numerical Experiments", we created an inflationary meshing scheme using a combination of patch conforming and patch independent meshing approaches, which results in a high quality computational cells at contact regions, followed by a detailed mesh refinement analysis. The workflow was benchmarked for simulations of hydrodynamics and heat transfer in laminar, transient and turbulent regimes in random packings of spheres, cylinders and Raschig rings with tube-to-pellet diameter ratios ranging from 2.29 to 6.1.

In the third step, the in-situ behavior of the velocity and thermal fields were investigated in detail by post-processing the results of RBD-CFD simulations. Overall, it was demonstrated that the proposed workflow can provide detailed information of flow and thermal fields, which in terms of resolution and precision is comparable to the results of advanced experimental techniques such as PIV, MRI, and 3D CT, which however are often very difficult to obtain. The contour map results reveal a tremendous influence of local structure on the velocity and temperature distributions at the pellet scale, particularly in narrow packings, where the spatial heterogeneity of the structure is very strong along the bed axis. Compared to random packings

of spheres, in random packings of cylinders and Raschig rings more intense inhomogeneities in local velocity and temperature fields were observed. This is ascribed to the role of sharp edges of such pellets in imposing stronger curvature of the flow streamlines along the packing. This result suggests inadequacy of the 120^0 wall-segment model proposed by Dixon et al. (2006, 2008) for analysis of heat transfer in a full fixed bed reactor. Furthermore, it was shown that the azimuthal averaging of velocity and temperature fields leads to an underestimation of the local velocity and temperature values by more than 400% and 50 K, respectively. The maximum deviation from the local data was found at a distance of 0.5dp from tube wall for the temperature field.

The last effort in this research was centered around the macroscopic pseudo-continuum models, where we used the results of our numerical experiments to elucidate the effective heat transfer parameters introduced in the k_{er} -h_w pseudo-homogenous model. The results of our multi-variable parameter estimation analysis demonstrated that the reactor length-dependency of the values of k_{er} and h_w is basically inherent in such effective thermal parameters and originates from the evolutionary trend of reaching thermal equilibrium in fluid and catalyst phases along the bed length. Furthermore, we showed that the procedures suggested in the review paper by Dixon (2012) and the publications by Borkink and Westertrep (1992,1994) do not solve the length-effect problem. In a detailed sensitivity analysis, we explained and addressed the influences of the pellet shape and thermal conductivity, as well as tube-to-pellet diameter ratio, on the effective heat transfer parameters. The results provide an intuitive picture of the contributions of the different transport mechanisms to the effective thermal properties. We also investigated the differences between the most promising theoretical- and empirical-based literature correlations for Peer and Nuw in a comparison analysis based on the azimuthally-averaged temperature data obtained from RBD-CFD simulation results.

It was concluded that the models of Specchia/Baldi/Gianetto/Sicardi for all flow regimes and of Martin/Nilles for the turbulent regime agree reasonably well with the results of our numerical experiments and can be recommended for practical use for fixed beds of spherical pellets.

7.2.   Recommendations for future work

One of the main obstacles in the design and optimization of fixed bed and even fluidized bed reactors is to address the role of non-sphericity of catalytic and adsorbent particles in fluid flow (drag, lift, pressure drop, etc.) and in heat and mass transfer (transport and kinetic mechanisms at pellet scale). The capabilities of the proposed workflow for providing a detailed understanding of flow and heat transfer inside random packings of non-spherical pellets were

evidenced and discussed. We can now use the RBD-CFD methodology as a tried and tested tool to look deeply into a variety of subjects relevant to the field of fixed bed and even fluidized bed reactors, such as:

1) Exploring the topological properties of random packing structures of non-spherical particles such as cylinders with different aspect ratio, multi-hole cylinders, pall rings, saddle rings, trilobed particles, etc.

2) Using RBD as an alternative approach for modelling fluidization processes.

3) Correlating the bed pressure drop in packed columns of non-spherical pellets using particle-resolved CFD simulations.

4) Coupling reaction kinetics and adsorption isotherms with the particle-resolved CFD simulations to analyse pellet-scale behaviour of physio-chemical phenomena inside fixed bed reactors of non-spherical particles.

5) Improving the pseudo-continuum reactor models for non-spherical catalytic particles based on numerical experiments.

Appendix A

Let us define the relative position of the contact point $\mathbf{p}$ with respect to the center-of-mass of each body as $\mathbf{r}_i(t_c)$ and $\mathbf{r}_k(t_c)$, meaning $\mathbf{r}_i(t_c) = \mathbf{p}(t_c) - \mathbf{x}_i(t_c)$ and $\mathbf{r}_k(t_c) = \mathbf{p}(t_c) - \mathbf{x}_k(t_c)$. Let us also describe the pre-impulse and post-impulse variables by superscripts of $-$ and $+$ respectively. Therefore, Eq. (3.12) can be rewritten for post-impulse contact point velocity as:

$$\mathbf{v}^+_{pi}(t_c) = \mathbf{v}^+_i(t_c) + \boldsymbol{\omega}^+_i(t_c) \times \mathbf{r}_i \tag{A.1}$$

since at the first step we assume that the impulsive force acts only in normal direction, the spatial variable, i.e. linear and angular velocities, of the ith pellet after collision can be computed based on the normal impulse as:

$$\mathbf{v}^+_i(t_c) = \mathbf{v}^-_i(t_c) + \frac{j_{ik,n}\widehat{\mathbf{n}}_{ik}(t_c)}{m_i} \tag{A.2}$$

$$\boldsymbol{\omega}^+_i(t_c) = \boldsymbol{\omega}^-_i(t_c) + \mathbf{I}^{-1}_i(t_c)\left[\mathbf{r}_i \times j_{ik,n}\widehat{\mathbf{n}}_{ik}(t_c)\right] \tag{A.3}$$

where m_i is the mass of pellet i. Substitution of Eqs. (A.2-3) into Eq. (A.1) will result in:

$$
\begin{aligned}
\mathbf{v}^+_{pi}(t_c) &= \mathbf{v}^-_i(t_c) + \frac{j_{ik,n}\widehat{\mathbf{n}}_{ik}(t_c)}{m_i} + \left(\boldsymbol{\omega}^-_i(t_c) + \mathbf{I}^{-1}_i(t_c)\left[\mathbf{r}_i \times j_{ik,n}\widehat{\mathbf{n}}_{ik}(t_c)\right]\right) \times \mathbf{r}_i \\
&= \mathbf{v}^-_{pi}(t_c) + j_{ik,n}\left(\frac{\widehat{\mathbf{n}}_{ik}(t_c)}{m_i} + \mathbf{I}^{-1}_i(t_c)\left[\mathbf{r}_i \times \widehat{\mathbf{n}}_{ik}(t_c)\right] \times \mathbf{r}_i\right)
\end{aligned}
\tag{A.4}
$$

Similarly, the velocity of point $\mathbf{p}$ on the body space of packing j with the mass of m_j after collision can be computed using the exertion of opposite impulse, i.e. $j_{ik,n}\widehat{\mathbf{n}}_{ik}(t_c)$, yielding:

$$\mathbf{v}^+_{pk}(t_c) = \mathbf{v}^-_{pk}(t_c) - j_{ik,n}\left(\frac{\widehat{\mathbf{n}}_{ik}(t_c)}{m_k} + \mathbf{I}^{-1}_k(t_c)\left[\mathbf{r}_k \times \widehat{\mathbf{n}}_{ik}(t_c)\right] \times \mathbf{r}_k\right) \tag{A.5}$$

Using Eqs. (A.4-5) to compute $\mathbf{v}^+_{pik}(t_c)$, followed by a scalar product with $\widehat{\mathbf{n}}_{ik}(t_c)$, yields the following relationship for $v^+_{pik,n}(t_c)$:

$$v^+_{pik,n}(t_c) = \underbrace{\widehat{\mathbf{n}}_{ik}(t_c) \cdot \left(\mathbf{v}^-_{pi}(t_c) - \mathbf{v}^-_{pk}(t_c)\right)}_{v^-_{pik,n}(t_c)} + j_{ik,n}\left[\begin{array}{l}\frac{1}{m_i} + \frac{1}{m_k} + \widehat{\mathbf{n}}_{ik}(t_c)\mathbf{I}^{-1}_i(t_c)\left[\mathbf{r}_i \times \widehat{\mathbf{n}}_{ik}(t_c)\right] \times \mathbf{r}_i \\ +\widehat{\mathbf{n}}_{ik}(t_c)\mathbf{I}^{-1}_k(t_c)\left[\mathbf{r}_k \times \widehat{\mathbf{n}}_{ik}(t_c)\right] \times \mathbf{r}_k\end{array}\right] \tag{A.6}$$

Using Eq. (3.20) in which $v_{\text{pik,n}}^{+}(t_{c})$ is expressed in terms of $v_{\text{pik,n}}^{-}(t_{c})$ and COR, the magnitude of normal impulse can be computed by substitution of Eq. (A.6) in to Eq.(3.20).

$$j_{\text{ik,n}} = \frac{-\left(1 + \text{COR}\right)\mathbf{v}_{\text{pik}}^{-}\widehat{\mathbf{n}}_{\text{ik}}(t_{c})}{\widehat{\mathbf{n}}_{\text{ik}}^{\text{T}}\mathbf{K}_{\text{ik,n}}\widehat{\mathbf{n}}_{\text{ik}}}$$

and

$$\mathbf{K}_{\text{ik,n}} = \left(1/m_{\text{i}} + 1/m_{\text{k}}\right)\mathbf{I}_{0} + \left[\mathbf{I}_{\text{i}}^{-1}(t_{c})\left(\mathbf{r}_{\text{i}} \times \widehat{\mathbf{n}}_{\text{ik}}(t_{c})\right)\right] \times \mathbf{r}_{\text{i}} + \left[\mathbf{I}_{\text{k}}^{-1}(t_{c})\left(\mathbf{r}_{\text{k}} \times \widehat{\mathbf{n}}_{\text{ik}}(t_{c})\right)\right] \times \mathbf{r}_{\text{k}}$$

(A.7)

Appendix B

Considering the notation presented in Fig. 4, for a particular contact point $\mathbf{P}_{ik}$ with the normal vector $\widehat{\mathbf{n}}_{ik}(t_c)$ pointing out from body k towards body i, we can express $\ddot{d}_{p,ik}(t_c)$ in terms of all unknown contact forces that directly affect $\mathbf{P}_{ik}$ as:

$$\ddot{d}_{p,ik}(t_c) = a_{ik,j}\varphi_{ij} + a_{ik,i}\varphi_{ik} + a_{ik,l}(-\varphi_{il}) + b_{ik} \tag{B.1}$$

It is worth noticing that here $\widehat{\mathbf{n}}_{ij}(t_c)$ points out from body i towards body j and $\widehat{\mathbf{n}}_{lk}(t_c)$ points out from body k towards body i. Let us start by determining $a_{ik,j}$ which specifies how the φ_{ij} contact force affects the acceleration of the contact distance between i and k, i.e. $\ddot{d}_{p,ik}(t_c)$. Using Eq. (3.28), we realize that the second term, i.e. $2\dot{\widehat{\mathbf{n}}}_{lk}(t_c).\left[\mathbf{v}_{pi}(t_c)-\mathbf{v}_{pk}(t_c)\right]$, is velocity dependent, and is thus part of b_{ik}. Therefore, the $\varphi_{ik}(t_c)$ dependent part of Eq. (3.28) is $\widehat{\mathbf{n}}_{lk}(t_c).\left[\dot{\mathbf{v}}_{pi}(t_c)-\dot{\mathbf{v}}_{pk}(t_c)\right]$ and since pellets i and j are in resting contact, the trace of $a_{ik,j}$ should be found in $\dot{\mathbf{v}}_{pi}(t_c)$, which is expressed by Eq. (3.29). Looking at this equation, the last term, i.e. $\boldsymbol{\omega}_i(t_c)\times\left(\boldsymbol{\omega}_i(t_c)\times\mathbf{r}_i(t_c)\right)$ is a velocity dependent term as well, and hence can be considered as a part of b_{ik}. The linear and angular accelerations of body i, in Eq. (3.29), contributed by the contact force $\varphi_{ik}(t_c)$ can be expressed as:

$$\dot{\mathbf{v}}_i(t_c) = \varphi_{ik,j}\widehat{\mathbf{n}}_{ij}\big/m_i \tag{B.2}$$

$$\dot{\boldsymbol{\omega}}_i(t_c) = \mathbf{I}_i^{-1}(t_c)\underbrace{\left[\left(\mathbf{P}_{ij}(t_c) - \mathbf{x}_i(t_c)\right)\times\varphi_{ik,j}\widehat{\mathbf{n}}_{ij}\right]}_{\text{torque caused by contact force acting at } P_{ij}} + \mathbf{I}_i^{-1}(t_c)\left[\mathbf{L}_i(t_c)\times\boldsymbol{\omega}_i(t_c)\right] \tag{B.3}$$

where the second part of Eq. (B.3) is also velocity dependent term and can be transferred to b_{ik}.

Substituting for linear and angular velocity contributions into $\dot{\mathbf{v}}_{pi}(t_c)$ followed by a dot product with $\widehat{\mathbf{n}}_{ik}(t_c)$, the total dependence of $\ddot{d}_{p,ik}(t_c)$ on $\varphi_{ik}(t_c)$ is:

$$a_{ik,j}\varphi_{ik,j} = \widehat{\mathbf{n}}_{ik}(t_c).\left[\widehat{\mathbf{n}}_{ij}(t_c)\big/m_i + \mathbf{I}_i^{-1}(t_c)\left(\left(\mathbf{P}_{ij}(t_c) - \mathbf{x}_i(t_c)\right)\times\widehat{\mathbf{n}}_{ij}(t_c)\right)\times\mathbf{r}_i\right]\varphi_{ik,j} \tag{B.4}$$

Similarly, we can determine the dependence of $\ddot{d}_{p,ik}(t_c)$ on $\varphi_{lk}(t_c)$ with the same procedure, which will result in a derivation of $a_{ik,l}$:

$$a_{ik,l}(-\varphi_{ik,l}) = \hat{\mathbf{n}}_{ik}(t_c).\left[\hat{\mathbf{n}}_{lk}(t_c)\big/m_k + \mathbf{I}_k^{-1}(t_c)\left((\mathbf{P}_{lk}(t_c) - \mathbf{x}_k(t_c)) \times \hat{\mathbf{n}}_{lk}(t_c)\right) \times \mathbf{r}_k\right](-\varphi_{ik,l}) \qquad \text{(B.5)}$$

To determine b_{ik} we also have to take the contributions of $\dot{\mathbf{v}}_{pi}(t_c)$ and $\dot{\mathbf{v}}_{pk}(t_c)$ due to unknown external forces such as gravity as well as the force independent terms into account. Thus, the contribution of $\dot{\mathbf{v}}_{pi}(t_c)$ to b_{ik}, after scalar product to $\hat{\mathbf{n}}_{ik}(t_c)$ can be expressed as:

$$\frac{\mathbf{F}_i(t_c).\hat{\mathbf{n}}_{ik}(t_c)}{m_i} + \hat{\mathbf{n}}_{ik}(t_c).\begin{bmatrix} \left(\mathbf{I}_i^{-1}(t_c)\boldsymbol{\tau}_i(t_c)\right) \times \mathbf{r}_i + \boldsymbol{\omega}_i(t_c) \times \left(\boldsymbol{\omega}_i(t_c) \times \mathbf{r}_i\right) \\ + \left(\mathbf{I}_i^{-1}(t_c)(\mathbf{L}_i(t_c) \times \boldsymbol{\omega}_i(t_c))\right) \times \mathbf{r}_i \end{bmatrix} \qquad \text{(B.6)}$$

where $\mathbf{F}_i$ and $\boldsymbol{\tau}_i$ are the net external force and torque acting on pellet i, belonging to the previous time step. The same formula can be derived for contribution of $\dot{\mathbf{v}}_{pk}(t_c)$ to b_{ik}. Combining these contributions and adding them to the velocity term in Eq. (3.29), i.e. $2\dot{\hat{\mathbf{n}}}_{ik}(t_c).\left[\mathbf{v}_{pi}(t_c) - \mathbf{v}_{pk}(t_c)\right]$, the value of b_{ik} is simply determined.

Appendix C

This appendix presents the optimization code developed for solution of the multivariable parameter estimation problem for evaluating Pe_{er} and Bi dimensionless numbers.

```matlab
function opt
clc
clear
%options = optimset('Display','iter','TolFun',1e-10)
options=optimset('Display','iter','TolFun',1e-
7,'LargeScale','off','Algorithm',...
    'active-
set','UseParallel','always','MaxFunEvals',10000,'PlotFcns',@plotfun_fmi
n);%,'MaxIter',1e5,'NonlEqnAlgorithm','lm'
N=input('please enther the tube-to-particle diameter ratio =');
Re=input('please enter the particle Reynolds number =');
Bi0=5.73*N^0.5*Re^-0.262
%%%%%%%Dixon(1988)%%%%%
eps=0.491;
Pr=0.701;
%Zehner-Schulander (1973)
kp=1.01;
kf=0.076;
K=kf/kp;
%Fluid Phase Radial Peclet Number
 Prfinf=7; %9.98 and 8.56
 Perf=(1/Prfinf+(2/3)*eps/Re*Pr)^-1;
%Fluid Phase Radial Biot Number
 Nufw=.24*Re^.75*Pr^.334;   %100<Re<  best result
%Nufw=.2*Re^.8*Pr^.34;   %40<Re<2000  Good Result
 Bif=Nufw.*(N/2).*Perf./(Re*Pr);
 Bis=2.41+.156*(N-1)^2;
%Solid Phase Radial Peclet Number
 C=2.5;
 B=C*((1-eps)/eps)^(10/9);
 kesPkf=2/(1-K*B)*((1-K)*B/(1-K*B)^2*log(1/(B*K))-(B+1)/2-(B-1)/(1-
K*B));
 krsPkf=(1-eps)^0.5*kesPkf;
 Pers=Re*Pr/(krsPkf);
 pehr0=Bi0/(Bi0+4)*((Perf)^-1*Bif/(Bif+4)+Pers^-1*Bis/(Bis+4))^-1
```

```matlab
%%%%%%%%%% Yagi and WAKAO 1959%%%%%%%%
%   kerPkf= 6+0.11*Re*Pr;  %Glass sphere
%      Per= Re*Pr/(kerPkf);
%       kerPkf= 13+0.11*Re*Pr;  %Metal sphere
%        Per= Re*Pr/(kerPkf);
%         pehr0=12;
x0=[Bi0,pehr0];
 A=[];
 b=[];
 Aeq=[];
 beq=[];
lb=[0.01,1];
ub=[30,30];
nonlcon=[];
  [x,fval] = fmincon(@myfun,x0,A,b,Aeq,beq,lb,ub,nonlcon,options)
% [x,fval] = lsqnonlin(@myfun,x0)
 function answ = myfun(xx)
Bi=xx(1);
pehr=xx(2);
x=6.736653006;
tet=[…]';
y=[…]';
m=size(tet,2);
for i=1:m
    f(i)=teta(Bi,pehr,x,y(i));
end
answ=norm(real(f-tet));


function tet=teta(Bi,pehr,x,y)
N=3.114;
eps=0.491;
Re=600;
n=100;
Pr=0.701;
%Zehner-Schulander (1973)
kp=1.01;
kf=0.07601;
K=kf/kp;
%C=1.25 for sphere
%C=2.5 for Cylinder and Raschig rings
```

```matlab
%C=1.4 cruhed particles
%C=2.5*(1+(di/do)^2) Hollow Cylinder
C=2.5;
B=C*((1-eps)/eps)^(10/9);
kasPkf=(1-eps)^0.5*2/(1-B*K)*((1-K)*B/(1-K*B)^2*log(1/(B*K))-(B+1)/2-
(B-1)/(1-K*B));
Peas=Re*Pr/(kasPkf);
Peafinf=2;
peha=1/(1/Peafinf+1/Peas);
%Vortmeyer (1974)
slan=1;
i=1;
lani=2;
lan(i) = fzero(@(L) Bi*besselj(0,L)-L*besselj(1,L),lani);
i=2;
while slan<n+1
    lani=lani+1;
    lan(i) = fzero(@(L) Bi*besselj(0,L)-L*besselj(1,L),lani);
    if abs(lan(i)-lan(i-1))>0.00001
        i=i+1;
    end
    slan=size(lan,2);
end
lan(end)=[];
lan';
tet=0;
for i=1:n
%     B=(1+4*lan(i)^2/peha/pehr)^0.5;
%     tet=tet-
Bi*(1+B)*besselj(0,lan(i)*y)/(Bi^2+lan(i)^2)/B/besselj(0,lan(i))...
%          *exp(-peha*(B-1)*x/2);
B=4*x/pehr/N/(1+(1+16*lan(i)^2/peha/pehr/N^2)^0.5);
     tet=tet+besselj(0,lan(i)*y)*exp(-
lan(i)^2*B)/(lan(i)*(1+(lan(i)/Bi)^2)...
        *besselj(1,lan(i)));
end
% tet;
tet=2.*tet;
```

Acknowledgments

The completion of my PhD research has experienced a strenuously challenging journey. During this soul-searching work, I realized that life is riddled with mysteries. I am, however, grateful to all those who, in more ways than one, selflessly guided and chaperoned me so as to overcome the ensued obstacles and reach the set goalpost.

First and foremost, I would like to express my heart-felt appreciation to Prof. dr. ir. Andrzej I. Stankiewicz (my promotor at TUDelft) and Prof. dr. Esmail A. Foumeny (my earlier promotor at LSB University) for their immeasurable contribution in enabling me to fulfil my PhD research. I can never forget the generosity being offered, and words cannot adequately replicate my sentiments. The appreciation is extended to Prof. dr. John F. Missenden (at LSB University) for his continued support.

Heartily, I would like to extend my sincere gratitude to my daily supervisor and promotor Prof. dr. ir. Johan Padding for his infinite patience and a big "Thank You" for the vast impact he had on my both personal and professional development. You are always available, whenever needed, to answer my scientific queries and also to guide me even for daily life issues in the Netherlands. I will never forget our constructive discussions and his logical/methodical approach which enriched my research reasoning. His leadership certainly enabled me to handle the more-than demanding research task and the Graduate School courses. Johan, I am extremely indebted and thankful to you for all you have done for me.

I would also like to responsively acknowledge the project manager and policy adviser at 3mE's Graduate School, Ms. Mascha Toppenberg, for her time and guidance, particularly in paving the way for completion of all the requirements laid down by the Faculty Graduate School.

It is very appropriate to register my appreciation to all the support staff of the Process & Energy Department as well as to the P&E office professionals, in particular to Leslie and Helma, who have always been more than willing to assist me. Expression of gratitude is pleasurably extended to my colleagues and friends, who made my research period memorable; thank you to Sathish, Rong, Ivan, Vinay and Stephan, also special thanks to Seyed Hossein, Ahmadreza, Gustavo, Farnaz, Nikolaos, Hadi, Mohammad, Mariëtte, Fatima, Vilborg, Mara, Andrea, Ali, Andrew, Luis, Fatma, Christos, Ahad, Sergio, Simone, Jelle and Stephan.

Curriculum Vitae

Elyas M. Moghaddam was born on September 21st, 1983 in Gonabad, Iran. He fulfilled his higher education degrees, BSc. (2006) and MSc. (2008) both in the field of chemical engineering at the Ferdowsi University of Mashhad and Iran University of Science and Technology (the first university in Iran to have established chemical engineering discipline). His major specialization during the Bachelor degree centered on the design of natural gas refining process, while the Master level centered on investigation of transport phenomena in porous media. He has constantly secured top positions during his MSc. Study, as evidenced by his grades and was duly awarded medals and certifications to signify his academic achievements.

Elyas has around eight years of hands-on experiences as a process senior and lead engineer in some of the most famous research institutes and engineering/construction consultant companies in Iran. In this capacity, Elyas published numerous industrial reports and publications.

In 2012, Elyas commenced his PhD research concerning fixed bed catalytic reactor design at London South Bank University. This initial PhD research was pursued under the supervision of Prof. dr. Esmail A. Foumeny and Prof. dr. John F. Missenden with the goal of assessing the role of tortuous structures on local flow fields and heat transfer typified by effective lumped parameters in narrow tubular fixed bed arrangements. In October 2017, Elyas moved to the Netherlands to complete his doctoral research in the Process and Energy Department at Delft University of Technology under supervision of Prof. dr. ir. Johan T. Padding and Prof. dr. ir. Andrzej A. Stankiewicz. The objective of his research was to further extend towards addressing the in-situ behavior of the flow field and heat transfer in tubular fixed beds of non-spherical and non-convex pellets. The results of this research have been published in peer-reviewed journals and presented at a number of European and international symposia in the field of chemical reactor engineering. Besides this, Elyas has worked as lecturer and teaching assistant for a process technology course for bachelor students. Since 2018, Elyas is working as a postdoctoral researcher in the Large-Scale Energy Storage Group in the same P&E department on the subject of supercritical water gasification of wet biomass, under the leadership of Prof. dr. ir. Wiebren de Jong.

Publications

1. **E.M. Moghaddam,** E.A. Foumeny, A.I. Stankiewicz, J.T. Padding, **A Rigid Body Dynamics Algorithm for Modelling Random Packing Structures of Non-Spherical and Non-Convex Pellets,** Ind. Eng. Chem. Res. 57 (2018) 14988–15007. doi:10.1021/acs.iecr.8b03915.

2. **E.M. Moghaddam,** E.A. Foumeny, A.I. Stankiewicz, J.T. Padding, **Fixed Bed Reactors of Non-Spherical Pellets; Importance of Heterogeneities and Inadequacy of Azimuthal Averaging,** Submitted to Chem. Eng. Sci. (September 2018).

3. **E.M. Moghaddam,** E.A. Foumeny, A.I. Stankiewicz, J.T. Padding, **Sequential RBD-CFD Simulations of Hydrodynamics in Narrow-Tube Fixed Bed Reactors with Raschig Rings,** (to be submitted).

4. **E.M. Moghaddam,** E.A. Foumeny, A.I. Stankiewicz, J.T. Padding, **RBD-CFD Simulations of Wall-to-Bed Heat Transfer in Tubular Fixed Bed Reactors with Non-Spherical Pellets,** (to be submitted).

5. **E.M. Moghaddam,** E.A. Foumeny, A.I. Stankiewicz, J.T. Padding, **The Problem of Length-Dependency of Effective Heat Transfer Parameters in Pseudo-Continuum Modelling of Fixed Bed Reactors** (in preparation).

6. **E.M. Moghaddam,** E.A. Foumeny, A.I. Stankiewicz, J.T. Padding, **Fluid-to-Pellet Heat Transfer Coefficients in Tubular Fixed Bed Reactors with Non-Spherical Pellets** (in preparation).

7. **E.M. Moghaddam,** E.A. Foumeny, A.I. Stankiewicz, J.T. Padding, **Wall-to-Bed Heat Transfer Coefficients in Tubular Fixed Bed Reactors with Non-Spherical Pellets** (in preparation).

Oral/Poster Presentations

1. **E.M. Moghaddam,** E.A. Foumeny, A.I. Stankiewicz, J.T. Padding, **A Novel Computational Approach in Modelling Tubular Fixed Bed Reactors: Aspects of Hydrodynamics and Heat Transfer,** the 25th International Symposium of Chemical Reaction Engineering, 25-May-2018, Florence, Italy.

2. **E.M. Moghaddam,** E.A. Foumeny, A.I. Stankiewicz, J.T. Padding, **A Novel Physics-Based Algorithm for Modelling Random Packing Structures of Non-Spherical and Non-Convex Pellets,** the 25th International Symposium of Chemical Reaction Engineering, 25-May-2018, Florence, Italy.

3. **E.M. Moghaddam,** A.I. Stankiewicz, J.T. Padding, **RBD-CFD Simulations of Hydrodynamics and Heat Transfer in (Non-)Spherical Fixed Beds,** the 15th Netherlands Process Technology Symposium Symposium of Chemical Reaction Engineering, 30-May-2018, Twente, Netherlands.

4. **E.M. Moghaddam,** A. Farbod, **A Novel Approach in Modelling Narrow-Tube Fixed Bed Reactors; The Role of Tortuous Structure on Transport Properties,** European Symposium of Chemical Reaction Engineering, 27-October-2015, Munich, Germany.